Markus Kratzer

Reaction Kinetics & Dynamics of H_2, O_2 and CO on modified Pd(111) surfaces

Dissertation
zur Erlangung des akademischen Grades
Doktor techn.
der Studienrichtung Technische Physik

Technische Universität Graz

Betreuer:
Ao.Univ.-Prof. Dipl.-Ing. Dr.techn. Adolf Winkler
Institut für Festkörperphysik

Graz, Jänner 2009

Acknowledgement

When the present work came into being it was a challenging task which could not be accomplished by one single person. There have been many helping hands of many people that helped me with their technical skill, their experience, their knowledge and with encouraging words.
I specially would like to thank my supervisor Prof. Dr. Adolf Winkler for his great support during this PhD thesis. Furthermore, I owe many thanks to Johanna Stettner, Anton Tamtögl and Jörg Killmann for their valuable contribution. Special thanks appertain to Gernot Pauer for his guidance during the first months at the institute. Additionally, I have to acknowledge Martin Kornschober who understood it brilliantly to realize my sometimes confused construction plans into working devices.
Great thanks also go to my Lab mates Paul Frank and Stefan Müllegger for many pleasant hours of working in a climate of friendship. The same applies to Robert Schennach, Axel Stupnik and Hans Peter Koch who always had time for my concerns.
I specially want to thank Peter Lichtenberger who was a friend to me for almost the whole time at the university.
Last but not least I am deeply grateful to my family Paul and Nicola who always gave me the greatest support.

Abstract

Detailed understanding of the interaction of gases with surfaces is crucial for the design of catalysts. Ultra high vacuum conditions provide an environment to study specific aspects of the influence of different surfaces and surface structures on adsorption and desorption processes. Especially metal/metal-oxide surfaces are of interest due to their importance in the field of heterogeneous catalysis. In this work the interaction of hydrogen, deuterium, oxygen and carbon monoxide with modified Pd(111) single crystal surfaces has been investigated. The desorption of deuterium and the water formation reaction between deuterium supplied by permeation through the palladium bulk and impinging molecular oxygen on clean and vanadium oxide covered Pd(111) was studied. Quadrupole mass spectrometry has been utilised to determine the flux of reaction products desorbimg from the surface. The stability of the vanadium oxide structures under reaction conditions was studied by low energy electron diffraction (LEED) and Auger electron spectroscopy (AES). The (2×2) s-V_2O_3 phase turned out to be the most stable at 523 K. At temperatures above 700 K the VO phase is preferred. Evidence for a change in the VO_x structure during water formation at 700 K could be found. The kinetics of water formation on clean Pd(111), as found by flux measurements, is mainly determined by the oxygen sticking coefficient. For the VO_x covered surface it could be shown that the water formation rate drops with increasing VO_x coverage and increases with rising sample temperature. The mean translational energy of the desorbing D_2 as determined by time-of-flight (TOF) spectroscopy is indicative for a total thermalization with the surface. The value for the D_2O corresponds to a slightly higher temperature suggesting that higher energetic permeating deuterium contributes with higher probability to the water formation. The angular distribution of the desorbing deuterium turned out to be uninfluenced by the vanadium oxide.
The angular distribution for deuterium desorption at 523 K is close to a cosine distribution whereas at 700 K the distribution gets somewhat forward focused. An even more forward focusing effect has been found on the 0.2 ML potassium covered surface. A comparison with existing TOF data made it possible to get information about the applicability of detailed balancing and normal energy scaling.
Additionally the preparation, structure, stability and kinetics of thin Zn layers (from submonolayer up to 16 ML) deposited on Pd(111) was investigated by scanning tunneling microscopy (STM), LEED, AES and thermal desorption spectroscopy (TDS). The results were compared with density functional theory calculations. It could be shown that Zn exhibits a reduced sticking coefficient on contaminated surfaces which violates the requirements for a proper application of a quartz microbalance for thickness measurements. Therefore much care has to be taken when calibrating the Zn coverage. A ZnPd surface alloy starts to form above 300 K,

which exhibits a (2×1) structure as determined by STM and LEED. TDS measurements show that Zn desorbs in a low temperature feature (400 K - 600 K) which exhibits a complex multiple peak structure and in a broad high temperature desorption feature starting at 780 K (heating rate 2 K/s). The high temperature desorption peak can be attributed to the decomposition of a surface near ZnPd alloy whereas the low temperature feature stems from the Zn multilayer and the desorption of surface near Zn layers.
Furthermore the adsorption and thermal desorption of H_2 and CO on Zn/Pd(111) was studied. Thick Zn layers block the adsorption of molecular hydrogen and CO. Thin Zn layers just act as site blockers for hydrogen adsorption indicated by non shifting desorption peaks with increasing Zn coverage. The energetics of CO desorption is crucially influenced due to the presence of Zn indicated by the appearence of new CO desorption peaks which shift to lower desorption temperatures with increasing Zn coverage. On the ZnPd surface alloy a single CO desorption feature centred around 220 K occurs. The initial sticking coefficient of CO on the ZnPd surface alloy is still close to unity as on the clean Pd surface, indicating a precursor mediated adsorption process.

Kurzfassung

Die vorliegende Arbeit behandelt die Untersuchung unterschiedlicher Aspekte der Gas-Oberflächen Wechselwirkung von Wasserstoff, Deuterium, Sauerstoff und CO mit modifizierten Pd(111) Einkristalloberflächen. Eine experimentelle Besonderheit war, dass Deuterium in atomarer Form über Permeation durch den Palladiumkristall an die Oberfläche gebracht wurde. Die D_2 Desorption als auch die Wasserformierung durch Reaktion mit molekularem Sauerstoff aus der Gasphase wurden untersucht. Als Substrat diente dabei die reine Pd(111) Oberfläche sowie VO_x modifizierte Pd(111) Oberflächen. Die betreffenden Flüsse von Reaktionsprodukten von der Oberfläche wurden mittels Quadrupol Massenspektrometrie bestimmt. Auch die Stabilität der Vanadium Oxid Strukturen unter Reaktionsbedingungen wurde mittels Niederenergie Elektronen Beugung (LEED) und Auger Elektronen Spektrometrie (AES) untersucht. Dabei erwies sich die (2×2) s-V_2O_3 Phase als die stabilste bei einer Probentemperatur von 523 K. Bei Temperaturen oberhalb von 700 K wurde die VO Phase bevorzugt. Unter den Reaktionsbedingungen für die Wasserformierung bei 700 K wurden Veränderungen der VO_x Strukturen beobachtet.
Die Kinetik der Wasserbildung wird, wie Flußmessungen zeigten, hauptsächlich durch den O_2-Haftkoeffizienten bestimmt. Für die VO_x modifizierten Oberflächen zeigte sich eine Reduktion der Wasserproduktionsrate mit zunehmender VO_x Bedeckung aber eine Zunahme mit steigender Substrattemperatur.
Die mittlere translatorische Energie des desorbierenden D_2, bestimmt durch Flugzeitmessungen (time-of-flight, TOF), ist indikativ für eine totale Thermalisierung mit der Oberfläche. Die für das Reaktionsprodukt D_2O bestimmte mittlere kinetische Energie entspricht einer etwas höheren Temperature als sie die Oberfläche aufweist, was darauf hindeuten könnte, dass präferenziell hochenergetisches Deuterium aus dem Permeationsprozess an der Reaktion teilnimmt. Die komplementär zu den Flugzeitmessungen durchgeführte Bestimmung der Winkleverteilungen der Desorptionsflüsse zeigten keinen messbaren Einfluß der VO_x Bedeckung.
Für reines Palladium konnte die Winkelverteilung des desorbierenden D_2 als nahezu kosinusförmig bestimmt werden. Eine Erhöhung der Substrattemperatur auf 700 K ergab eine etwas stärker vorwärts fokussierte Verteilung. Eine noch stärker vorwärts gerichtete Verteilung kann durch eine Bedeckung mit 0.2 ML Kalium erzielt werden. Eine Gegenüberstellung mit existierenden TOF-Daten ließ Schlüsse darauf zu ob und inwieweit das Prinzip des Detailierten Gleichgewichtes und der Normalenergieskalierung auf diese Systeme anwendbar ist.
Zusätzlich wurde auch noch eine Studie über die Präparation, Struktur, Stabilität und Kinetik von dünnen Zn Schichten (Submonolage bis 16 ML) unter Verwendung von Thermischer Desorptionsspektroskopie (TDS), Rastertunnelmikroskopie (STM), LEED und AES durchgeführt.

Die experimentellen Resultate wurden auch mit Rechnungen basierend auf Dichtefunktional Theorie (DFT) verglichen.
Es konnte gezeigt werden, dass Zn auf kontaminierten Oberflächen einen reduzierten Haftkoeffizienten aufweist, was Probleme bei der Bedeckungsbestimmung mittels Schwingquarzmikrowaage verursacht.
Bei Probentemperaturen oberhalb von 300 K beginnt die Formierung einer ZnPd Oberflächenlegierung, welche, wie STM und LEED Messungen zeigen, durch die Bildung einer (2×1) Struktur gekennzeichnet ist. Thermodesorptionsmessungen zeigen zwei deutlich unterscheidbare Desorptionsereignisse, eines zwischen 400 K und 600 K welches eine komplizierte Mehrfachpeakstruktur aufweist und eines mit breiter einfacher Peakstruktur beginnend bei 780 K (Heizrate 2K/s). Der Hochtemperatur-Peak kann auf die Auflösung einer oberflächennahen PdZn--Legierung zurückgeführt werden, wohingegen die Desorption bei niedrigerer Temperatur von der Zn Multilage bzw. von oberflächennahen Zn-Lagen herrührt.
Zusätzlich wurde die Adsorption und thermische Desorption von H_2 und CO auf Zn/Pd(111) untersucht. Dicke Zn-Schichten verhindern die Adsorption von molekularem Wasserstoff und CO. Zn verursacht nur eine Reduktion der aufgenommenen Wasserstoffmenge, führt darüberhinaus aber zu keiner weiteren Veränderung der H_2 Desorptionsspektren, was auf ein einfaches Blockieren von Adsorptionsplätzen schließen läßt. Beim CO TDS jedoch ergeben sich neue Desorptionspeaks welche mit zunehmender Zn Bedeckung zu niedrigeren Temperaturen hin verschieben. Dies deutet auf eine starke Beeinflussung der CO-Substrat Bindung hin. Bei einer reinen ZnPd Legierungsoberfläche besteht nur noch ein einzelner CO Desorptions-Peak bei 220 K. Der Anfangshaftkoeffizient für CO auf dieser Oberfläche bleibt nahe bei eins gleich wie auf der reinen Pd(111) Oberfläche, was auf Adsorption über einen Vorläuferzustand hinweist.

Contents

1 Introduction **1**

2 Theoretical background **3**
2.1 Gas-surface Interactions: . . . 3
2.2 Adsorption and Desorption . . . 4
2.2.1 Adsorption Kinetics . . . 8
2.2.2 Desorption Kinetics . . . 11

3 Experimental Setup **24**
3.1 Ultrahigh-Vacuum-System . . . 24
3.2 Permeation Source . . . 29
3.3 Time-of-Flight Spectrometer . . . 32
3.4 Line-of-Sight detector . . . 34
3.5 Evaporation Unit . . . 36
3.6 Zn Source . . . 39
3.7 Auger Electron Spectroscopy . . . 40
3.8 Low Energy Electron Diffraction . . . 41
3.9 Sample Mounting and Preparation Procedures . . . 42
3.9.1 Sample Cleaning . . . 42
3.9.2 Preparation of vanadium oxide layers . . . 44
3.9.3 Preparation of Zn /ZnO layers . . . 44
3.9.4 Measuring the Angular Distribution . . . 44
3.9.5 Monitoring Reaction Processes using a Permeation Source . . . 45

4 Data Evaluation **47**
4.1 Calibration of Gas Amounts . . . 47
4.1.1 Determination of the Gas Flux . . . 49
4.2 Evaluation of Thermal Desorption Spectra . . . 51
4.2.1 The Leading Edge Method . . . 51
4.2.2 The Redhead Concept . . . 52
4.2.3 Determination of the Absolute Rate . . . 53
4.3 Determination of the Angular Distribution . . . 53
4.4 Evaluation of Time-Of-Flight Spectra . . . 55
4.5 Coverage Determination by AES . . . 58

4.6 Density Functional Theory Calculations 60

5 D_2 on clean Pd(111) 62
5.1 Angular dependence of the deuterium desorption from clean Pd(111) 62
5.2 Summary of Chapter 5 66

6 D_2 on potassium modified Pd(111) 67
6.1 Angular dependence of the deuterium desorption from K modified Pd(111) . . . 67
6.2 Summary of Chapter 6 69

7 D_2O formation on clean Pd(111) 70
7.1 Water Formation Kinetics on Clean Pd(111) 70
7.1.1 Modeling of the Reaction Process. 72
7.2 Summary of Chapter 7 75

8 D_2 and D_2O on VO_x modified Pd(111) 78
8.1 Vanadium Oxide Structures on Pd(111) 79
8.2 Stability of VO_x structures on Pd(111) under reaction conditions 81
8.2.1 Discussion: Stability under Reaction Conditions 85
8.3 Time-of-flight measurements on permeating/desorbing deuterium and D_2O on VO_x modified Pd(111) surface 86
8.3.1 Discussion: TOF spectra 93
8.4 Angular distribution of desorbing deuterium from VO_x covered Pd(111) surfaces 94
8.4.1 Discussion: Angular Distribution 95
8.5 D_2O formation kinetics on VO_x covered Pd(111) 96
8.5.1 Results and Discussion 96
8.6 Summary of Chapter 8 103
8.6.1 TOF Measurements and Stability 103
8.6.2 Angular Distribution 104
8.6.3 Water Formation Kinetics 104

9 Zn on Pd(111) 105
9.1 Calibration of the Zn coverage 105
9.1.1 Results and Discussion 106
9.2 Kinetics of Zn adsorption and desorption on Pd(111) 112
9.2.1 Results and Discussion 112
9.3 Summary of chapter 9 120
9.3.1 Zn coverage calibration 120
9.3.2 Zn Adsorption/Desoption Kinetics on Pd(111) 121

10 H_2 and CO on Zn modified Pd(111) 123
10.1 H_2 on Zn/Pd(111) 123
10.2 CO on Zn/Pd(111) 126

10.3 Summary of Chapter 10 136

11 Summary **137**

12 Bibliography **140**

List of Figures **153**

List of Publications and Conference Contributions **153**

1 Introduction

In many modern technologies a number of different materials tailored for a specific function is used. There are particular matter specific properties utilised. For example steel is the most important material in construction due to its mechanical stability at rather low cost. Copper is superior to other materials concerning electrical conductivity. Typically the term "material property" is adressed to qualities of the bulk material. However for many applications the surface specific properties are crucial. The surface is the interface through which a material has contact with its surrounding. The surface-surface interaction of solids is determining properties like friction, electrical or thermal contact resistance. The interaction of solid surfaces with liquids, vapours or gases has severe influence on corrosion processes. Optical properties are crucially determined by the surface quality. As the invironement has an influence on the surface the surface can have an influence on its surrounding. Important examples for such an interaction can be found in the field of heterogeneous catalysis. In many cases bringing two reactants into contact is not sufficient to obtain a desired product. Not even when the reaction should formally be exothermic. The reason for this is most often that for one or more intermediate reaction steps an energetic barrier has to be overcome. In some cases this problem might be solved by increasing the temperature to provide the needed energy and/or increasing the pressure (density of the reactants) to increase the probability for the reaction. Even these measures might not yield the desired result because there might be a second reaction path with a slightly lower activation barrier which is favored. In such cases the reactivity and selectivity can be dramatically increased by utilising a catalyst. In heterogeneous catalysis there are solid catalysts used. The reactants are supplied in liquid or gaseous form and interact with the surface. Specific reactions on the surface then yield the demanded results. Famous examples for such heterogeneous catalytic processes are the Fischer-Tropsch synthesis [1] or the Haber-Bosch method [2]. The Fischer-Tropsch synthesis provides the generation of more complex hydrocarbons from a H_2/CO gas mixture via solid iron-, magnesiumoxid-, thoriumdioxid- or cobalt-catalysts. The Haber-Bosch method makes the synthesis of ammonium from N_2/H_2 gas mixtures possible using an ironoxide based catalyst.

Even though the heterogeneous catalysis is a widely used standard technique in many cases the microscopic processes are not clear yet. To gain some understanding of the mechanism which leads to the macroscopic visible results the microscopic processes which determine the overall behaviour have to be studied. This can just be accomplished by studying each single process separately under idealized conditions. A maximum of idealization can be achieved by using single crystal surfaces under ultra high vacuum conditions.

Especially the modification of metal single crystal surfaces with ultra thin metal oxide layers

has attracted scientific interest in the rescent years. Since catalysts are normally built up by metal oxide substrates which are coated with thin metal layers these systems can be considered as model systems for "inverse catalysts".
Within this work a Pd(111) single crystal surface was modified by VO_x, Zn and potassium. Vandium oxide is known to form a number of various oxide nano structures on Pd(111) [3–9] and only little is known about their influence on the gas surface interaction. Therefore a part of this work deals with the interaction of hydrogen, deuterium and oxygen with these surfaces in view of dynamic and kinetic aspects utilising time-of-flight (TOF) spectroscopy, angular distribution measurements and desorption flux measurements.
In addition to the hydrogen/deuterium desorption from clean and VO_x modified Pd(111) surfaces the influence of potassium adlayers on the desorption of hydrogen was studied. Especially the angular distribution of the desorption flux was investigated, which represents a completion of the time-of-flight measurements performed in foregoing works [10–13].
Another system which has attracted the curiosity of scientists is Zn and ZnO on palladium. Pd/ZnO based catalysts have shown superior performance in the methanol processing technology [14–27], which is important for the storage of hydrogen and the operation of methanol fuel cells [21; 28; 29]. Especially the formation of ZnPd alloys are suspected to be responsible for the good catalytic performance [14–16; 20; 24; 25; 27]. Only few experimental work has been done on the Zn/Pd(111) system, yet [30–32]. Hence a big part of this thesis deals on the one hand with the preparation and kinetics of Zn/Pd(111) and on the other hand with the interaction of hydrogen and CO with this surface.

2 Theoretical background

2.1 Gas-surface Interactions:

The adsorption of reactants is always the initial step to any chemical reaction on a surface. This statement sounds trivial but represents one of the most important issues in catalysis and surface science. Particles that approach the surface from the gas phase can undergo a number of processes which are in first line related to the energy transfer between the particle an the surface. These processes are determined by the inital conditions right before the collision like translational energy, rotational and vibrational states of the particle, surface temperature, location of the impact, relative position of the molecule axes to the surface and so on:

Elastic scattering: A particle can be just reflected by the surface. In this case no net energy transfer between particle and surface is possible. This case is just explainable by quantum mechanics because scattering without energy transfer is not possible from the classical point of view.

Inelastic scattering: Some energy transfer from particle to surface or vice versa is involved. Not only the total energy of the particle (molecule) is changed but additionally the energy is redestributed in the internal degrees of freedom. Therefore vibrational and rotational excitation as well as the opposite is possible.

Trapping: Is the loss of energy due to the impact high enough the particle cannot directly rebounce back to the gas phase. Initally the particle remains in a weakly bound state provided by the surface. There it can perform oscillations against the surface with a frequency which is typically in the 10^{13} Hz range. Nevertheless, the particle is generally not trapped forever. Due to energy absorption from the phonon bath provided by the solid at temperatures above 0 K an escape back to the gas phase is possible. The dwelltime is much longer than a period in the surface oscillation.

Sticking: Once a particle is trapped in the sense of the latter paragraph it can be transferred to lower energy levels of the attractive potential well provided by the surface. There is a certain probabilty for a particle in the initial state i occuring in a bound state j after a vibrational period. After every period in the potential well an energy transfer process given by the energy transfer function $P(\Delta\epsilon)$ is possible. The mean energy transfer over time is negative but the deviation of $P(\Delta\epsilon)$ can yield an energy win sufficient for leaving the potential well (see trapping). The longer the residence time of the particle is the less probable an escape back into the gas phase gets. The reason for this is that the particle relaxes rather fast from the states near

the vacuum level to stronger bound states deep in the potential well. The probabilty for a particle of the gas phase to reach a state near the bottom of the potential well is called sticking probability.

In principle two energy transfer mechanisms can be distinguished. Phonon interaction and elctron-hole interaction.

Phonon interaction: An impinging particle can hit a single surface atom which is elastically bound to its neighbours. The elongation of the surface atom due to the collision leads to excitation of vibrations in the solid (phonon excitation). Complementary can the thermal motion of the surface atoms be transferred to a gas phase particle in the range of interaction (phonon absorption).

Electron-hole interaction: The energy transfer to the electronic system is normally the minor part of energy dissipation. An atom or molecule approaching the surface can feature an unoccupied electronic state slightly above the fermi level of the solid. Induced mirror charge effects can lead to a shift of the unoccupied electronic state below the Fermi edge. Then an elctron from the solid can tunnel into the unoccupied level generating an elctron-hole pair.

2.2 Adsorption and Desorption

If the interactions between a surface and an approaching particle lead to a situation where the particle is kept in close distance to the surface this is called adsorption. The involved bonding mechanisms are distinguished with respect to their physical origin [33–37].

Physisorption: The weakest form of bonding of an atom or molecule (adsorbate) to a solid surface is named physical adsorption or in a short term physisorption. The characterizing feature of physisorption is the lack of a true chemical bond between the adsorbate and the surface. It is convenient to consider the interaction to be divided into two parts, a weakly attractive van der Waals force and a strong repulsion (Pauli repulsion) [33]. In principle all atoms and molecules experience a van der Waals interaction when they are brought close to a surface. Nevertheless they show different chemical interaction depending on their individual electronic configuration. Those with closed electron shells will provide poor chemical reactivity and therefore the pure van der Waals interaction will be dominat. Molecules and atoms with open shells show greater chemical reactivity when they are close to the surface. For those van der Waals interactions play a minor role. Therfore a prime example for physisorption is the bonding of a rare gas atom to a solid surface. The van der Waals force originates from the polarizable solid interacting with dipolar quantum mechanical fluctuations of the atomic charge distribution. The electrons in the atom are attracted to their image charges in the solid.

When an atom gets closer to a surface the nature of interaction begins to be more chemical in that sense that the electron wave functions of the atom and the surface begin to overlap. In case of physisorption systems (like rare gases) this results in two effects: Firstly, the kinetic energy of the Bloch electrons in the solid is increased because they are forced to orthogonalize to the localized states of the approaching atom. Secondly, the potential energy of the Bloch electrons is decreased due to the presence of the positively charged atomic core. The first effect

dominates in practice which explains the strong repulsive force.
The attractive dipol interaction potential between two atoms at distance r is proportional to r^{-6}. The potential for the Pauli repulsion between two atoms is typically approximated by r^{-12} [34]. The total potential describing an atom-atom interaction can then be approximated by the so called Lennard-Jones potential

$$V(r) = V_0 \left\{ \left(\frac{r_0}{r}\right)^{12} - 2\left(\frac{r_0}{r}\right)^{6} \right\} \tag{2.1}$$

in which $-V_0$ is the potential at the equilibrium distance r_0. The van der Waals interaction takes place between the adsorbate and all atoms of the solid. Therefore the total interaction potential between an atom at position $\mathbf{r}_a$ and the surface is given by the sum over all two-body potentials (2.1)

$$V_{surf}(\mathbf{r}_a) = V_0 \sum_{\mathbf{n},\alpha} \left\{ \left(\frac{r_0}{\left|\mathbf{r}_a - \mathbf{r}_{\mathbf{n},\alpha}\right|}\right)^{12} - 2\left(\frac{r_0}{\left|\mathbf{r}_a - \mathbf{r}_{\mathbf{n},\alpha}\right|}\right)^{6} \right\} \tag{2.2}$$

The triplet $\mathbf{n}$=(n_1, n_2, n_2) account for summation over all unit cells and the index α denotes the atoms in the unit cell. However the results obtained from the latter model are just useful for large distances between the adsorbate and the surface. At short distances chemical interactions come into play which make the simple van der Waals model invalid.
Chemisorption: At short distances between the adsorbate and the surface an increasing overlap of the electron wave functions takes place. Due to this overlap the electronic configurations of the approaching molecules or atoms undergo a significant change. The solid and the adsorbate perform an exchange of charge leading to a binding of chemical character. The analogy to a normal chemical bond between two atoms or molecules is not quite consistent. Each sharp electronic level of the adsorbate involved in the surface interaction is split in two bands, a bonding band and an antibonding band. Due to the interaction of the adsorbate electrons with the total electronic surface band the bond is less localized compared to an atom-atom bond [35]. The disturbance of the electronic configuration can be more or less pronounced depending on the individual properties of adsorbate and surface.
Dissociative Adsorption: For molecules the change of the electronic structure can end up in a partly or even total dissociation of the molecule. In this case the process is called dissociative adsorption [34–37]. The first work which provided a qualitative understanding of the dissociative adsorption of a diatomic molecule was given by Lennard-Jones [38]. He introduced a one dimensional interaction potential composed from the potential energy curve of the intact molecule on the one hand and the potential energy curve of the single atoms of the dissociated molecule as shown in figure (2.1).

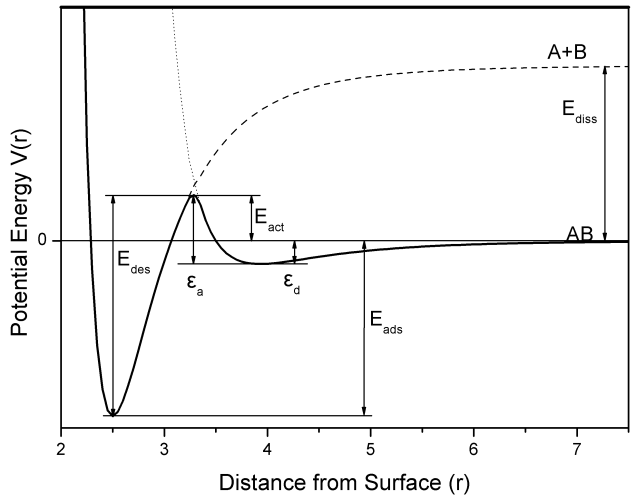

(a) Potential for activated dissociative adsorption

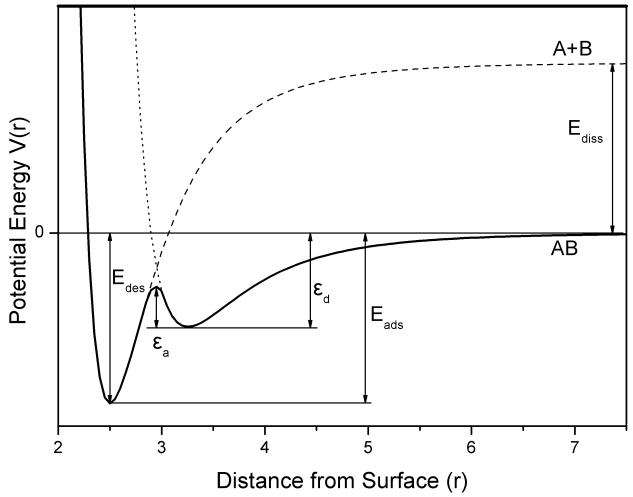

(b) Potential for non-activated dissociative adsorption

Figure 2.1: Lennard-Jones potentials for activated (a) and non-activated (b) dissociative adsorption.

The intact molecule (AB) at infinite distance from the surface is chosen to define the zero-point of the potential energy (in practice this is a distance where the molecule is not influenced by the surface and vice versa). As the molecule approaches the surface it experiences a potential V(r) which exhibits a physisorption minimum at some distance from the surface (thin dotted line in figure(2.1(a))). The dashed thin line corresponds to the potential energy of the single constituents A and B approaching the surface. At infinite distance V(r) starts at a value above the latter defined zero-point which is just given by the dissociation energy E_{diss}. At closer distances to the surface V(r) can show a deep minimum which is determined by the

chemisorptive bonding of the individual atoms A and B to the surface.
However, in reality the adsorption process always starts with the intact molecule far away from the surface. Additionally, one has to assume that the molecule has some initial translational momentum pointing towards the surface and therfore additional kinetic energy. Otherwise the molecule would never approach the surface but stay right at its starting point. Now the molecule approches the surface just experiencing the physisorption potential. If it has sufficient (translational) energy it can reach the point where the potential energy curve of the intact molecule (AB) crosses the potential energy curve of the dissociated molecule (A+B). At this point both states, molecular and atomic, are energetically equal. Therefore a transition from the molecular to the dissociated state does not demand additional energy and the molecule can dissociate and pass into the chemisorption well. This process does not necessarily occur every time when a molecule with sufficient translational energy hits the surface. It is possible that the molecule first undergoes transient physisorption where it is scattered back into the physisorbed state. From there it can then either escape back into the gas phase or reach the chemisorbed state. The sojourn of the molecule in the physisorption well before chemisorption is called a precursor to the chemisorbed state. Whether there is direct chemisorption, physisorption, chemisorption via a precursor state, or scattering depends on the details of the competing potential energy curves. Especially the location of the crossing point of the two potential energy curves defines the character of the process. If the crossing point lies in the negative energy region a molecule can spontaneously dissociate by passing the intersection and no additional energy is needed like shown in figure (2.1(b)). In case of a crossing point located at positive energies the molecule has to overcome an energy barrier E_{act} which is given by

$$E_{act} = E_{des} - E_{ads}$$

(see figure (2.1(b))). Of course this simple one dimensional and adiabatic model is a rough simplification of the real problem and does not allow generalization if more than one coordinate is necessary to describe the process. For a quantitative theory, a number of curves between AB and A+B have to be introduced corresponding to vibrational and rotational states of the molecule. Additionally, for any position in the surface unit cell a separate band of potential energy curves is needed. Calculating all these curves within a unit cell and connecting the points of constant energy would then yield a potential energy surface (PES) which describes the whole interaction. Thus in principle a high dimensional problem has to be solved which means a high computational cost and/or some approximations [38–41]. Fortunately, in most cases it is not necessary to account for all degrees of freedom. In many cases it is possible to reduce the problem to a few relevant coordinates. Consideration of cross sections along highly symmetric planes in the configuration space yields additional simplification.
A well known example of such a simplification is the so-called elbow plot. In this case typically the distance of the centre of mass of the molecule and an additional degree of freedom is used. In figure (2.2) the elbow plot of a hydrogen molecule approaching the Pd(100) surface upon a specific site of the surface unit cell with its molecular axes parallel to the surface is shown. The used coordinates are the distance of the molecular centre of mass to the surface and the molecular bond length [42].

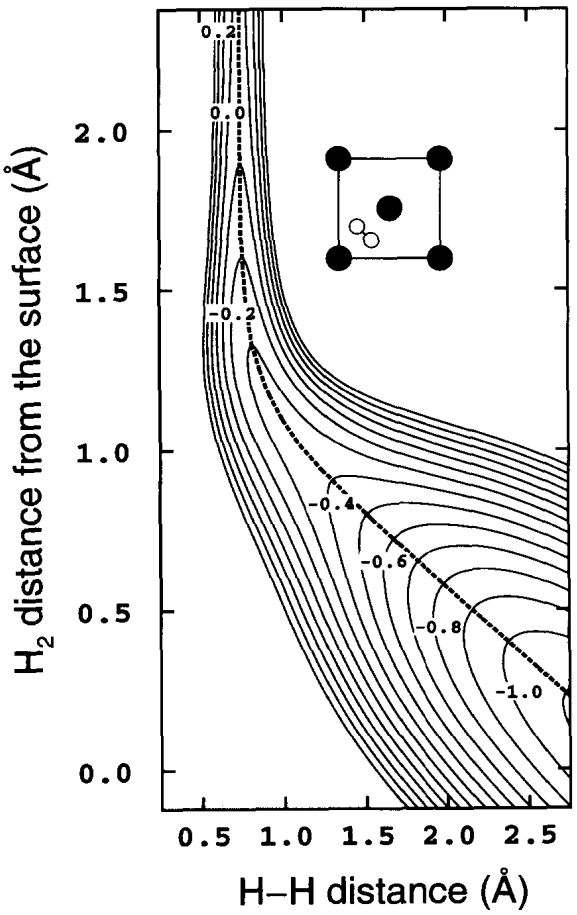

Figure 2.2: Contour plot of the PES along a two-dimensional cut through the six-dimensional coordinate space of H_2/Pd(100). The inset shows the location of atoms above the surface as well as the orientation of the molecule axis.(Taken from [42])

2.2.1 Adsorption Kinetics

Coverage Dependence of the Sticking Coefficient

As already mentioned in section 2.1 particles can be trapped at the surface just by loosing energy to the lattice so that its residual energy is not sufficient to leave the surface again. The phenomenon of sticking is fundamentally different. Again the energy loss to the surface is a cruicial point but additionally the particle has to form a strong bond to the surface. Therefore sticking depends on both the rate of energy transfer and the ability of the surface to form bonds.

Sticking is commonly treated in terms of a sticking probability $S(\Theta)$ which is a function of the coverage Θ. The sticking probability or sticking coefficient is defined as the ratio of the number of molecules that stick (N_{ads}) and the number of molecules that impinge on the surface (N_{imp}).

$$S(\Theta) = \frac{N_{ads}}{N_{imp}} \tag{2.3}$$

The adsorption rate r_{ads} is then related to the flux of impinging molecules f by

$$r_{ads} = S(\Theta) \cdot f \tag{2.4}$$

For isotropic impinging molecules of mass $m_{Mol.}$ the flux f onto the surface area dA per time dt can be calculated as

$$f = \frac{d^2N}{dA \cdot dt} = \frac{p}{\sqrt{2 \cdot \pi \cdot m_{Mol.} \cdot k_B \cdot T_g}} \tag{2.5}$$

where p is the isotropic pressure, k_B is the Boltzmann constant and T_g is the gas temperature. An experimental method to determine the coverage dependent sticking coefficient is to measure so called uptake curves. For this purpose the surface is exposed to various amounts of gas (EX) and the amount of adsorbed gas A_{ads} is then determined. The uptake curve is then a plot auf A_{ads} as a function of EX. From this uptake curve one can determine $S(\Theta)$ by

$$S(\Theta) = \frac{dA_{ads}}{dEX} \tag{2.6}$$

The exposure EX can be calculated by integration of equation 2.5 over time

$$EX = \int_0^{t_{exp}} \frac{p}{\sqrt{2 \cdot \pi \cdot m_{Mol.} \cdot k_B \cdot T_g}} \cdot dt \tag{2.7}$$

The sticking probability derived from uptake curves usally is not very accurate. There are methods described in the literature which allow a determination with higher accuracy [43–45]. Typically the sticking probability in the limit of zero coverage $S(0)$ is measured and the variation of the sticking probability with coverage $S(\Theta)$ is expressed as the ratio $\frac{S(\Theta)}{S(0)}$. Usually the sticking coefficient drops from its initial value at zero coverage to zero at saturation coverage. This behaviour can be described by the adsorption model introduced by Langmuir [46].
The Langmuir Adsorption Model is based on the following assumptions

- adsorption is limited by the monolayer coverage
- all adsorption sites are equivalent
- only one molecule can reside in an adsorption site

An incident molecule can now stick with some probability at a free site and is scattered at an occupied site. If a molecule dissociates into n species there are n free adsorption sites needed. In the simple case the fact that a molecule might need adjacent free adsorption sites to dissociate is neglected. The probability for a molecule to find an adsorption site at a coverage Θ can then generally be expressed as $(1 - \Theta)^n$ where n is called the kinetic order. Equation (2.4) can then be rewritten into

$$r_{ads} = S(0) \cdot (1 - \Theta)^n \cdot f \tag{2.8}$$

where S(0) is the initial sticking coeffcient at zero coverage. There are some real chemisorption systems that are described well by expression (2.8). However, for many systems one has to consider that adsorption takes place via a precursor state.
One can define a trapping coefficient s_P which represents the probability for a molecule to be trapped in the precursor state. Molecules in the precursor state can then desorb back to the gas phase at a rate k_d or pass into the chemisorbed state at rate k_a. By introducing the parameter $K = \frac{k_a}{k_d}$ one can write the overall sticking coefficient as [46]

$$S(\Theta) = s_P \cdot \frac{(1+K)\cdot(1-\Theta)^n}{1+K\cdot(1-\Theta)^n}. \tag{2.9}$$

In case of low desorption rates k_d from the precursor state $K \longrightarrow \infty$ and $S \longrightarrow 1$. For high values of k_d the sticking coefficient S approaches the Langmuir adsorption kinetics. In figure (2.3) the qualitative differences between non-dissociative adsorption (first order, curve b), dissociative adsorption (second order, curve a) and precursor mediated dissociative adsorption (second order, curve c) according to the latter model are shown.
Even though the descibed models for adsorption kinetics reflect the adsorption process of some systems quite well there are still deviations for many systems due to the simplification of the problem. There can be more than one possible adsorption site for a molecule. Different adsorption sites can provide different sticking probabilities and different adsorption orders. A precursor state might be located spacially right over a free adsorption site (intrinsic precursor) or might be provided by an already adsorbed molecule (extrinsic precursor). Both, extrinsic and intrinsic precursors can be energetically different due to interaction between adsorbates. The adsorbates can be mobile in the precusor state, which means that they are not necessarily scattered if they hit an occupied site but can rather diffuse along the surface and find another free adsorption site. Additionally there might be active centres for adsorption like surface defects [47].
Temperature Dependence of the Sticking Coefficient: In the case of a simple chemisorption system which can be represented in the picture of a one-dimensional potential as a single chemisorption well the sticking probability is effectively independent of the sample temperature as long as $E_{ads} >> k_B \cdot T_{surface}$. For a precursor mediated system things are different because there is an additional shallow well adjacent to the deep chemisorption well. Both wells are separated by an energy barrier. If a particle is trapped in the shallow precursor well it can be desorbed back into the gas phase or it can be adsorbed in the chemisorbed state. The rates of adsorption k_a and desorption k_d can be expressed as [46]

$$k_d = \Theta_p \cdot \nu_d \cdot e^{\frac{-\epsilon_d}{k_B \cdot T_s}} \tag{2.10}$$

and

$$k_a = \Theta_p \cdot \nu_a \cdot e^{\frac{-\epsilon_a}{k_B \cdot T_s}} \tag{2.11}$$

where ν_d and ν_a are the rate constants and Θ_p is the coverage in the precursor state. The expressions ϵ_d and ϵ_a represent activation energies for desorption and adsorption (see figure

2.1) and T_s is the surface temperature. Therefore the initial sticking coefficient can be written as

$$S(0) = \frac{k_a}{k_a + k_d} = \left[1 + \frac{\nu_d}{\nu_a} \cdot e^{-\frac{\epsilon_d - \epsilon_a}{k_B \cdot T_s}}\right]^{-1} \tag{2.12}$$

Therefore it is clear that the temperature dependence is crucially determined by the relative values of ϵ_d and ϵ_a. For the case of activated adsorption as illustrated in figure (2.1(a)) one has $\epsilon_d < \epsilon_a$ and s_0 increases as the substrate temperature increases. In case of non-activated adsorption (figure (2.1(b))) $\epsilon_d > \epsilon_a$ and s_0 decreases with increasing substrate temperature.

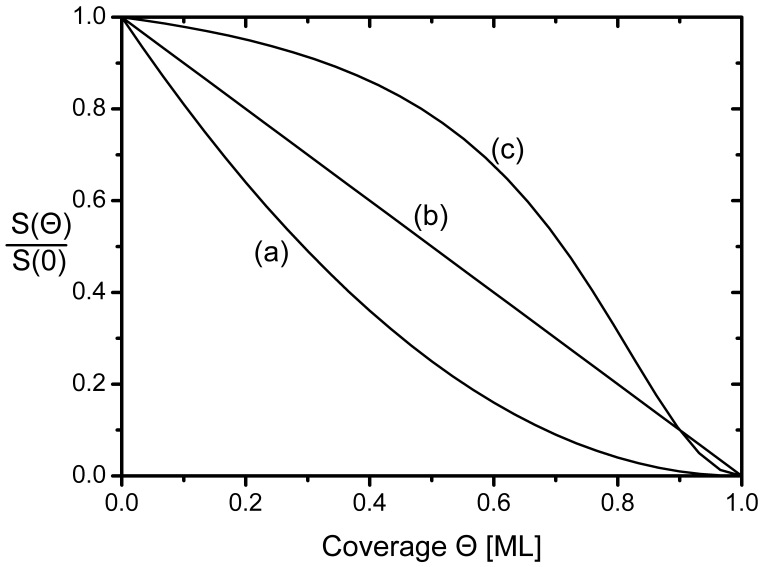

Figure 2.3: Calculated coverage dependent sticking coefficient $S(\Theta)$ normalized to the initial sticking coefficient $S(0)$ as a function of coverage Θ. Dissociative adsorption with n=2 (a), non-dissociative adsorption with n=1 (b) and precursor mediated dissociative adsorption with n=2 and K=8 (c).

2.2.2 Desorption Kinetics

The Principle of Detailed Balance

By considering a system where a gas phase is in equilibrium with a surface one can find a close relation between adsorption and desorption. In this case particles can interact with the surface as described in the previous sections. To maintain equilibrium the rates of the forward step and the reverse step of any process has to be equal. In case of gas surface interaction this means that the rate of adsorption of molecules from state i must equal the desorption rate of molecules into state i [35]. This principle is called **detailed balancing** [48–50] due to the fact that in thermodynamic equilibrium this has to be generally valid no matter what the detailed processes are which are considered.

The concept of detailed balancing can be expressed in terms of a transition probability λ_{ij} which reflects the transition of a system in state i to state j per unit time and an occupation probability p_i for the system to be in state i. The λ_{ij} are considered to be time independent. Detailed balancing can then be written as

$$p_i \cdot \lambda_{ij} = p_j \cdot \lambda_{ji} \tag{2.13}$$

in equilibrium [51]. Under equilibrium conditions the principle of detailed balance is valid irrespectively of the kind of interaction since the describing equations of motion are invariant under time reversal [52]. This condition is often called **microscopic reversibility**. The trajectory of a molecule is determined by the forces acting on the particle and the acting forces are determined by the kind of interactions which are taking place. Sometimes the trajectory ends at an adsorption site on the surface and sometimes the molecule is just scattered. Considering a particle that is adsorbed on the surface it is quite clear that it had to follow a trajectory which led to sticking. If now the particle could run the trajectory backwards one would see a particle desorbing from the surface. If all the forces acting on the particle are the same during adsorption and desorption their describing equations of motion will be related via time reversal. This means one gets the equation for desorption just by changing $t \rightarrow -t$ in all the corresponding equations for the adsorbing particle. This can generally be written as

$$\lambda_{ij} = \lambda_{ji} \tag{2.14}$$

In cases where detailed balancing is applicable, the data obtained by examining a specific process, e.g. desorption, may be used to gain equivalent information about the reverse process, adsorption or vice versa, independent of any theoretical model [48]. Detailed balancing can even be applied under non-equilibrium conditions if for a subset of particles a distinction between equilibrated and non-equilibrated particles in the phase space can be made [48]. Brenig did the distinction by analysing the typical time scales of the involved processes. He stated that by identification of a proper set of slow variables as first important step for a kinetic model detailed balance always serves as an important principle to reduce the number of independent variables of the model [53]. From that point of view the concept of detailed balance is quite robust if it is applied deliberately.

Angular and Velocity Distribution of Desorbing Particles

The use of detailed balancing is an effective strategy to obtain information about complementary processes. In the following the angular and the velocity distribution of desorbing particles will be discussed and important coherences will be derived based on detailed balance arguments [49]. Let us consider a volume filled with gas in thermal equilibrium at temperature T. Due to the equilibrium condition the gas within the volume exhibits a constant density n (homogeneity) and the gas is isotropic which means that there is no preferred direction of emission of particles

of velocity v from any chosen differential volume. Additionally the velocity distribution for the particles within the volume is Maxwellian corresponding to the Temperature T:

$$F(v) = 4 \cdot \left(\frac{m}{2k_B T}\right)^{3/2} \cdot v^2 \cdot e^{-\frac{mv^2}{2k_B T}} \tag{2.15}$$

where m is the particle mass. The number of particles impinging in unit time from a solid angle $d\Omega$ on the surface element dA located in the volume is

$$I(\theta) dA d\Omega = \left(\frac{n\bar{v}}{4}\right) \cdot cos(\theta) \cdot \frac{dA d\Omega}{\pi} = C \cdot cos(\theta) \cdot dA d\Omega \tag{2.16}$$

where $\bar{v}$ is the mean velocity given by $\bar{v} = 2 \cdot \left(\frac{2k_B T}{\pi \cdot m}\right)^{\frac{1}{2}}$ as obtained from equation (2.15). $\frac{n \cdot \bar{v}}{4}$ is the total impingement rate per unit area and is independent from θ.

In equilibrium, according to detailed balance, equation (2.16) should also apply for particles leaving the surface. The angular distribution of the leaving particle flux is obviously cosine. One has to keep in mind that this cosine distributed flux consists of all particles leaving the surface, scattered, short time trapped and desorbed. For further consideration it is useful to classify the different particle fluxes from the surface by the typical time scale of the corresponding processes. For the sake of simplicity the desorption will be considered to be slow and all other processes will be considered as prompt specular reflection. Other fast processes like diffraction and inelastic scattering are neglected. A particle hitting the surface is either instantaneously scattered or it sticks and desorbs later. This can be expressed by

$$S(\theta) + R(\theta) = 1 \tag{2.17}$$

where $S(\theta)$ represents the sticking probability for a particle at an incident angle θ to the surface normal and $R(\theta)$ the reflection probability. Accordingly, the number of molecules that stick per unit time by hitting the surface element dA at incident angle θ is given by $I(\theta) \cdot S(\theta) dA d\Omega$ and the reflected flux can be written as $I(\theta) \cdot R(\theta) dA d\Omega$. The angular distribution of the specular reflected particles of course equals $I(\theta) \cdot R(\theta) dA d\Omega$ because in specular reflection the incident angle and reflection angle are the same. According to detailed balancing the incident flux has to be equal to the leaving flux. Therefore the angular distributions of impinging molecules and leaving molecules have to be identical which can be written as

$$D(\theta) \cdot dA d\Omega + R(\theta) \cdot I(\theta) \cdot dA d\Omega = I(\theta) \cdot dA d\Omega \tag{2.18}$$

and then by inserting expression (2.16) for the incident flux $I(\theta)$ one gets

$$D(\theta) = C \cdot (1 - R(\theta)) \cdot cos(\theta). \tag{2.19}$$

The term $D(\theta) \cdot dA d\Omega$ is the number of molecules desorbing from the surface element dA per unit time into the solid angle element $d\Omega$ at polar angle θ. Additionally the connection between the desorbing flux $D(\theta)$ which is equal to the adsorption flux $A(\theta)$ and the sticking coefficient $S(\theta)$ can be found by combining equation (2.17) and equation (2.19):

$$A(\theta) = D(\theta) = C \cdot S(\theta) \cdot cos(\theta) \tag{2.20}$$

From equations (2.19) and (2.20) it is clear that for the desorbing flux a cosine distribution can only be expected for a constant sticking coefficient.

The functions $I(\theta), A(\theta), D(\theta)$ are integral fluxes and the sticking and reflection probability $(S(\theta), R(\theta))$ are mean values with respect to their velocity distribution. Due to the generality of detailed balancing it can also be applied to the velocity (energy) distribution of the involved fluxes. Again a surface element dA located in a volume filled with gas equilibrium shall be considered. The number of particles hitting the surface dA in unit time from a solid angle $d\Omega$ at a polar angle θ and a velocity in the interval $(v, v + dv)$ is

$$i(\theta, v) \cdot dAd\Omega = \left(\frac{n\bar{v}}{4}\right) \cdot \left(\frac{2 \cdot (2k_BT)^4}{m^4}\right) \cdot v^3 \cdot e^{-\frac{mv^2}{2k_BT}} \cdot cos(\theta) \cdot \frac{dAdvd\Omega}{\pi}. \tag{2.21}$$

By introducing the constant $C' = (\frac{n\bar{v}}{4\pi}) \cdot \left(\frac{2(2k_BT)^4}{m^4}\right)$ one can rewrite the expression (2.21) to

$$i(\theta, v) \cdot dAdvd\Omega = C' \cdot v^3 \cdot e^{-\frac{mv^2}{2k_BT}} \cdot cos(\theta) \cdot dAdvd\Omega \tag{2.22}$$

The flux $I(\theta)$ can be extracted by integration over the velocity

$$I(\theta) = \int_0^\infty i(\theta, v)dv$$

The mean translational energy of the impinging particle flux can be obtained by calculating the second moment of the velocity distribution

$$\langle E_i \rangle = \frac{m}{2I(\theta)} \cdot \int_0^\infty v^2 \cdot i(\theta, v)dv = 2k_BT \tag{2.23}$$

Here it should be emphasized that both distribution functions, $\propto v^2 \cdot e^{-\frac{mv^2}{2k_BT}}$ and $\propto v^3 \cdot e^{-\frac{mv^2}{2k_BT}}$ describe the same thermodynamic state of the gas. The difference is just the population of particles that is taken into account. The distribution function $\propto v^2$ accounts for the particles currently present in the volume and the function $\propto v^3$ accounts for the particles that travel through a cross sectional area per unit time.
Analogous to the latter procedure detailed balancing can come into play. The desorbing flux has to be equal to the adsorbing flux. By introducing the angular and velocity dependent sticking coefficient $s(\theta, v)$ we may write the differential desorption flux d as

$$d(\theta, v) \cdot dAdvd\Omega = s(\theta, v) \cdot i(\theta, v) \cdot dAdvd\Omega \tag{2.24}$$

and using equation (2.22) this yields

$$d(\theta, v) \cdot dAdvd\Omega = C' \cdot s(\theta, v) \cdot e^{-\frac{mv^2}{2k_BT}} \cdot cos(\theta)dAdvd\Omega. \tag{2.25}$$

From this result one can clearly see that even at thermodynamic equilibrium the velocity distribution of particles desorbing into the solid angle $d\Omega$ at polar angle θ is Maxwellian only in case of a velocity (energy) independent sticking coefficient $s(\theta)$.

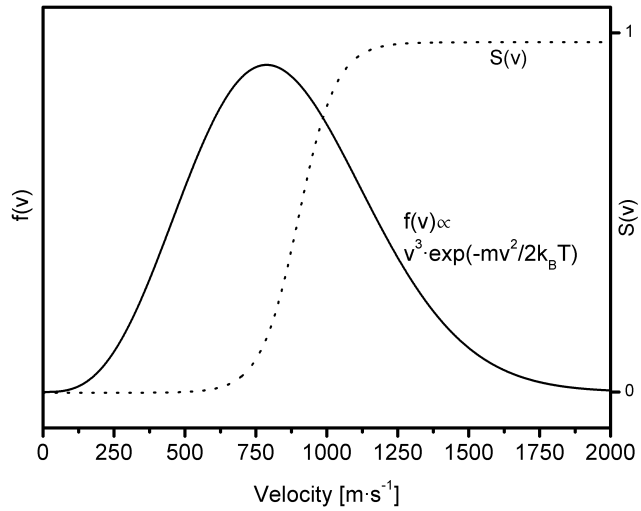

(a) Hypothetical sticking coefficient $S(v)$ and velocity distribution $f(v)$ of the incident flux.

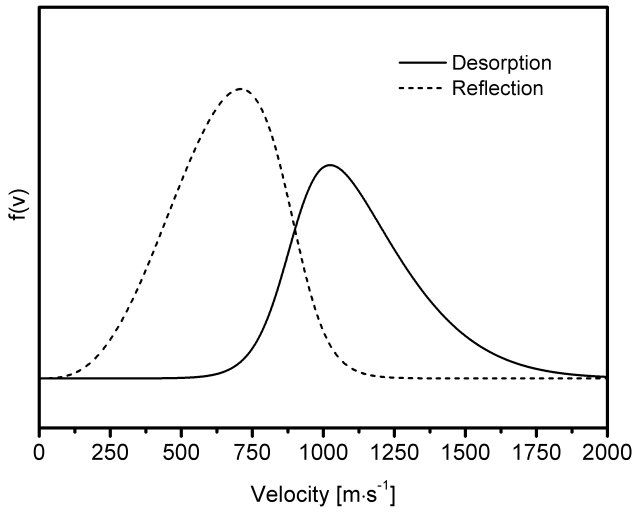

(b) Velocity distribution of the desorbing and the reflected flux.

Figure 2.4: Relationship between a hypothetical sticking coefficient $S(v)$ (a) and the velocity distribution of the desorbing (solid line) and scattered (dashed line) flux (b). The solid line in (a) corresponds to the velocity distribution of the incident flux.

In figure (2.4) the result (2.25) is visualized. In figure (2.4(a)) a hypothetical s-shaped sticking coefficient is shown and the velocity distribution of the incident flux. The corresponding velocity distributions of the desorbing and the scattered flux are shown in (2.4(b)). From that it is quite clear that a sticking coefficient which increases with energy yields a desorption flux with a mean energy $\langle E \rangle > 2k_BT$. Is the sticking coefficient decreasing with energy one will find $\langle E \rangle < 2k_BT$.

Generally not only the molecular velocity (translational energy) and the angle of impingement are determining factors but also the rotational and vibrational states as well as electronic excitations can have an influence on the adsorption/desorption dynamics. For example it could be shown that rotationally cold H_2 molecules are preferably adsorbed on Pd(111) compared to rotational highly exited H_2 [54; 55]. This observation was explained by the so called rotational steering. Metaphorically speaking it is easier for slowly rotating molecules to follow the meander of the reaction path through the potential energy surface than for fast rotating ones which often collide hard with the bumps of the potential.

Energy Scaling and Desorption

So far a description of the adsorption and desorption processes based on detailed balance and equilibrium arguments has been done. In this section a short demonstration of the consequences of the barrier model should be given.
As simplest model the Lennard-Jones potential (2.1) will be considered. In this case the adsorption is governed by the translational energy necessary for overcoming a possible activation barrier. More concrete, the adsorption probability depends only on the translational energy associated with the translational momentum normal to the surface. This behaviour is usually called **normal energy scaling (NES)**[41]. Of course the momentum component normal to the surface $p_\perp$ depends on the angle of incident θ and is therefore also visible in the angular distribution of the desorbing/adsorbing molecules. For the momentum component normal to the surface one gets

$$p_\perp = p \cdot cos\theta$$

and because of $E = \frac{p^2}{2m}$ one gets for the "normal energy"

$$E_\perp = E \cdot cos^2\theta.$$

and

$$E_{||} = E \cdot sin^2\theta$$

for the "parallel energy". Of course it is formally not correct to divide an energy which is a scalar into vectorial components but this is a widespread modus operandi in surface science and should therefore be used here as well.
It turned out from measurements that the flux of desorption can be well approximated by [56]

$$D_0(E,\theta) = D_0(E,\theta = 0) \cdot cos^n(\theta).$$

The subscript 0 indicates that here the initial differential quantities are meant. Otherwise the dependence of the current coverage has to be taken into account which would complicate the demonstration. One can switch to the desorption probability P_0^{des} and obtains [57]

$$P_0^{des} = P_0^{des}(E,\theta = 0°) \cdot cos^n\theta. \tag{2.26}$$

From equation (2.20) it follows that

$$P_0^{des}(E,\theta) = P_0^{ads}(E,\theta) = s_0(E,\theta) \cdot cos\theta \tag{2.27}$$

where P_0^{ads} is the adsorption probability and s_0 the sticking coefficient. P_0^{ads} and P_0^{des} are defined via the adsorption flux and desorption flux, respectively, whereas the sticking coefficient s_0 is defined as probability for a particle to stick. Due to these different definitions the factor $cos\theta$ appears in equation 2.27. Therefore the angular distribution of the sticking coefficient has to be written as

$$s_0(E,\theta) = s_0(E,\theta = 0) \cdot cos^{n-1}\theta. \tag{2.28}$$

This guarantees that for an energy independent sticking coefficient the desorption flux is cosine distributed.
In case of NES the energy dependence of s_0 can be expressed as

$$s_0(E,\theta) = s_0(E_\perp, \theta = 0°) = s_0(E \cdot cos^2\theta, \theta = 0°). \tag{2.29}$$

In a more general case the energy and angular dependence will be more complex. Usually the energy scaling of the sticking coefficient is then expressed by

$$s_0(E,\theta) = s_0(E \cdot cos^x\theta, \theta = 0°). \tag{2.30}$$

A further special case besides NES ($x = 2$) is then the so called total energy scaling ($x = 0$) which means that the sticking coefficient is independent of the energy. Generally $x < 2$ if the parallel momentum enhances the adsorption and $x > 2$ in the opposite case.
For most of the real systems the simple one dimensional barrier model does not hold. One reason is that the barrier hight will change depending on the position upon the surface unit cell [58–60]. That means that a measured sticking coefficient alway is a mean value.
By assuming NES one can obtain a relation which yields the mean energy of the particles that desorb at an angle θ. The barrier height distribution can be expressed as [57; 60]

$$\sigma(E_a) = \frac{1}{A}\frac{dA}{dE_a} \tag{2.31}$$

where E_a is the energetic barrier height and dA/A is the area fraction of the unit cell upon which the barrier height lies in the interval $(E_a, E_a + dE_a)$ Molecules which overcome the barrier shall stick with probability 1 ($s_0 = 1$). The sticking coefficient $s(E)$ for particles with energy E can be calculated as

$$s_0(E) = \int_0^E \sigma(E_a) dE_a. \tag{2.32}$$

This is actually what is measured by molecular beam experiments. From the experimental data one can obtain the barrier height distribution just by the derivative $\frac{\partial s_0(E)}{\partial E}$. Assuming NES it is possible to deduce the energy and the angular dependence from $\sigma(E_a)$

$$s_0(E,\theta) = \int_0^{E \cdot cos^2\theta} \sigma(E_a) dE_a$$

Is for example the velocity distribution within the molecular beam Maxwellian corresponding to the gas temperature T

$$f_E(E,T) = \frac{E}{(k_B T)^2} e^{-\frac{E}{k_B T}}$$

one can obtain the sticking coefficient $s_0^{MB}(T,\theta)$.

$$s_0^{MB}(T,\theta) = \int_0^\infty s_0(E \cdot cos^2\theta, \theta = 0°) \cdot f_E(E,T) dE \tag{2.33}$$

Further the sticking coefficient for isotropic impinging gas can be calculated by integrating 2.33 over the angle of impingement (azimuth ϕ and polar θ). The mean kinetic energy of molecules desorbing at a polar angle θ can also be obtained by integration

$$\langle E(T,\theta)\rangle = \frac{\int_0^\infty E \cdot s_0(Ecos^2\theta, \theta = 0°) \cdot f_E(E,T) dE}{\int_0^\infty s_0(Ecos^2\theta, \theta = 0°) \cdot f_E(E,T) dE}. \tag{2.34}$$

The same formalism can be used for other types of energy scaling just by replacing $E \cdot cos^2\theta \rightarrow E \cdot cos^x\theta$. Is the energy scaling expressed in the form (2.30) exactly valid over the whole energy range ($x \neq f(E)$) the sticking coefficient can be separated into an energy dependent and an angular dependent part [57; 61]:

$$s_0(E,\theta) = s_0(E, \theta = 0°) \cdot F(\theta) = G(E) \cdot F(\theta). \tag{2.35}$$

The only combination of functions which obey (2.35) and (2.30) is

$$F(\theta) = cos^{n-1}\theta$$

and

$$G(E) = K \cdot E^{\frac{n-1}{x}}$$

with K as normalization factor.

The desorption probability can be written as

$$P_0^{des}(E,\theta) = K \cdot E^{\frac{n-1}{x}} \cdot cos^n\theta.$$

The proportionality to $cos^n\theta$ is just due to the energy scaling in form of $cos^x\theta$ and the demand for separability. Additionally it is implied that the energy barrier distribution has a form which yields $s_0(E, \theta = 0°) = G(E)$ by applying $\sigma(E_a) = \frac{\partial s_0(E)}{\partial E}|_{E=E_a}$. For the mean energy of desorbing molecules from a surface with temperature T one gets

$$\langle E(T,\theta)\rangle = \langle E\rangle = \left(\frac{n-1}{x} + 2\right) k_B T \tag{2.36}$$

by applying (2.34). Here n is the exponent of the "cosine" distribution and x the exponent of the energy scaling. For NES $\langle E\rangle$ would be given by $(\frac{n+3}{2})k_B T$.

Thermal Desorption

The adsorption process can be characterized by an interaction potential as described in section 2.1. Adsorbed particles sit in a potential well of depth E_{ads} which corresponds to the energy difference between the systems surface + adsorbed particle and surface + free particle. As can be seen from scheme (2.1) a particle needs to overcome an energy barrier $E_{des} = E_{ads}$ in the non activated case and $E_{des} = E_{ads} + E_{act}$ in the activated case to desorb back into the free gas phase. The rate of desorption r_{des}, which is the number of particles desorbing from the unit surface area per unit time, can be described by the **Polanyi-Wigner equation**:

$$r_{des} = -\frac{d\Theta}{dt} = \nu_n(\Theta) \cdot \Theta^n \cdot e^{-\frac{E_{des}(\Theta)}{k_B T}}. \tag{2.37}$$

The desorption rate depends on the coverage Θ, the so called desorption order n, the surface temperature T, the desorption energy $E_{des}(\Theta)$ and the preexponential factor ν_n. Generally the desorption energy is a function of coverage due to possible adsorbate-adsorbate interactions. The desorption order n has the same meaning as the kinetic order of adsorption in the Langmuir model (2.8). For $n = 0$ there is no coverage dependence as typically observed for multilayer desorption, $n = 1$ describes non associative desorption which is the case when single atoms or intact molecules desorb directly into gas phase independend from their specific adsorption site. When the desorbing molecules have to be formed from two components which initially were adsorbed at seperate sites (associative desorption) $n = 2$ is the appropriate kinetic order. The preexponential factor ν_n generally depends on coverage and kinetic order. A simple interpretation of ν_n is just possible for $n = 1$ where ν_1 can be regarded as representing the frequency of attempts of the adsorbed particle to run in the direction of the desorption reaction [37]. The Arrhenius term in equation (2.37) is then just the number of successful attempts or in other words the fraction of particles having sufficient energy. In case of low coverages there can be found an interpretation of ν_2 for second order kinetics, which is just the collision frequency of two adsorbed particles assuming that the adsorbates are present as a completely mobile 2-D gas [37]. A general formulation of the preexponential factor can be found by applying the so called **transition state theory (TST)**. It is assumed that desorption is mediated by the formation of a so called "activated complex" out of the reactants which are the adsorbed particles. To use the picture of the one dimensional interaction potential (2.1(a)) the activated complex represents particles which are sitting right in a small area around the local maximum of the interaction potential ($E_{des} + E_{act}$ in figure (2.1(a))), the **transition state**. A statistical equilibrium between the adsorbed species and the activated complex is assumed to be established and the rate limiting step is the formation of the activated complex. The complexes are thought of as vibrating against the surface at frequency ω which is the frequency of decomposition of the complexes. Based on these premises an expression for the preexponential factor can be found [37]:

$$\nu_1 \approx \frac{k_B T}{h} \cdot \frac{q^{\ddagger}_{-1}}{q_{ad}}$$

for first order desorption and

$$\nu_2 \approx \frac{k_B T}{h} \cdot \frac{q^{\ddagger}_{-1}}{q^2_{ad}} \cdot \frac{1}{N}$$

for second order desorption. The expressions $q^{\ddagger}_{-1}$ and q_{ad} are the corresponding partition functions of the activated complex minus the vibrational degree of freedom in the reaction coordinate and of the adsorbed species. The factors h and N are the Planck constant and the number of adsorbed particles, respectively. It has to be pointed out that the preexponential factors of different desorption orders have different dimensions. Non associative desorption is typically a first order desorption process. In the simple case of desorbing atoms the partition functions $q^{\ddagger}_{-1}$ and q_{ad} are almost equal. Therefore ν_1 can be approximated by $\frac{k_B T}{h}$ which is 10^{13} for 500 K. If the activated complex has more degrees of freedom than the adsorbed species (e.g. delocalized parallel to the surface) ν_n will have a bigger value, is the activated complex restricted to a small number of degrees of freedom the value of ν_n will be low.
Due to the complex dependence of the factors in equation (2.37) the evaluation of thermal desorption data is often difficult. Typically so called **thermal programmed desorption (TPD)** spectra are measured. For this method the surface temperature is increased at constant heating rate β and the desorption rate is measured. For this purpos the time t in equation (2.37) is substituted by the temperature: $t = (T - T_0) \cdot \beta^{-1}$:

$$r_{des} = -\frac{d\Theta}{dT} = \frac{\nu_n(\Theta)}{\beta} \cdot \Theta^n \cdot e^{-\frac{E_{des}(\Theta)}{k_B T}}. \tag{2.38}$$

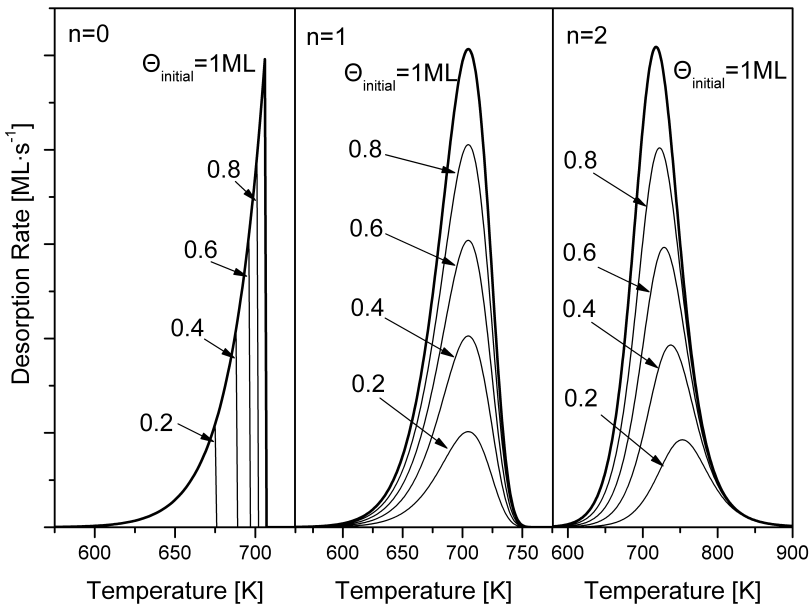

Figure 2.5: Simulated TPD spectra for kinetic orders $n = 0, 1, 2$. For all spectra a desorption energy of $E_{des} = 2eV$ and a heating rate $\beta = 1K \cdot s^{-1}$ was chosen. The corresponding preexponential factors were chosen to be $10^{28} molecules \cdot cm^{-2} \cdot s^{-1}$ for $n = 0$; $10^{13} s^{-1}$ for $n = 1$ and $10^{-2} cm^2 \cdot s^{-1} \cdot molecule^{-1}$ for $n = 2$.

In figure (2.5) simulated TPD-spectra for desorption order $n = 0, 1, 2$ are shown. A desorption energy $E_{des} = 2eV$ and a heating rate of $\beta = 1K \cdot s^{-1}$ were used for all spectra. The desorption energy and the preexponential factor were assumed to be independent of the coverage.
For zero order kinetics the desorption rate exhibits an exponential increase which instantaneously drops to zero when the reservoir of adsorbed species is depleted. The peak maximum shifts to higher temperatures with increasing coverage. For the simulation a preexponential factor of ν=$10^{28} molecules \cdot cm^{-2} s^{-1}$ and a desorption energy of $E_{des} = 2eV$ were used.
In case of first order desorption ($n = 1$) the TPD spectra show an asymmetric peak shape with respect to the peak maximum. The peak maximum stays at constant temperatures independent of the initial coverage. A preexponential factor of ν=$10^{13} s^{-1}$ was used in the simulation.
Symmetric peak shapes with respect to the peak maximum one gets for second order kinetics ($n = 2$). The peak maximum shifts toward lower temperatures with increasing initial coverage. A preexponential factor ν=$10^{-2} cm^2 \cdot s^{-1} \cdot molecule^{-1}$ was chosen.

Fractional Desorption Kinetics

The Polanyi-Wigner equation (2.37) provides a commonly used basis for the evaluation of flash desorption data. However the interpretation of the individual parameters occuring in this equation is not always that simple (e.g. pre-exponential factor). The desorption order n

accounts for the influence of the coverage on the desorption rate. This parameter is of great importance due to the fact that it reflects the basic desorption/adsorption mechanism. First order desorption just means that single atoms or intact molecules desorb randomly from a finite reservoir. Second order desorption can typically be assumed when diatomic molecules like H_2 have to recombine from their atomic components adsorbed on the surface. There the adsorbed atoms just diffuse along the surface and recombine via random collisions which leads to immediate desorption. Of course if lateral interactions come into play the desorption spectra are distorted which makes an assignment to a specific mechanism difficult. Zero order desorption is quite easy to understand when assuming a quasi infinite reservoir of equivalent adsorption states. This is the case when solids or fluids vaporize. Nevertheless, zero order desorption behaviour is also observed for adsorbate coverages in the monolayer regime like for the systems Xe/W(110) [62] or Hg/W(110) [63]. For these systems a more complex model is needed. In the literature a number of ideas are proposed for explaining zero order desorption from finite reservoires [62–68]. The proposed models all invoke the coexistent of at least two different adsorbate phases which are in equilibrium with each other. The simplest model proposes the coexistence of a dense adsorbate phase which is in equilibrium with a dilute phase (2 dimensional lattice gas). The particles desorb just from the dilute phase. Once the dilute phase has lost particles due to desorption the equilibrium condition between both phases causes a material transport from the dense phase to the dilute phase. This means that the density in both phases is kept constant at the cost of the dense phase. As long as the desorption from the dilute phase is slow compared to the equilibration processes between the two adsorbed phases the rate of desorption will be independent of coverage which specifies a zero order process [68].
An further interesting process is fractional order desorption. In this case the exponent n that characterizes the kinetic order has a value between 0 and 1. The basic process can be understood by a simple, but escapist model. A certain extend of lateral interaction between the adsorbates which leads to the formation of two dimensional adsorbate islands shall be assumed. For the sake of simplicity the adsorbates shall be condensed in a fixed number of islands N of circular shape with a mean radius r. The total number of adsorbed particles on the surface may be m and the density within an island is ρ. The total perimeter length L of these island can then be expressed by

$$L = 2 \cdot \sqrt{\frac{\pi \cdot N}{\rho}} \cdot \sqrt{m} \tag{2.39}$$

If one assumes that only those particles can desorb which are sitting at the edge of the island (lower coordination number means lower binding energy) the desorption rate has to be proportional to the island perimeter length L. Since the total number of adsorbed particles m is proportional to the coverage Θ the desorpion rate is also proportional to $\Theta^{1/2}$. This gives automatically a fractional kinetic order with n=1/2.
Real systems are much more complicated due to a number of additional facts which have to be considered. Particles which are detached from an island might not desorb immediately but diffuse along the surface for some time. Hence there is a chance that some particles are readsorbed by other islands. Additionally there is generally not a uniform island or cluster size

but rather a cluster size distribution. The vapour pressure of an island depends on the surface curvature [69]. Therefore for islands of roughly circular shape it is essential that small islands have a higher vapour pressures than bigger ones [70]. This means that small islands desintegrate faster than bigger ones or large islands even grow at the cost of smaller ones (Ostwald ripening [71; 72]). This leads to a redistribution of the island size. One consequence is that the total length of the island perimeter decreases faster than it would do only due to desorption. If there is a mechanism that keeps the total periphery length constant througout the desorption process (splitting of islands, needle like island structures) even zero order desorption might be observed. Processes following a fractional order kinetics might often involve a sensitive balance between different surface phases. Therefore it is not exceptional that the kinetic order changes during desorption, which makes the analysis of such data difficult.

3 Experimental Setup

3.1 Ultrahigh-Vacuum-System

For the investigation of surface adsorbate interactions it is indispensable to have fully control about the surface condition as well as about the interacting gas. Such well defined conditions can only be provided by ultrahigh vacuum (UHV). This guaranties that the cleaned/prepared surface keeps unalterd on an atomical level for the reqired time scales of the experiments.
For this Thesis the components of the used UHV system had to be modified several times to meet the experimental demands. In principle there were two basic configurations employed: the time-of-flight (TOF) configuration which allowed the measurement of dynamical parameters like the velocity distribution of desorbing particles and a line-of-sight (LOS) configuration which was used for TPD measurements and determination of reaction rates as well as the measurement of the angular distribution of the desorption fluxes. The TOF configuration, which was basically designed by C. Eibl is already described in detail elsewhere [10; 13; 57]. Therefore only a short description will be given here. The two different setups are shown schematically in figure (3.1) and figure (3.2). The basic UHV system designed by VARIAN can be separated into two chambers by a plate valve. The pumping chamber is located at the bottom and the main chamber in the upper part. The pumping chamber is equipped with an ion pump (nominal pumping speed 240 l/s), an turbo molecular pump (LEYBOLD Turbovac 361 /nominal pumping speed 345 l/s) (TMP4 in figure (3.1)) and a titanium sublimation pump. As a forepump a double stage rotary vane pump (PFEIFFER DUO 20/ nominal pumping speed 20 m^3/h)(RVP2 in figure (3.1)) with an adsorption trap installed upstream is used. The sampleholder is fixed onto a differentially pumped rotary stage in the main chamber. This setup allows an almost 360° rotation of the sample and additionally a linear shifting in x, y -and z-direction of ± 10 mm. The differential pumping of the rotary stage is managed by the forepump (RVP2) and an additional small turbo molecular pump (PFEIFFER TMU 071 P /nominal pumping speed 60 l/s)(TMP3). This pump is additionally used to pump the gas reservoir of the hydrogen/oxygen doser via a bypass pipe. The tubomolecular pump TMP5 with forepump MP1 in figures (3.1) and (3.2) is used for pumping the gas reservoir of the permeation source which is explained in more detail in section3.2.
The main chamber was equipped with a set of analytical instruments for surface characterisation. A topview of the principle arrangement as used during the TOF measurements is depicted schematically in figure (3.3). For the LOS measurements the TOF spectrometer was just replaced by the LOS detector.

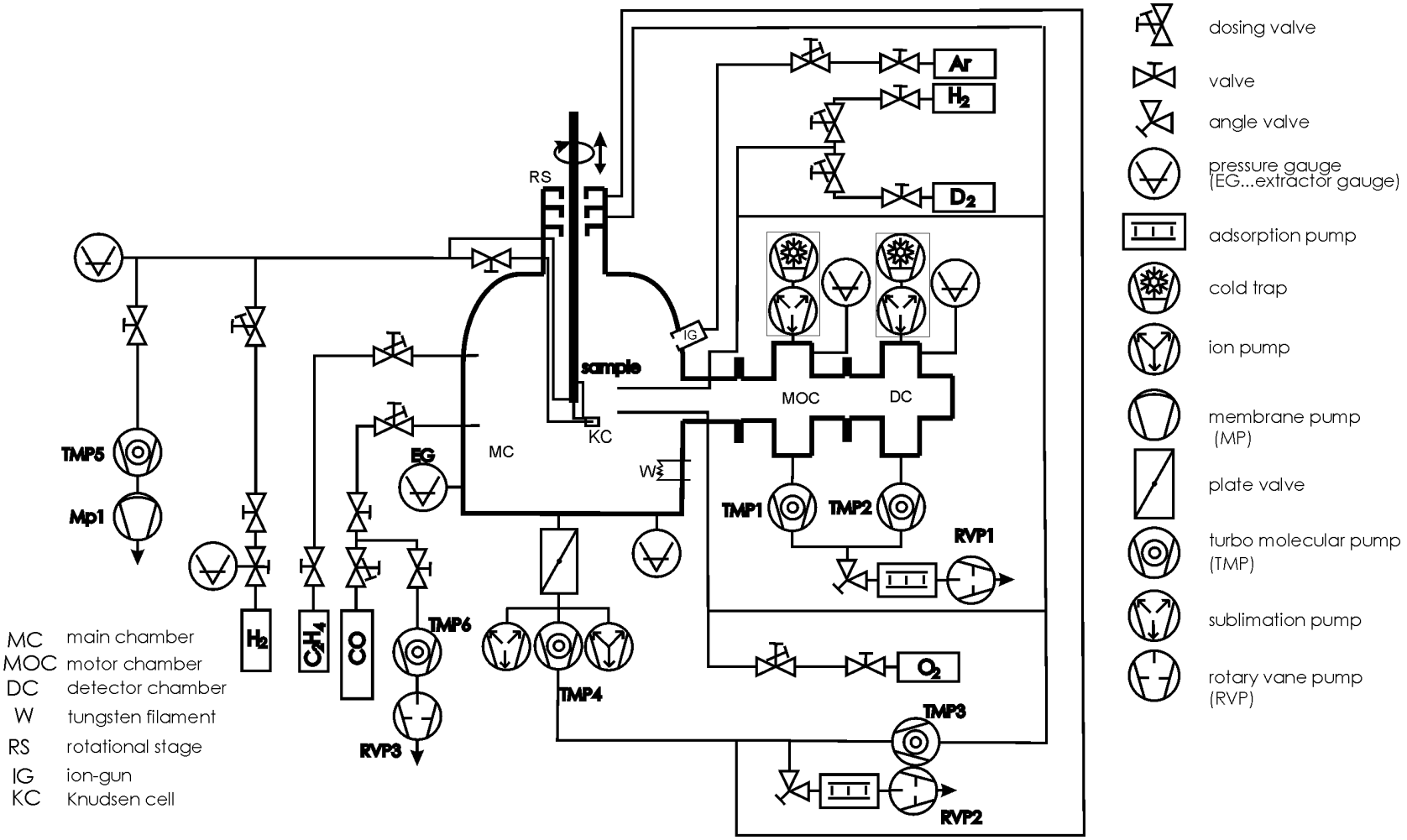

Figure 3.1: Illustration of the UHV setup for time-of-flight measurements.

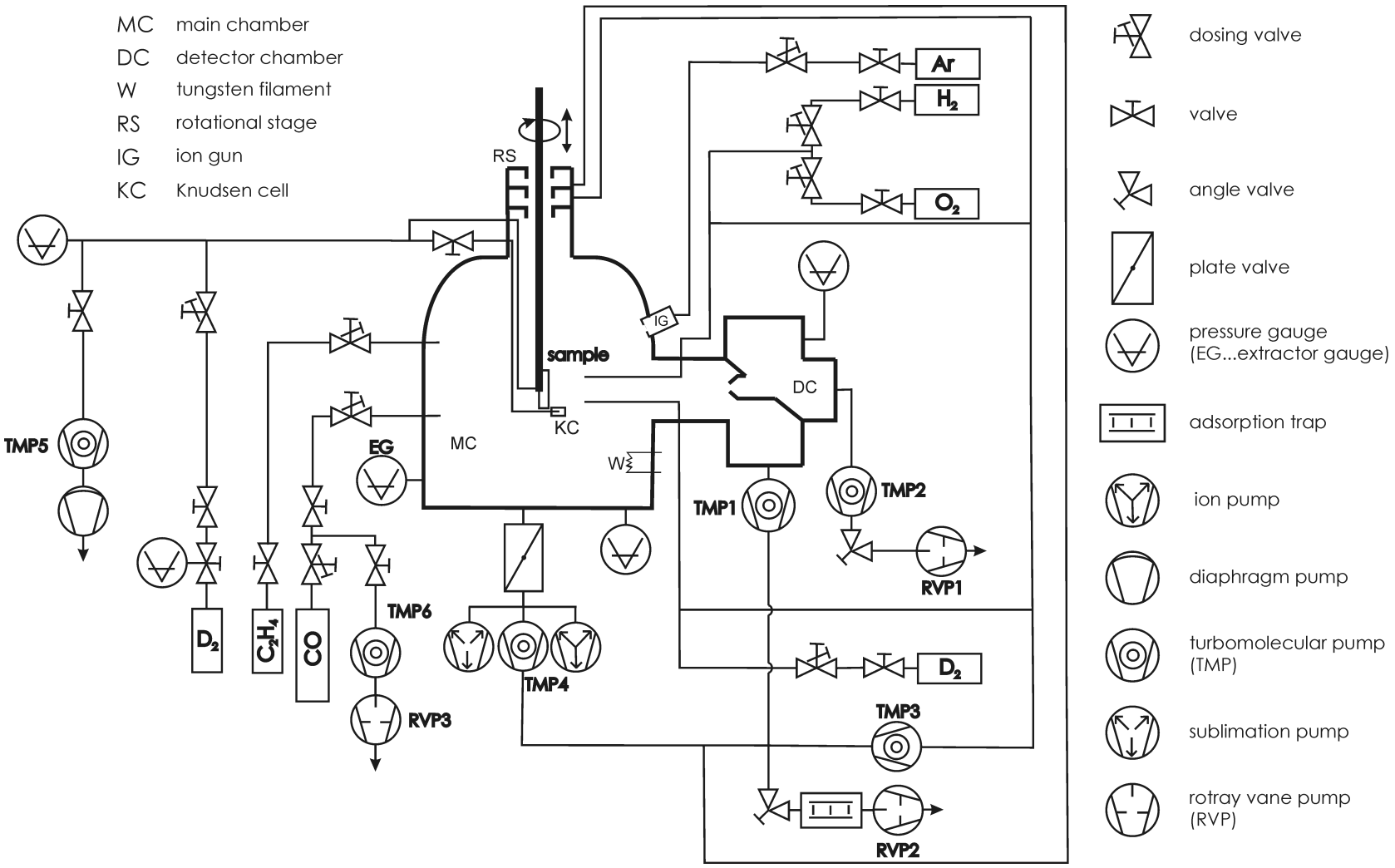

Figure 3.2: Illustration of the UHV setup for line-of-sight mass spectroscopy.

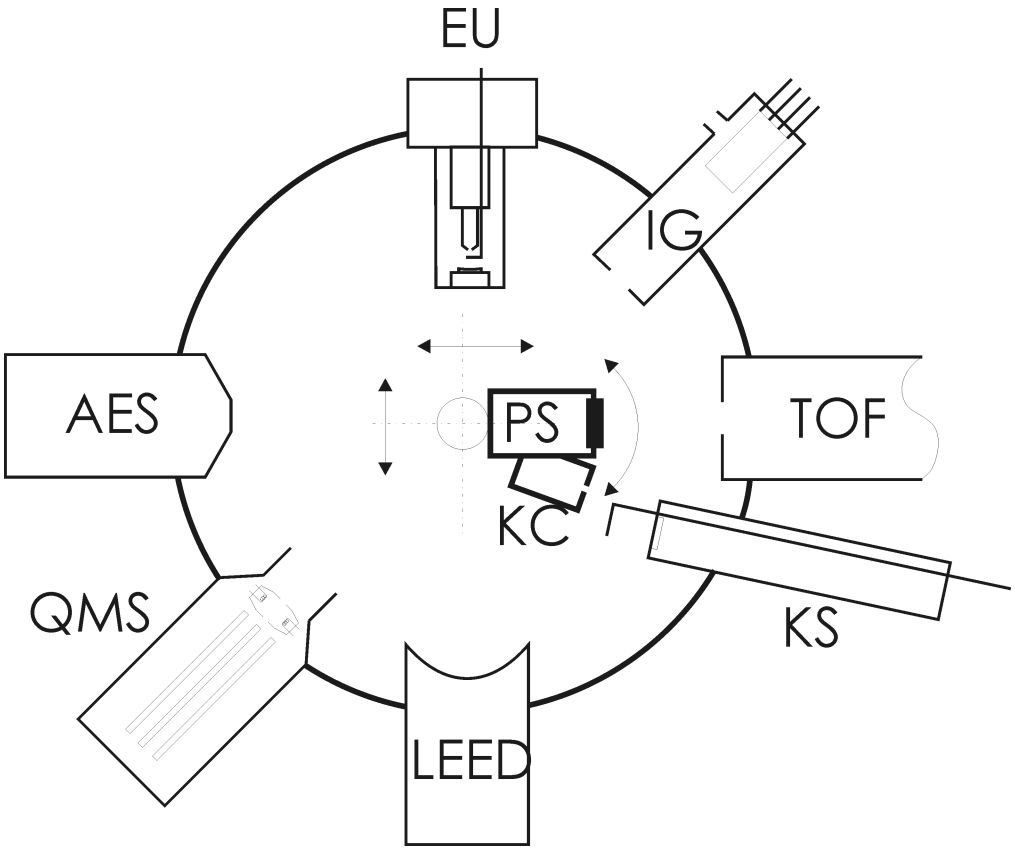

Figure 3.3: Topview of the principle arrangement of devices in the main chamber. EU...evaporation unit; IG...ion gun; TOF...time-of-flight spectrometer; KS...potassium source; LEED...low energy electron diffraction optics; QMS...quadrupole mass spectrometer; AES..Auger electron spectrometer

The actual arrangement in the main chamber can be seen in figures 3.4 and 3.5. In 3.4 the chamber is shown with the sample as part of a permeation source (described in section 3.2) as used for TOF, angular distribution and flux measurements. The sample holder with the "normal" single crystal disc as used for thermal desorption experiments can be seen in 3.5.
The Auger electron spectrometer (AES) was used to check the purity of the surface and in some cases for coverage calibration. During the progress of this work two different types of AES were used: a VARIAN Auger-electron-spectrometer with cylindrical mirror analyser (CMA) and a STAIB INSTRUMENTS AES Model ESA 100 spectrometer with CMA. Determination of the surface structure was performed by a VG MICROTECH low-energy-electron-diffraction optics (LEED) type RVL 900. The pressure in the main chamber was measured by a LEYBOLD Ionivac IM 510 extractor ionisation gauge, which was calibrated by a spinning rotor gauge which allowed pressure determination within an accuracy of 5-10% [44; 73]. Surface cleaning was achieved by means of Ar sputtering with 0.6 keV Ar^+ ions at an Ar pressure of $4 \cdot 10^{-7} - 3 \cdot 10^{-6}$ mbar (built by VARIAN, model 981-1045). The main chamber was additionally equipped with a quadrupole mass spectrometer (QMS) (BALZERS QMA 125) for monitoring the partial pressures of several masses in multiplex-mode or for analysis of the residual gas composition in normal scan mode.

The other devices used like the permeation source, the TOF spectrometer, the LOS detector chamber and the evaporation unit will be explained in more detail in the following sections.

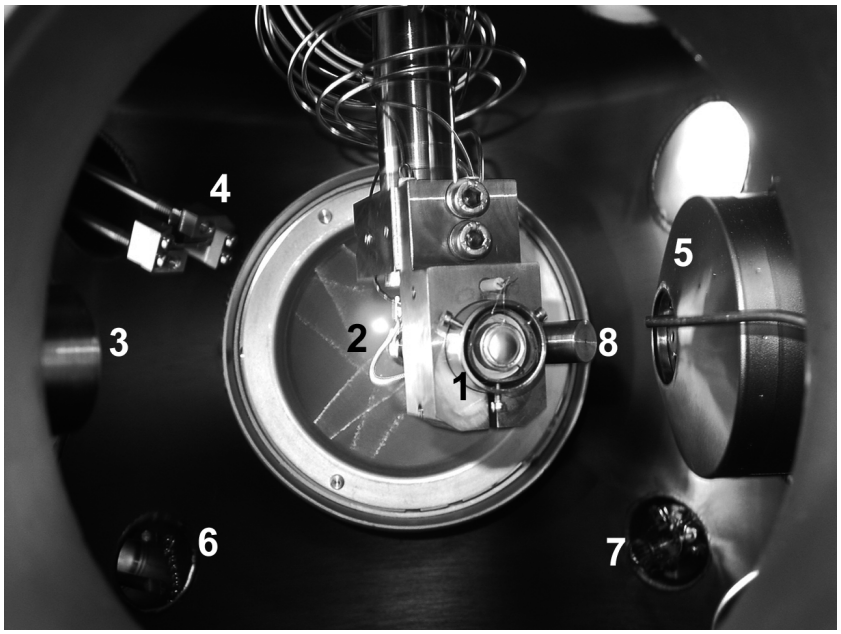

Figure 3.4: UHV-main chamber setup from the point of view of the evaporation unit as used during the TOF measurements: 1 Permeation source; 2 LEED screen; 3 ion gun; 4 potassium source; 5 AES; 6 tungsten filament; 7 QMS; 8 Knudsen cell.

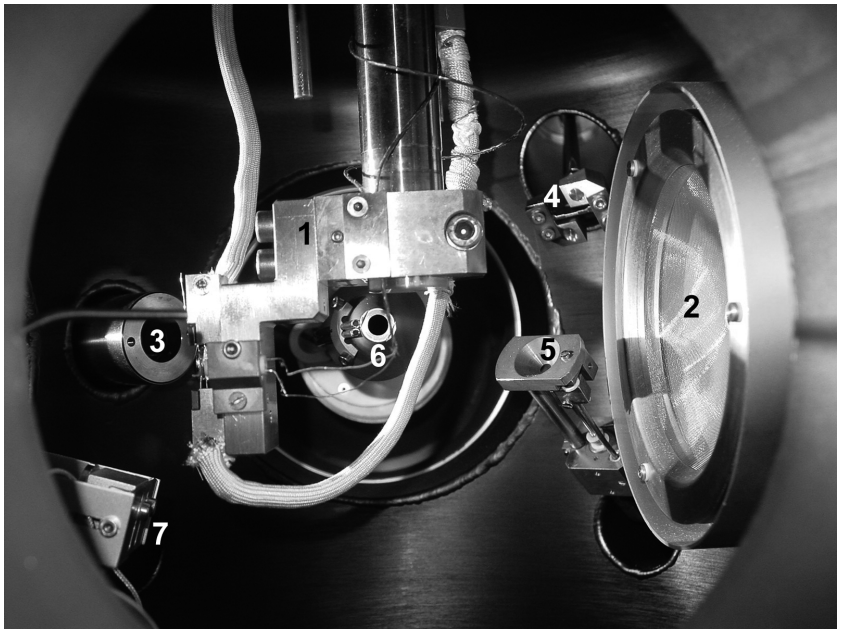

Figure 3.5: Picture of the main chamber setup during the LOS mass spectrometry measurements as seen from the Auger electron spectrometer. 1 sample holder with Pd disc; 2 LEED screen; 3 ion gun ; 4 potassium source; 5 atomic hydrogen source; 6 LOS detector + gas dosers; 7 pivoting quartz micro balance from evaporation unit

3.2 Permeation Source

For some measurements a constant desorption flux at constant sample temperature is needed on a long time scale (hours). In this case the standard method of adsorbing gas at low temperatures and desorbing it by a linear increase of the sample temperature fails. Especially for the TOF measurements long data acquisition times are needed to obtain a satisfactorily high signal to noise ratio. The measurement of TOF spectra of desorbing hydrogen- and water molecules formed on specifically prepared palladium surfaces was one of the major objectives in this work. The yield of reaction products is limited by the amount of reactants that adsorb on the surface. By dosing from the gas phase it is quite clear that a considerable part of the gas just contributes to a rise of the background level because on the one hand the sample area is a rather small target to hit and on the other hand not all molecules that hit the sample will participate on the desired reaction. A more efficient continuous gas supply for at least one of the reactants (hydrogen/deuterium) can be obtained by using a **permeation source**.
The used permeation source was designed by G. Pauer [10] and can be seen in figure 3.4 at its position in the main chamber. A cross sectional scheme is depectied in 3.6. The palladium single crystal disc (∅ 10 mm, 1mm thick) (1 in 3.6) was vacuum soldered with gold onto a high purity nickel cylinder (2). The nickel cylinder was closed by a stainless steel cap (5) which was soldered onto the back side. For gas inlet a stainless steel tube ($\frac{1}{16}''$)(6) was welded to the cap. The assembly was tightly surrounded by two concentric ceramic tubes containing a molybdenum heating coil (3) for restitive heating up to 1000 K. Several layers of tantalum foil were wrapped around the outermost ceramic cylinder for thermal radiation shielding (4).
Permeation means the penetration of a gas, liquid or vapour through a solid. The rate of mass transport is in principle dependent on the kind of solid, the kind of permeate, the thickness of the solid, the temperature and the concentration (pressure) of the permeate throughout the solid. The whole process of permeation through a membrane/crystal involves adsorption on the surface, diffusion from the surface into the bulk, diffusion from the bulk back to the surface and desorption from the surface [74]. Considering a system where a region held on constant pressure (concentration) is separated by a membrane/crystal from a region with lower constant pressure (concentration) one can find a solution for the arising equilibrium permeation particle transport per unit time $\frac{dN_X}{dt}$. If the rate limiting process for the permeation is the bulk diffusion one ends up at *Sievert's law* [75]:

$$\frac{dN_X}{dt} = K \cdot P_X \cdot \frac{A \cdot (\sqrt{p_{Xh}} - \sqrt{p_{Xl}})}{d} \tag{3.1}$$

where P_X is the so called "permeation constant" which can be written as a product of the diffusion coefficient D_X and the solubility S_X. K is just a conversion factor to obtain the desired unit of $\frac{dN_X}{dt}$. A is the effective area which is available for permeation and d is the thickness of the membrane. The subscript X just accounts for the specific permeate and therefore p_{Xh} and p_{Xl} means the high and the low pressure of the permeate X. In practice a direct calculation of $\frac{dN_X}{dt}$ from equation (3.1) does not yield precice results. The reason for that is that surface effects are not considered (e.g. formation of barrier layers by CO [76]) and

the surface conditions at least at the high pressure side are mostly ill defined. Additionally the diffusion is influenced by crystal defects and impurities which are not taken into account. In [77] one can find a parametrization for the permeation constant P_{H_2} for hydrogen through palladium in the following form:

$$P_{H_2} = 4.3 \cdot 10^{-4} \cdot exp(-\frac{3745}{R \cdot T})$$

with the universal gas constant $R = 2 \cdot \frac{cal}{mol \cdot K}$ and T the crystal temperature. The parametrization is valid for temperatures between 273 K and 673 K. For deuterium a similar expression can be found in [78]:

$$P_{D_2} = 4.4 \cdot 10^{-4} \cdot exp(-\frac{4430}{R \cdot T})$$

which is valid for $673K < T < 973K$. Using the latter parametrizations one has to insert the specific variables in 3.1 in the correct units to obtain the permeation particle transport per unit time in $[\frac{molecules}{s}]$. The perameation constant has the unit $[Torr^{\frac{1}{2}} \cdot l \cdot cm^{-1}]$ and therefore the pressures p_{Xh} and p_{Xl} have to be inserted in $[Torr]$. The effective area of permeation and the membrane thickness then have the units $[cm^2]$ and cm, respectively. To convert $[Torr \cdot l]$ into a particle number the conversion factor K is $K = 3.24 \cdot 10^{19}[\frac{molecules}{Torr \cdot l}]$. This value is strictly valid only for T=293 K (20°C) and can be calculated from the ideal gas law

$$p \cdot V = N \cdot k_B \cdot T. \tag{3.2}$$

Here again p is the pressure, V the volume to which the gas is confined, N the number of gas particles and T the absolute gas temperature. From equation (3.2) one gets

$$\frac{p \cdot V}{k_B \cdot T} = N$$

which can be used to express a particle number in terms of pressure and volume. For one $Torr$ ($= 131Pa$) and a volume of one l ($= 10^{-3}m^3$) for a temperature $T = 293K$ and $k_B = 1.38 \cdot 10^{-23}\frac{J}{K}$ one obtains the latter value for $K = 3.24 \cdot 10^{19}\ \frac{particles}{Torr \cdot l}$. From the latter considerations it is quite obvious that temperature significantly influences the permeability and therefore governs the particle transport $\frac{dN_X}{dt}$ through the membrane/crystal. To have good control over the crystal temperature a Ni/CrNi-thermocouple was spot welded close to the rim of the palladium sample (position 1 in figure (3.6)). The temperature was then regulated by the interplay of heating the high purity Ni-cylinder (position 2) which enclosed the sample disc by means of a molybdenum heating coil (position 3) and the cooling upon the contact with the liquid nitrogen cooled sample holder. For pressure measurement in the gas inlet system of the permeation source a piezoresistive pressure transmitter (KELLER, PAA-35HTT/3bar/81248 SN 19754) was used (see figure (3.1)). The typically applied back pressure ranged from the sub millibar region (reaction rate measurements) up to 1500 mbar (TOF measurements). The sample temperature was varied between 523 K and 700 K. In figure (3.7) the calculated equilibrium permeation flux through a 1.5 mm thick palladium membrane for various temperatures is shown.

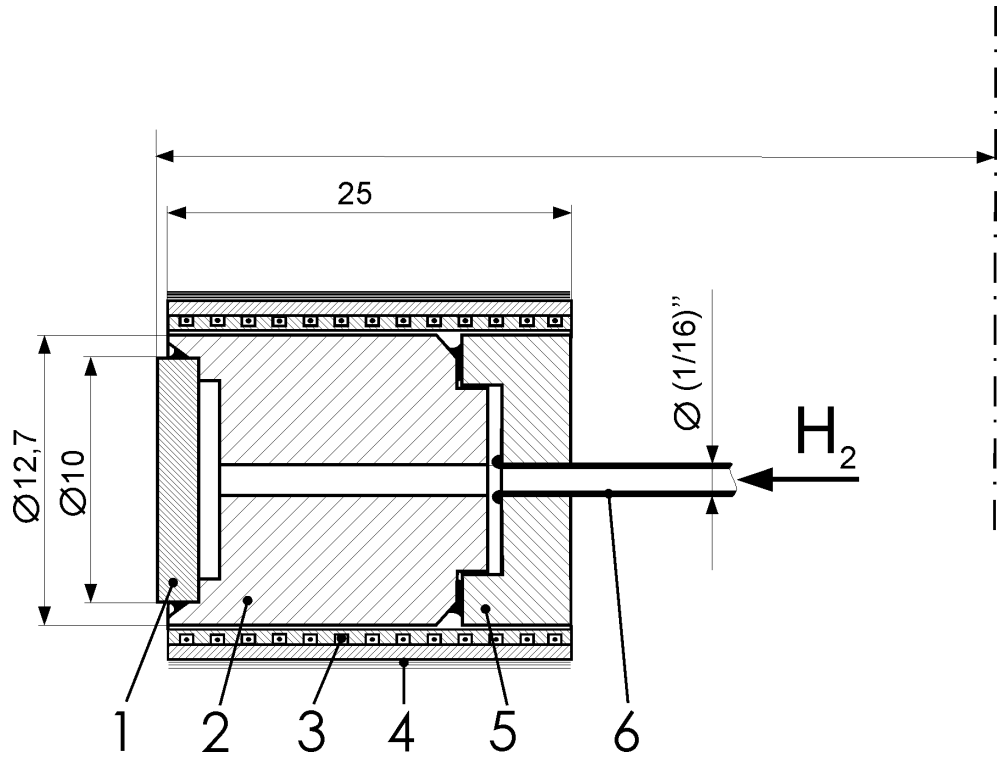

Figure 3.6: Cross section of the used permeation source as designed by G. Pauer [10]. 1 palladium crystal; 2 nickel cylinder; 3 molybdenum heating coil nestling between concentric ceramic tubes ; 4 several layers of tantalum foil for heat radiation shielding ; 5 stainless steel cap; 6 stainless steel tube $\frac{1}{16}$"(gas supply).

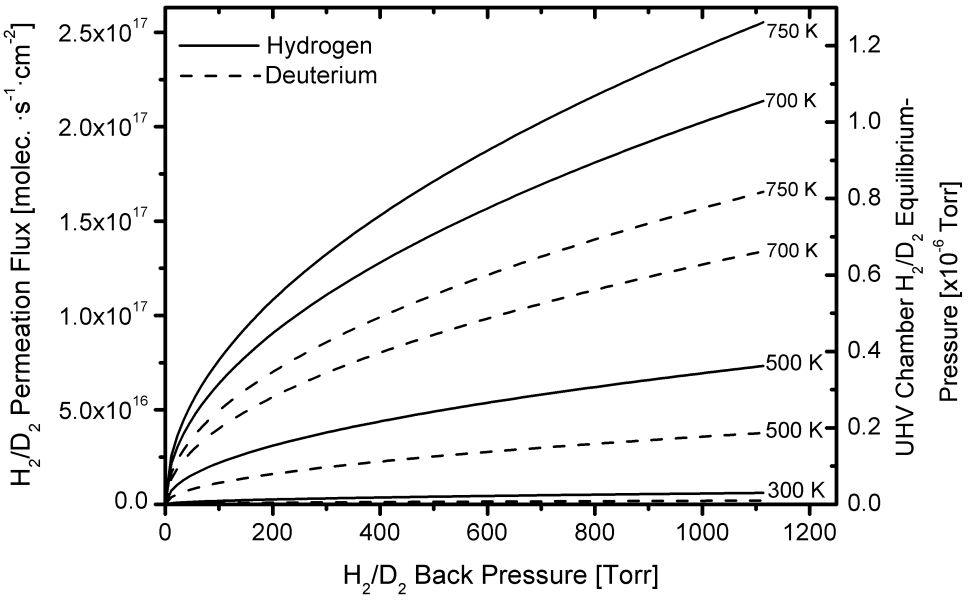

Figure 3.7: Calculated equilibrium permeation flux through a 1.5 mm thick palladium membrane according to Sievert's Law (3.1). The right hand side scale indicates the theoretical equilibrium pressure in the UHV chamber assuming an effective permeatiing area of 0.38 cm^2 (circular sample ⌀ 7 mm) and an effective pumping speed of 1000 l/s.

It turned out that in the course of time the permeation source was in use the sample crystal changed. The sample suffered increased stress due to the permeating deuterium/hydrogen which induced the formation of a macroscopic visible bulge across the sample surface. This on the one hand is a disadvantage because due to the increased surface defect concentration caused by the stress the surface is microscopically roughened which can change the sticking coefficient for gases, on the other hand the visible deformation provided a good opportunity to measure the diameter of the effective area which was available for the permeation (⌀ 7 mm).

3.3 Time-of-Flight Spectrometer

A time of flight spectrometer in principle allows the determination of the velocity distribution of a molecular gas flux. The basic idea of the method is simple: just measure the time t it takes for a particle to traverse a distance l. The mean velocity v of the particle is then simply given by

$$v = \frac{l}{t} \tag{3.3}$$

Applying the time measurement to a great number of particles yields a time-of-flight distribution which is related to the velocity (translational energy) distribution of the particles (at least for one direction). This method implies the problem that it is not possible to obtain

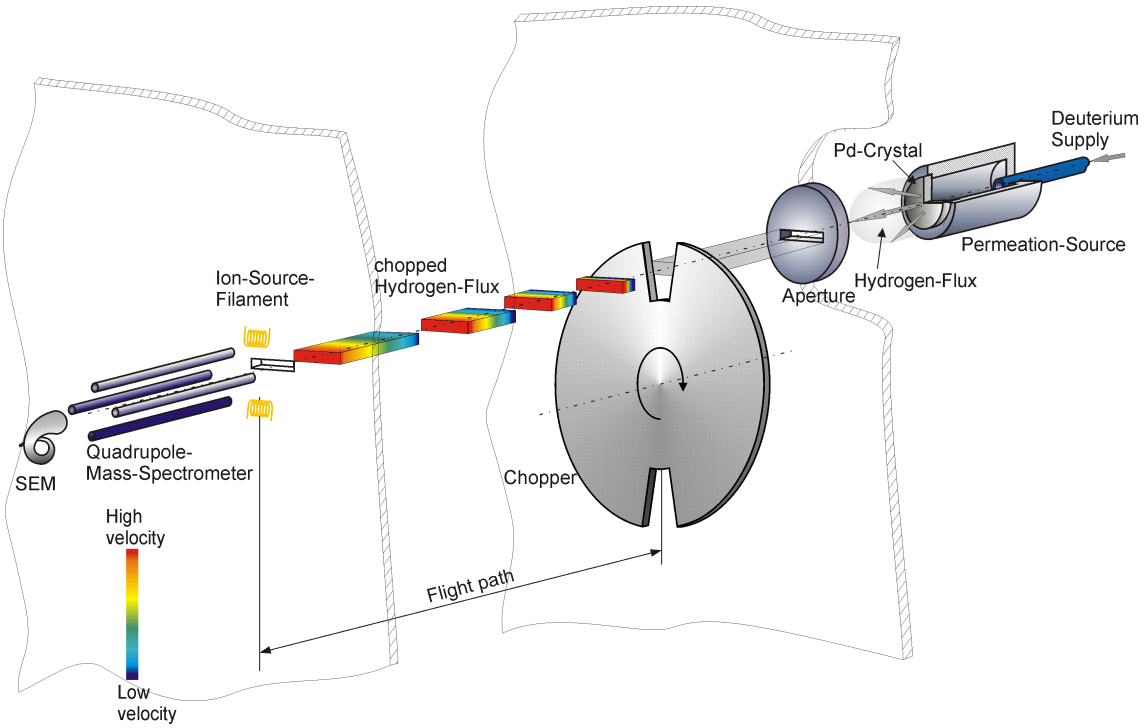

Figure 3.8: Basic assembly for the measurement of a TOF-distribution from a particle flux effusing from the permation source. The walls separating the different chambers are just indicated by thin lines.

information about the moment when a specific particle desorbs from the surface, even less it is possible to get this information for a great number of particles. The way out of this problem is to impress a time periodic structure on the desorbing particle flux. In practice this is done by a chopper that periodically blocks the particle flux. In this case the TOF system consists of three differentially pumped chambers: the main chamber containing the particle source (permeation source), the motor chamber housing the chopper disc and the detector chamber equipped with a quadrupole mass spectrometer (QMS) for particle detection. The chambers are connected by a set of aligned apertures.

In this case two slits on opposite sides of the chopper disc (chopper gates) block and deblock the particle flux coming through the aperture from the main chamber. Every time one chopper gate deblocks the flux the other opposite gate activates the data acquisition of a multi-channel-analyser (MCA) via a photo-sensor. The MCA counts the particles which are detected within a certain time slot by the QMS. The basic assembly of a TOF experiment is shown schematically in figure (3.8). The total UHV setup used for the TOF mesurements is depicted schematically in figure (3.1). A concrete description of the real assembly as designed by C. Eibl can be found in [10; 13; 57]. The finite width of the chopper slits cause a convolution of the actual TOF distribution with the chopper-gate-function. Therefore the measured distribution does not directly correspond to the velocity distribution. Additionally, there are some more influences which have to be taken into account. The data evaluation procedure is briefly outlined in chapter 4.

For the investigations carried out during this thesis, the MCA channel width was set to $\Delta t = 2\mu s$ and the chopper slit frequency was typically set to 400 Hz which corresponds to a 200 Hz chopper motor frequency due to the double slit arrangement. (800 Hz slit frequency (400 Hz motor frequency) was only applied in special cases). Due to the chopper disc geometry (⌀ 79.5 mm, slot width ≈ 4mm) a 400 Hz slit frequency yielded an chopper opening time of about 80 μs. The flight path length was 476 mm which is the distance between chopper disc and the ion-source filament plane of the QMS.

3.4 Line-of-Sight detector

Another major part of this work is the water formation reaction on modified palladium surfaces. To examine this subject it is advantageous to use a so called line-of-sight detector. To initiate reactions on the reactive surface one has to provide the supply with reactants. For UHV experiments the reactants are available as vapours or gases which have either to be dosed on the surface via a capillary or from the isotropic gas phase. Both methods imply that practically all surfaces in the UHV chamber are exposed to the reacting gases. Since there are a number of possible active surfaces in the UHV chamber as hot filaments and various metallic surfaces (chamber walls, sample holder, Ti getter,...) there might occur a number of unwanted reactions which generate additional background signals. These background signals then might overlap the primary rate signal which stems from the reactions on the sample surface. A possibility to distinguish between the reaction products coming from the sample and those coming from elsewhere in the chamber is the line-of-sight detector. In figure 3.9 a cross section of the LOS detector chamber is shown. The sample-to-aperture distance was 13 mm at neutral manipulator position. The circular entrance aperture had a diameter of 8 mm. Between main chamber and detector chamber a connector ring (DN 160 CF) was attached containing 4 flanges (DN 16 CF / attachment SWAGELOK $\frac{1}{8}''$) for gas supply lines. A BALZERS QME 200 Prisma quadrupole mass spectrometer was installed as particle detector (5). The detector chamber was pumped by a turbo molecular pump (PFEIFFER TMU 521). In addition a small cooling finger (6) was mounted to reduce condensable vapours (water,...). At the bottom part of the assembly an additional flange was accessible (9) to mount another pump (PFEIFFER TMU 521) for increasing the pumping speed in the main chamber. The main chamber and the detector chamber were connected via a bypass line (DN 63 CF-R) and an angle valve to balance possible pressure differences during evacuation. Additionally the detector chamber was equipped with a shutter (8) which allowed blocking of the direct inline signal which is sometimes important for the correction of inline signals (see chapter 4).

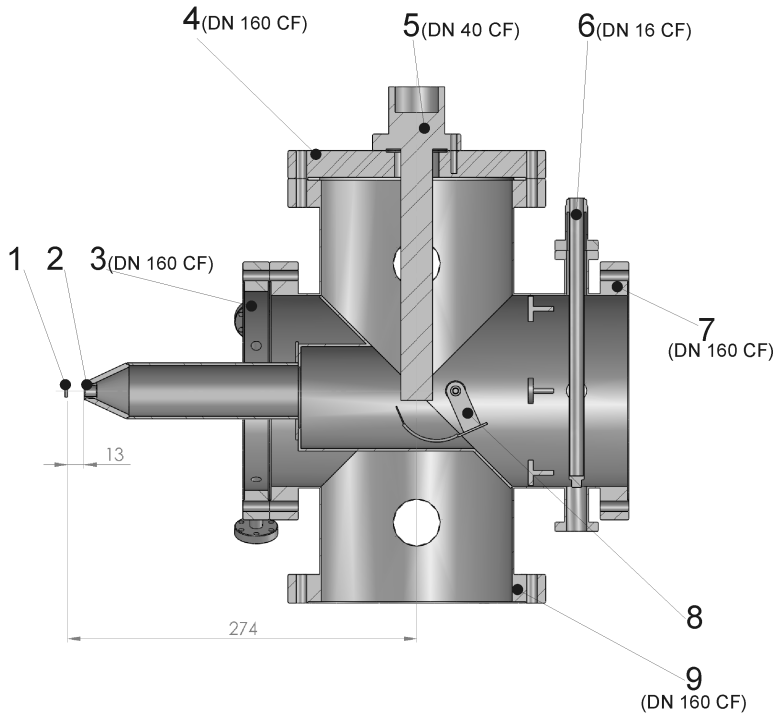

Figure 3.9: Cross section of the line-of-sight detector chamber: 1 palladium sample; 2 entrance aperture; 3 connector ring for gas inlet; 4 flange cover; 5 quadrupole mass spectrometer; 6 cooling finger; 7 flange for turbo molecular pump (detector chamber); 8 shutter; 9 flange for turbo molecular pump (main chamber)

Figure 3.10 shows a photograph of the LOS chamber without the turbo molecular pumps. On the right hand side the entrance aperture is clearly visible as well as two $\frac{1}{8}''$ pipes which are used as gas dosers (oxygen/hydrogen). In this configuration the gas is dosed from an angle of about 25° to the sample surface normal.

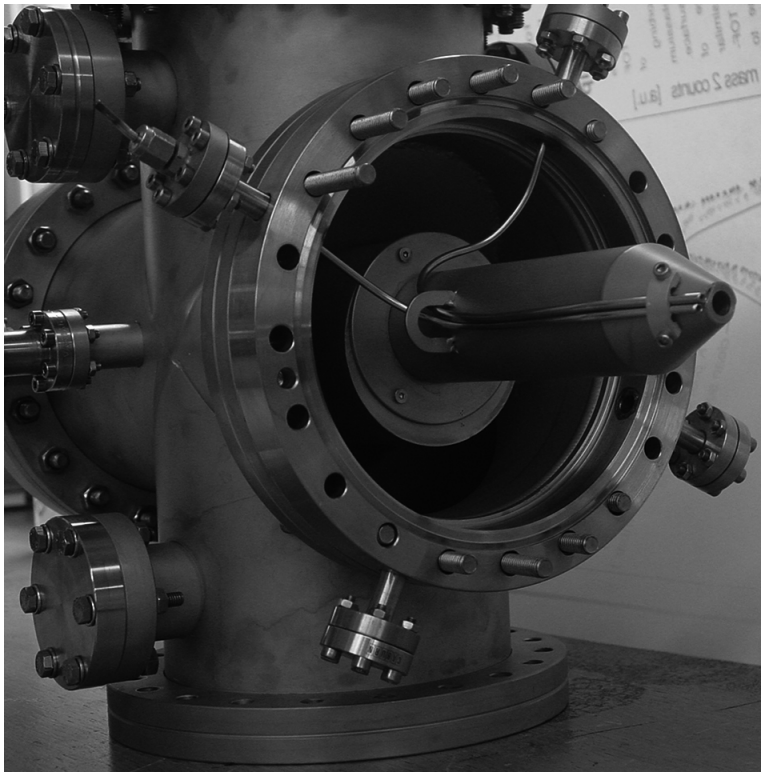

Figure 3.10: LOS detector chamber. The entrance aperture as well as the $\frac{1}{8}''$ gas dosers are clearly visible.

3.5 Evaporation Unit

For the experiments done in this work thin metal films were deposited onto the sample surface. To provide a flexible system which allowed deposition of different metals and calibration of the film thickness an evaporation unit was designed. The whole assembly evaporation source and film thickness monitor were mounted onto a standard DN 160 CF flange. As film thickness monitor a quartz microbalance (INFICON Compact Crystal Sensor) was used which was mounted onto a traversable cantilever. For deposition rate control the microbalance was just pivoted into the effusing particle flux. After determination of the deposition rate the microbalance could be turned away from the evaporator and the sample was positioned in front of the evaporator. As evaporators a commercial electron beam evaporator (OMICRON EFM 3 UHV Evaporator) and a home built Knudsen cell were used. A scheme of the evaporation assembly with installed Zn evaporator is shown in figure (3.11). A photograph of the actual assembly can be seen in figures (3.12(a)) and (3.12(b)). As can be seen in figure (3.11) the sample can not be moved to the exact same position as the microbalance. The distance between the microbalance and the Zn source d_1 31.5 mm shorter than the distance source to sample (d_2). The Zn deposition rate as monitored by the microbalance has therefore to be corrected by the factor

$$\left(\frac{d_2}{d_1}\right)^2 = \left(\frac{134.8}{103.3}\right)^2 = 1.7.$$

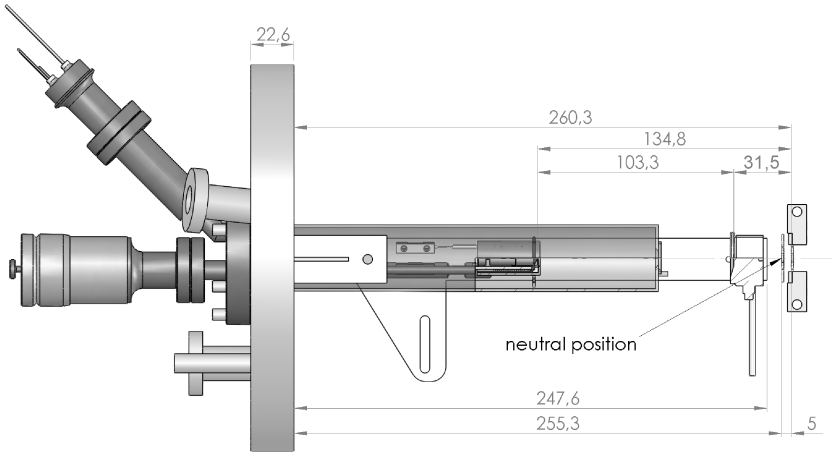

Figure 3.11: Cut through the evaporator unit with installed Zn evaporator. The microbalance is positioned for monitoring the deposition rate. The sample disc is indicated at its neutral position and at the optimum distance for Zn deposition (5 mm off neutral position).

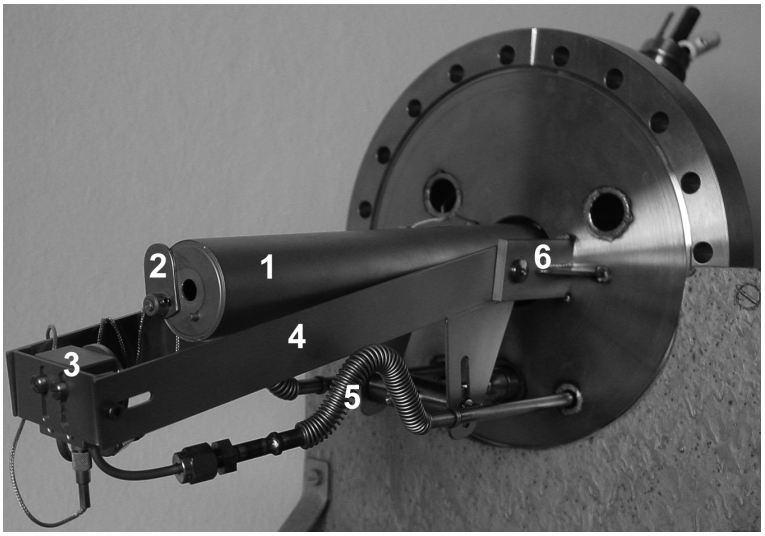

(a) Evaporation unit on the vacuum side: 1 Zn source; 2 shutter; 3 microbalance; 4 cantilever; 5 flexible water feed pipe; 6 cantilever mount

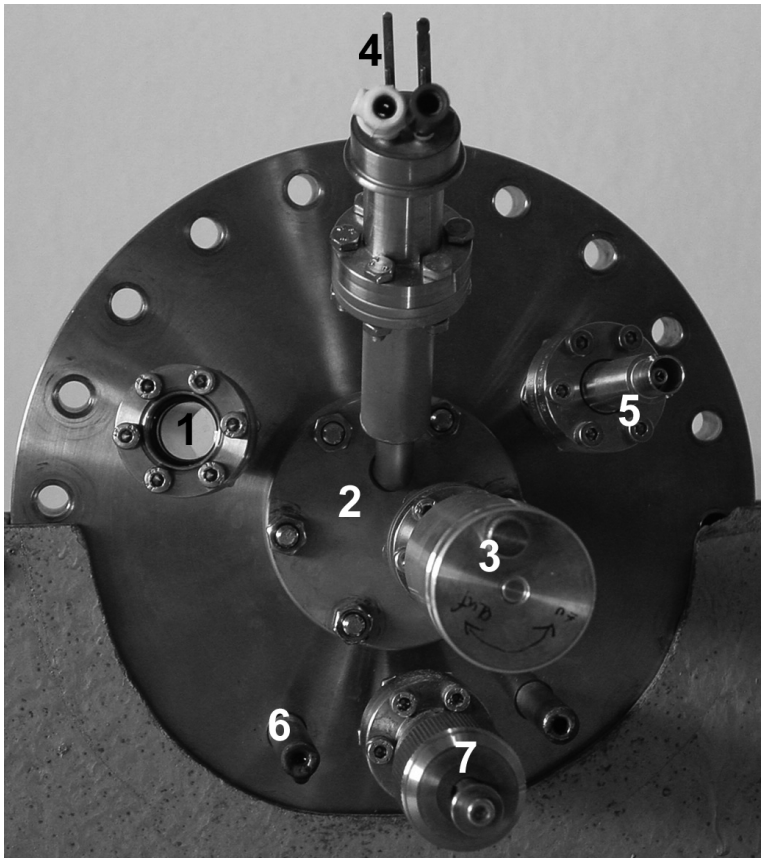

(b) Evaporation unit outside: 1 viewport; 2 evaporator flange (DN 40 CF); 3 rotary feedthrough (shutter); 4 electrical feedthrough evaporator (heating and thermocouple); 5 BNC feedthrough microbalance; 6 cooling water connection; 7 linear feedthrough to cant the microbalance.

Figure 3.12: Photograph of the evaporation unit with installed Zn source (a) on the vacuum side, (b) on the outside.

3.6 Zn Source

In the latter section the evaporation unit was introduced. The unit consists essentially of an evaporator and a microbalance. For the Zn deposition a special evaporator was designed by M. Kornschober. The main part is a simple Knudsen cell consisting of two interleaved molybdenum cylinders. One of them is provided with a hole of 1 mm in diameter for Zn outlet and the other has a tap hole for mounting a Ni/CrNi-thermocouple. The molybdenum cell was tightly sourrounded by two concentric ceramic cylinders which contained a tantalum coil inbetween for resistive heating. The whole assembly was embedded in a stainless steel tube which was centered in a second stainless steel shroud. A shutter placed at the outlet (∅ 8 mm) of the outer shroud provided an exact regulation of the deposition time. A schematic drawing of the Knudsen cell is depicted in figure (3.13) and an assembly drawing of the whole evaporator is shown in figure (3.14).

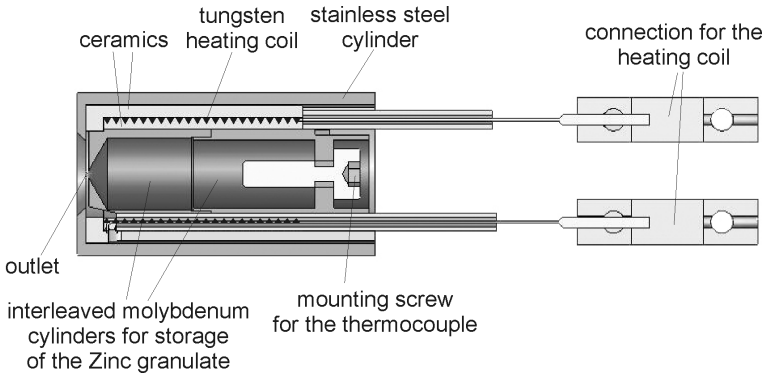

Figure 3.13: Cross section of the Zn Knudsen cell.

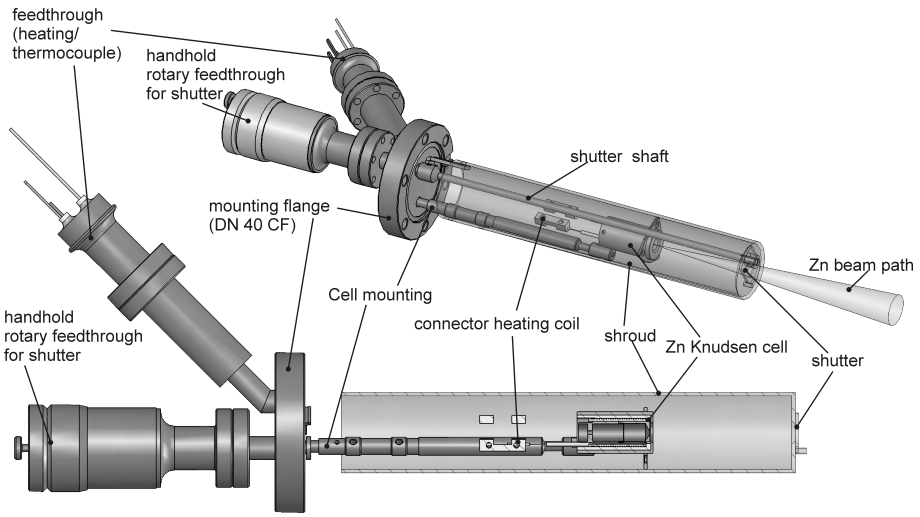

Figure 3.14: Different views on the Zn evaporator.

The evaporator was loaded with high purity Zn shot (GOODFELLOW, lump size max. 2 mm; purity: 99.98 %) just by lifting the rear molybdenum cylinder. The desired Zn deposition rate was controlled by the Zn cell temperature and checked by a quartz microbalance. Due to the rather massive design of the Zn Knudsen cell it took a rather long time until the cell temperature was stabilised. For an equlibrium temperature of 300°C a heating current of 0.8 A was needed which took more than 2 hours until the temperature and in turn the deposition rate were stabilized. Nevertheless, the deposition rate was frequently checked during the experiments to be sure of the evaporation conditions.

3.7 Auger Electron Spectroscopy

A valuable tool in surface analysis is the Auger electron spectroscopy, which is a standard method for probing the surface chemical composition under high and ultra-high vacuum conditions. The method is based on the **Auger effect** which generates secondary electrons of element specific kinetic energy which in turn can be detected by an energy dispersive analyser. In this work a so called cylindrical mirror analyser (CMA) [46; 79] is used. Due to the impact of a high energy electron (typically 1-10 keV) an electron near the atomic core can be removed. In this state the ionized atom is highly excited and tends to minimize its energy by filling the hole in the core shell by an electron of an outer shell. The refilling electron changes from a state of lower binding energy to a state of higher binding energy. Due to the energy conservation law the excess energy has to be transferred. This can either happen by emitting a photon (Fluorescence) or by energy transfer to another electron which in turn is catapulted out of the atom leaving a double ionized atom behind. The leaving electron is then called the Auger electron and carries an energy which depends on the energetic location of the initially removed electrons and the final two elctron holes. The deexcitation processes are illustrated in figure (3.15). According to the example illustrated in figure (3.15) the energy of the Auger electron can be estimated by

$$E_{KL_1L_{2,3}} = E_K - E_{L_1} - E_{L_{2,3}} - \Phi$$

where the subscripts define the initial energy levels of the electrons and Φ means the work function. Considering the whole measurement procedure it turns out that the work function of the sample has no influence on the final electron energy but the work function of the detector has to be taken into account. Thus one has to insert the detector work function into the latter expression. Of course this can just be a rough estimation because in the latter relation the specific energy levels of the neutral atom are used and not those from the ion. For a more detailed description of the method the reader may be referred to the corresponding literature [46; 80–84].

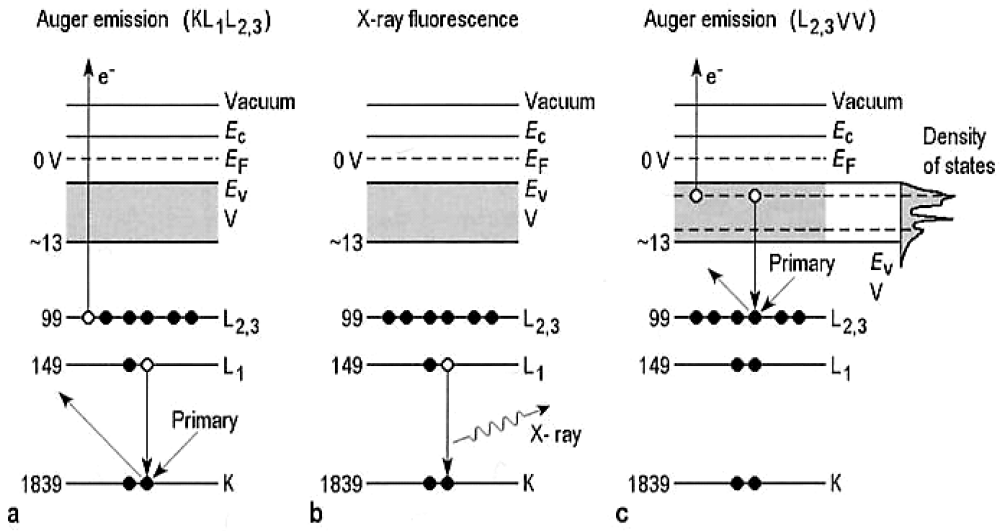

Figure 3.15: Generation of a fluorescence photon or an Auger electron due to deexcitation following a primary ionization process. a) and b) are illustrations of two competing deexitation processes as response to a core level ionisation. c) Auger emission process involving valance band states.(after [46; 80])

3.8 Low Energy Electron Diffraction

A further standard method for surface analysis is the low energy electron diffraction (LEED) method. This procedure allows the determination of surface periodicities and symmetries. A principle arrangement is shown in figure (3.16).

An electron gun produces a collimated monoenergetic electron beam which is directed parallel to the surface normal towards the sample. This defines the direction of k-vector **k** of the incident electrons, whereas the length of the k-vektor is determined by the wavelength λ which is a function of the beam energy E which is typically varied between 20 and 500 eV.

$$|\mathbf{k}| = \frac{2 \cdot \pi}{\lambda}; \lambda\,[\text{Å}] \approx \sqrt{\frac{150}{E\,[eV]}}. \tag{3.4}$$

The electron wavelength is in the range of the interatomic distances (1-2Å) on the surface and the electrons are therefore diffracted at the periodic surface structure. The interference of the backscatterd electron wave functions yield diffraction maxima and minima. The condition for constructive interference is given by [37]

$$n \cdot \lambda = d_{hk} \cdot sin\theta \tag{3.5}$$

where n is the diffraction order and d_{hk} is the distance between the 2D-real-space scattering rows. The angle θ gives the scattering angle at which a diffraction maximum can be expected (angle to the surface normal, see also figure (3.16)). A more detailed description of the LEED method with kinematic as well as dynamic scattering theory can be found in the corresponding literature [37; 46; 82; 85]

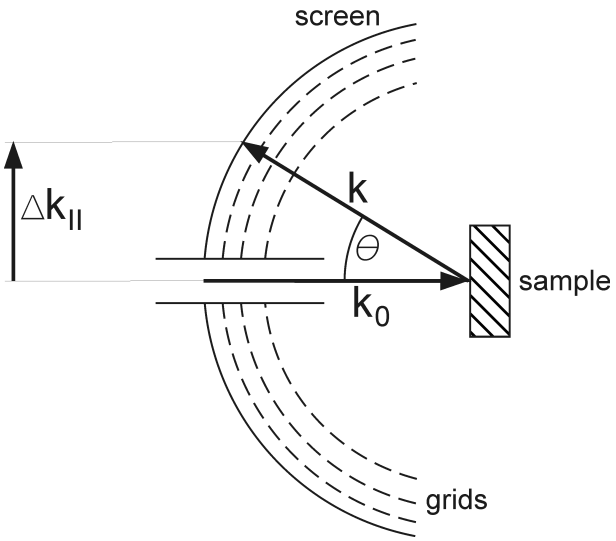

Figure 3.16: Principle arrangement for a LEED experiment.

3.9 Sample Mounting and Preparation Procedures

3.9.1 Sample Cleaning

For the present work exclusively Pd(111) single crystals were used. Either as part of a permeation source as explained in section 3.2 or as simple crystal disk which was fixed onto an ordinary sample holder. The conventional sample holder consists of a cylindrical, stainless steel tube (⌀ 3 cm) which is vertically mounted onto a manipulator stage on its top end. The manipulator is typically a rotational stage (360° rotation possible) which additionally provides translational movement of the rod in x- ,y- , and z-direction (maximum amplitude in all directions ± 20 mm). The bottom end of the sample holder tube is closed by a copper cup (⌀ 3 cm, length 3 cm) which is soldered onto the tube with its open end. The copper cup provides excellent thermal conductivity which is necessary for the liquid nitrogen (LN_2) cooling of the sample. As actual holder for the sample serves a block of copper which is tightly clamped onto the coppery end of the sample holder tube. The sample disc provides a groove which is milled into its rim. Two tantalum wires (⌀ 0.25 mm) are engaged in the groove forming two intricate loops which hold the disc at its diameter (see figure (3.17)). The ends of the wires are clamped between two electrical contacts which are mounted onto the copper block. The contacts are isolated from the copper block by ceramic inlays which provide good thermal conductivity but are electrical isolators. A side view of the installed sample holder can be seen in figure (3.5). The sample temperature was measured by means of a NiCr/Ni-thermocouple which was spot welded close to the sample rim at the backside. By concurrent resistive heating of the tantalum wires and liquid nitrogen cooling the sample temperature could be controlled in a range of 100 K to 1200 K. A LAB-View based computer program provided a comfortable regulation of the sample temperature.
The cleaning procedures of the "normal" Pd(111) sample and the sample as part of a permeation source were somewhat different. The permeation source was much more inertial concerning tem-

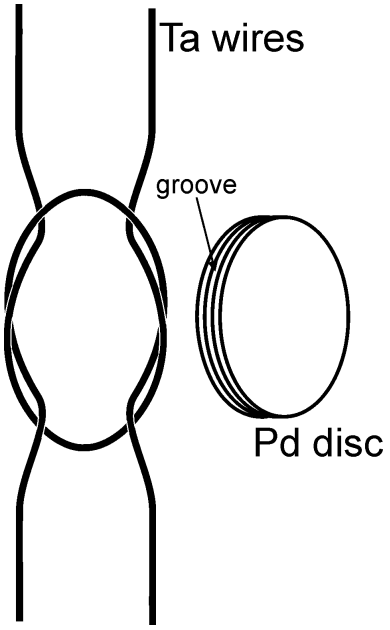

Figure 3.17: Scheme of the sample fixing by two intricate tantalum wire loops.

perature changes. Indeed, the time constants were that large that the source temperature was regulated by hand. Due to the sensitivity of the gold soldering joints the maximum applicable temperature was limited to 1000 K. The minimum attainable temperature was approximately 200 K. The permeation source palladium sample was typically sputtered at 650 K and annealed at 900 K. The Ar^+ sputtering parameters were $5{\cdot}10^{-7}$ to $1{\cdot}10^{-6}$ mbar of Argon and an acceleration voltage of 0.6 kV. The purity was checked by AES and the surface structure by LEED. Due to an overlap of the Pd 279 eV Auger peak and the carbon 272 eV peak small C contaminations were not directly detectable. Therefore the sample was baked in $5{\cdot}10^{-8}$ mbar of oxygen at 550 K followed by a flash up to 800 K in $1{\cdot}10^{-7}$ mbar of hydrogen. During the oxygen baking possible C contaminations on the surface are converted into CO_2 which instantaneosly desorb at 550 K. The hydrogen baking then converts the residual oxygen at the surface into water which also desorbs immediatly. On the palladium soldered into the permeation device sometimes traces of molybdenum were detectable which might stem from the soldering process during construction. A total removal of the molybdenum was not possible. The cleaning procedure for the simple Pd(111) sample which was used as substrate for thin Zn layers was done differently. It turned out that flashing Zn off worked faster than sputtering. Therefore the sample was first flashed to 1180 K at a heating rate of 2K/s and then held at 1170 K for about 2 minutes. Then the sample was sputtered at $1{\cdot}10^{-6}$ mbar of Argon slightly below room temperature just to avoid the diffusion of residual Zn into deeper layers. Subsequently the sample was annealed by flashing it to 1180 K at a heating rate of 2 K/s and held at 1170 K for 2 minutes. Possible residual contaminations of carbon and Zn were checked by performing CO thermal desorption measurements because the CO TD spectrum is very sensitive to surface contaminations.

3.9.2 Preparation of vanadium oxide layers

For the preparation of vanadium oxide layers the evaporation unit described in section 3.5 assembled with a commercial electron beam evaporator (OMICRON EFM 3 UHV Evaporator) was used. The evaporator was loaded with a high purity vanadium rod (GOODFELLOWS) (⌀ 2 mm). After cleaning the surface as described in section 3.9.1 the VO_x layers were prepared by reactive evaporation of vanadium under an oxygen pressure of $2{\cdot}10^{-7}$ mbar. The sample temperature was 523 K during deposition and the typically used vanadium deposition rate was 0.15-0.2 ML/min as determined by the quartz microbalance (evaporator settings: 780 V electron acceleration voltage, 1.9-2 A filament current, 25-30 mA emission current, 6-10 nA ion flux). The resulting structure can be checked by LEED.

3.9.3 Preparation of Zn /ZnO layers

The Zn layers were deposited by means of a home built evaporator as described briefly in section 3.6. In principle the deposition was carried out as for the vanadium/vanadium oxide layers. It turned out that Zn does not stick well on contaminated surfaces as will be discussed in chapter 9 in detail. Therefore the calibration of the deposited amount of Zn by means of a quartz microbalance is at first not very useful because initially the quartz crystal surface is ill defined. The microbalance just workes satisfactorily when all the impurities on the quartz crystal surface are buried by a thick, pure Zn layer which takes several 100 monolayers of Zn due to the resurfacing tendency of sulphur which inhibits Zn adsorption strongly. As alternative method for depostion rate control the mass 64 signal (Zn isotope: occurence 48.6 %) which is detectable by the quadrupole mass spectrometer in the residual gas during deposition is useable. Due to progressive adsorption of Zn at the sample holder and the chamber walls the sticking coefficient of Zn increases there, which in turn means an increase of the effective pumping speed for Zn. Therefore the "mass spectrometer method" is not very robust over long time periods (depending on the extend of Zn evaporation).

3.9.4 Measuring the Angular Distribution

The differentially pumped LOS detector can be used for the determination of the angular distribution of the desorption flux. For that purpose usually the sample is tilted in front of the detector and the signal can directly be assigned to the tilting angle. In this case a proper tilting of the permeation source (see section 3.2) was not possible because the rotational axes did not lie in the sample surface plane. A tilting of the sample would have caused an additional lateral offset and a slight change in the sample detector distance for each tilting angle. Therefore a different approach was chosen. Instead of tilting the permeation source it was laterally shifted in ± x and ± y direction with respect to the detector entrance aperture. A similar approach was applied in the group of J.T.Yates, where the distance between sample and detector was varied to gain information about the angular distribution [86; 87]. The obtained signal as function of the sample displacement was then evaluated by comparison with a Monte Carlo (MC) simu-

lation for the geometric arrangement, assuming a $cos^n\theta$-distributed desorption flux [88]. The angular distribution measurements were performed exclusively with the QMS shielded by the shutter of the LOS detector (see section 3.4) to provide a reliable density measurement (avoid influence of the particle velocity distribution). Additionally, this simplified the MC simulation because otherwise it would have been necessary to handle a two-aperture system (entrance of the detector chamber and entrance of the QMS) instead of a one aperture system (only the entrance aperture of the detector chamber). In figure (3.18) the basic measurement principle is drafted. The diameter of the entrance aperture was 8 mm and the effective sample-aperture distance was 17 mm. A maximum lateral displacement of ± 20 mm was possible.
The first step within this experiments was the adjustment of a constant permeation flux which was obtained by the use of a proper combination of deuterium backpressure and sample temperature. Initially the sampe was in off-line position which allowed to determine the background signal in the LOS detector caused by the general pressure increase due to permeation. Before the sample was directed towards the detector the manipulator was set to a maximum lateral position (+ 20 mm or -20 mm in x or y direction). Typically the sample was kept for 30-60 seconds at a specific lateral position and then shifted to the next position. When the opposite maximum position was reached the sample was again tilted to a off-line position. Thus a set of two data points for each displacement (symmetric sample) was obtained. This increased the accuracy and provided an opportunity to check whether the permeation flux keept constant throughout the measurement.

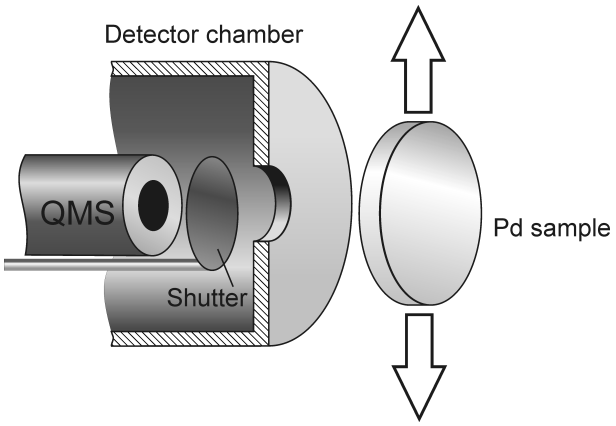

Figure 3.18: Principle geometric arrangement for measuring the angular distribution of the desorbing flux.

3.9.5 Monitoring Reaction Processes using a Permeation Source

Especially for the accurate monitoring of reaction products desorbing form a sample surface the permeation technique is very useful (see section 3.2). In figure (3.19) the setup is shown for measuring the particle flux from the permeation source surface. One reactant (deuterium) is delivered by the permeation process through the palladium bulk and the other reactant (O_2) is provided by a doser. The sample was positioned at a distance of 17 mm in front of the aperture (⌀ 8 mm) of the LOS detector. To provide a reliable partial pressure measurement the

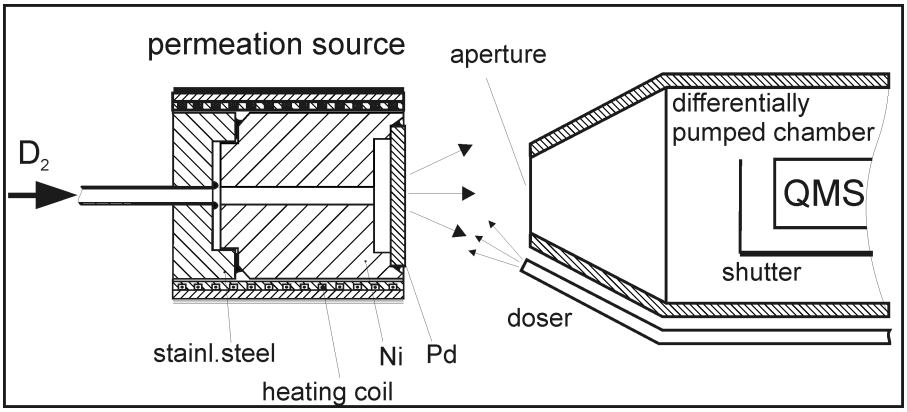

Figure 3.19: Arrangement for the in-line detection of reaction products formed by effusing/permeating D_2 and dosed oxygen.

QMS ion source was shielded by a shutter against the direct impinging particle flux. Therefore only isotropic gas, thermalized with the chamber walls, contributed to the QMS signal which guaranteed a strict proportionality to the ingoing flux (see section 4.1.1).

4 Data Evaluation

4.1 Calibration of Gas Amounts

For the quantitative evaluation of TD spectra or reaction rates a precice pressure measurement is necessary. Common pressure gauges which are used in the high and ultra-high vacuum technique are based on indirect methods. This means that actually not really pressure but gas density dependent quantities are measured, which makes the pressure measurement dependent on specific properties of the individual gases. Typically, pressure gauges based on indirect methods are calibrated for N_2. Therefore the displayed pressure during measuring of other gases has to be corrected by a factor (F_{gas}). This factors can be determined experimentally by a spinning rotor gauge. In this work the mainly used pressure gauge was an extractor-ionisation gauge and the determined correction factors ($F_{gas} = p_{spin.rot}/p_{extr}$) are compiled in table (4.1). Formally the correction factor F_{gas} can be written as product of another two parameters $I \cdot K = F_{gas}$. The parameter K is the correction factor for N_2-gas which is generally used as calibration standard. $I = F_{gas}/K$ gives the correction factors for all other gases relative to K. Thus I is a measure for the ionisation probability relative to nitrogen. Therefore this value can be used for comparison with the literature data or the literature values can be used for calibration when K is known [44].

Table 4.1: Correction factors for the extractor-ionisation gauge
$p_{gas} = F_{gas} \cdot p_{extr}$; $I = F_{gas}/K$; $K = F_{N_2}$

Gas	F_{gas}	I	K
N_2	1.47	1.00	1.47
H_2	3.60	2.45	1.47
D_2	3.37	2.29	1.47
Ar	1.08	0.73	1.47
O_2	1.60	1.09	1.47
CO	1.42	0.97	1.47

Based on this correction factors the extractor-ionisation gauge could be used to calibrate the quadrupole mass spectrometer (QMS) as partial pressure gauge. For that purpose the main chamber (base pressure 10^{-10} mbar) was flooded by a pure gas up to 10^{-8} mbar. The pressure and the QMS-ion-current signal were simultaneously monitored. Plotting the corrected pressure versus the QMS-signal yielded a straight line at constant slope. The slope could be identified

as conversion factor between QMS-ionisation-current signal and pressure. A direct calibration of the QMS via a spinning rotor gauge is problematic because quadrupole mass spectrometers tend to drift in their sensitivity within days and spinning rotor calibrations take long time, whereas the ionisation gauge exhibits quite a good long term stability (months/years) [44].
Once the pressure is known the total number of impinged molecules can be determined by using equation (2.7). Equation (2.7) is only valid for isotropically impinging gas molecules. Using a doser makes a correction necessary which can be obtained experimentally.
Using the permeation source the determination of the oxygen dosing enhancement factor can be performed by adjusting a constant hydrogen or deuterium permeation flux. Then one just has to measure the change in the $H_2O(/D_2O)$ production by providing the oxygen from the isotropic gas phase (2π) and via the doser. This can simply be achieved by putting the sample in dosing position and off dosing position. In figure (4.1) the evolution of the D_2O signal is shown. The experiment was done at two different oxgen pressures to enhance the accuracy. The data shown in figure (4.1) were acquired by the following procedure: Initially a constant deuterium permeation flux was adjusted (523 K sample temperature, back pressure $\approx$ 5 mbar) and the sample was then put in front of the oxygen doser. Subsequently the oxygen pressure was increased via the doser until a constant D_2O signal was measured by the QMS. This configuration was kept unchanged for about 60 seconds. Then the sample was turned away from the doser into off dosing position. Hence only isotropic impinging oxygen could contribute to the water formation on the sample surface. As can be seen in figure (4.1) the water formation dropped significantly. The doser was deactivated, the sample was again positioned in front of the doser and the whole procedure was repeated at doubled oxygen pressure. The dosing enhancement factor was determined to be 5.0. The crucial point for measurements of this kind is just that the water formation reaction is still below its maximum rate. Is the maximum water formation rate reached, which is in principle determined by the permeation flux, a change in the oxygen impingement rate will not be correctly reflected in the water formation rate.

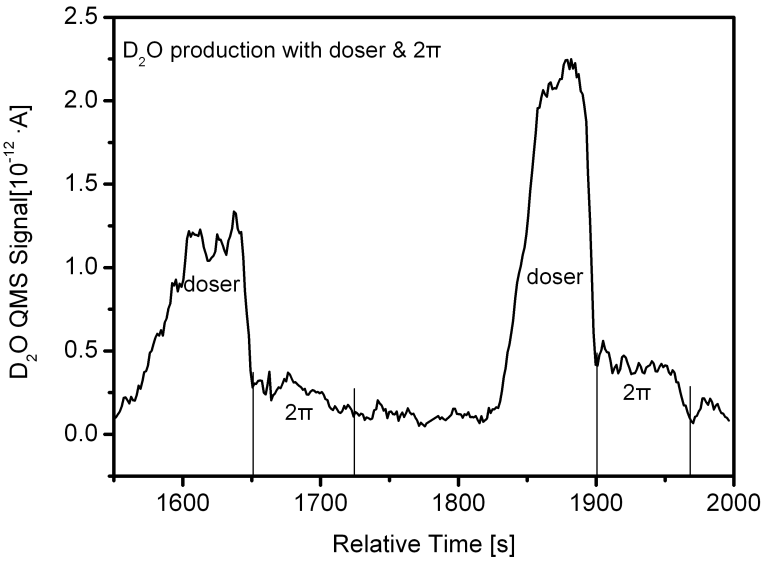

Figure 4.1: Determination of the O_2 dosing enhancement factor by monitoring the D_2O formation at constant permeation flux for direct oxgen dosing and 2π exposure.

For a standard sample the latter described method of course is not applicable. In that case one has to compare TD spectra which were gained by isotropic exposure and by direct dosing. Here one has to take care that the sample coverage keeps small. Otherwise the coverage dependency of the sticking coefficient will strongly affect the result (see section 2.2.1).

4.1.1 Determination of the Gas Flux

For closed, fix volumina the release of a number of particles at constant temperature always yields an increase of the pressure according to the ideal gas law equation (3.2). An UHV system deviates significantly from a fixed closed volume. There is always a certain rate of leakage which is compensated by the pumps which continuously remove gas from the volume which gives rise to a certain equilibrium pressure. Releasing a fixed number of particles into a UHV chamber, for example in an TDS experiment, the pressure will first rise and then drop again to its initial value. A stable increase of the pressure is just possible by maintaining a constant flux of particles which is released into the chamber. According to Redhead [89] the pressure increase Δp in a vacuum chamber of volume V is related to the gas flux $\frac{dN}{dt}$ into the chamber by

$$\frac{dN}{dt} = K \cdot S_{gas} \cdot \Delta p_{gas} + K \cdot V \cdot \frac{d\Delta p_{gas}}{dt} \tag{4.1}$$

where S_{gas} is the pumping speed ($\frac{dV}{dt}$[l/s]) for the gas under consideration and K is a factor that accounts for the conversion of pressure times volume into a particle number ($K = 3.24 \cdot 10^{19}$

$\frac{molecules}{Torr \cdot l}$ or $2.44 \cdot 10^{19}$ $\frac{molecules}{mbar \cdot l}$). Integrating equation (4.1) over time yields

$$N = K \cdot S \int_0^\infty \Delta p_{gas} \cdot dt + K \cdot V \cdot \int_0^\infty \frac{d\Delta p_{gas}}{dt} \cdot dt \tag{4.2}$$

which is the total number of gas molecules correlated with the pressure burst. For any sufficiently high pumping speed the last term in equation (4.2) vanishes and one gets

$$N \approx K \cdot S \cdot \int_0^\infty \Delta p_{gas} \cdot dt. \tag{4.3}$$

The flux $\frac{dN}{dt}$ can be calculated from the pressure increase Δp_{gas} by

$$\frac{dN}{dt} = S_{gas} \cdot K \cdot \Delta p_{gas}. \tag{4.4}$$

The pumping speed S_{gas} can be determined experimentally by using a method introduced by A. Winkler [44]. For this work the effective pumping speed for hydrogen/deuterium was of importance. A calibrated tungsten filament was loaded with hydrogen/deuterium and then the filament was heated up linearly. The desorbing hydrogen/deuterium lead to a characteristic pressure evolution. Since the total saturation hydrogen/deuterium coverage was known ($N_{Hsat} = 1.33 \cdot 10^{15}$ H-atoms) the pumping speed had been determined according to [89] by rewriting equation 4.3:

$$S_{H_2} = \frac{N_{Hsat}}{2 \cdot K \cdot \int_0^\infty \Delta p_{H_2} \cdot dt}. \tag{4.5}$$

The factor $\frac{1}{2}$ accounts for the fact that hydrogen desorbs in form of H_2 molecules and not as atoms.

The latter calibration method by determining the effective pumping speed is not very common in the literature for several reasons. First, the preparation and calibration of the tungsten filament is extremely time consuming and does not work for all gases. For noble gases the filament would have to be cooled to very low temperatures. More complex gas molecules dissociate on the W-surface and might not entirely desorb in their initial configuration. For example hydrocarbons or alcohols crack at the surface and one will get H_2, CO, CO_2, H_2O and a number of debris in the desorption spectra instead of the intact molecule.

A more common method is to take the thermal desorption spectrum of a specifically prepared sample as a reference. For example, exposing the clean Pd(111) surface to oxygen at room temperature gives rise to a (2x2) LEED pattern which corresponds to an oxygen coverage of 0.25 ML [90; 91]. The corresponding TD spectrum shows a single peak centered at 770 K [92]. The peak area of this single peak at its saturation is then assigned to a quater ML of oxygen and serves as a calibration standard.

A main focus of this work deals with thermal desorption spectra obtained from differently prepared palladium surfaces. Typically TD spectra are measured in an in-line experiment as explained in chapter 3 section 3.4. This inline detection contains a further complication concerning the quantitative determination of the adsorbed coverage. A quadrupole mass spectrometer

is a density detector. For an in-line experiment actually a flux detector is needed otherwise the measured data has to be corrected. A flux Φ can be expressed in terms of velocity v and density ρ:

$$\Phi = \rho \cdot v. \tag{4.6}$$

A QMS is sensitive to the gas density, which for an ideal, isotropic homogeneous thermally equilibrated gas is proportional to the partial pressure. By probing particle beams, however, things are somewhat different. The detection probability of molecules that traverse the ionisation volume at velocity v is proportional to $\frac{1}{v}$ [93]. During a thermal desorption experiment the surface temperature and therewith the mean velocity of the desorbing molecules change. The translational energy scales with temperature T and the velocity therefore with $\sqrt{T}$ [94]. Therefore one gets

$$\rho \propto \frac{1}{v} \propto \frac{1}{\sqrt{T}}.$$

The QMS ion current signal has to be corrected by multiplying with $\sqrt{T}$. In real experiments there is a mixing of in-line and isotropic signal which can be more or less pronounced. For systems that exhibit a high isotropic part a correction is not necessary.

4.2 Evaluation of Thermal Desorption Spectra

Based on the Polanyi-Wigner equation (2.37) an evaluation of the TD spectra is possible. An interesting point is that for determining the desorption energy E_{des} the knowledge of the absolute desorption rate r_{des} is not necessary.

4.2.1 The Leading Edge Method

Neglecting a coverage dependence of the preexponential factor ν and E_{des} the Polanyi-Wigner equation has the form for zero order desorption:

$$r_{des} = -\frac{d\Theta}{dT} \cdot \frac{dT}{dt} = -\frac{d\Theta}{dT} \cdot \beta = \nu_0 \cdot e^{-\frac{E_{des}}{k_B T}} \tag{4.7}$$

where β is the heating rate [K·s^{-1}]. Taking the logarithm of equation (4.7) one gets

$$ln(|r_{des}|) = -\frac{E_{des}}{k_B T} + ln\left(\frac{\nu_0}{\beta}\right). \tag{4.8}$$

When plotting the logarithm of the rate versus $\frac{1}{T}$ one gets a straight line with slope $\frac{E_{des}}{k_B}$. From the intercept at the axis of the ordinate one can calculate the preexponential factor only if the desorption rate was calibrated correctly. In figure (4.2) the leading edge method for the multilayer desorption of Zn/Pd(111) is shown.

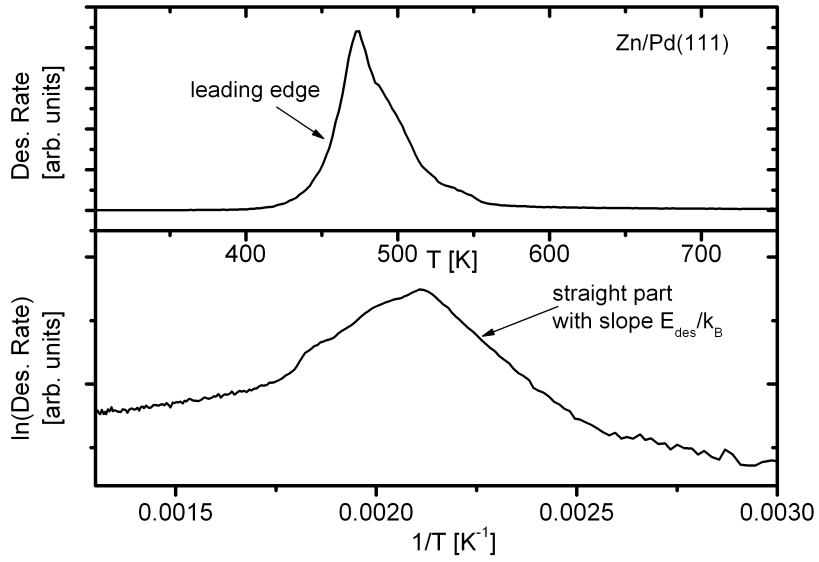

Figure 4.2: Top figure: multilayer Zn desorption spectrum of Zn/Pd(111). Bottom figure: plot of the logarithm of the desorption rate versus 1/T. The slope of the straight part gives the desorption energy.

4.2.2 The Redhead Concept

For the analysis of thermal desorption spectra of first and second order kinetics a number of methods are suggested [95–98]. Indeed, for a full analysis without any assumption time consuming and complex evaluation procedures are necessary. A more simple approach was introduced by P. A. Redhead [89] for first order desorption systems. Starting point is again the assumption that the activation parameters in the Polanyi Wigner equation (2.38) are independent of coverage. For first order kinetics the desorption spectra qualitatively look like shown in figure (2.5). The peak maxima always occur at the same temperature $T = T_m$ independent from coverage. At the peak maximum the derivative of the desorption rate has to vanish $\frac{dr_{des}}{dT}|_{T_m} = 0$. Since r_{des} can be expressed as $-\frac{d\Theta}{dt} = -\beta \cdot \frac{d\Theta}{dT}$ it follows that $\frac{d^2\Theta}{dT^2}|_{T_m} = 0$. Therefore

$$\frac{d^2\Theta}{dT^2} = \frac{\nu}{\beta} \cdot \frac{d\Theta}{dT} \cdot exp\left(-\frac{E_{des}}{k_B T}\right) + \frac{\nu}{\beta} \cdot \Theta \cdot \frac{E_{des}}{k_B T^2} \cdot exp\left(-\frac{E_{des}}{k_B T}\right).$$

Evaluation of that expression at $T = T_m$ yields

$$\left.\frac{d\Theta}{dT}\right|_{T_m} = \Theta \cdot \frac{E_{des}}{k_B T_m^2}$$

The expression $\frac{d\theta}{dT}$ can be substituted by the right hand side of the Polanyi Wigner equation (2.38) for first order desorption. Thus one obtains

$$\frac{E_{des}}{k_B T_m^2} = \frac{\nu}{\beta} \cdot exp\left(\frac{-E_{des}}{k_B T_m}\right).$$

Taking the logarithm of the latter equation and solving for the desorption energy yields

$$E_{des} = k_B \cdot T_m \left[ln\left(\frac{\nu \cdot T_m}{\beta}\right) - ln\left(\frac{E_{des}}{k_B T_m}\right)\right] \tag{4.9}$$

The desorption energy is still contained in the the second term within the square brackets but this term is small relative to the first term and can be estimated as $ln\left(\frac{E_{des}}{k_B T_m}\right) \approx 3.64$. The error that originates due to the introduction of the latter value is less than 1.5 % for $10^8 < \frac{\nu}{\beta} < 10^{13} \cdot \mathrm{K}^{-1}$. Although an estimated value for the preexponential factor ν has to be introduced the method provides the calculation of E_{des} from one single desorption spectrum. For many first order systems the preexponential factor can safely be estimated to be $10^{13} \cdot \mathrm{s}^{-1}$ without being too inaccurate.

4.2.3 Determination of the Absolute Rate

As mentioned in section 4.2.1 the knowledge about the absolute rate is necessary to gain the correct preexponential factor by applying the leading edge method. The determination of the rate can in principle be done by using the relation (4.4). In practice, particularly for in-line experiments, this is not very convenient. The rate determination via a calibrated TDS is more applicable.
A properly corrected QMS signal (see equation (4.4)) is proportional to the desorption rate r_{des}. If the QMS signal $I_{QMS}(t)$ is plotted versus the acquisition time t of the measurement the area obtained by integration of $I_{QMS}(t)$ over t is proportional to the total number of detected (desorbed) molecules N_{des}.

$$N_{des} = C \cdot \int_0^\infty I_{QMS}(t) \cdot dt. \tag{4.10}$$

Is the total number of adsorbed molecules known e.g. from other calibration methods (quartz microbalance, literature,...) the correction factor C can be calculated. To obtain the rate related to the surface unit area one has just to divide by the sample surface area A_{sample}.

$$r_{des} = \frac{I_{QMS}(t) \cdot C}{A_{sample}} \tag{4.11}$$

4.3 Determination of the Angular Distribution

The line-of-sight detector introduced in section 3.4 can be used to determine the angular distribution of the desorbing particle flux by assuming a $cos^n\theta$ function. As already stated in section 2.2.2 the angular dependence of the desorption flux can in many cases be approximated by

$$D(E, \theta) = D(E, \theta = 0^\circ) \cdot cos^n\theta.$$

Based on the latter assumption one can determine tha angular distibution by a the simple experiment described in section 3.9.4 and comparison with a MC simulation. The obtained

dataset consisted of ion-current signals which were assigned to the lateral displacement of the sample. The raw data of such a measurement are shown in figure (4.3 a). The signal level at the beginning and the end of the spectrum in figure (4.3 a) is the background signal caused by the general pressure increase in the main chamber due to the permeating flux. After subtracting the background level the mean signal value at every position can be determined and normalized to the maximum signal (figure 4.3 b).

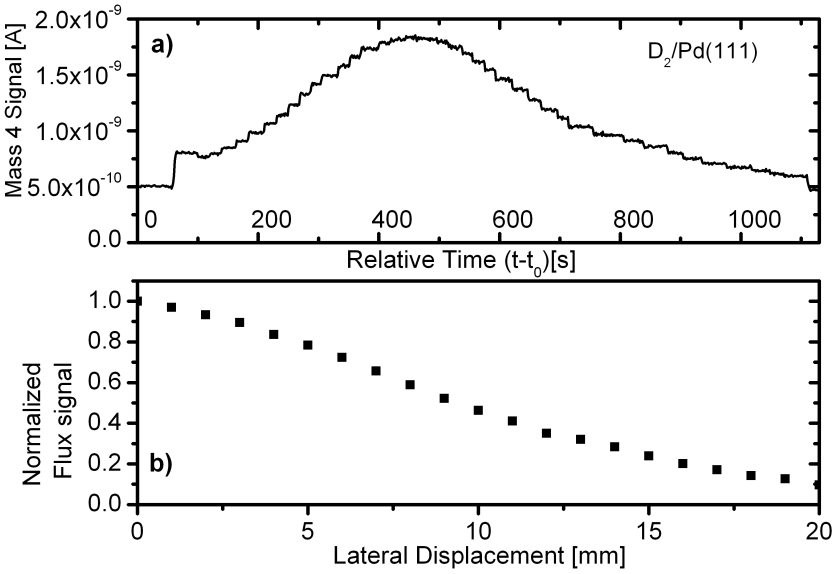

Figure 4.3: a): Raw data of the detected flux at different lateral displacements. Approximate acquisition time per position ≈ 60 seconds per position. b): Edited data obtained from (a) normalized to the maxium flux.

The normalized signal versus lateral displacement can then be compared with the results of a MC simulation for the same geometry as used in the experiment and various $cos^n\theta$-distributions (n=1,...).
Details about the simulation procedure can be found in [88]. The basic steps within the simulation are:

1. A starting point is randomly selected on the emitter (sample).
2. Random determination of the polar angle θ and the azimuth angle ϕ according to a $cos^n\theta$ distribution. The ϕ values have to be uniformly distributed in the interval [0,2π], whereas the polar angle can be obtained from $\theta = arccos \cdot \sqrt[n+1]{1-b}$, with b uniformly distributed in the interval [0,1].
3. Calculate the coordinates of the receiving point of the trajectory on the the detector plane.
4. Count the arrival point if its coordinates lie within the detector area (aperture). Typically, the evaluation of 10^5 trajectories is sufficient for a reliable result.

Figure 4.4 shows a compilation of simulated fluxes for various $cos^n\theta$ distributions normalized to the maximum flux as a function of the lateral displacement.

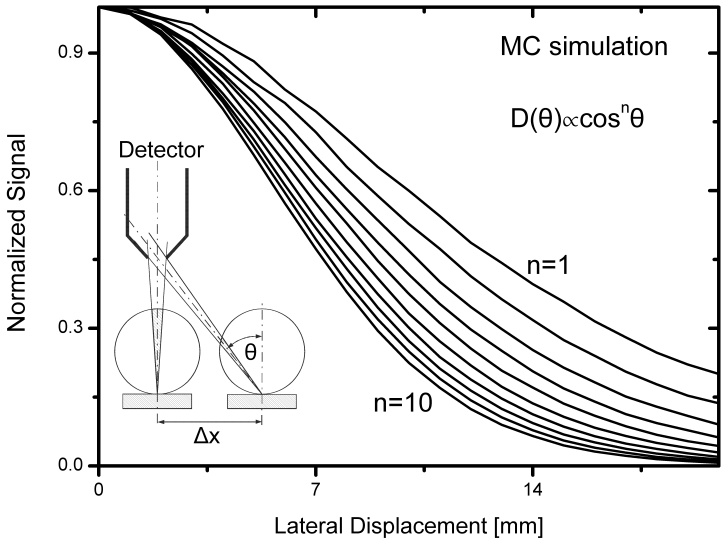

Figure 4.4: Monte Carlo simulation of the flux dependence as a function of the lateral displacement. The parameter n of the angular distribution in form of $cos^n\theta$, ranging from n=1 to 10 with increment 1. The geometric parameters are detector aperture:⌀ 8 mm; aperture sample distance: 17 mm; effective sample diameter:⌀ 7 mm.

4.4 Evaluation of Time-Of-Flight Spectra

The evaluation of TOF-spectra is a complex task due to a number of influences that cause a distortion of the "real" spectrum as already outlined in section 3.3. The evaluation procedures have already been explained in detail in the works of C. Eibl [57] and K.-H. Allers [99]. Therefore only a brief description will be given here.
The TOF distribution and the corresponding velocity distribution are in principle correlated by a simple transformation $f(v) = f\left(\frac{l}{t'}\right)$. Here t' is the time it took a particle to traverse the distance l. Nevertheless the following major influences generate a more complex correlation:

- The detection probability scales with $\frac{1}{v}$, therefore the fast particles produce a underweighted signal compared to the slower ones.
- The chopper-gate-function generates a spectrum distortion due to its finite size.
- The finite length of the ionisation volume of the detector QMS influences the effective length of the flight path.
- The finite time slots for the data acquisition yield an additional spectrum distortion.

- First order effects of the phase jitter of the chopper motor are compensated by the synchronized triggering of the multi channel analyser. The high production tolerance of the chopper disc yields a positioning error that is neglectable.

The remainig points can be treated simultaneously in a single mathematical expression that gives the correlation between the number of counted particles z_i in the i-th channel (distribution of the arrival times at the detector) and the velocity distribution [99; 100]:

$$z_i = \int_{t=(i-1)\cdot\Delta t}^{i\cdot\Delta t} \int_{l=l_1}^{l_2} \int_{t'=0}^{t} P(t-t') \cdot \frac{l}{t'^2} \cdot I(t') \cdot R(l) \cdot f\left(\frac{l}{t'}\right) \cdot dt' dl dt \tag{4.12}$$

where $P(t)$ is the chopper-gate-function, $\frac{l}{t'^2}$ is the Jacobian determinant $\left|\frac{dv}{dt'}\right|$ from the transformation $dv \rightarrow dt$. $I(t')$ represents the ionisation probabilty for a particle with flight time t' and $R(l)$ resembles the normalized electron density along the ioniation volume axes. The integration over t accounts for the finite analyser channel width, whereas the integration over l together with $R(l)$ accounts for the axial spreading of electrons around the ion source filament plane, which yields a smearing of the flight path length which is defined as distance between chopper disc and ion source filament plane. The convolution with $P(t)$ resembles the broadening of the TOF spectrum by the finite width of the chopper gates.
Due to the channel width of $2\mu s$ a measured spectrum consisted of 1200 equidistant interpolation points. Therefore the spectrum can be considered to be quasi continuous and the integration over t can be omitted. The electron density $R(l)$ is symmetric about the filament plane in first approximation and the ionisation volume is small compared to the length of the flight path which means that the influence of $R(l)$ can be neglected as well [99]. Since a QMS works as ideal density detector [57] the detection probability is proportional to the inverse velocity of the incoming particles $\frac{1}{v} = t' \propto I(t')$ which can easily be considered. The chopper-gate-function can be sufficiently approximated by a rectangular function with an effective chopper opening time τ_c. Introducing all the latter considerations into equation (4.12) yields a relation between the measured TOF distribution and the velocity distribution:

$$z(t) = \int_0^t P(t-t') \cdot \frac{l}{t'} \cdot f\left(\frac{l}{t'}\right) \cdot dt'. \tag{4.13}$$

According to equation (4.13) the obtained distribution function is not "normalized" anymore due to the influence of the $\frac{1}{v}$ proportionality of the detection probability. Additionally the finite chopper opening time τ_c causes a broadening of the spectrum and a shift of the total spectrum of $\frac{\tau_c}{2}$ along the time axes. A further time shift of the spectrum caused by the delay time of the trigger impulse and the time between the moment of ionisation and the registration (flight time in the rod system of the QMS, electronic reaction time,...) can be considered by an effective delay time parameter which can be determined experimentally [57].
A straight forward method to evaluate the TOF data is a numerical deconvolution of the integral (4.13). Formally the deconvolution can be obtained via a Laplace transformation by using the "Faltungssatz" [101]:

$$f\left(\frac{l}{t}\right) = \frac{t}{l} \cdot \mathfrak{L}^{-1}\left\{\frac{\mathfrak{L}\{z(t)\}}{\mathfrak{L}\{P(t)\}}\right\} \tag{4.14}$$

where $\mathfrak{L}^{-1}$ means the inverse transformation. Assuming a rectangular chopper gate function $P(t)$ with openeing time τ_c one gets for $\mathfrak{L}\{P(t)\} = \tilde{P}(s)$

$$\tilde{P}(s) = \frac{1}{s \cdot \tau_c} \cdot \left(1 - e^{-s \cdot t}\right) \tag{4.15}$$

which can also be rewritten as

$$\tilde{P}(s)^{-1} = s \cdot \tau_c \sum_{r=0}^{\infty} e^{-r \cdot s \cdot \tau_c} \tag{4.16}$$

Insertion of equation (4.16) into (4.14) and applying the "Differentiationssatz" and the "Verschiebungssatz" [101] one obtains the following sum:

$$f\left(\frac{l}{t}\right) = \frac{t}{l} \cdot \tau_c \cdot \sum_{r=0}^{\infty} \frac{d}{dt} z(t - r \cdot \tau_c). \tag{4.17}$$

The sum (4.17) can in principle be used to perform a numerical evaluation of the measured spectra. Unfortunately the spectra exhibit a rather high noise level in general which is amplified by the differentiation in (4.17). Only for spectra with good signal to noise ratio and adequate smoothing procedures this straightforward method is applicable.
A more robust method is the so called **Moment Method** which is introduced in [102]. This method allows the extraction of parameters like particle number or mean kinetic energy. Alcalay and Knuth [103] suggested the following way to evaluate the moments of the distribution. Applying the definition of a moment M_n of degree n on the velocity distribution $f(v)$ one gets

$$M_n = \int_0^{\infty} v^n \cdot f(v) \cdot dv.$$

Substitution of v by $\frac{l}{t}$ then yields

$$M_n = \int_0^{\infty} \frac{l^{n+1}}{t^{n+2}} \cdot f\left(\frac{l}{t}\right) \cdot dt. \tag{4.18}$$

The TOF distribution $f\left(\frac{l}{t}\right)$ can be substituted by equation (4.17) and partial integration leads to

$$M_n = \int_0^{\infty} \underbrace{\sum_{r=0}^{\infty} \frac{\tau_c \cdot l^n \cdot (n+1)}{(t' + r \cdot \tau_c)^{n+2}}}_{w_n(t')} \cdot z(t') \cdot dt' \tag{4.19}$$

where $w_n(t')$ acts as a weighting function which can be evaluated or approximated separately.
A further comfortable way for TOF data evaluation is a least-squares fitting procedure by using a single Maxwellian (MB) velocity distribution as initial approximation. In order to fit the obtained data the velocity distribution has to be converted into a TOF distribution according to equation (4.13). A fitting algorithm was developed by C. Eibl [57] who also implemented the required calculations into the widely used data manipulation program ORIGIN. Using the fitting procedure of Eibl the following parameters are treated:

- T_{MB}: temperture according to the Maxwellian velocity distribution
- A_0 : hight of the spectrum baseline
- A_1 : amplitude of the MB distribution
- t_0 : time offset (effective delay time between ionisation and electronic registration)
- τ_c: effective chopper opening time.

The last two parameters in the list above can be obtained experimentally. An isothermal scattering experiment at room temperature provides a scattered particle flux which exhibits an angular cosine distribution and a room temperature Maxwellian velocity distribution. Since the corresponding temperature of the distribution were known they could be introduced into the fitting procedure yielding a time delay of $1.6{\cdot}10^{-5}$ s and an effective chopper opening time of $6{\cdot}10^{-5}$ s for a chopper slit frequency of 800 Hz for deuterium, which is a bit longer than the expected 40μs according to the disc geometry. For D_2O a delay time of $6{\cdot}10^{-5}$ s and an effecive chopper opening time of $1{\cdot}10^{-4}$ s at a chopper slit frequency of 400 Hz were obtained.
The drawback of this method is that in principle a Maxwellian distribution can only by expected if the sticking coefficient does not show too much energy dependence (see section 2.2.2). Most interestingly a fitting of the obtained data was often possible just by applying a single Maxwellian distribution. This indicates that the systems always aspire an equilibrium distribution which is Maxwellian. For systems with a strong energy dependence of the sticking coefficient the moment method was applied.

4.5 Coverage Determination by AES

Typically AES is used to identify the different species which are present on the surface and the near subsurface region (3-5 ML). Generally the energy resolution of AES is not as good as those of XPS but the sensitivity is much higher. Therefore AES is a valuable tool for the qualtitative characterisation of the chemical surface composition. To obtain quantitative informations one can use different approaches depending on the degree of accuracy which is needed.
In the following paragraphs the calibration of a Zn overlayer on the Pd substrate as relevant for the present work is carried out exemplarily. For the evaluation of the coverage by Auger peak to peak ratios the screening of the substrate intensity by the overlayer and the intensity contribution of the multiple layers of the substrate bulk have to be considered. Additionally, one has to take into account that the Auger electron yield of Pd and Zn bulk differ significantly. The corresponding intensities can be obtained experimentally by measuring the clean surface and the surface covered with a Zn layer thick enough to damp the Pd substrate signal totally. The measurements yielded a Zn-bulk to Pd-bulk intensity ratio of $I_{Zn,bulk}/I_{Pd,bulk}$=0.10±0.02. The attenuation of the Pd signal by a Zn layer of thickness d_{Zn} can be characterized by the

ratio of the Pd signal weakened by the Zn layer $I_{Pd,dZn}$ and the undisturbed Pd signal $I_{Pd,bulk}$:

$$\frac{I_{Pd,dZn}}{I_{Pd,bulk}} = f_{Pd,Zn} = exp\left(-\frac{d_{Zn}\cdot cos^{-1}\theta}{\lambda_{Pd330,Zn}} - \frac{d_{Zn}}{\lambda_{prim,Zn}}\right) \tag{4.20}$$

The factor $\lambda_{x,y}$ gives the value of the inelastic mean free path (IMFP) of electrons with a kinetic energy characteristic for source x ($Pd330$=330 eV Auger electrons, $prim$=3keV primary beam energy) in the material y. Due to the geometry of the used cylindrical mirror analyser only Auger electrons emitted under the acceptance angle θ (For the used device this is 31.2° with respect to the surface normal [79]) can be detected. The factor $cos^{-1}\theta$ accounts for the fact that the detected electrons have to transit an effective distance longer than d_{Zn}.
The contribution f_{Zn} of the uppermost Zn layer to the total Zn bulk intensity can be approximated by

$$f_{Zn} = 1 - exp\left(-\frac{d_{Zn}\cdot cos^{-1}\theta}{\lambda_{Zn994,Zn}} - \frac{d_{Zn}}{\lambda_{prim,Zn}}\right) \tag{4.21}$$

In equation (4.21) the intensity of the Zn surface layer was just calculated by subtracting the Zn bulk signal attenuated by an additional Zn layer from the total bulk intensity taking into account that all the underlying layers in principle generate the same intensity due to their quasi unlimited number. A further point to consider is the backscattering of the primary beam in the solid which leads to additional generation of Auger electrons. Ichimura et al [104; 105] accounted for that by a backscattering factor

$$R = 1 + \frac{I_{back}}{I_{prim}}$$

where I_{back} is the intensity of a specific Auger line caused by the backscattered electrons and I_{prim} is the Auger intensity due to the primary electron beam. This factor R is inherently included in every measurement. The corresponding values for the backscattering factor $R_{A,B}$ were taken from the literature [104; 105] ($R_{1keV,Pd}$=1.625; $R_{1keV,Zn}$=1.51). Here the subscript A denotes the energy necessary for the ionisation process foregoing to a specific Auger process which is A=340.9 eV for the Pd 330 eV Auger electrons and A=1021.8 eV for the Zn 994 eV Auger electrons [104; 105] and subscript B specifies the scattering material. For a 1 ML Zn layer one can assume that all the back scattered electrons originate from the underlying palladium which leads to a modification of equation (4.21) to

$$f_{Zn}^{Pd} = \left[1 - exp\left(-\frac{d_{Zn}\cdot cos^{-1}\theta}{\lambda_{Zn994,Zn}} - \frac{d_{Zn}}{\lambda_{prim,Zn}}\right)\right]\cdot\frac{R_{1keV,Pd}}{R_{1keV,Zn}}. \tag{4.22}$$

Therefore one can express the Auger intensity ratio for palladium covered with a Zn layer of thickness dZn by:

$$\frac{I_{dZn}}{I_{Pd,dZn}} = \frac{I_{Zn,bulk}}{I_{Pd,bulk}}\cdot\frac{f_{Zn}^{Pd}}{f_{Pd,Zn}}. \tag{4.23}$$

By using $\lambda_{Zn994,Zn}$=16Å, $\lambda_{prim,Zn}$=38Å, $\lambda_{Pd330,Zn}$=7Å [106; 107] and d_{Zn}= 2.47Å [108] in equation (4.23) one gets for the Zn994/Pd330 Auger intensity ratio a value of 3.8% for a Zn coverage of 1 ML.

4.6 Density Functional Theory Calculations

Various experimental methods are used to determine the structure of surfaces and adsorbate configurations. A long established method is the low energy electron diffraction (LEED) (see section 3.8) which provides an analysis of the surface periodicities. A further method is the reflection adsorption infrared spectroscopy (RAIRS) for the observation of dipole active vibrations on the surface which allows some conclusions on binding angles when polarized light is used. A real space map of the surface can be measured directly by scanning tunneling microscopy (STM). Nevertheless, the experimental results are often difficult to interpret. Therefore a comparison with ab initio calculated results is necessary. A method which has become essential in the past decades is the so called density functional theory (DFT) calculation. DFT is a quantum mechanical theory which allows the calculation of the electronic structure of a many body systems. The method is based on the findigs of Hohenberg und Kohn [109] who proved that the electronic ground state of a many electron system in a static potential ($v(\boldsymbol{r})$) can be expressed by a unique functional of the elctron density $n(\boldsymbol{r})$. In a further work Kohn and Sham introduced self-consistent equations including exchange and correlation effects for the electronic ground state [110]. For a practical implementation of DFT it is customary to separate the functional for the interacting electrons into a noninteracting kinetic part $T[n]$ and two interacting parts namely the coulomb part (representing the electrostatic energy) and the exchange-correlation energy part $E_{xc}[n]$ (non-classical electronic interaction).

$$E = \int v(\boldsymbol{r}) \cdot n(\boldsymbol{r}) \cdot d\boldsymbol{r} + \frac{1}{2} \cdot \int \int \frac{n(\boldsymbol{r'}) \cdot n(\boldsymbol{r})}{|\boldsymbol{r} - \boldsymbol{r'}|} \cdot d\boldsymbol{r} \cdot d\boldsymbol{r'} + T[n] + E_{xc}[n] \qquad (4.24)$$

In equation (4.24) the first term accounts for the interaction with an external potential $v(\boldsymbol{r})$. The second term gives the classical electrostatic electron-electron interaction. All the parts can be dealt with simply except the correlation-exchange expression. There were a number of methods invented to approximate the correleation-exchange energy. The simplest one as introduced by Kohn and Sham is the so called local density approximation (LDA) [110]. LDA is based on the assumption that the contribution of each volume element to the total correlation energy is the same as it would be within a homogeneous electron gas with the same density as is found in the corresponding volume element. Therefore $E_{xc}[n]$ depends only on the local density at the coordinate where the functional is evaluated. The latter idea can be generalized to a spin dependent system (local spin density approximation: LSDA). A further formalism is the so called generalized gradient approximation (GGA) which is also a local but additionally accounts for the gradient of the local density [111].
In practice the problems are solved by reformulating them as periodic. Then a solution based on the expansion into plane waves with a limited number of possible k-vektors can be introduced.

For calculating surfaces the solid is simulated by periodicly arranged slabs of a certain thickness (typically a few atomic layers) with a vacuum spacing in between. The slabs have to be thick enough to reproduce the bulk behaviour satisfactorily, but not too thick because of the limited computer power. Similar requirements have to be considerd for the vacuum layer. It has to be large enough to prevent significant interactions between successive slabs.
Within this thesis DFT calculations were carried out by using the Vienna Ab-initio Simulation Package (VASP) [112–116] utilising the PW91 generalized gradient approximation (GGA) [111]. The Pd(111) substrate was modelled by a 4 layers thick slab with a vacuum spacing larger than 20 Å. The PdZn surface alloy was simulated by a 5th layer forming a 2×1 structure of Pd and Zn. For most of the calculations one layer consisted of 4 atoms which allowed the testing of the coverages down to quarter of 1 monolayer. For the slab model calculations a (7×7×1) Monkhorst Pack grid was applied in combination with the Methfessel-Paxton [117] smearing with a default smearing width of 0.2 eV [118]. The energy cut-off was set to 400 eV for all presented results. Furthermore the atomic coordinates of the adsorbates were optimized until the force acting on each atom became less than 0.01 eV/Å.

5 D_2 on clean Pd(111)

The adsorption/desorption of hydrogen and deuterium on palladium has been studied extensively within the last decades. The system D_2/Pd(111) is especially relevant for hydrogen storage [119] and fuel cell technology [120]. Within the experimental and theoretical work palladium single crystal surfaces (Pd(111) [10–12; 54; 88; 121],Pd(100) [55; 122], Pd(110) [60; 123–129]) as well as polycrystalline palladium ([10–12]) have been examined. Even though, a lot of work has been done there is still scientific interest on this topic. Palladium is an essential component in the field of heterogeneous catalysis due to its special attributes concerning hydrogenation and dehydrogenation reactions as relevant for fuell cells [15; 21; 130].
In the following chapter the focus was laid on the dynamics of hydrogen/deuterium desorption from Pd(111) single crystal surfaces. Complementary to the time-of-flight studies as performed by G. Pauer [10] angular distribution measurements were carried out. In case of Pd(111) which can be considered as one of the classical model systems in surface science [42; 56; 131] this additionally provides the opportunity to test fundamental principles like detailed balance [48–50] and energy scaling [41]. A short decription of these principles has been given in chapter 2. Measurements of the angular distribution [132; 133] and the translational energy distribution[12; 134] as well as the determination of the energy distribution of the internal degrees of freedom [122; 135; 136] using the permeation technique has been successfully applied in the past. For these experiments most often the Pd(100) and Pd(110) surfaces have been used because they exhibit a certain corrugation which is more promising for finding angular dependent effects. Consequently there have been rather less basic studies carried out on the smooth Pd(111) surface so far.
The angular distribution was determined by evaluating the deuterium flux signal in the LOS detector as a function of the lateral sample displacement. The experimental procedure has been explained briefly in chapter 3. The data evaluation which was done by comparison with MC simulations is described in 4. The following description can also be found in [137].

5.1 Angular dependence of the deuterium desorption from clean Pd(111)

The experimental results of the deuterium flux measurements after permeation/desorption from the clean Pd(111) surface as a function of the lateral sample displacement are shown in figure (5.1) for two different sample temperatures, 523 K and 700 K, respectively. In addition, the best fits to the experimental data points according to the MC calculations are drawn. For the sample temperature of 523 K, the data points can be approximated by an angular distribution

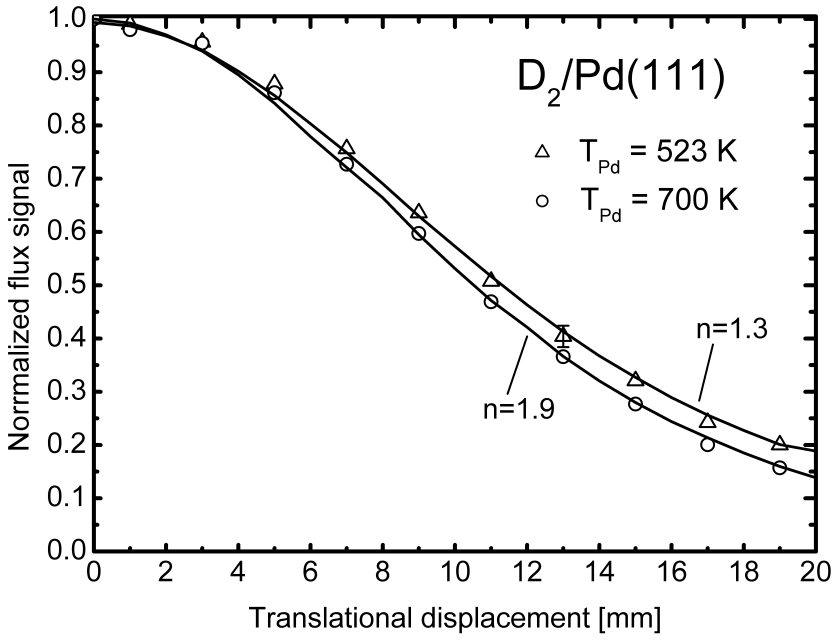

Figure 5.1: Experimentally obtained change of the deuterium desorption flux signal from clean Pd(111) as a function of the lateral sample displacement, for two different temperatures, 523 K and 700 K, respectively. Best fits of simulated curves to the experimental data are shown as solid lines.

function of $cos^n\theta$, with $n = 1.3$. In the case of the sample at 700 K, the angular distribution is somewhat forward focused and can be best approximated by $n = 1.9$. The still rather broad angular desorption distribution tells us that only a small activation barrier for adsorption exists for this system. This is in good agreement with previous experiments obtained using monoenergetic molecular beams [138]. It has been found that the initial sticking coefficient as a function of the translational energy of the impinging hydrogen (deuterium) molecules slightly decreases up to energies of about 100 meV, but then slightly increases for higher beam energies [131; 138]. The integral initial sticking coefficient of H_2 (D_2) at room temperature is about 0.5.

Before the measured data on the angular distribution is discussed and compared to adsorption data in the context of detailed balance (DB) and energy scaling some specific properties of the system H/Pd(111) shall be mentioned. The initial sticking coefficient of hydrogen on this surface behaves quite differently to that on the (111) planes of nickel [60] and platinum [139], which are materials of the same group in the periodic table. For these materials the sticking coefficient increases steeply with increasing kinetic energy in the whole energy range, indicating a strong activation barrier for adsorption. The integral sticking coefficient for a room temperature gas is below 0.03 [50]. This difference has been explained by subtle differences in the band structure along the ΓL direction of the Brillouin zone [131]. The L'_2 point in palladium is above the Fermi

level, in contrast to that for nickel and platinum [140]. This leads to non-occupied surface states in the centre of the surface Brillouin zone, which has a consequence on the charge density profile outside the surface. The smaller charge density on the Pd(111) surface, as compared to the Ni(111) and Pt(111) surface, leads to a decreased Pauli repulsion and therefore to a decreased or even non-existing activation barrier for dissociative hydrogen (deuterium) adsorption.
A comparison of adsorption and desorption data of a particular system can be performed by applying the principle of DB. It is clear that detailed balancing has to be fulfilled in a true equilibrium situation. But it has been shown in the past that for many adsorption/desorption systems the principle of detailed balance is even applicable for non-equilibrium systems (i.e., for independent adsorption and desorption measurements at usually different temperatures and coverages) if quasi-equilibrium is maintained under the given experimental conditions [48; 50; 141; 142]. According to Comsa [49] quasi-equilibrium means that the distribution of the molecules adsorbed on the different kinds of adsorption sites continues to be an equilibrium-like distribution, even if the supply with molecules is interrupted. This is in particular true for surfaces with a rather small corrugation of the potential energy surface (PES), e.g., for the flat (111) planes of the transition metals. In order to make a correlation between the energy dependent sticking coefficient and the angular distribution of adsorption requires the fulfilment of a second phenomenon, namely normal energy scaling (NES) [41]. In fact it has been shown experimentally for a number of systems with a flat PES that NES is fulfilled with reasonable accuracy [60; 61]. Therefore, the evaluation of the angular distribution of deuterium desorption from Pd(111) was tried by applying NES and DB to literature data and comparing it to the experimental results. In figure (5.2) the energy dependent sticking coefficient $S(E)$ for D_2 on Pd(111) under normal incidence is plotted, according to Ref. [138]. For further calculations the data points were fitted by a polynomial function, as shown by the full line. In addition, the kinetic energy distribution of Maxwellian beams according to 523 K and 700 K, respectively, are drawn in the figure.

The energy distribution $N(E)$ of a Maxwellian beam with temperature T at normal incidence is described by

$$N_T(E, \theta = 0^\circ) \propto E \cdot e^{-\frac{E}{k_B \cdot T}} \tag{5.1}$$

According to the definition of the sticking coefficient equation (2.3) the sticking coefficient $S_T(0^\circ)$ for a Maxwellian gas under normal incidence at the temperature T is given by

$$S_T(0^\circ) = \frac{\int_0^\infty N_T(E) \cdot S(E) \cdot dE}{\int_0^\infty N_T(E) \cdot dE} \tag{5.2}$$

The applicability of NES can be described by equation (2.29)

$$S(E, \theta) = S(E_\perp, 0^\circ) = S(E \cdot cos^2\theta, 0^\circ)$$

where $E \cdot cos^2\theta$ means the energy of particles impinging under an angle θ to the surface normal associated with the momentum normal to the surface [41]. The number of particles $N(E)$ of a Maxwellian impinging under an angle θ is equal to the number of particles with energy

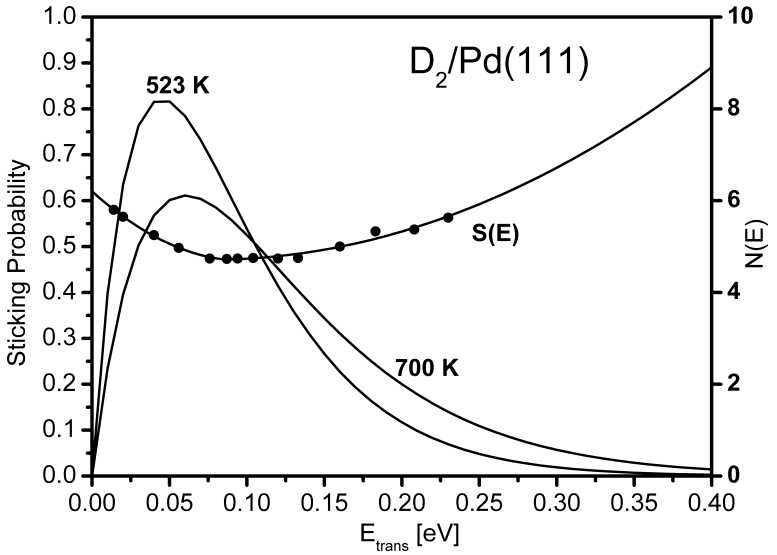

Figure 5.2: Initial sticking coefficient for deuterium on Pd(111) as a function of the kinetic beam energy (taken from Ref. [138]). The solid line through the data points stems from a polynomial best fit function. The kinetic energy distribution of Maxwellian beams with 523 K and 700 K are included.

$E_\perp/cos^2\theta$ of a Maxwellian impinging normal to the surface. Hence, the sticking coefficient $S_T(\theta)$ for a Maxwellian gas flux at temperature T impinging under an angle θ can be calculated

$$S_T(\theta) = \frac{\int_0^\infty N_T\left(\frac{E_\perp}{cos^2\theta}\right) \cdot S_\perp(E_\perp, 0°) \cdot dE_\perp}{\int_0^\infty N_T\left(\frac{E_\perp}{cos^2\theta}\right) \cdot dE_\perp} \tag{5.3}$$

The evaluation of the experimental data set of figure (5.2) according to equations (5.1) - (5.3) together with the detailed balance relation equation (2.20) yields the angular distribution of deuterium desorbing from Pd(111) at a specific sample temperature. The results for sample temperatures of 523 K and 700 K are depicted in figure (5.3). In addition, the angular distribution function with $cos\theta$ is shown for comparison. For 523 K the overall behaviour of a close to $cos\theta$ distribution is nicely reproduced. Moreover, the increased forward focusing of the desorption distribution with increasing gas temperature (700 K), as depicted in figure 5.1, can be observed. One could argue that it is somewhat counterintuitive that the angular distribution at higher temperature is sharper than at low temperature, since thermally induced roughening could be expected. But the result just reflects the behaviour of the energy dependent sticking coefficient, which is nearly constant in the low temperature range, but increases at higher energies (figure (5.2)). The small differences between the angular desorption distribution measured with the permeation source (figure (5.1)) and the distribution calculated form the sticking coefficient by applying NES and DB (figure (5.3)) can be attributed to slightly different surface conditions (different samples), rather than to the non-applicability of DB and NES. It is well known that small changes of the surface quality (defects, impurities below the AES detection

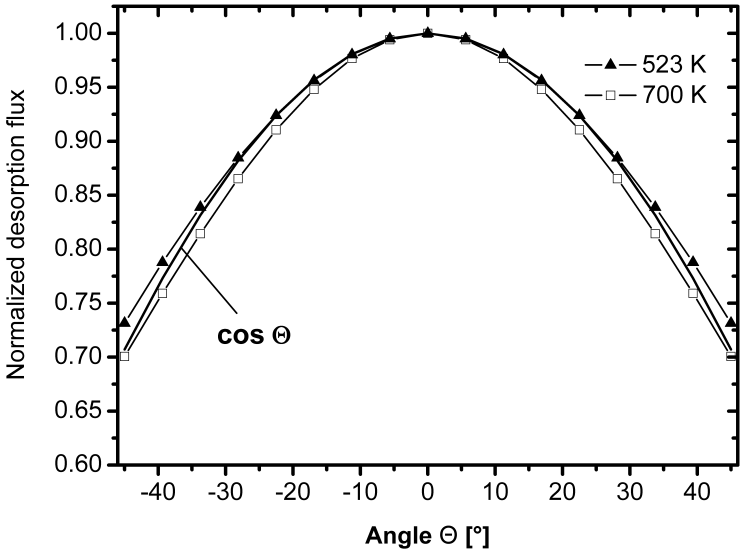

Figure 5.3: Angular distribution of deuterium desorbing from Pd(111) as obtained from molecular beam data (figure (5.2)) by applying NES and DB for two different sample temperatures, 523 K and 700 K. The full line corresponds to a $cos\theta$ distribution which is shown for comparison.

limit) can have a pronounced influence on the adsorption and desorption dynamics [143].

5.2 Summary of Chapter 5

The angular distribution of desorbing deuterium form a Pd(111) surface has been investigated at 523 K and 700 K sample temperature. The deuterium supply was performed by deuterium permeation through the single crystal bulk. Under these conditions the angular desorption distribution for deuterium is close to a cosine distribution at 523 K and changes to a slightly forward focused distribution in the form of $cos^{1.9}\theta$ at 700 K. Comparison of these data with adsorption data leads to the conclusion that the principle of detailed balance is applicable for this system. Furthermore, the adsorption and desorption process is governed by normal energy scaling, as deduced from the comparison of the angular distribution data with the kinetic energy distribution of the desorption flux. The important point is that these basic features even hold for the desorption process when deuterium is fed to the surface via permeation of atomic deuterium from the bulk.

6 D_2 on potassium modified Pd(111)

For comparison the angular distribution of the deuterium desorption flux from a potassium covered Pd(111) surface was studied. The influence of K on the adsorption and desorption behaviour of deuterium/hydrogen has been described in the literature to some extend [10; 12; 123; 131; 144]. The reduced sticking coefficient for deuterium(/hydrogen) on palladium due to potassium deposited onto the surface indicates the built up of an activation barrier for adsorption [144]. Additionally, a hyper-thermal energy distribution for the desorbing deuterium from this surface was found by time-of-flight measurements [10–12]. According to detailed balancing a clear deviation from a cosine shaped desorption flux should be expected. Therefore angular distribution measurements on desorbing deuterium from potassium covered Pd(111) have been performed complementary to the TOF measurements of Pauer et al. [10–12]. The angular distribution was determined by evaluating the deuterium flux signal in the LOS detector as a function of the lateral sample displacement. The experimental procedure has been explained briefly in chapter 3. The data evaluation which was done by comparison with MC simulations is described in 4. The following description can also be found in [137].

6.1 Angular dependence of the deuterium desorption from K modified Pd(111)

In figure (6.1) the experimental results for the angular distribution of deuterium desorbing from the Pd(111) surface covered with 0.2 ML of potassium at 523 K are presented. The best fit with a $cos^n\theta$ distribution yields an exponent $n = 3.0$. This is in good agreement with the value obtained from TOF measurements and applying normal energy scaling. From these results one can conclude that the potassium covered Pd(111) surface exhibits a very smooth PES which allows the application of NES and DB.

The integral sticking coefficient for an isotropic deuterium gas impinging on the clean surface is about 0.5. Adding potassium to the surface leads to a strong decrease of the sticking coefficient. At a coverage of 0.2 ML of K on Pd(111) the sticking coefficient for deuterium decreases to less than 0.02 [144]. A similar influence of potassium on the initial sticking coefficient for hydrogen was also observed for Ni(111) [145] and Pt(111) [146]. This is a clear indication for the build-up of an activation barrier due to potassium. The generally accepted explanation for the "poisoning" of the palladium surface with respect to dissociative hydrogen (deuterium) adsorption is the increase of the Pauli repulsion barrier and hence the activation barrier. The increase of the Pauli repulsion is caused by the larger spill-over of electrons normal to the surface due to the decreased work function [146]. The large decrease of the work function up to

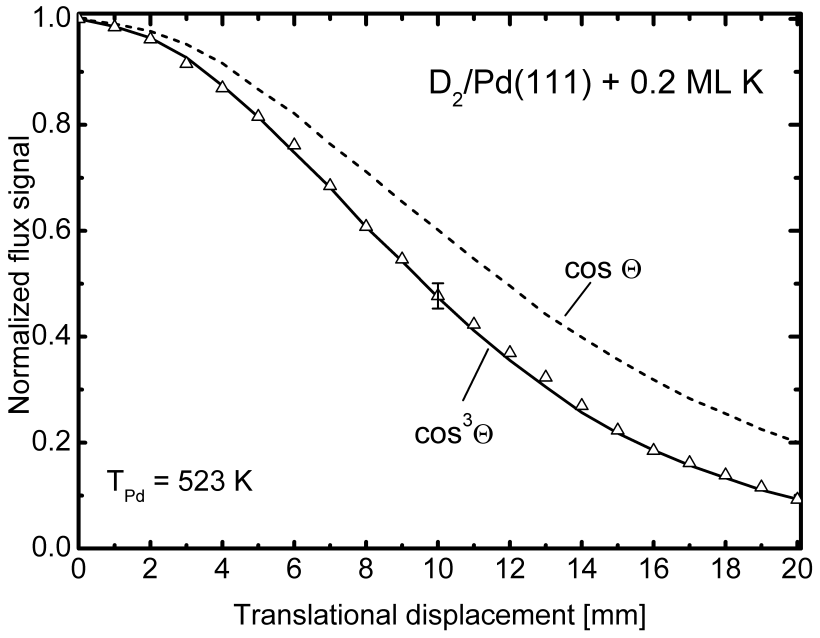

Figure 6.1: Experimentally obtained change in the desorption flux signal for deuterium from the Pd(111) surface, pre-covered with 0.2 ML potassium, at 523 K. The full line through the data points is the MC simulated signal change according to an angular distribution of $cos^3\theta$. For comparison the signal change of a cosine distribution is shown as dashed line.

a coverage of 0.2 ML is due to a strong charge transfer and the build-up of a potassium layer with ionic character. Increasing the coverage further up to the saturation at 0.33 ML leads to a partial depolarisation and to a potassium film with more metallic character [147]. The influence of potassium on the surface electronic structure is a long range effect. For hydrogen adsorption on Ni(111) it has been found that depending on the energy of the impinging hydrogen molecules each potassium atom may lead to an increase of the activation barrier in an area of up to 400 Å^2 [145]. Therefore it is reasonable to assume that adsorbed potassium atoms create a rather uniform activation barrier on the surface, which can be well described by a one-dimensional barrier model. Time-of-flight measurements on deuterium molecules after permeation/desorption from a potassium covered Pd(111) surface, as used in this work, have resulted in a hyper-thermal kinetic energy distribution [12]. In that case the potassium coverage was 0.23 ML and the sample temperature was 523 K. The mean kinetic energy was calculated from the TOF spectra to be $\langle E \rangle = 2.9\ k_B T_S$, with T_S being the surface temperature during desorption. The mean energy of a Maxwellian flux which is thermalized to the surface temperature would be $\langle E \rangle = 2.0\ k_B T_S$. By assuming detailed balance and normal energy scaling one can calculate the corresponding angular distribution of desorption. According to equation 2.36 [61] the mean desorption energy and the exponent n in the angular distribution in the form of

$cos^n\theta$ are correlated by:

$$\langle E \rangle = \frac{n+3}{2} \cdot k_B \cdot T_S$$

Therefore an exponent $n = 2.8$ should be expected for desorption of deuterium under the experimental conditions as described above. In figure (6.1) the experimental results for the angular distribution of deuterium desorbing from the Pd(111) surface covered with 0.2 ML of potassium at 523 K are presented. The best fit yields an exponent $n = 3.0$. This is in good agreement with the value obtained from TOF measurements and applying normal energy scaling. From these results one can conclude that the potassium covered Pd(111) surface exhibits a very smooth PES which allows the application of NES and DB.

6.2 Summary of Chapter 6

The modification of the Pd(111) surface with 0.2 ML potassium leads to a more strongly forward focused angular distribution for desorption ($cos^3\theta$), indicating the build-up of an activation barrier for adsorption. This is in accord with the observed hyper-thermal kinetic energy distribution of the desorption flux with a mean kinetic energy of $\langle E \rangle = 2.9\ k_B \cdot T$ [12]. The comparison of the angular distribution data with the kinetic energy data leads to the conclusion that normal energy scaling is also fulfilled in this case. This can be explained by the fact that the influence of the potassium atoms is of long range character, leading to a nearly one-dimensional activation barrier with negligible corrugation of the PES.

7 D_2O formation on clean Pd(111)

The water formation reaction on surfaces has been extensively studied in the past. Especially the formation of water on palladium from the coadsorbed reactants hydrogen and oxygen has attracted some scientific interest due to its importance in heterogeneous catalysis[148], hydrogen storage [119] and fuel cell technology [120]. Methods like molecular beam techniques [149], STM [150; 151] or TDS [152] have been applied to the system O/H/Pd(111). Typically both species O and H were supplied from the gas phase. In this work the reaction of impinging O_2 with deuterium supplied by permeation through the crystal bulk has been studied. This kind of deuterium (hydrogen) supply provides a possible opening of new reaction channels that may exhibit different reaction kinetics (raction rates) and reaction dynamics (energy distribution of the reaction products) compared to the conventional way of reactant supply via the gas phase. Although the experimental details are presented in chapter 3 the great advantage using the permeation device for this kind of experiments should be emphasized here. Additionally, the most important design parameters are specified.
Using the permeation techniques allows the total pressure to be kept low which helps to suppress the unwanted background signal. In addition, deuterium was used instead of hydrogen to obtain better signal-to-noise ratios for the reaction products. The effective surface area where permeation/desorption could take place has been estimated to 0.38 cm^2. The sample was positioned at a distance of 17 mm in front of the aperture of the LOS detector. The dosing enhancement factor (ratio of the impingement rate to the equivalent impingement rate of isotropic dosing) was experimentally determined to be 5.0 (see chapter 4). The principle arrangement is the same as for the angular distribution measurement (figure (3.19)). The oxygen supply was performed by dosing via a stainless steel tube.

7.1 Water Formation Kinetics on Clean Pd(111)

The water formation on the clean palladium surface at 523 and 700 K was investigated. For this purpose a constant deuterium permeation flux was adjusted by setting a proper back pressure in the permeation source which resulted in an equilibrium pressure in the main chamber of about 1.5 to $4{\cdot}10^{-9}$ mbar. From the determined pumping speed for deuterium of about 650 l/s and an effective sample area of 0.38 cm^2 this corresponds to a flux of $8{\cdot}10^{13}$ to $2{\cdot}10^{14}$ molecules $cm^{-2}{\cdot}s^{-1}$. After the sample was positioned in front of the LOS detector the dosing was started with molecular oxygen by slowly increasing the oxygen partial pressure from the oxygen base pressure ($<10^{-11}$ mbar) to about $1{\cdot}10^{-6}$ mbar. Due to experimental reasons it is easier to continually decrease the oxygen pressure than to increase it. Furthermore, this

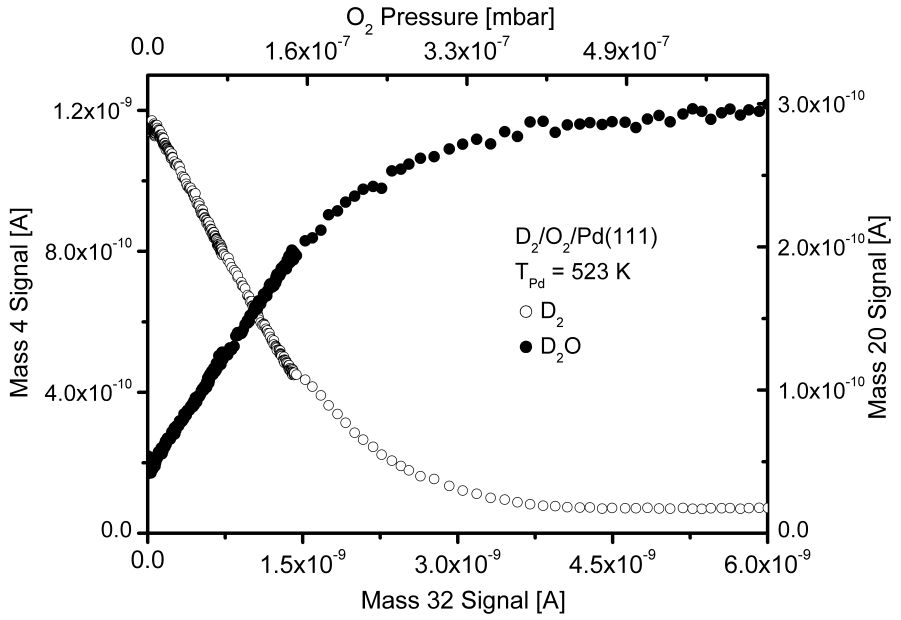

Figure 7.1: Evolution of the deuterium signal (○) and the D_2O signal (●) versus oxygen pressure during water formation on clean Pd(111) at 523 K. At oxygen pressures above $1.5{\cdot}10^{-7}$ mbar the pressure change was faster.

assures that the system has already reached its equilibrium condition during reaction. Figure (7.1) shows the decrease of the D_2 (mass 4) and the evolution of the D_2O (mass 20) signal versus the O_2 partial pressure (mass 32) at a sample temperature of 523 K, as seen by the LOS spectrometer. For quantification the whole procedure was also monitored with the QMS in the main chamber. At low oxygen pressures the deuterium signal decreases almost linearly with the increasing oxygen pressure until it starts to level off at about $2{\cdot}10^{-7}$ mbar and finally reaches the residual pressure level. The water signal behaves, besides a somewhat higher background level, diametrically. Indeed, the sum of the normalized D_2O and D_2 signal is constant throughout the whole experiment. This indicates that all the deuterium is converted into D_2O only. This clear evidence can only be gained from this type of permeation experiment. It would be very difficult to obtain this result by dosing both reactants from the gas phase. From the knowledge of the pumping speed for deuterium and the partial pressures of O_2 and D_2 one can calculate quantitative values for the deuterium desorption flux and the oxygen impingement rate. Figure (7.2) illustrates the correlation of these two values for the clean Pd(111) surface and makes a comparison between the two surface temperatures of 523 and 700 K. The change of the D_2 flux as a function of the O_2 impingement rate shows clearly that the water formation on the 700 K sample is less efficient than on the 523 K sample. In this presentation of the data the slope of the linear part of the D_2 decrease can be interpreted as the initial reaction probability. The reaction probability shall be defined as

$$P_r = \frac{\Delta F_{D2}}{\Delta F_{O2}}. \tag{7.1}$$

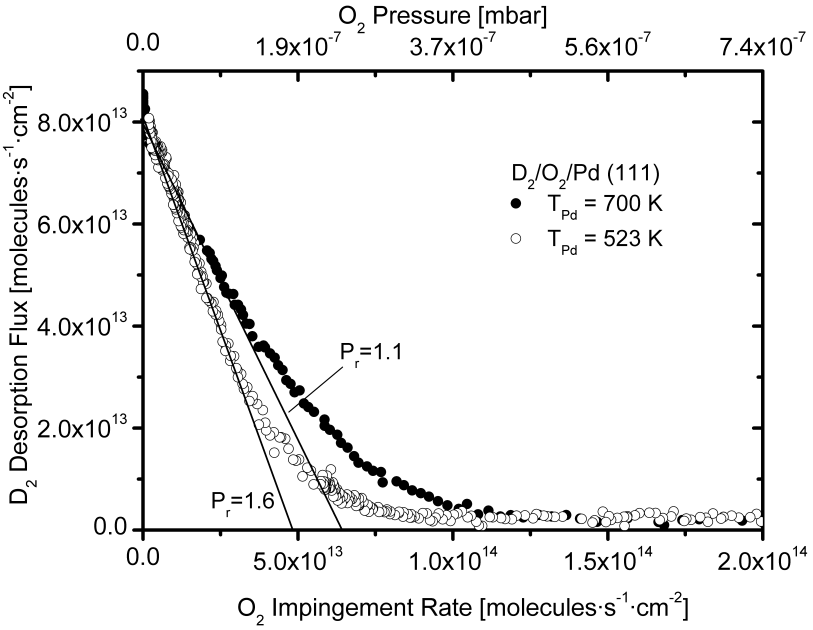

Figure 7.2: Comparison between the deuterium decrease at 523 K (○) and at 700 K (●) as a function of the oxygen impingement rate. Data are normalized to the same flux.

The reaction probability is an expression for how many D_2 molecules out of the initial deuterium flux F_{D2} have been converted to D_2O due to a certain O_2 impingement rate F_{O2}. Note that due to the latter definition equation (7.1) the probability is not normalized to 1 which is not allowed in the strict mathematical sense but in this case the given values are more intuitive. For the clean sample at 523 K a value of 1.6±0.2 is obtained (1.6 converted D_2 molecules per impinged oxygen molecule). For the clean sample at 700 K a value of 1.1±0.2 was calculated. The theoretical maximum reaction probability is just given by the stoichiometric relation between oxygen and deuterium in D_2O and is therefore 2. Since the permeation technique is used for the deuterium supply the only factor that determines the reaction probability is the sticking coefficient of oxygen. Thus the lower reaction rate on the 700 K surface can be attributed to a lower sticking coefficient for oxygen on Pd(111). This drop of the oxygen sticking coefficient due to increasing surface temperatures has been reported in the literature, where values of S^0_{O2} ($T_{Pd} = 523$ K) ≈ 0.5-0.6 and S^0_{O2} ($T_{Pd} = 523$ K) ≈ 0.4-0.5 have been determined [91].

7.1.1 Modeling of the Reaction Process.

To gain a deeper understanding of the processes involved an attempt to model the reaction and compare the results with the measurements was made. The starting point are simplified rate equations assuming that the rate limiting step is the O + D → OD formation [149; 151]. Following the ideas of Engel and Kuipers [149] one can assume that the D + OD → D_2O reaction is fast, and the formed D_2O should immediately leave the surface. Additionally, the decay of OD back into D and O is neglected. This leads to the following rate equations for the

change of deuterium and oxygen coverage on the surface:

$$\frac{d\Theta_D}{dt} = -k_D \cdot \Theta_D^2 - 2 \cdot k_{OD} \cdot \Theta_D \cdot \Theta_O + F_D \tag{7.2}$$

$$\frac{d\Theta_O}{dt} = -k_O \cdot \Theta_O^2 - k_{OD} \cdot \Theta_D \cdot \Theta_O + 2 \cdot k_{OD} \cdot p_{O2} \tag{7.3}$$

Θ_D and Θ_O are the deuterium and oxygen coverages, respectively. Analogous k_D and k_O are the rate coefficients for D_2 and O_2 recombination. The factor k_{OD} is the rate coefficient for OD formation and thus for the D_2O formation as well. The rate factor k_{O2} describes the transition from gas-phase oxygen to dissociated oxygen atoms, and F_D is the permeation flux refilling the deuterium coverage. Due to the slow variation of the oxygen pressure during the experiments it is assumed that the system is in equilibrium at any time. Taking this fact into account, the time derivatives on the left-hand side of equations (7.2) and (7.3) vanish, and the system of differential equations is transformed into a system of algebraic equations. The rate factors for the recombinative desorption of deuterium and oxygen were taken from the literature ($k_D = 4.6{\cdot}10^{-12}$ cm^2·atom^{-1}·s^{-1} for 523 K and $7.3{\cdot}10^{-10}$ cm^2·atom^{-1}·s^{-1} for 700 K [121] and $k_O = 7 \cdot 10^{-19}$ cm^2·atom^{-1}·s^{-1} for 700 K [153]). The rate factors for the OD formation were taken to be $k_{OD} = 5.4{\cdot}10^{-11}$ cm^2·atom^{-1}·s^{-1} at 523 K and $2.9 \cdot 10^{-10}$ cm^2·atom^{-1}·s^{-1} at 700 K [149]. The oxygen recombination factor k_O is negligibly small at 523 K. The permeation flux F_D was taken from the measured equilibrium D_2 flux during pure deuterium permeation experiments, which remains constant throughout the experiment within the experimental error. For the coefficient k_{O2} the form $k_{O2} = C \cdot S^0_{O2} \cdot (1 - \alpha \cdot \Theta_O)$ was taken. Here a linear decrease of the oxygen sticking coefficient was assumed which goes to zero at a quarter of a monolayer ($\alpha = 4$) which of course does not reflect the real circumstances exactly but reproduces the overall behavior of the oxygen/Pd(111) system quite well [91]. The constant C is the factor that connects the pressure with the impingement rate. The oxygen desorption rate is exceedingly small due to the big difference of the rate factors in this temperature range. Thus the oxygen partial pressure was the independent variable, and the initial sticking coefficient of oxygen was the parameter varied.

In figures (7.3(a)) and (7.3(b)) the results for a sample temperature of 523 and 700 K (thin black line) are shown, respectively. The best results were obtained with an initial oxygen sticking coefficient of S^0_{O2}=0.85 for 523 K and S^0_{O2}= 0.55 for 700 K. These values are rather high compared with the literature values, although the overall behavior of the temperature dependence is roughly described. Especially, the constant slope of the deuterium decrease is reproduced satisfactorily, but the transition region where the deuterium flux goes into depletion deviates from the simulated result.

Additionally, an attempt was made to simulate the experimental results by taking into account the total two-step process of water formation. For that reason the second term on the right hand side of equation (7.2) was substituted by

$$-k_{OD} \cdot \Theta_D \cdot \Theta_O - k_{D2O} \cdot \Theta_{OD} \cdot \Theta_D \tag{7.4}$$

and a third equation concerning the OD coverage was introduced

$$\frac{d\Theta_{OD}}{dt} = k_{OD} \cdot \Theta_D \cdot \Theta_O - k_{D2O} \cdot \Theta_{OD} \cdot \Theta_D \tag{7.5}$$

Due to the latter modification a second tunig parameter k_{D2O} was obtained which just represents the formation of D_2O out of OD an D. Best results were obtained by setting S^0_{O2}=0.85 and k_{D2O}=4·10^{-13} cm^2·atom^{-1}·s^{-1} at 523 K. Surprisingly, it turned out that the experimentally obatained data could only be approximated well by a rate factor for D_2O formation which is two orders of magnitude smaller than the value of OD formation given in the literature [149]. Lowering the paramter k_{OD} instead of k_{D2O} yields the same results which makes it impossible to decide which of these is the rate limiting process. But to retain the concept that the formation of hydroxyl from D and O is the rate limiting step one can turn back to the simple two-equation model and tune the rate parameter k_{OD} properly. The results are depicted in figures (7.3(a)) and (7.3(b)) by the thick black line. For the clean Pd(111) sample at 523 K the best results were obtained by setting S^0_{O2}=0.85 and $k_{OD} = 3.2 \cdot 10^{-13}$ cm^2·atom^{-1}·s^{-1}. The data for the 700 K sample were described best by S^0_{O2}=0.6 and k_{OD} = 8·10^{-12} cm^2·atom^{-1}·s^{-1}. The rather high sticking coefficient for oxygen obtained from the measurements can be attributed to an increased defect concentration on the Pd(111) surface caused by the stress in the sample during the permeation process. In the course of time that the permeation source was in use the formation of a small bulge across the sample surface was observable.This morphological change suggests an increased step density and corrugation of the surface. As provided by literature, the sticking coefficient of oxygen is significantly lower on the flat Pd(111) surface (S^0_{O2} between 0.5 at 623 K and 0.75 at 323 K [92]) than on the corrugated Pd(110) ($S^0_{O2} \approx 1$ at 427 K [154]) surface. Therefore an increased sticking coefficient for oxygen can be expected. From the obtained rate factors k_{OD} at 523 and 700 K the activation energy for OD formation E_{act} as well as the preexponential factor ν can be calculated by using $k_{OD} = \nu \cdot exp(-E_{act}/k_BT)$. E_{act} is determined to be 0.56 eV (13 kcal/mol) and ν = 8.6·10^{-8} cm^2·atom^{-1}· s^{-1}. These values are about twice as high as those given by Engel and Kuipers [149] where E_{act} = 0.3 eV (7 kcal/mol) and $\nu = 4.4 \cdot 10^{-8}$ cm^2·atom^{-1}·s^{-1}. But the results are quite consistent with those obtained on Pt(111) surfaces, namely E_{act} = 0.52 eV (12 kcal/mol) as published by Smith and Palmer [155]. STM studies of the water formation reaction on Pd(111) indicated that the water formation occurs at the step edges yielding an activation energy for OH formation of $E_{act} < 0.42$ eV (9.7 kcal/mol) and a frequency factor of $\nu = 4.4 \cdot 10^{-8}$ cm^2·atom^{-1}·s^{-1} [151]. The calculations also support the assumption that the water formation between impinging oxygen molecules and permeating deuterium atoms is predominantly governed by the sticking probability of the oxygen. Varying the OD reaction coefficient k_{OD} within 1 order of magnitude has not much influence on the slope of the decrease of the deuterium flux at a given S^0_{O2} and at low oxygen pressures. The oxygen and deuterium coverages as a function of the oxygen pressure are depicted in figure (7.4(a)) for 523 K and figure (7.4(b)) for 700 K, respectively. As long as the oxygen coverage remains small there is no significant change in the oxygen sticking coefficient which leads to a constant decrease of the hydrogen desorption flux. The smaller the deuterium coverage becomes, the less water is produced, and therefore the oxygen coverage increases. The

increase of the oxygen coverage then leads to a decrease of the oxygen sticking probability which delays the further increase of the oxygen coverage. Since the deuterium recombination is faster than the water formation it would take more oxygen to keep the reaction going as efficiently as at higher deuterium coverages. Therefore, the decrease of the deuterium signal is flattening before all the deuterium is consumed by water formation.

7.2 Summary of Chapter 7

The D_2O formation reaction from deuterium and oxygen on the Pd(111) single crystal surface has been investigated. The reaction was supplied on the one hand by direct dosing of oxygen onto the surface and on the other hand by atomic deuterium via permeation through the bulk of the Pd sample. The experiments were carried out at 523 K and 700 K, respectively. The water formation turned out to be more efficient at 523 K than at 700 K due to a temperature dependent sticking coefficient for oxgen. A simplified model of the water generation provided an oxygen sticking coefficient of 0.85 at 523 K and 0.6 at 700 K, respectively. The activation energy for the OD formation on Pd(111) was determined to be E_{act}= 0.56 eV, and a pre-exponential factor of $\nu = 8.6{\cdot}10^{-8}$ cm$^2{\cdot}$atom$^{-1}{\cdot}$ s^{-1} was calculated. All the effused deuterium atoms were either consumed by reacting with adsorbed oxygen to water or desorbed associatively as D_2.

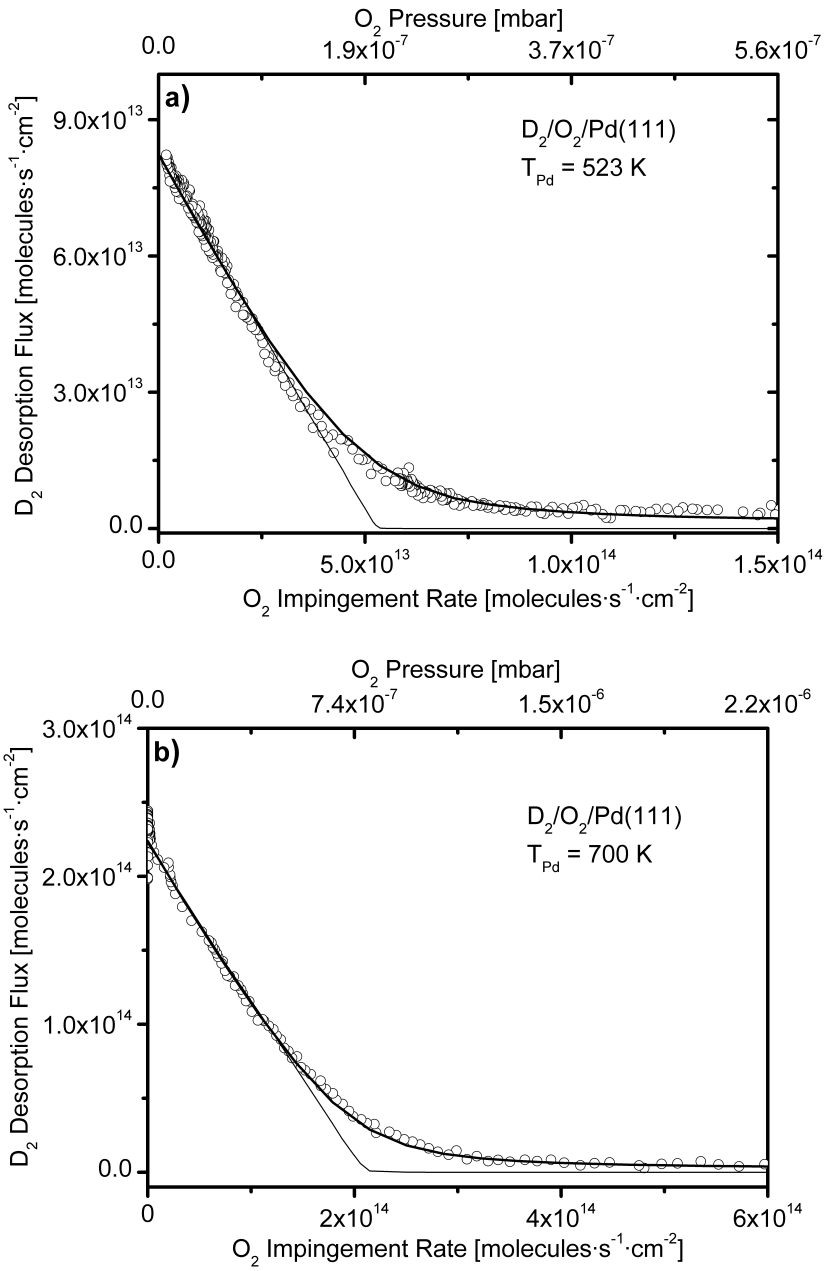

Figure 7.3: Comparison of the calculated deuterium decrease (solid black lines) during water formation on clean Pd(111) with the measured results (∘). (a) Sample temperature 523 K. The thin black line corresponds to the simulation results obtained by using a rate coefficient of $k_{OD} = 5.4{\cdot}10^{-11}$ cm^2·atom^{-1}·s^{-1} for OD formation (literature value [149]). The thick line was calculated using $k_{OD} = 3.2{\cdot}10^{-13}$ cm^2·atom^{-1}·s^{-1}. (b) Sample temperature 700 K. The thin line was obtained by using a rate factor of $k_{OD} = 7.3{\cdot}\ 10^{-10}$ cm^2·atom$^{-1}{\cdot}$ s^{-1}(literature value [121]), and the thick line was calculated by applying k_{OD}=$8 \cdot 10^{-12}$ cm^2·atom^{-1}·s^{-1}.

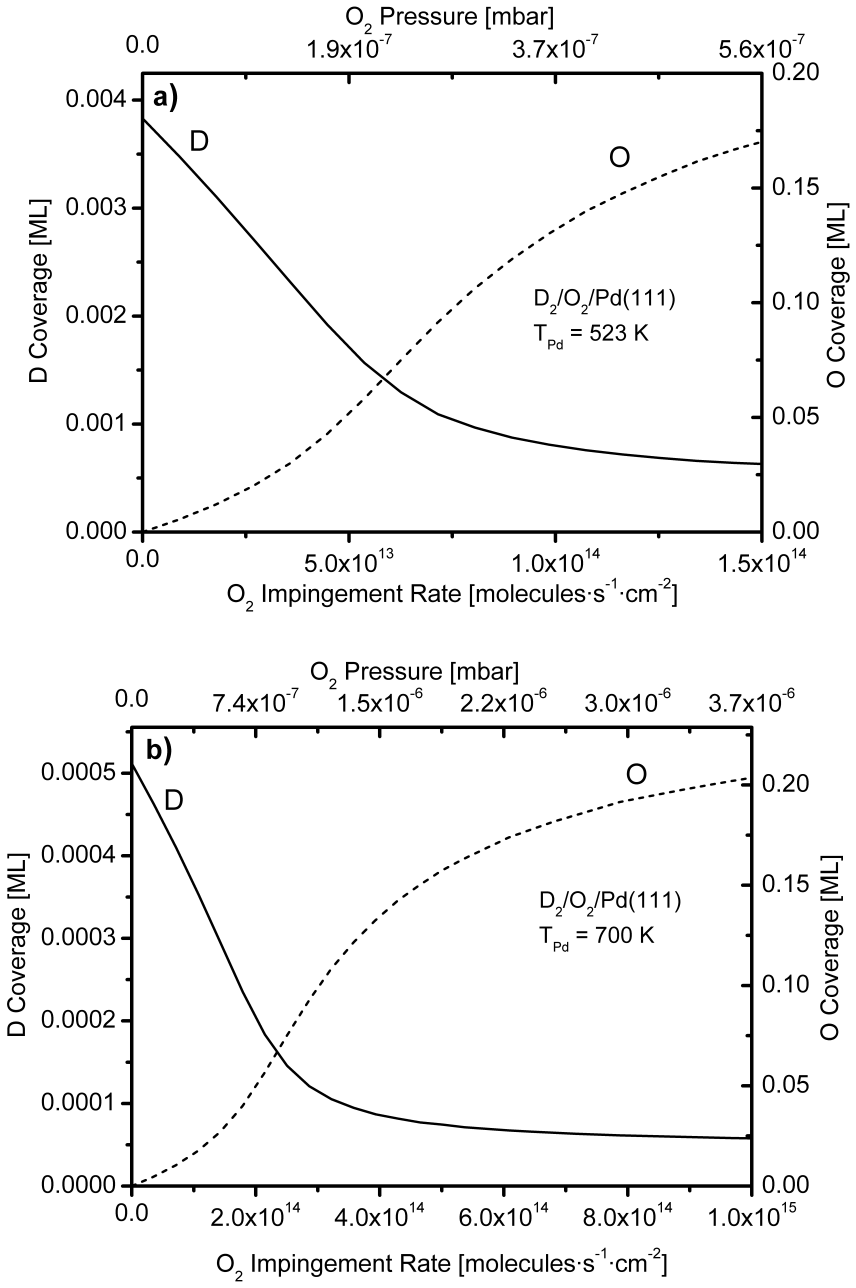

Figure 7.4: Evolution of the deuterium (solid black line) and oxygen (dashed line) coverage during water formation as calculated for clean Pd(111) at a sample temperature of 523 K (a) and 700 K (b).

8 D_2 and D_2O on VO_x modified Pd(111)

Many modern technologies take advantage of the specific physical and chemical properties of nanostructured surfaces. In particular, the catalytic activity of surfaces depends strongly on the chemical composition and the atomic scale structure of the surface. In this context ultra-thin oxide films on metal supports have attracted considerable interest, because they represent a model system of an "inverse catalyst". Commonly used catalysts are built up by a metal oxide substrate which is covered by a thin metal layer. The systems under consideration are considered to be "inverse" due to the metal substrate which is covered by a metal oxide.
Vanadium oxide nanostructures in the monolayer regime have recently been studied extensively because they form a variety of interesting nanostructures with varying oxidation states [3–9]. For the model systems VO_x/Pd(111) and VO_x/Rh(111) a number of experimental studies using LEED, STM, x-ray photoelectron spectroscopy (XPS), near-edge x-ray-absorption fine structure (NEXAFS), and high resolution electron-energy-loss spectroscopy (HREELS) have been performed to reveal the electronic and geometric structures of the individual oxides. Density functional theory (DFT) calculations have been carried out in this context and a quite comprehensive understanding of the oxide structures is available [6; 7].
In this chapter the behaviour of VO_x /Pd inverse catalyst surfaces under reaction conditions is described. As model reactions the recombination of deuterium and the formation of D_2O were chosen on the one hand due to their simplicity and on the other hand due to their possible technical relevance in the fields of heterogeneous catalysis [148], hydrogen storage [119] and fuel cell technology [120]. The experiments were carried out by using the permeation source described in section 3.2. The permeation source allowed the supply of deuterium (or hydrogen) atoms by diffusion from the palladium bulk to the surface. This kind of deuterium (hydrogen) supply provides a possible opening of new reaction channels that may exhibit different reaction kinetics (raction rates) and reaction dynamics (energy distribution of the reaction products) compared to the conventional way of reactant supply via the gas phase (see figure (8.1) [11; 12]). The focus was put on the influence of different ultra thin vanadium oxide structures on the translational energy distribution of the reaction products as well as on the stability of the prepared structures under reaction conditions. Additionally, the effect on different VO_x layers on the water formation kinetics is studied. In the following the vanadium oxide coverage is characterized by the amount of vanadium contained in the surface oxide layer and will therefore be specified in monolayer equivalents (MLE). 1 MLE of vanadium oxide on the Pd(111) surface is equivalent to $1.53 \cdot 10^{15}$ V atoms/cm^2.

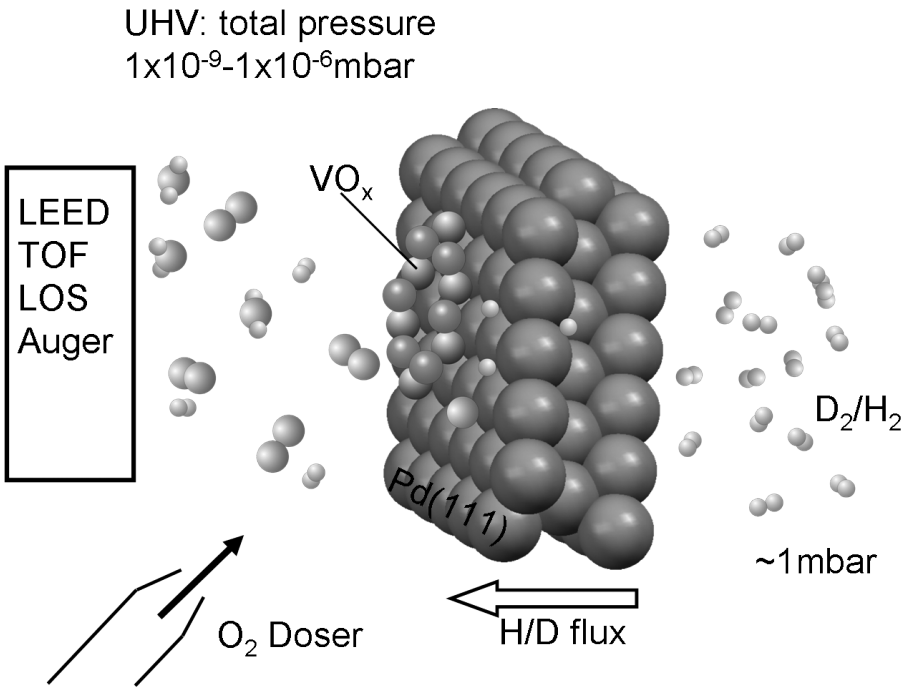

Figure 8.1: Scheme of the measurement principle using the permeation source.

8.1 Vanadium Oxide Structures on Pd(111)

Depending on the preparation conditions a number of different VO_x structures develop on the Pd(111) surface. An overview about the most important structures and the corresponding preparation conditions is given in the following [3–9].

Evaporation of 0.5 ML vanadium on a Pd(111) surface at 523 K under oxygen pressure, typically $2{\cdot}10^{-7}$ mbar, leads to a number of surface oxides with structures that are quite different from that of bulk vanadium oxides. The most frequently observed surface oxide shows a 2×2 honeycomb structure. This structure has been identified by combined STM measurements and DFT calculations as a surface vanadium oxide (s-V_2O_3) phase and consists of a layer of two V atoms per unit cell located in threefold palladium hollow sites and three oxygen atoms above V-V bridge sites [6]. Exposing this surface to further oxygen changes the LEED pattern to a 4×4 structure. The structure of this phase has also been clarified by STM and DFT and can be described by a surface oxide with V_5O_{14} stoichiometry. In this case the oxide layer is oxygen terminated at both the metal interface and the oxide surface and contains V atoms in tetrahedral O coordination. This layer is quite unstable and can easily be reduced to the so-called zigzag structure, as observed with STM. From DFT calculations a structure model for the zigzag phase is derived which contains V_6O_{14} units [9]. Further reduction by hydrogen yields again the stable 2×2 s-V_2O_3 phase. In the case of higher vanadium coverage (1 ML) other vanadium oxide surfaces can be produced. The observed "flower LEED pattern" can be ascribed to a structure of rotational domains of rectangular unit cells and the formal stoichiometry of this phase is VO_2 [8]. In addition, also a hexagonal oxide phase with formal VO_2 stoichiometry has been observed in the 1ML range. For thicker oxide films (5 ML vanadium) a

$(\sqrt{3} \times \sqrt{3})$R30° LEED pattern is found which can be described as being due to the (0001) face of the corundum V_2O_3 bulk phase [9]. The reason for this LEED pattern is that the lattice mismatch between the V_2O_3 bulk lattice and the $\sqrt{3}$ direction of Pd(111) is only 3.7%. The $(\sqrt{3} \times \sqrt{3})$R30° LEED pattern of the vanadium oxide is therefore a pseudosuperstructure of the Pd(111) surface. STM images of the corresponding structures are shown in figure (8.2).

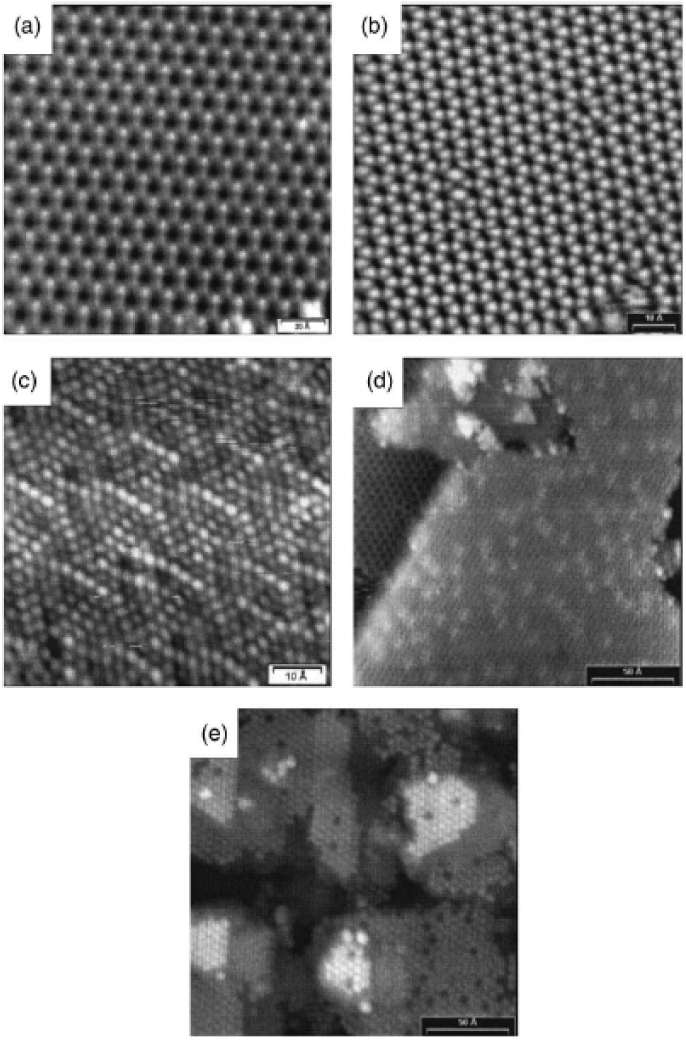

Figure 8.2: STM image of various VO_x structures on Pd(111): (a) 4×4 V_5O_{14} (160×160 Å^2, U=2.0 V, I=0.1 nA); (b) 2×2 s-V_2O_3 (78×78 Å^2, U=0.04 V, I=1 nA); (c) "wagon-wheel" VO (70×70 Å^2, U=0.1 V, I=1 nA); (d) rectangular VO_2 (200×200 Å^2, U=0.25 V, I=0.5 nA); (e) bulk V_2O_3 (0001) (200×200 Å^2, U=-0.33 V, I=0.1 nA)

8.2 Stability of VO_x structures on Pd(111) under reaction conditions

The crucial question in the context of reaction studies on modified or nanostructured surfaces concerns the real structure of the surface layer under reaction conditions. LEED was used to follow the structure during reaction and the patterns were compared with the corresponding LEED patterns obtained at room temperature under vacuum conditions. The stability of vanadium oxides was studied for 0.3, 1, and 5 MLE, respectively, for different temperatures and different reaction conditions: (a) permeation/desorption of pure deuterium yielding a typical D_2 pressure of $8{\cdot}10^{-7}$ mbar and (b) permeation of deuterium and reaction with impinging oxygen (typically $1{\cdot}10^{-6}$ mbar) to form water.

0.3 MLE Vanadium Oxide

After the preparation of 0.3 MLE vanadium oxide at T=523 K in an oxygen atmosphere of $2{\cdot}10^{-7}$ mbar a 4×4 LEED pattern was observed (figure (8.3a)). This pattern is very unstable and changes within a few minutes to a 2×2 structure. This is due to the fact that in the used chamber the hydrogen and/or deuterium residual partial pressure is rather high. The 4×4 structure has been recently described as a rather open network structure where the surface unit cell consists of 5 V atoms and 14 O atoms, forming a honeycomb-like arrangement. A high-resolution STM image of the 4×4 structure is shown in figure (8.2a). The 4×4 phase reduces easily by hydrogen [6; 9]. The stable structure which is quite resistant to hydrogen at 523 K is the 2×2 structure (figure (8.3b)), which has also been described in detail in the literature; [5] see figure (8.2b) for a STM image. In this case a V_2O_3 surface oxide is formed that also exhibits a honeycomb-like structure. Since at a vanadium coverage of 0.3 MLE the s-V_2O_3 layer covers only about 60% of the surface one is confronted with the coexistence of well ordered 2×2 phases and bare Pd(111) areas, as verified by STM measurements [8; 9]. Such a surface layer is particularly interesting for reaction investigations because one could expect a special influence of the island borders on the reaction. The 2×2 structure remains stable for deuterium permeation/desorption at 523 K for extended time (many hours) at a D_2 partial pressure of $8{\times}10^{-7}$ mbar during permeation. This pressure corresponds to a deuterium desorption flux of about $6{\cdot}10^{15}$ $D_2/(cm^2{\cdot}\ s)$ (at a pumping speed of 140 $l{\cdot}s^{-1}$, effective surface area of 0.5 cm^2). After the oxygen partial pressure in the chamber is increased to $1{\cdot}10^{-6}$ mbar (corresponding to an impingement rate of $2.7{\cdot}10^{14}$ $O_2/(cm^2{\cdot}\ s)$), water is formed on the vanadium oxide covered Pd(111) surface which desorbs immediately at this temperature. As the amount of permeating/desorbing deuterium is much larger than the amount of impinging oxygen, still a considerable amount of permeating deuterium desorbs associatively in the form of D_2, in addition to the formation of water with the impinging and adsorbed oxygen. It is generally accepted that water formation on Pd(111) proceeds via the formation of hydroxyl intermediates [150]. In this reducing atmosphere the 2×2 structure is retained (figure (8.3b)). Heating the 0.3 MLE vanadium oxide surface to 700 K in vacuum or under reducing conditions leads to a change of the LEED pattern (figure (8.3c)). This structure can be assigned to a

surface oxide of VO stoichiometry. Similar LEED patterns for vanadium oxide on Pd(111) and Rh(111) and corresponding STM investigations and DFT calculations have described this structure as the "wagon-wheel" structure [3–5; 7]. Figure (8.2c) displays a high-resolution STM image of the wagon-wheel phase. Exposing this surface again to oxygen changes the LEED pattern back to the 2×2 structure (figure (8.3d)). The background signal in the LEED pattern is increased compared with figure (8.3b) due to the Debye-Waller factor. Apparently, under these reaction conditions the surface vanadium oxide layer s-V_2O_3 is conserved at 700 K.

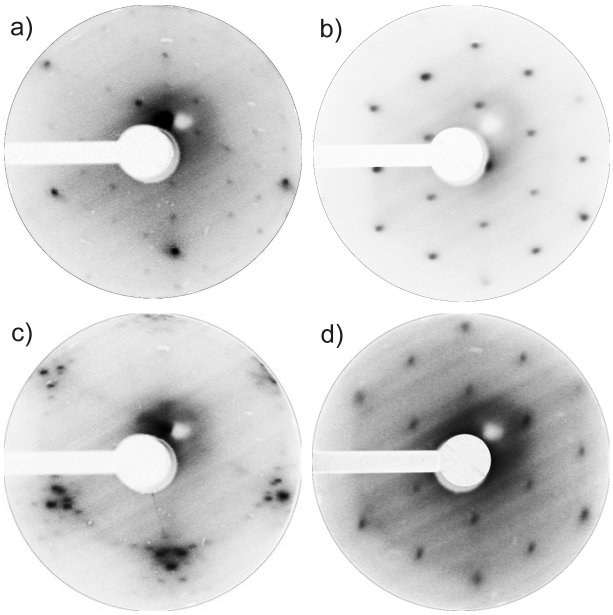

Figure 8.3: LEED patterns for different 0.3 MLE VOx structures on Pd(111): (a) after preparation at 523 K, 4×4 structure, E=67 eV; (b) during reaction of deuterium with oxygen at 523 K, 2×2 structure, E=60 eV; (c) during deuterium desorption at 700 K, VO structure, E=56 eV; (d) during reaction of deuterium with oxygen at 700 K, 2×2 structure, E=64 eV.

1 MLE Vanadium Oxide

Evaporation of 1 MLE vanadium under oxygen atmosphere at 523 K leads to a LEED pattern as shown in figure (8.4a). This "flowerlike" pattern has recently been described as being the superposition of diffraction from domains with rectangular unit cells of VO_2 stoichiometry and the 2×2 V_2O_3 structure [8]. This is clearly apparent from the STM image in figure (8.2d). After initiation of the deuterium permeation the LEED pattern changes to the pure 2×2 structure (figure (8.4b)). The VO_2 structure is reduced to the more stable V_2O_3 surface oxide [156]. Adding oxygen at 523 K retains the 2×2 structure, but additionally a faint ringlike structure appears in the LEED pattern (figure (8.4c)). Heating the 1 MLE vanadium oxide surface to 700 K in vacuum leads to a LEED pattern similar to that in figure (8.3c), which is again indicative of the wagon-wheel VO structure. Pure permeation of deuterium does not change this pattern. Exposing this surface to oxygen without permeation of deuterium leads to a LEED pattern which is a superposition of the VO structure and the 2×2 structure (figure (8.4d)). However,

exposing oxygen to the surface when deuterium is permeated concomitantly, a change in the LEED pattern appears which has not been observed so far (figure (8.4e)). In addition to the 2×2 structure a new superstructure appears which can be explained by the superposition of rotational and mirror domains of a rectangular structure. This structure is similar to the flowerlike pattern but with a different size of the unit cell. A more detailed description of this phase will be given later. After the oxygen exposure has been terminated and only deuterium permeation still exists, the 2×2 structure and the rectangular structure disappear and the remaining pattern is again indicative of the VO structure (figure (8.4 f)).

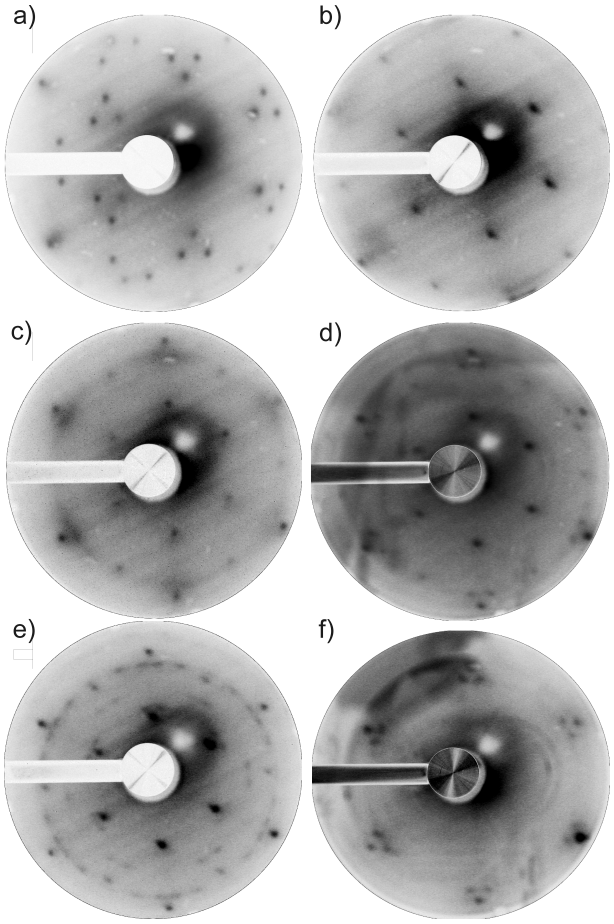

Figure 8.4: LEED patterns for 1 MLE VO_x structures on Pd(111): (a) after preparation at 523 K, "flower pattern", E=39 eV; (b) during deuterium desorption at 523 K, 2×2 structure, E=40 eV; (c) during reaction of deuterium with oxygen at 523 K, 2×2 structure, E=60 eV; (d) during oxygen exposure at 700 K, 2×2 structure+VO structure, E=58 eV; (e) during reaction of deuterium with oxygen at 700 K, 2×2 structure+rectangular structure, E=57 eV; (f) after reaction at 700 K, VO structure, E=62 eV.

5 MLE Vanadium Oxide

Evaporation of 5 MLE vanadium under oxidative conditions at 523 K leads to a $(\sqrt{3}\times\sqrt{3})$R30° LEED pattern (figure (8.5a)). This pattern has been identified as being due to diffraction from

the (0001) plane of V_2O_3 bulk phases [4]. No palladium signal is seen in the AES, indicating a continuous oxide film on the substrate. However, from the fact that the LEED spots are rather broad in this case we conclude that the film consists of quite small V_2O_3 crystallites. The STM measurements on such surfaces produced under similar conditions indicate a mean crystallite diameter of about 5-10 nm [4]. The STM image presented in figure (8.2 e) shows the hexagonal pattern of the corundum V_2O_3 (0001) top facets of these crystallites. The LEED structure remains stable at 523 K, both under reducing conditions as well as under reaction conditions (figure (8.5b)). This is also true for a sample temperature of 700 K, without (figure (8.5c)) and with (figure (8.5d)) oxygen exposure. It should be noted that after the reaction experiment AES revealed a significant palladium signal, but the LEED pattern still shows the $(\sqrt{3} \times \sqrt{3})$R30° structure, albeit with increased spot size. Apparently, the crystallites have changed their shape and size during the reaction. The corresponding AES spectra for the reactions at 523 K and 700 K are shown in figure (8.6).

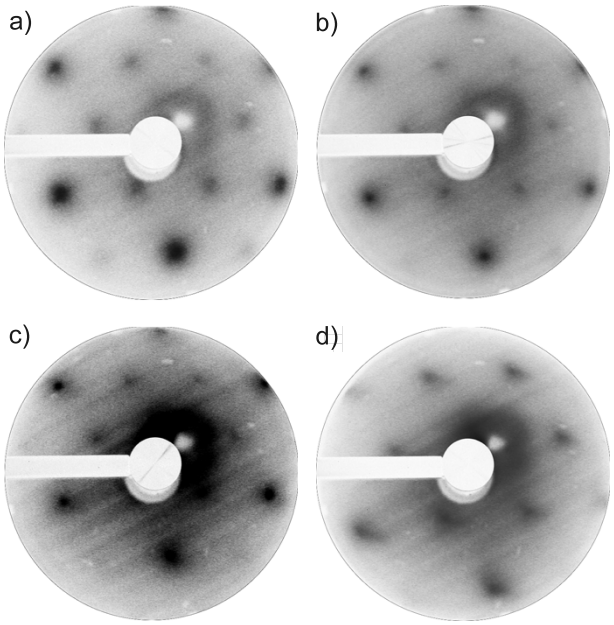

Figure 8.5: LEED patterns of 5 MLE VO_x structures on Pd(111): (a) after preparation at 523 K, bulk V_2O_3 structure $(\sqrt{3} \times \sqrt{3})$R30°, E=57 eV; (b) during reaction of deuterium with oxygen at 523 K, $(\sqrt{3} \times \sqrt{3})$R30°, E=56 eV; (c) during deuterium desorption at 700 K, $(\sqrt{3} \times \sqrt{3})$R30°, E=63 eV; (d) during reaction of deuterium with oxygen at 700 K, $(\sqrt{3} \times \sqrt{3})$R30°, E=42 eV.

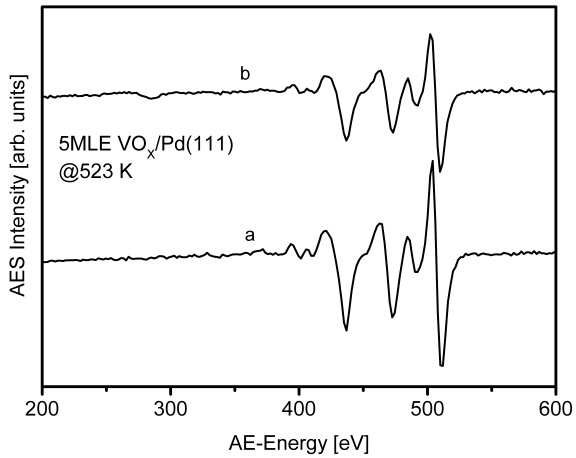

(a) AE spectra of the 5 MLE VO_x covered Pd(111) surface: curve (a) as prepared at 523 K; curve (b) after reaction/permeation at 523K

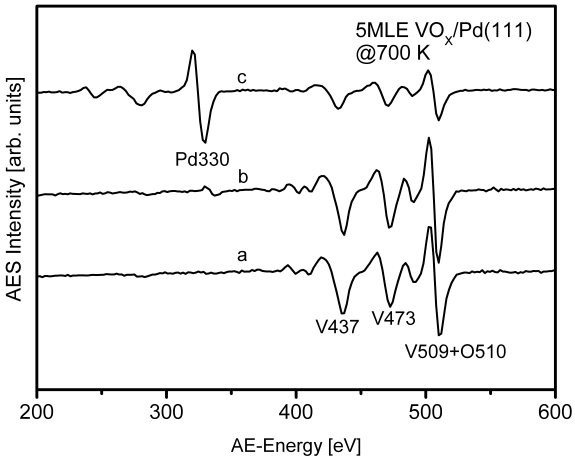

(b) AE spectra of the 5 MLE VO_x covered Pd(111) surface: curve (a) as prepared at 523 K; curve (b) after heating up to 700 K; curve (c) after reaction/permeation at 700 K

Figure 8.6: Comparison of the AE spectra for the 5MLE VO_x covered Pd(111) surface before and after reaction at 523 K and 700 K.

8.2.1 Discussion: Stability under Reaction Conditions

The 0.3 MLE vanadium oxide prepared under oxidizing conditions at 523 K forms a layer of 4×4 V_5O_{14} which fully covers the Pd(111) surface (figures (8.3a) and (8.2a)). This highly oxidized phase can only be stabilized when the oxidizing conditions are maintained as already stated in the literature [6; 9; 156; 157]. However, under the applied experimental conditions, where a quite high deuterium (hydrogen) partial pressure exists, the 4×4 phase quickly reduces to the 2×2 s-V_2O_3 phase. This phase covers about 60% of the Pd(111) surface [9] and is stable at 523 K, both under reducing conditions as well as under reaction conditions (deuterium+oxygen). However, the reaction conditions are also largely reducing conditions (p_{O2}=$1\cdot10^{-6}$ mbar equals $2.7\cdot10^{14}$ $O_2/(cm^2\cdot s)$ impinging on the surface, deuterium pressure increase during permeation of $8\cdot10^{-7}$ mbar equals about $1.2\cdot10^{16}$ $D/(cm^2\cdot s)$ emanating from the bulk). It is known from STM that at this temperature under reducing conditions the s-V_2O_3 phase forms compact two-dimensional islands on the bare Pd(111) surface [9]. At 700 K in UHV or under reducing conditions the s-V_2O_3 phase transforms into a VO structure as indicated by a change in the LEED pattern figure (8.3c) [3–5; 7]. Again under the applied reaction conditions this VO structure transforms back to the 2×2 s-V_2O_3 which is therefore the relevant configuration.

The 1 MLE VO_x structure at 700 K under reaction conditions showed an interesting feature which shall be discussed in the following. In addition to the 2×2 LEED pattern extra diffraction spots appear which have not been observed so far (figure 8.4e)). These additional spots can be fully explained by rotational and mirror domains of a rectangular structure with similar surface unit cell as that proposed for the flowerlike pattern. The schematic LEED pattern together with a schematic geometric model is depicted in figure (8.7). The direction of the short axis of

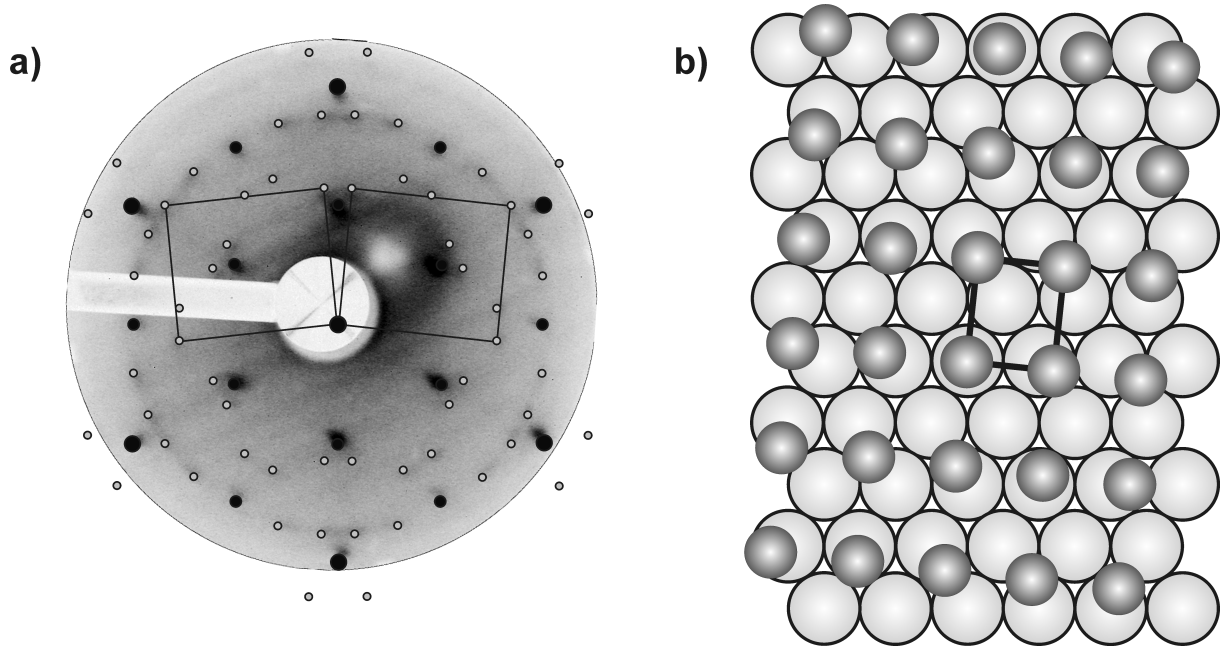

Figure 8.7: (a) LEED pattern of figure (8.4e) with calculated LEED spots and rectangular reciprocal unit cell and (b) corresponding geometrical model in real space.

the superstructure is rotated with respect to the (01) direction of the substrate unit cell by $\pm 6°$ and the length ratio of the rectangular unit cell is 1:1.2. This is close to the ratio of the unit cell axes of the flowerlike pattern. The only difference is a contraction of the reciprocal unit cell by about 10%, equivalent to an expansion of the geometric unit cell by 10%. This leads to a better matching of the atoms of the rectangular structure along the diagonal with respect to the (110) rows of the palladium substrate. On the other hand the direction of the diagonal is 3.5° off the (110) direction (figure (8.7b)). Apparently, at 700 K the VO_2 rectangular structure relaxes to an energetically more favorable expanded structure. In this case a larger number of oxygen atoms can occupy on-top positions which have been shown to be the energetically most favorable ones [8].

8.3 Time-of-flight measurements on permeating/desorbing deuterium and D_2O on VO_x modified Pd(111) surface

Hydrogen or deuterium permeates easily through palladium samples, even at relatively low temperature [158]. It therefore offers a convenient way to expose a surface to atomic H or D, which originates from the interior of the sample (see section 3.2). One could imagine that this permeating deuterium or hydrogen reacts quite differently with other adsorbed species than molecular H_2 or D_2 impinging from the gas phase. This is also expected to hold for modified palladium surfaces, e.g., modified by chemical additives or by a nanostructuring of the surface

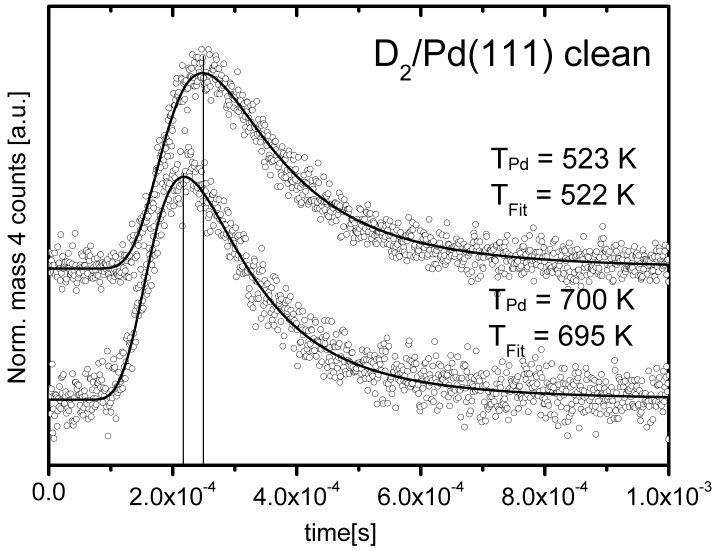

Figure 8.8: Time-of-flight spectra for deuterium desorbing from clean Pd(111) at 523 and 700 K, respectively. The best fit temperatures T_{Fit} for a Maxwellian distribution are also given, indicating a thermalized desorption.

[12]. Surface vanadium oxides, which exhibit a large variety of different stoichiometries and form different nanostructures on Pd(111), are excellent model systems which can be taken to study the permeation and desorption of deuterium and its reaction with impinging oxygen to water. In this section the focus lies on the translational energy distribution of the desorption flux and the reaction products, which have been measured by TOF spectroscopy (see section 3.3 and 4.4). In figure (8.8) TOF spectra of permeating/desorbing deuterium from a clean Pd(111) surface at two different surface temperatures are depicted for comparison. Least squares fits to the data points using Maxwellian distributions (see section 4.4) yield mean translational energies of the desorption flux, $\langle E \rangle = 2k_B T_{Fit}$, where the fit temperature T_{Fit} is close to the sample temperatures. This shows that associative desorption of deuterium from Pd(111) is largely unactivated and accordingly the sticking coefficient does not show pronounced energy dependence, as already described for hydrogen desorption in the literature [12; 56]. The error of the Maxwellian fits to the data points is approximately 5% throughout the experiment and will not be cited explicitly for all the individual fit temperatures in the following.

TOF spectra from 0.3 MLE vanadium oxide covered Pd(111)

The TOF spectrum for deuterium from a Pd(111) sample covered with 0.3 MLE vanadium oxide at 523 K is shown in figure (8.9(a)) (curve 1). The surface vanadium oxide film in this particular case is characterized by the s-V_2O_3 2×2 structure. A least squares fit of a Maxwellian TOF distribution to the experimental data points leads to T_{Fit}=481 K. Although this value is not far off the surface temperature of 523 K, this decrease in the mean translational

energy was reproducibly measured within the margin of error. The TOF measurement of D_2 during molecular oxygen exposure ($1 \cdot 10^{-6}$ mbar) leads to a TOF spectrum as depicted in figure (8.9(a)) (curve 1). As already outlined above not all deuterium atoms react with oxygen to water. In addition, due to the much higher deuterium permeation rate compared to the oxygen impingement rate, associative desorption of deuterium molecules still takes place. The best fit temperature is now T_{Fit}=476 K. Apparently the TOF spectrum is not changed significantly.

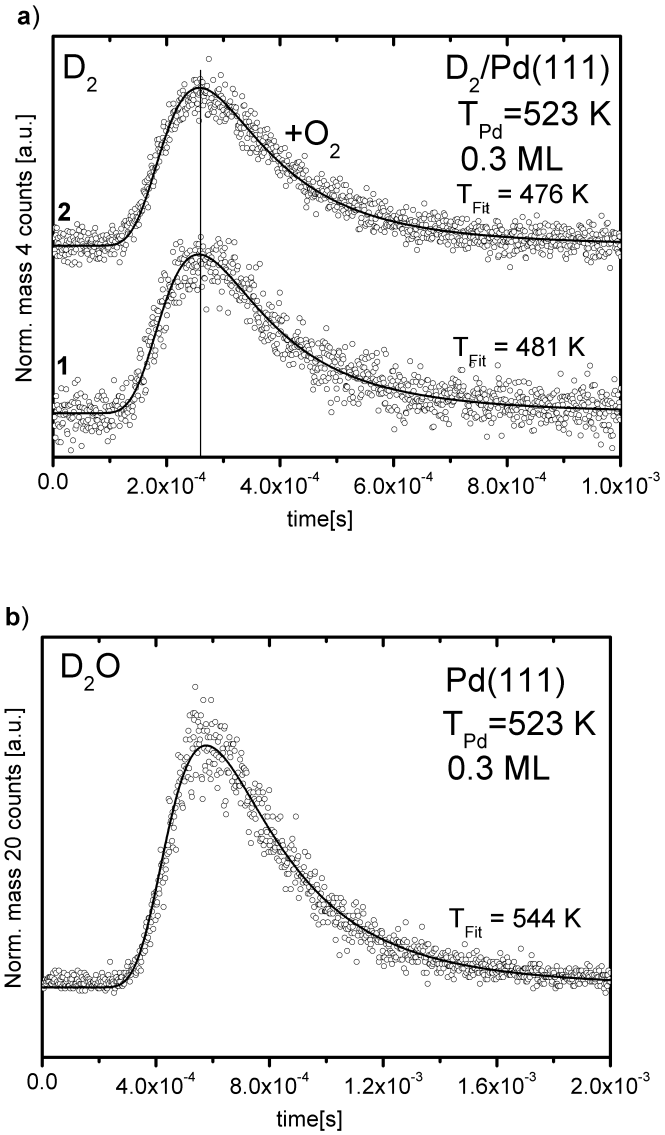

Figure 8.9: (a) Time-of-flight spectra for pure deuterium desorption (curve 1) and deuterium desorption during concomitant oxygen exposure (curve 2) from 0.3 MLE VO_x on Pd(111) at 523 K. (b) Time-of-flight spectrum of D_2O resulting from the reaction of permeating D and impinging O_2 on 0.3 MLE VO_x on Pd(111) at 523 K.

In the latter case we have also measured the TOF distribution of the water reaction product

(figure (8.9(b))). A best fit temperature T_{Fit}=544 K is obtained, indicating that water desorption is close to thermal, but slightly hyperthermal. The same experiments were performed at a sample temperature of 700 K. The backpressure of deuterium in the permeation source was changed in such a way that the permeation flux was approximately the same as for the 523 K situation. The TOF spectrum for pure deuterium desorption is depicted in figure (8.10(a)) (curve 1).

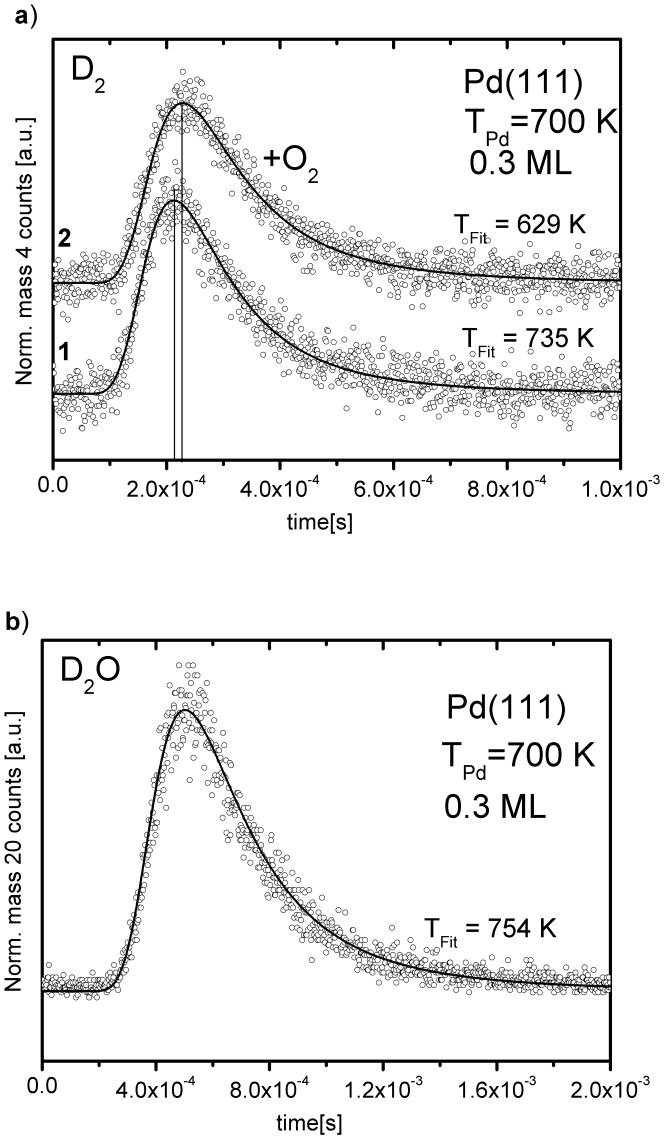

Figure 8.10: (a) Time-of-flight spectra for pure deuterium desorption (curve 1) and deuterium desorption during concomitant oxygen exposure (curve 2) from 0.3 MLE VO_x on Pd(111) at 700 K. (b) Time-of-flight spectrum of D_2O resulting from the reaction of permeating D and impinging O_2 on 0.3 MLE VO_x on Pd(111) at 700 K.

A best fit yields T_{Fit}=735 K. From the LEED investigations we know that in this case the

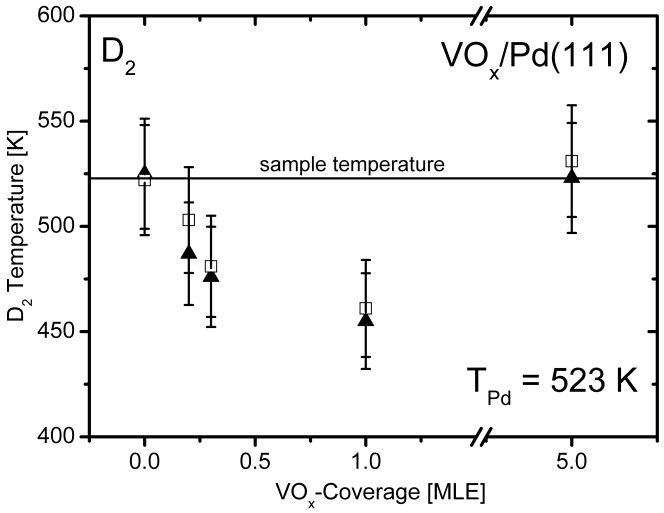

Figure 8.11: Maxwellian fit temperatures for desorbing deuterium as a function of the VO_x coverage on Pd(111) at 523 K: (□) pure deuterium desorption and (▲) deuterium desorption during oxygen exposure.

surface consists of a surface vanadium oxide with VO stoichiometry. After adding the appropriate oxygen pressure the surface is changed to the 2×2 vanadium oxide structure with s-V_2O_3 stoichiometry. Deuterium desorption during oxygen impingement yields a TOF spectrum which now indicates a significantly smaller value for the mean translational energy of T_{Fit}=629 K (figure 8.10(a), curve 2). Apparently, the specific oxide layers which are stable at the individual reaction conditions influence the TOF spectra. The corresponding water-TOF spectrum (figure (8.10(b))) yields a best fit temperature of T_{Fit}=754 K, again slightly hyperthermal.

TOF spectra from 1 and 5 MLE vanadium oxide covered Pd(111)

The 1 MLE surface vanadium oxide at 523 K is characterized by a 2×2 structure, with additional spots in the LEED pattern, resulting in the flowerlike pattern. From STM measurements it is known that this surface consists of a full layer of surface V_2O_3 with additional islands of VO_2 stoichiometry [8]. This surface should exhibit only few border lines between oxide islands and bare Pd(111). We have carried out pure deuterium desorption as well as deuterium + oxygen reaction TOF studies on this surface, both at 523 and 700 K. Since the shape of the spectra and the signal noise behavior are similar as in the above described circumstances all the individual TOF spectra will not be presented but only the determined fit temperatures will be quoted. The data are compiled, together with the data for the 0.3 and 5 MLE surface vanadium oxides in figures (8.11), (8.12) and (8.13).

Pure deuterium desorption from the 1 MLE surface at 523 K (LEED shows the 2×2 structure) yields a mean translational energy corresponding to a temperature of T_{Fit}=461 K, which is again significantly smaller than the surface temperature (figure (8.11)).

In the case of concomitant oxygen exposure the D_2 TOF yields a mean desorption tempera-

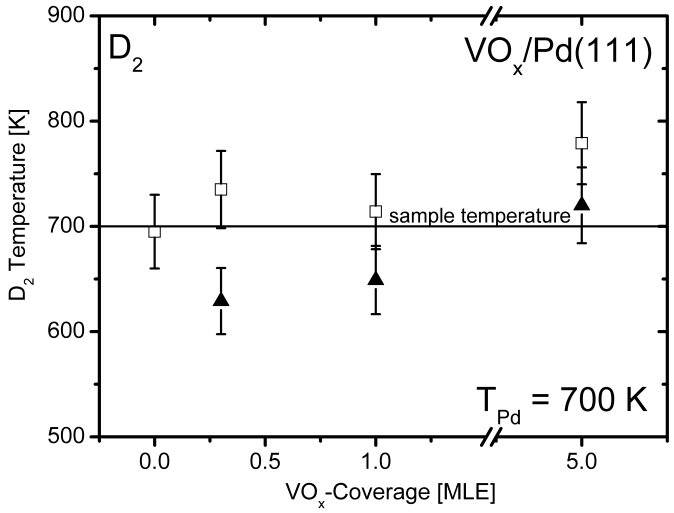

Figure 8.12: Maxwellian fit temperatures for desorbing deuterium as function of the VO_x coverage on Pd(111) at 700 K: (□) pure deuterium desorption and (▲) deuterium desorption during oxygen exposure.

ture of T_{Fit}=455 K. The TOF spectrum for D_2O can be approximated by a mean desorption temperature of 567 K (figure (8.13)). The TOF measurements at 700 K yield the following best fits to the spectra: pure deuterium desorption (LEED shows VO structure), T_{Fit}=714 K; deuterium during oxygen exposure (LEED shows (2×2) + rectangular VO_2 structure), T_{Fit}=649 K (figure (8.12)); water desorption, T_{Fit}=727 K. Again, for 1 MLE vanadium oxide different structures are stable under different reaction conditions which have an influence on the TOF spectra.

In the case of the 5 MLE vanadium oxide the structure is characterized by the LEED pattern indicating bulk V_2O_3. The desorption and reaction studies yield the following results: At 523 K pure deuterium desorption gives T_{Fit}=531 K, deuterium concomitant with oxygen yields a best fit temperature T_{Fit}=523 K (figure (8.11)), and the water TOF can be described by T_{Fit}=548 K (figure (8.13)). At 700 K pure deuterium desorption gives T_{Fit}=779 K, deuterium concomitant with oxygen yields T_{Fit}=720 K (figure (8.12)), and the water TOF can be described by T_{Fit}=744 K (figure (8.13)).

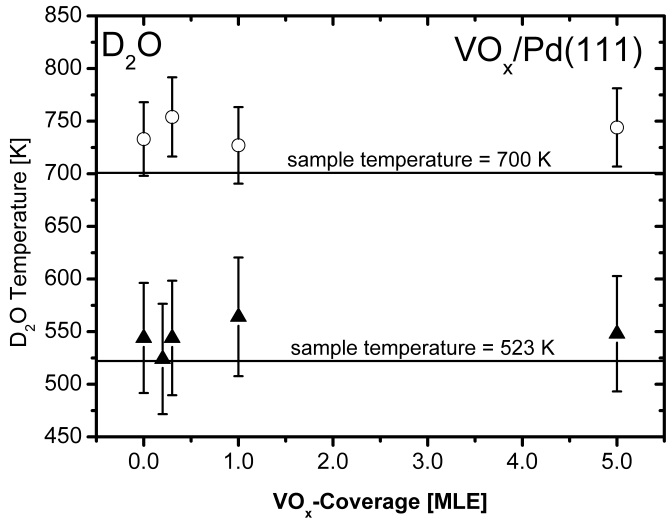

Figure 8.13: Maxwellian fit temperature for desorbing D_2O as function of the VO_x coverage on Pd(111) at (▲) 523 K and (○) 700 K.

8.3.1 Discussion: TOF spectra

As already stated in section 8.2 the 4×4 V_5O_{14} structure, which is formed by deposition of 0.3 ML vanadium under oxidizing conditions at 523 K, converts into the more stable 2×2 s-V_2O_3 configuration at redcucing conditions. This phase covers then about 60 % of the surfaces and keeps stable under the applied reaction conditions. The TOF spectrum for deuterium desorbing from this surface at 523 K can be approximated by a Maxwellian of T_{Fit}=481 K. It would be tempting to ascribe this feature of a "cooled" deuterium flux to particular changes of the potential energy surface (PES) for the desorption process. However, careful examination of the experiment leads to a different and quite simple explanation of this result. As outlined above the deuterium permeation/desorption flux of about $6{\cdot}10^{15}$ $D_2/(cm^2{\cdot}$ s) leads to a pressure increase in the chamber of $8{\cdot}10^{-7}$ mbar (at a pumping speed of 140 l / s as determined with the tungsten desorption standard [44]). This pressure equals an impingement rate of D_2 on the surface of $6{\cdot}10^{14}$ $D_2/(cm^2{\cdot}$ s). This means that about 10 % of the deuterium flux which leaves the surface originates from reflected or adsorbed/desorbed deuterium. On the bare Pd(111) surface the sticking coefficient for hydrogen (deuterium) is quite high (S_0=0.45 (Ref. [54])). In this case the permeated/recombined deuterium molecules and the adsorbed/desorbed deuterium molecules are close to thermal, as observed experimentally (figure (8.8)). In the case of the 0.3 MLE vanadium oxide about 60% of the surface is covered by the oxide. Deuterium molecules impinging on the oxide areas do not adsorb but are reflected without losing much of their kinetic energy, corresponding to 300 K. This contribution to the total desorption flux yields on the average a mean translational energy which is equivalent to a smaller temperature than the corresponding sample temperature (figure (8.11)).
For the 1 MLE oxide surface at 523 K, which is composed of a full layer of 2×2 s-V_2O_3 and islands with the rectangular oxide structure, no bare palladium is exposed and the contribution of reflected molecules with 300 K Maxwell temperature is even larger, as seen in figure (8.11). The result of these considerations is that the mean translational energy distribution of permeating/desorbing deuterium, which is thermalized on the Pd(111) surface, is also largely thermalized for the vanadium oxide layer. In the case of concomitant oxygen exposure the kinetic energy distribution of deuterium is not changed significantly. The reaction product water is also close to thermal, but slightly hyperthermal (by about 10%).
On the 5 MLE vanadium oxide at 523 K, which consists of small islands of bulk vanadium V_2O_3, pure deuterium desorption and D_2 desorption during water reaction are again thermalized (figure (8.11)). This is somewhat puzzling because this would mean that impinging deuterium is fully thermalized either by dissociative adsorption/recombinative desorption or by inelastic scattering with a high accommodation coefficient. Apparently, the deuterium adsorption behavior on the surface vanadium oxide and the bulk vanadium oxide is quite different. Here the question of the influence of the surface morphology at the accommodation process has to be considered. The morphology of the 5 MLE bulk-type V_2O_3 (figure (8.2e)) is quite rough at the atomic scale, compared to the monolayer surface vanadium oxide (figure (8.2d)). Multiple collisions in the interaction region on the bulk V_2O_3 surface may give rise to the more pronounced accommodation.

The permeation experiments at 700 K yield some differences compared to the 523 K case. Under reducing conditions, i.e., for pure deuterium desorption, the LEED patterns indicate the existence of the VO structure, both for 0.3 and 1 MLE. In this case the mean translational energy distribution of deuterium is close to thermal (figure (8.12)). Following the considerations made above leads to the conclusion that deuterium molecules impinging from the gas phase on the VO surface leave the surface fully accommodated, either due to adsorption/desorption or due to a large accommodation coefficient for the inelastically reflected molecules. Under reaction conditions, i.e., permeation of hydrogen during exposure to oxygen, LEED reveals the existence of the 2×2 s-V_2O_3 phase, both for 0.3 and 1 MLE. On this vanadium oxide layer with higher oxidation state again a cooled kinetic energy distribution is observed, due to the negligible sticking coefficient for deuterium on this oxide phase. For the 5 MLE case at 700 K the desorption features are similar to those for the 523 K case showing that the bulk vanadium oxide is less influenced by temperature and oxygen pressure. The D_2O desorption flux at 700 K is for all VO_x phases slightly hyperthermal, as for the 523 K case (figure (8.13)). This behavior suggests that those deuterium atoms with higher kinetic energy in the energy distribution react with higher probability with the intermediate hydroxide species on the surface, to form water.

8.4 Angular distribution of desorbing deuterium from VO_x covered Pd(111) surfaces

Supplementary to the time-of-flight measurements on the clean and VO_x covered Pd(111) surface the angular distribution of the desorbing deuterium was measured. The angular distribution was determined by evaluating the deuterium flux signal in the LOS detector as a function of the lateral sample displacement as already described in section 4.3 and chapters 5 and 6. The experimental procedure has been explained briefly in chapter 3. The data evaluation which was done by comparison with MC simulations is described in 4.
As already stated ultra-thin vanadium oxide layers on palladium as well as on rhodium single crystals form a variety of structures with different stoichiometries. The influence of some of these VO_x layers on Pd(111) on the deuterium desorption particularly on the angular distribution of the desorpton flux was studied. The most stable vanadium oxide configuration in the submonolayer coverage regime is the s-V_2O_3 oxide, which can be identified easily by a 2×2 LEED pattern. Even under reducing conditions like deuterium permeation/desorption at $8{\cdot}10^{-7}$ mbar D_2 partial pressure the structure keeps stable for hours. Above 700 K the already introduced wagon-wheel structure occurs which exhibits a VO stoichiometry. For the experiments 0.3 MLE as well as 0.5 MLE vanadium oxide layers were prepared. In case of the 0.5 MLE coverage the whole surface is covered by the s-V_2O_3 structure providing pockets that contain a single Pd atom as shown in figure (8.14) [3]. The 0.3 MLE vanadium oxide covered surface is just covered to about 60% by s-V_2O_3 islands providing a lot of metal-oxide boundaries. In this case it is possible to study the influence of these metal-oxide boundaries on the desorption. In figure (8.15) the desorption flux as a function of the sample displacement for var-

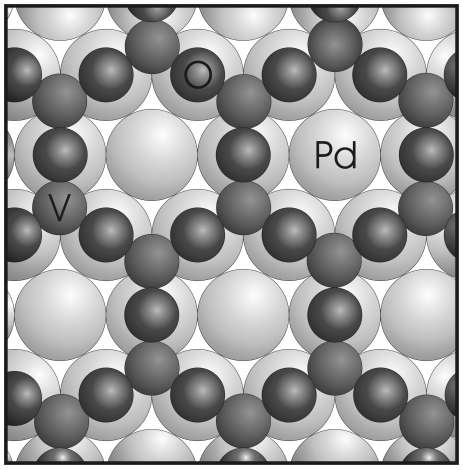

Figure 8.14: Structure model of the s-V_2O_3 surface oxide on Pd(111) (after Ref.[3])

ious experimental conditions are compiled. Additionally the MC simulated flux dependence for angular desorption distributions with n=1 and n=2 is shown for comparison. One can see that for all experimental conditions the obtained distributions are within this range. Apparently, no significant increase/change in the activation barrier for the adsorption/desorption process has been introduced by the vanadium oxide.

8.4.1 Discussion: Angular Distribution

From figure (8.15) where the data for various experimental conditions (different vanadium oxide coverages and sample temperatures) are compiled one can see by comparison with the MC simulated data that there is no significant influence of the vanadium oxide on the angular distribution of desorption. This result fits quite well to the measured time-of-flight distributions of the desorbing deuterium molecules from the vanadium oxide covered Pd(111) surface. For a sample temperature of 523 K the TOF distribution corresponds to a Maxwellian flux which is thermalized to the sample temperature, which again is a clear indication of a negligible activation barrier. In the case of 700 K the mean translational energy was slightly above thermal (T = 754 K), which qualitatively corresponds to the somewhat more forward focused angular desorption distribution at this temperature.
Most probably the particular structure of the vanadium surface oxide, as shown in figure (8.14), is responsible for this behaviour. This structure, which is also called the "pocket structure", is quite porous and allows for recombinative desorption in these pockets. The electronic influence of the vanadium and oxygen atoms is apparently of very short range character, in contrast to the long range electronic influence in the case of potassium adsorption. Interestingly, high-resolution XPS and HREELS experiments for CO adsorption on this s-V_2O_3 surface, in combination with DFT calculations, led to a similar conclusion that CO adsorbs in these "pockets"' as on the clean Pd(111) surface [9]. Furthermore, no significant difference for the desorption distribution between the 0.3 MLE and the 0.5 MLE vanadium oxide covered surface can be observed. Apparently, the influence of the oxide islands boundaries on the desorption

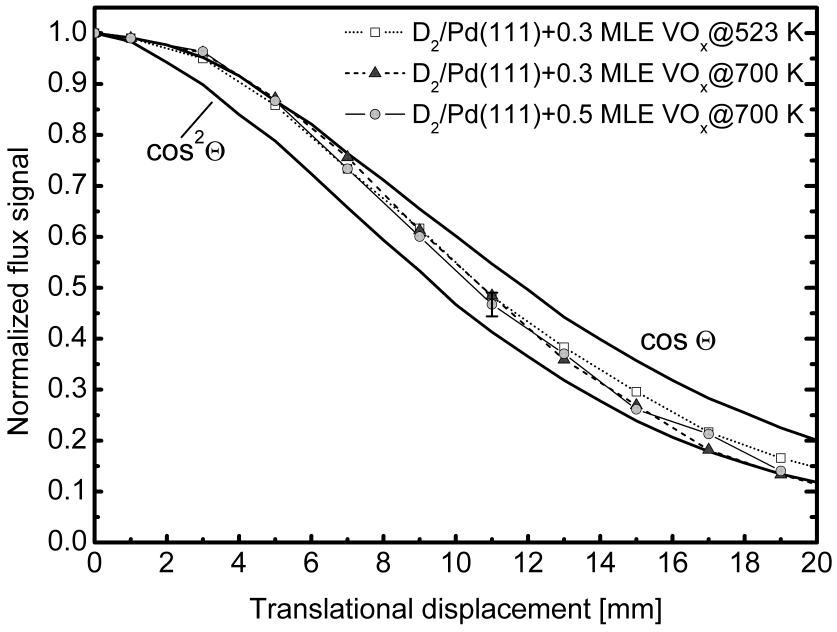

Figure 8.15: Experimentally obtained change of the desorption flux signal for deuterium from the Pd(111) surface, pre-covered with vanadium oxide.(□) 0.3 MLE V_2O_3 at 523 K, (▲) 0.3 MLE VO at 700 K, (○) 0.5 MLE VO at 700 K. The full lines stem from MC calculations for $cos^n\theta$ functions with n = 1 and n = 2.

process is not pronounced, since the reaction can proceed without significant activation barriers both on the clean Pd(111) surface and on the vanadium oxide covered islands.

8.5 D_2O formation kinetics on VO_x covered Pd(111)

Contrary to the latter sections which were focused on dynamical properties on the water formation/desorption and deuterium permeation/desorption, here a systematic study on the influence of varying VO_x coverages (0 - 5 MLE) on Pd(111) on the kinetics of water formation is shown. For the experiments again the permeation source (see section 3.2) was used. The arrangements and experimental procedures are identical with those used for the clean Pd(111) sample (see chapter 7). The data evaluation as well as the applied kinetic model of the D_2O formation is done analogous to chapter 7.

8.5.1 Results and Discussion

Deposition of 0.3 MLE VO_x at 523 K leads to a surface which is almost totally covered with the (4× 4) V_5O_{14} structure. Due to a rather high partial pressure of hydrogen in the residual gas, this configuration reduces within a few minutes and changes into the stable s-V_2O_3 phase which

then covers only 60% of the total surface area [8; 9]. Thus one gets a surface with coexisting bare Pd areas and s-V_2O_3 domains. Comparing the results between the formation of D_2O on the clean and on the 0.3 MLE VO_x covered Pd(111) surface yields some pronounced differences. First, the initial reaction probability is significantly lower on the oxide covered sample than on the clean one at both sample temperatures (figures (8.16(a)), (8.16(b))).

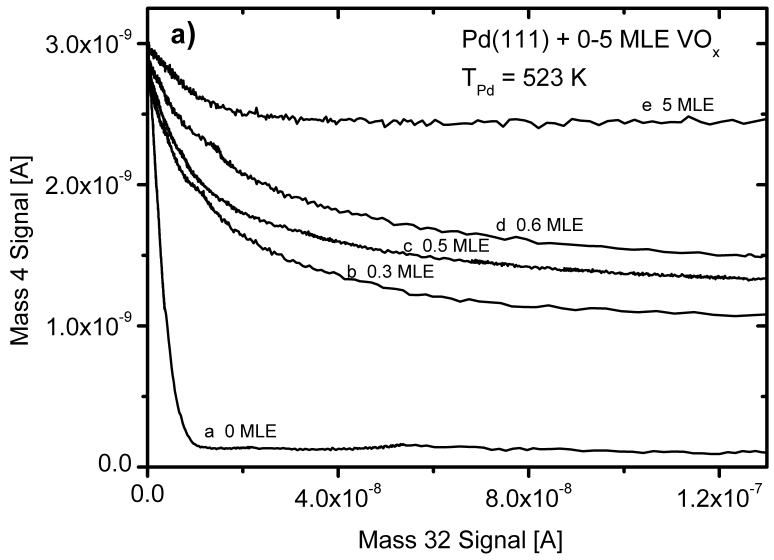

(a) Change of the D_2 flux versus oxygen pressure at 523 K

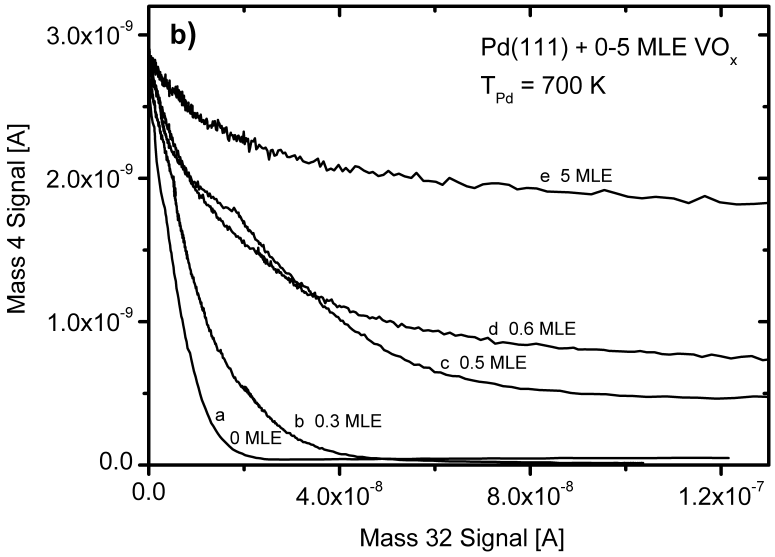

(b) Change of the D_2 flux versus oxygen pressure at 700 K

Figure 8.16: Change of the deuterium flux versus oxgen pressure during water formation reaction at different vanadium oxide coverages at 523 K (a) and 700 K (b) sample temperature. Data are normalized to the same initial flux.

Additionally, the reaction probability on the 0.3 MLE VO_x covered sample is higher at 700 K than at 523 K. Another difference is that the reaction on the s-V_2O_3 coated surface needs more time to equilibrate when the oxygen pressure is changed. This is shown in figure (8.17) where the mass 4 and mass 20 signal change as a function of the mass 32 signal are compared for clean palladium (figure (8.17(a))) and for 0.3 MLE covered palladium (figure (8.17(b))) at a sample temperature of 700 K. While for the clean sample the change of the deuterium and water signals is practically identical during the increase and the decrease of the oxygen pressure, there is a clear hysteresis for the oxide covered sample. Typical oxygen pressure changes of about $5 \cdot 10^{-10}$ mbar/s have been applied, both for increasing and decreasing the pressure. As already pointed out, it was experimentally difficult to increase the oxygen pressure smoothly. One can see in figure (8.17(b)) that the deuterium signal still changes even though the pressure is kept at a certain value during the increase of the oxygen pressure (positions 1, 2, and 3 in figure (8.17(b))). Just after several minutes of exposure at constant pressure the deuterium signal stopped changing, and the system had reached its equilibrium. This can be attributed to structural changes due to oxidation processes on the VO_x layer. Following the curve backward from high to low oxygen pressures approximates much better the equilibrium situation at each pressure. Evaporation of 0.5 MLE VO_x again generates an s-V_2O_3 layer which now covers nearly the entire surface. The behavior concerning water formation is similar to that on the 0.3 MLE covered surface. The initial reaction probability has slightly decreased for both sample temperatures, and again the hotter surface shows a slightly higher reactivity. Unlike for the 0.3 MLE covered surface at 700 K, the reaction on the 0.5 MLE covered surface saturated before the deuterium flux was depleted. The latter observation holds true for all higher vanadium oxide coverages. Furthermore, a higher oxygen pressure was needed until the reaction reached saturation. This can be seen in figures (8.16(a)) and (8.16(b)) where the decrease of the deuterium signal is compiled for different VO_x coverages as a function of the oxygen signal. The odd shape of curve c in figure (8.16(b)) can be attributed to an unintentional discontinuity in the adjustment of the oxygen pressure. From figure (8.18) one can see that there is no significant change in the initial reaction probability once the surface is entirely covered with vanadium oxide. Even though the initial reaction probability does not change so much above 0.5 MLE VO_x, there are clear differences in the amount of deuterium that contributes to the water formation. As illustrated in figure (8.19) the fraction of the converted deuterium flux in the saturation region decreases with increasing vanadium oxide coverage.

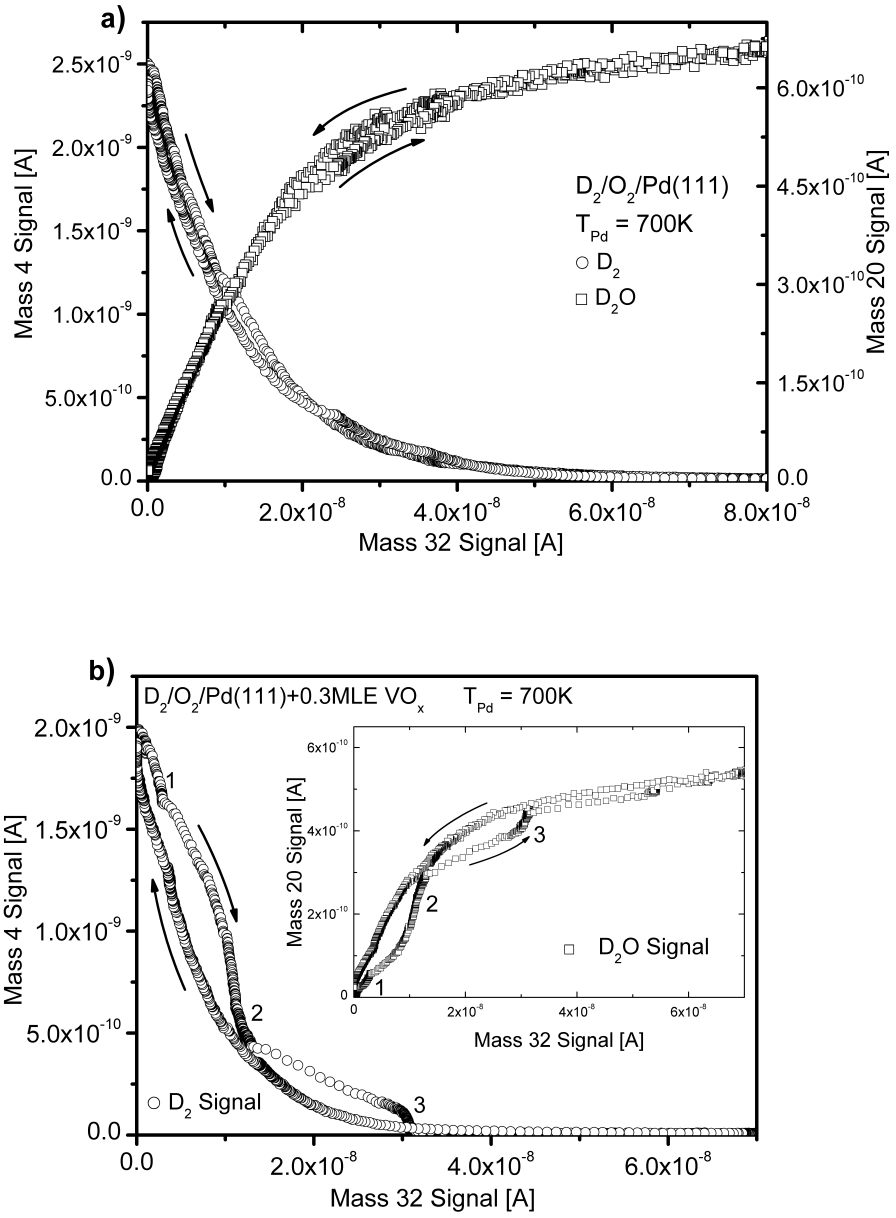

Figure 8.17: Change of the deuterium flux versus oxgen pressure during water formation reaction at different vanadium oxide coverages at 523 K (a) and 700 K (b) sample temperature. Data are normalized to the same initial flux.

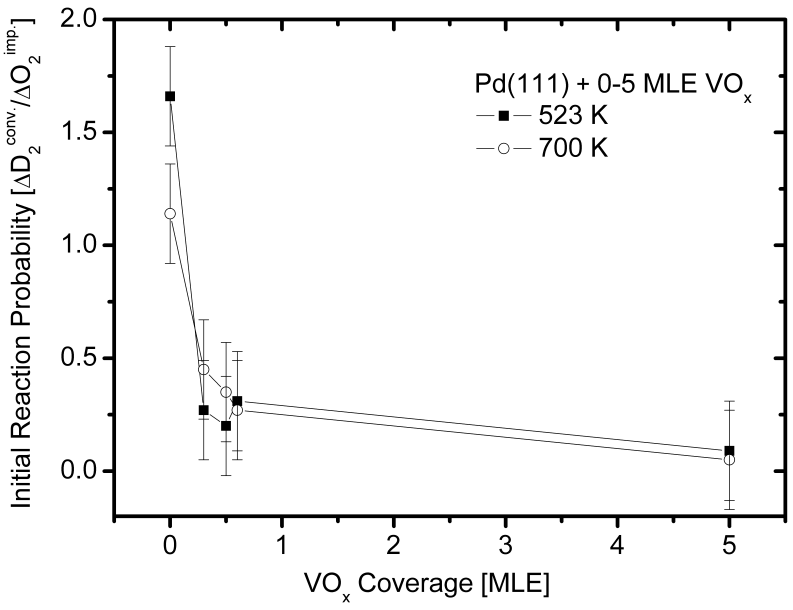

Figure 8.18: Initial reaction probability versus vanadium oxide coverage at 523 K (■) and 700 K (○).

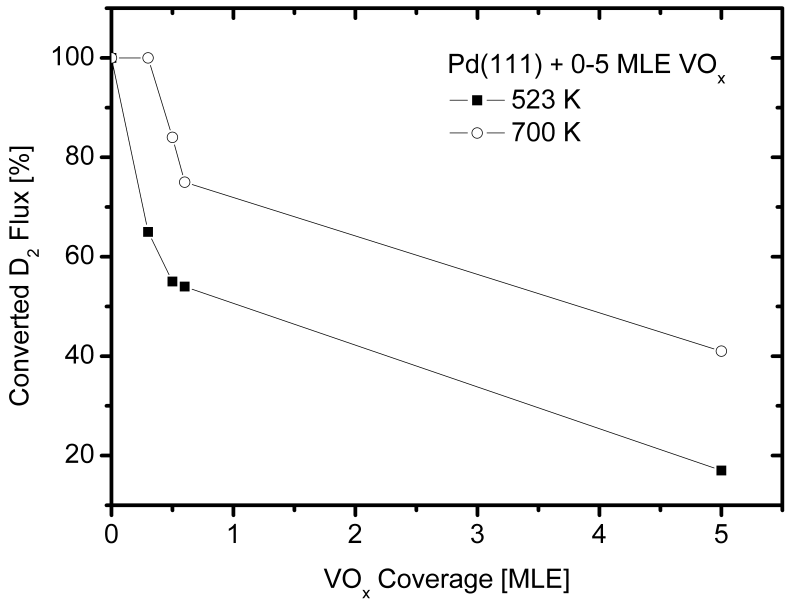

Figure 8.19: Fraction of the deuterium flux which was consumed by the water formation versus vanadium oxide coverage at 523 K (■) and 700 K (○).

The very fact that for the bare Pd(111) surface a total conversion of the D_2 flux into D_2O could be achieved but not for the VO_x covered surfaces (except for the 0.3 MLE covered surface at

700 K) implies that the water formation reaction proceeds much more efficiently on the clean than on the oxide covered palladium surface. Furthermore, the initial reaction probabilities turned out to be significantly higher on the clean surface for both temperatures. This indicates that at 523 K the s-V_2O_3 surface is permeable for deuterium and allows D_2 recombination but does not support oxygen dissociation to the same extent as the bare palladium. At 700 K the surface favors the lower oxidized VO "wagon-wheel" structure under UHV conditions. However, increasing the oxygen partial pressure, even during deuterium permeation, leads to a reoxidation of the surface to the s-V_2O_3 structure. Since under high oxygen pressures the surface configurations at both temperatures (523 K and 700 K) are the same (where about 60% of the total surface is covered with the s-V_2O_3 phase), the fact that on the 0.3 MLE VO_x covered surface at 700 K a total consumption of the deuterium is possible can be attributed to temperature enhanced diffusion. This means that deuterium is transported to the bare palladium areas where the reaction goes on more effectively than on the vanadium oxide. At coverages above 0.5 MLE VO_x there are no bare Pd regions left which could act as active areas. The water formation reaction on the vanadium oxide is not effective enough to achieve total conversion of the deuterium into D_2O. Finally, at a coverage of 5 MLE VO_x the surface is covered with small 3D vanadium oxide crystallites [4]. In this case there exist no 2D nanostructures on the surface anymore. The fraction of the converted deuterium flux turned out to be significantly higher at 700 K than at 523 K which again can just be attributed to the higher mobility of deuterium due to the elevated temperature.

Modeling the Reaction Process. The model used for the water formation on the clean palladium surface was applied to the 0.3 MLE covered surface to complete the picture. There are a couple of parameters necessary which cannot be found in the literature. These parameters are the rate parameters for oxygen and deuterium recombination, the sticking coefficient of oxygen and its coverage dependence, and also the rate factor for OD formation on surface vanadium oxide films. This means that the parameters k_D, k_O, k_{OD}, S^0_{O2}, and α in equations (7.2) and (7.3) are unknown. Therefore, in a first approach, the same values for k_D, k_O, and α as for the clean palladium surface were applied. On the basis of these assumptions S^0_{O2} and k_{OD} were varied for the calculations. It turned out that all the unknown parameters can have a significant influence on the results, and that a number of different parameter combinations can reproduce the experimentally obtained data. The best results of the performed calculations for the 0.3 MLE covered surface are depicted in figure (8.20) for 523 K and figure (8.21) for 700 K. For the 523 K sample a rate coefficient for the OD formation of $k_{OD} = 4.3{\cdot}10^{-14}$ cm^2 atom^{-1} s^{-1} was used and the initial sticking coefficient for oxygen was set to $S^0_{O2} = 0.15$. For the 700 K sample good agreement could be obtain with $k_{OD} = 1.8{\cdot}\ 10^{-12}$ cm^2 atom^{-1} s^{-1} and $S^0_{O2} = 0.3$. These results indicate that for the higher temperature both the OD reaction coefficient and the oxygen sticking coefficient are enhanced on the vanadium oxide layer.

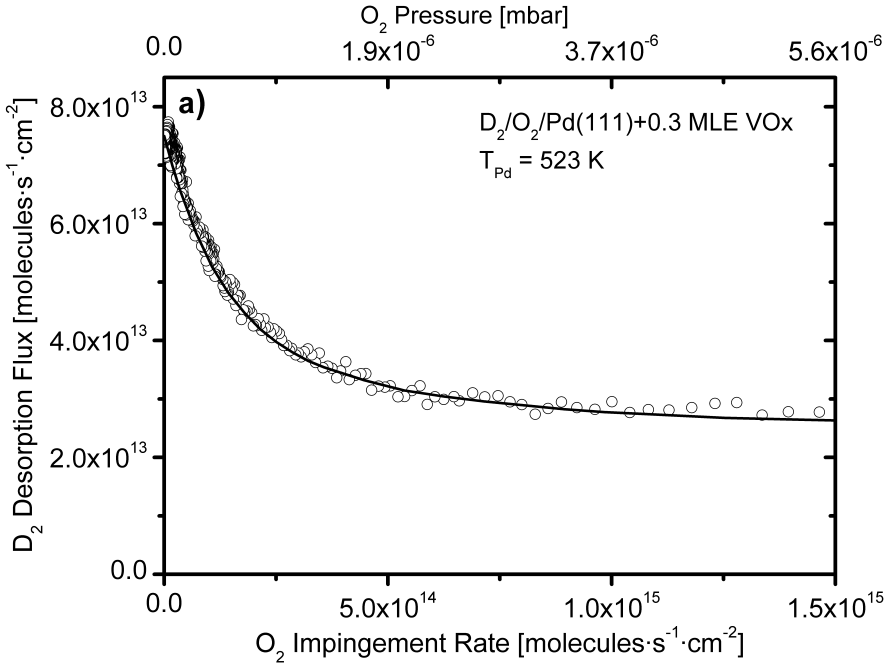

Figure 8.20: Initial reaction probability versus vanadium oxide coverage at 523 K (■) and 700 K (○).

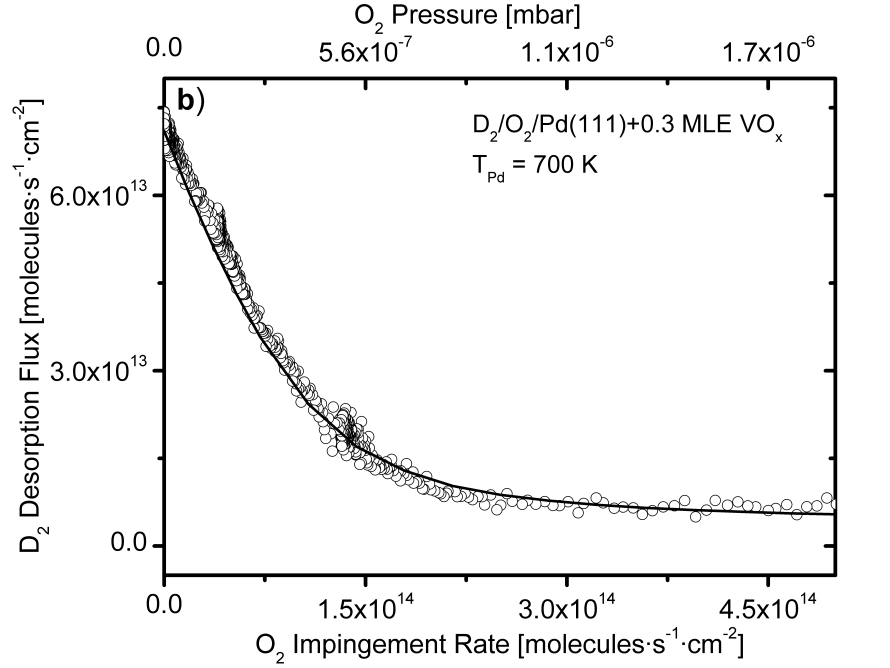

Figure 8.21: Fraction of the deuterium flux which was consumed by the water formation versus vanadium oxide coverage at 523 K (■) and 700 K (○).

8.6 Summary of Chapter 8

Various vanadium oxides in different oxidation states have been prepared on a Pd(111) surface. Their stability under reaction conditions have been analysed using LEED and AES. The palladium sample was part of a permeation source (see section 3.2), thus enabling the permeation of deuterium through the sample onto the surface. The permeation/desorption of deuterium from the clean and the oxide covered sample as well as the reaction of the permeating deuterium with impinging oxygen on the clean and oxide covered sample has been studied using TOF spectroscopy, LEED and angular distribution measurements. The results can be summarized as follows.

8.6.1 TOF Measurements and Stability

1. The stable phase of a 0.3 MLE vanadium oxide at 523 K, during deuterium desorption as well as during reaction between deuterium and oxygen, is the 2×2 s-V_2O_3 surface oxide. The experimentally obtained mean translational energy for desorbing deuterium is smaller than the thermal value. However, this is just due to a considerable contribution of reflected (non-accommodated) deuterium molecules that are at room temperature. The translational energy distribution of associatively desorbing deuterium itself is thermal.

2. The stable 0.3 MLE vanadium oxide at 700 K is the "wagon-wheel" VO phase. TOF shows a thermal distribution of deuterium from this surface, indicating that the reflected contribution is also thermal. The adsorption and accommodation behaviors of impinging deuterium are apparently quite different on the s-V_2O_3 surface and on the VO surface. Concomitant oxygen adsorption changes the vanadium oxide to s-V_2O_3. The TOF spectrum is again "cooled" due to the changed adsorption behavior of deuterium.

3. For the 1 MLE VO_x scenario more different stable oxide phases exist as a function of temperature and deuterium and/or oxygen pressures. However, the main feature is again that the different oxides existing at 523 and 700 K exhibit different adsorption behaviors for deuterium, resulting in different apparent TOF distributions.

4. The 5 MLE vanadium oxide forms a bulklike V_2O_3. Deuterium desorption from this surface yields thermalized TOF spectra, both for 523 and 700 K. This shows that the adsorption behavior for deuterium is different on the surface vanadium oxide and the bulk vanadium oxide. The influence of the different surface morphologies may be a possible reason.

5. The mean translation energy distribution of the water reaction product is on the average slightly hyperthermal. A possible explanation for this behavior is that those deuterium atoms which possess higher kinetic energy after permeation react more easily with the hydroxyl intermediate and channel their energy into the reaction product.

8.6.2 Angular Distribution

The existence of an ultra-thin vanadium surface oxide, s-V_2O_3, at 523 K and VO at 700 K on the Pd(111) surface, does not influence the angular distribution for deuterium significantly. This is most probably due to the specific structure of the oxide which is a porous network. The influence of the vanadium and oxygen atoms is of short range and therefore the potential energy surface in the "pockets" of the oxide structure does not change significantly. These findings are in good agreement with the TOF measurments which also indicate that no significant activation barrier for adsorption exists.

8.6.3 Water Formation Kinetics

A Pd(111) single-crystal surface has been modified with ultrathin vanadium oxide films in the range from 0 to 5 MLE. Their influence on the water formation reaction has been investigated by rate measurements of the desorbing reaction products. The reaction was supplied on the one hand by direct dosing of molecular oxygen onto the surface and on the other hand by atomic deuterium via permeation through the bulk of the sample. The experiments were carried out at a sample temperature of 523 and 700 K, respectively. Performing the water formation on a 0.3 MLE VOx resulted in a significantly lower initial reaction probability than on the clean Pd(111) sample. In this case at 523 K about 60% of the surface is covered with the (2×2) s-V_2O_3 phase, and 40% is still bare palladium. The initial reaction probability dropped significantly compared to the clean sample, and even for high oxygen pressures only about 65% of the deuterium flux could be converted into water, which indicates that at this temperature the oxide phase is not as accessible toward oxygen dissociation as the bare palladium. At a sample temperature of 700 K, all the permeating deuterium was consumed by the water formation, which can be attributed to enhanced diffusion of the reactants to the more reactive bare Pd areas at higher temperatures. Covering the sample surface with 0.5 MLE VO_x leads to a surface which is completely covered with the (2×2) s-V_2O_3 phase. Nevertheless, the water formation reaction is still possible. The change in the initial reaction probability compared to the 0.3 MLE covered sample is by far not as pronounced as the change between the clean and 0.3 MLE covered surface. The main difference compared with the 0.3 MLE sample is that at 700 K only about 80% of the deuterium flux could be converted to D_2O even at high O_2 pressures. A further increase of the oxide coverage does not have pronounced effects on the initial reaction probability. However, the total fraction of consumed deuterium decreases with increasing VO_x coverage.

9 Zn on Pd(111)

The interest in gaining access to alternative energy carriers has initiated research in the development of processes for the production as well as for the storage of hydrogen. Compounds with high hydrogen to carbon ratios like methanol have been proposed as hydrogen sources that can be stored easily. One of the most promising approaches for a mobile hydrogen supply is the steam reforming of methanol [21; 28; 29]. Catalysts for methanol reforming are typically based on Cu [159], Cu/ZnO [160–162] or Pd/ZnO and Zn/Pd [14–27]. The low cost Cu/ZnO catalyst suffers from deactivation due to the sintering of the metal particles if the process temperature exceeds 570 K. Compared to the copper based catalysts the thermal stability of those which contain group 10 transition metals (Ni, Pt, Pd) is superior. Anyhow, the drawback of these transition metal based catalysts is that the main product beside hydrogen is CO instead of CO_2 [16; 130]. This requires additional processing to convert the toxic CO into CO_2. In forgoing works described in the literature it could be shown that the catalytic properties of Pt and Pd supported on ZnO can be improved involving the reductive formation of ZnPd and ZnPt alloys [14–16; 20; 24; 25; 27]. The enhanced chemical selectivity in methanol steam reforming can be attributed to similar electronic properties of Cu and ZnPd alloys [30; 163]. However, experimental work done on thin Zn layers on Pd(111) still yield some discrepancies. Especially the surface structure which gives rise to a (2×2) low energy electron diffraction pattern (LEED) is still under discussion [30–32]. Additionally, the various methods used to determine the coverage of thin Zn films like x-ray photo electron spectroscopy (XPS), CO titration experiments and standard quartz microbalance measurements led to different interpretations of the formed zinc layer [30–32]. This indicates that the preparation and characterization of Zn/Pd(111) surfaces is still not well understood.

9.1 Calibration of the Zn coverage

As already mentioned a variety of methods has been applied to calibrate the Zn coverage which is most probably the reason for non-conforming results concerning structure and growth of thin Zn layers in the literature [30–32]. In this section a calibration of the Zn coverage will be worked out and some basic aspects of different calibration methods will be discussed briefly.
The success of spectroscopic methods like XPS or Auger electron spectroscopy (AES) for determining the coverage crucially depends on the film morphology. For CO titration the film morphology is also important but additionally one has to be sure that no configuration exists which allows binding of CO to already Zn covered surface areas, at least in a certain temperature range. Therefore deposition rates and consequently the coverage are usually controlled by

a quartz microbalance. For a proper application of this method the sticking coefficient on the sample and on the microbalance has to be the same. In case of metal vapors which are deposited at not too high sample temperatures this condition is mostly fulfilled. It is generally assumed that metal vapors stick everywhere with a probability of unity. This general statement does not hold for Zn which is vapor-deposited onto contaminated surfaces at room temperature and that consequently one has to be extremely careful by using a quartz microbalance for coverage calibration.

9.1.1 Results and Discussion

The experiments were carried out by using the Zn evaporation unit as described in chapter 3. For the initial measurements a quartz micro balance was used to determine the deposited amount of Zn. Surprisingly, the Zn coverage obtained by the quartz frequency change was typically underestimated by a factor of 10-100, as determined by comparison with TDS and Auger measurements. A wrong positioning or a malfunction of the microbalance could be ruled out. This was checked by replacing the Zn source by an electron beam vanadium evaporator where the microbalance showed a normal performance. The QMS signals of the Zn isotopes with masses 64, 66 and 68, which can be detected in the isotropic gas phase, can also be used as a measure of the Zn evaporation rate. However, one has to be extremely careful in this case. The fact, that a Zn signal can be measured at all in the isotropic gas phase already shows that the sticking coefficient for Zn on the sample holder or on the chamber walls is not unity. As outlined in detail below even small amounts of impurities on the palladium sample already lead to a significant decrease of the sticking coefficient for Zn at room temperature. Nevertheless, the QMS signal can be used as a measure for the Zn flux as long as the experimental conditions in the surrounding of the sample are kept constant. This observation already explains the bad reproducibility of the microbalance measurements. It is just the reduced sticking coefficient of Zn on contaminated surfaces such as on the ill defined quartz crystal surface right after installation. To proof this assumption a Zn thermal desorption series was performend on a not cleaned Pd(111) crystal right after installation and bake out. The main contamination on this surface was sulphur which was determined by AES. By proper annealing and sputtering of the surface different sulphur concentrations could be established on the palladium surface. Evaluation of the Zn TD-spectra for Pd surfaces with different degrees of contamination clearly showed that the sticking coefficient is decreased on the contaminated surface, as depicted in figure (9.1), where TDS peak areas are plotted as a function of the Zn exposure as determined by the isotropic QMS Zn signal.

An additional feature which one can see in figure (9.1) is that with increasing Zn coverage the sticking coefficient increases again up to the value of the clean surface. The highest Zn coverage in figure (9.1) corresponds to about 25 monolayers. Here one monolayer of Zn is again referenced to the atomic density of the Pd(111) plane ($1.53 \cdot 10^{15}$ atoms$\cdot$cm^{-2}). Apparently, with increasing Zn coverage the sulphur is more and more buried and a clean Zn surface layer develops. From these findings one can safely assume that on a clean Pd(111) surface the sticking coefficient of Zn is unity at room temperature. On the other hand, an interesting observation

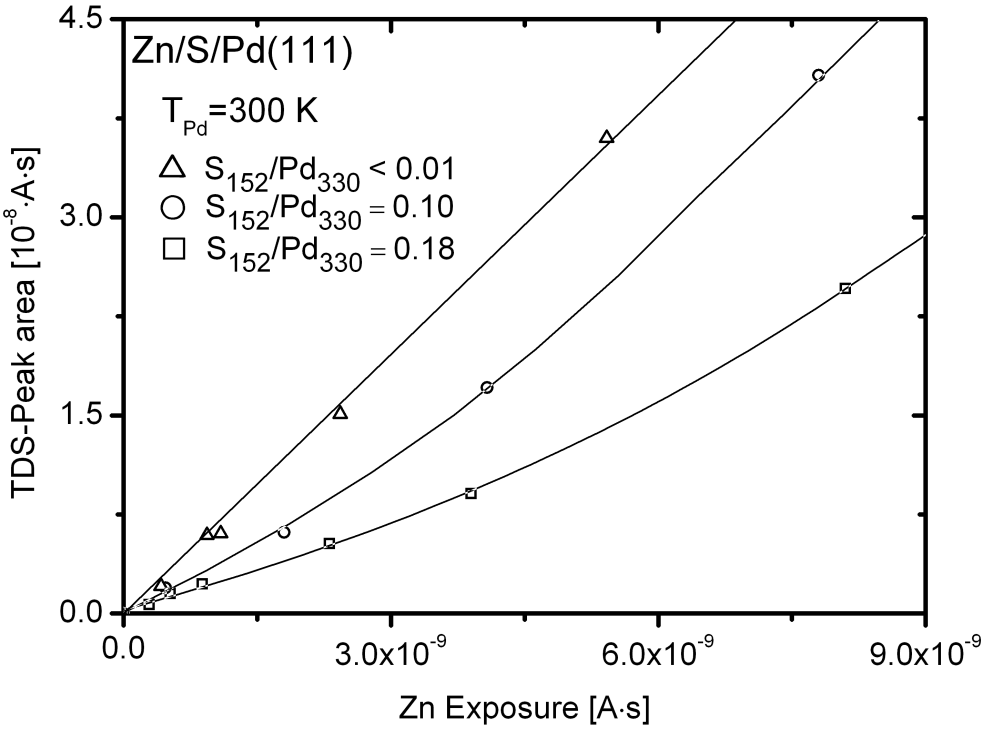

Figure 9.1: Integrated Zn TDS signals versus Zn exposure. The open triangles (△) represent the Zn uptake for the clean sample. The open circles (∘) and squares (□) show the Zn uptake at different sulphur surface concentrations. The surface temperature was 300 K.

can be made for small Zn coverages on the sulphur covered palladium surface. In figure (9.2) (curve a) the Auger spectrum of a partially sulphur covered Pd(111) surface is depicted. After the adsorption of about 4 monolayers of Zn, as shown in figure (9.2) (curve b), the sulphur peak can still be observed with almost the same intensity, even though the palladium signal has decreased considerably. In order to rule out possible contaminations by the Zn source a similar Zn amount has been evaporated onto a clean surface (figure (9.2), curve c). In this case nearly no S signal is detectable. This leads to the conclusion that sulphur tends to wet the surface acting as a surfactant. This is of course a frequently occurring feature but not yet described for the present system. Only after deposition of higher Zn amounts the sulphur is finally buried and the sticking coefficient for Zn reaches unity again. Coming back to the possible use of the quartz microbalance as a thickness monitor, one has to guarantee that the quartz is covered with a clean Zn film which adsorbs further Zn with a sticking probability of unity to give the correct evaporation rates.

Based on the latter findings the mass 64 signal in the mass spectrum can be used for the determination of the deposition rate under the proper experimental conditions. In particular one has to ensure that the effective pumping speed, which is basically determined by the adsorption properties of surfaces in the surrounding of the sample, remains constant. The long term stability, however, turned out to be poor due to the reasons described above. Hence for determination of the Zn exposure the mass 64 signal had to be measured before and after

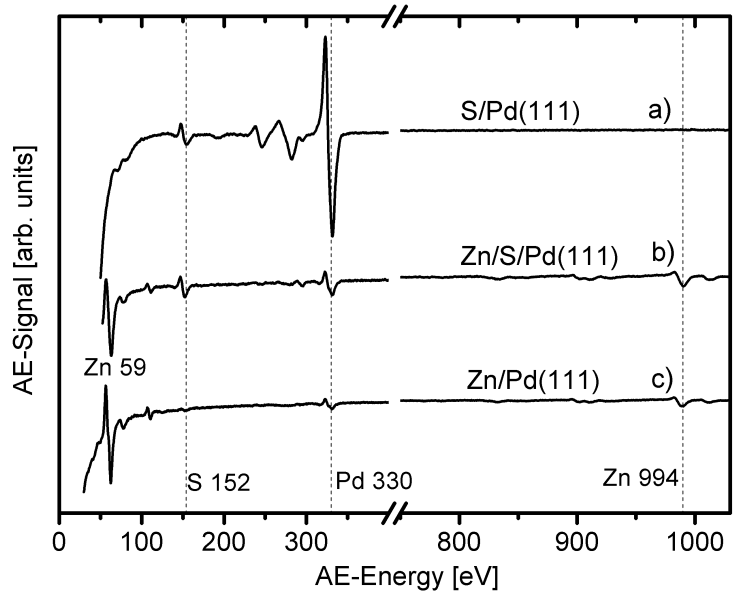

Figure 9.2: Comparison of the Auger electron spectra of a partially sulphur contaminated Pd surface (spectrum a), the S contaminated surface after Zn exposure (spectrum b) and a clean Pd surface after Zn exposure (spectrum c). The surface temperature was 300 K and the Zn coverage was approximately 4 ML

deposition when the sample was turned away from the source. It should be emphasized here that due to possible fluctuations of the QMS sensitivity, which often occurs, a direct comparison of two data sets is problematic if the time lag between the two measuremens is large (> week).

Additionally, a cross check of the measured frequency shift of the microbalance, which was covered with a clean, thick Zn film, by means of AES measurements and CO titration experiments was performed. For the experimental settings (different distance between source and sample/quartz (see also 3.5) ($d_1 \approx 103.5$ mm/ $d_2 \approx 135$ mm, integral mass sensitivity of the microbalance S=$2.3 \cdot 10^{-6}$ s·cm^2·g^{-1}, mass change per quartz crystal unit area for a Zn monolayer = $1.66 \cdot 10^{-7}$ g·cm^{-2}) a frequency change of 23 Hz on the microbalance corresponds to one monolayer of Zn on the palladium crystal. For the AES measurements increasing amounts of Zn (up to 60 Hz) were deposited on the Pd sample at 105 K, consecutively. For layer-by-layer growth, which is proposed by the literature for this system [30], both the substrate signal and the overlayer signals should exhibit a bend simultaneously when the monolayer is completed [164]. The Zn 994 eV and the Pd 330 eV Auger peaks were measured at 105 K, but no bending could be observed. Repetition of the experiment at 200 K and 300 K yielded the same result. Therefore an attempt was made to determine the Zn coverage directly from the Auger intensity ratios. In figure (9.3) the obtained ratios of the Zn 994 eV and the Pd 330 eV peak heights are plotted versus the frequency change of the microbalance. The applied AES based calibration method is explained in detail in section 4.5 and resulted in an Auger Zn 994 eV to Pd 330 eV peak-to-peak ration of about 3.8% for a monolayer which was reached for a micro balance

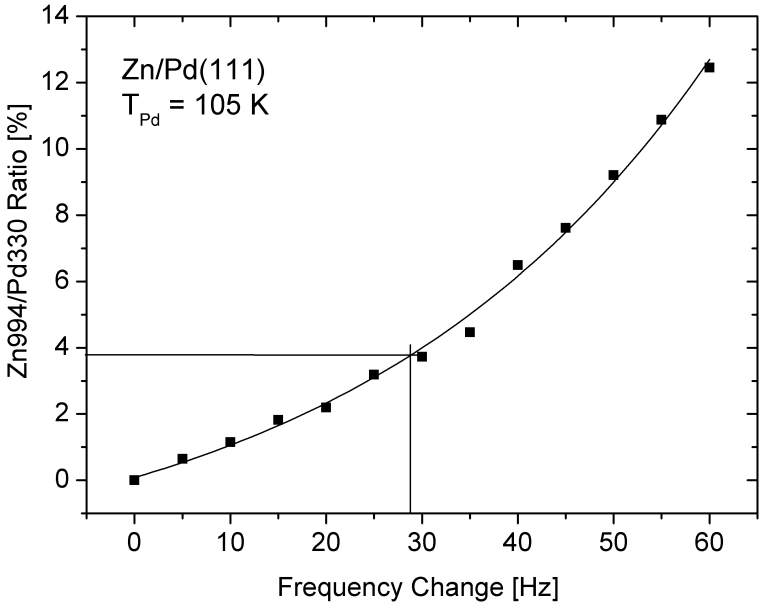

Figure 9.3: Evolution of the Zn994/Pd330 AES intensity ratio during Zn deposition on Pd(111) at 105 K. The intensity ratio for a Zn coverage of 1 ML was calculated to be 3.8%

frequency shift of 28 Hz. The difference of about 20% between the two methods can be attributed to deviations from a pure layer-by-layer growth mode. Obviously, the first layer is not totally completed when the second starts to grow. This can also explain the non-appearence of the simultaneous bend in the substrate and overlayer AES signal. Therefore the AES method rather leads to an underestimation of the Zn layer thickness.
For the CO titration experiments increasing amounts of Zn were deposited at 300 K and the sample was exposed to CO ($1{\cdot}10^{-7}$ mbar $\cdot$ 5 min) at 160 K subsequently. Then thermal desorption spectra were recorded. By integrating the mass 28 signal in the TD-spectra one obtains a measure for the residual (Zn free) CO adsorption sites on the surface [30; 31; 165]. The integrated CO TD peak areas as a function of the microbalance frequency change are shown in figure 9.4. The residual amount of CO on the surface shows a pronounced linear decrease with increasing Zn coverage. At 23 Hz the slope of the linear decrease of the integrated CO signal suddenly drops to a much smaller value. Actually, one would expect that the residual CO coverage vanishes when a Zn monolayer is reached. Unfortunately, during Zn deposition adsorption of small amounts of CO coming from the Knudsen source cannot be excluded. In addition to that the Zn layer could be partially incomplete and a contribution of some CO desorbing from the sample rim or adjacent surfaces can also be responsible for the residual CO. Nevertheless, the clear bend at 23 Hz is again a strong indication of the formation of a closed Zn layer which is in perfect agreement with the value calculated for the microbalance. The latter findings could then be used to calibrate the Zn TD spectra. A sample was prepared by evaporating 3.1 ML (72 Hz) of Zn at a sample temperature of 350 K. Consecutively the sample

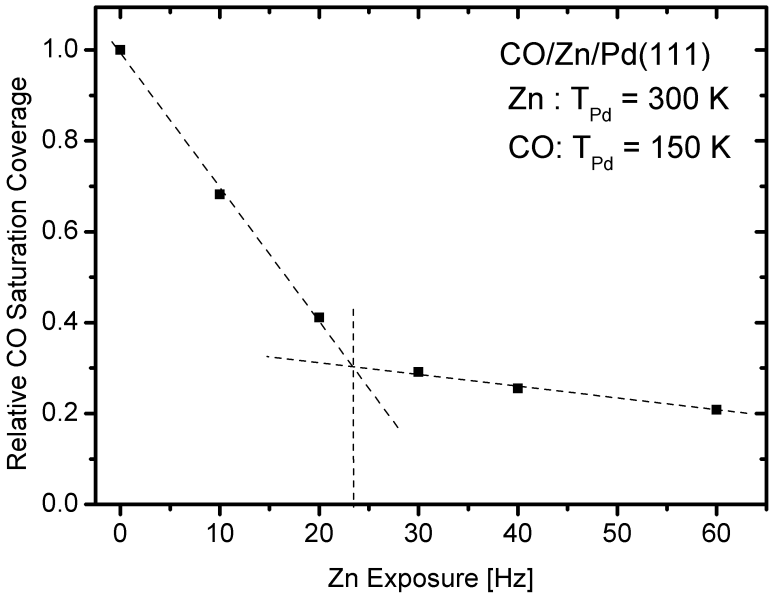

Figure 9.4: Amount of adsorbed CO obtained from TDS integration versus Zn exposure. The values are normalized to the maximum CO coverage on the clean Pd(111) surface. Zn was deposited at 300 K and CO exposure was done at 150 K sample temperature.

was cooled down to 150 K and the Zn was then flashed off by heating the sample up to 1160 K at a heating rate of 2 K/s. The resulting TD spectrum is shown in figure (9.5). One can clearly see two distinct desorption features, one occurring between 400 K and 580 K and a second one occurring above 780 K. Due to the large temperature gap between the two desorption phenomena the in-line detection of the signal might result in a distorted spectrum. One has to keep in mind that the desorption temperature has an influence on the velocity distribution of the desorbing particles. Particles at high velocity are less likely detected as particles at lower velocities ($I_{QMS} \propto v^{-1/2}$) due to the fact that a QMS is a density detector (for details see section 4.1.1). This results in TD spectra where the signal height in the low temperature region is exaggerated compared to the high temperature region. Therefore, two TD spectra of identically prepared samples (4.3 ML of Zn (100 Hz) evaporated at 170 K) were measured with different modes. One spectrum was obtained from the "normal" in-line signal and the second was measured in a mode where the in-line signal was blocked by a shutter right in front of the ionisation volume of the mass spectrometer. As can be seen in figure (9.6) both spectra are almost identical. Just at temperatures above 1000 K a very slight deviation is noticeable. Nevertheless, the deviation is small compared to the signal noise which means that no velocity correction is necessary in this case [93]. This observation can again be attributed to the low sticking probability of Zn on the contaminated chamber walls. The desorbing Zn atoms which are not detected inline are scattered at the surrounding surfaces and generate a high isotropic signal.

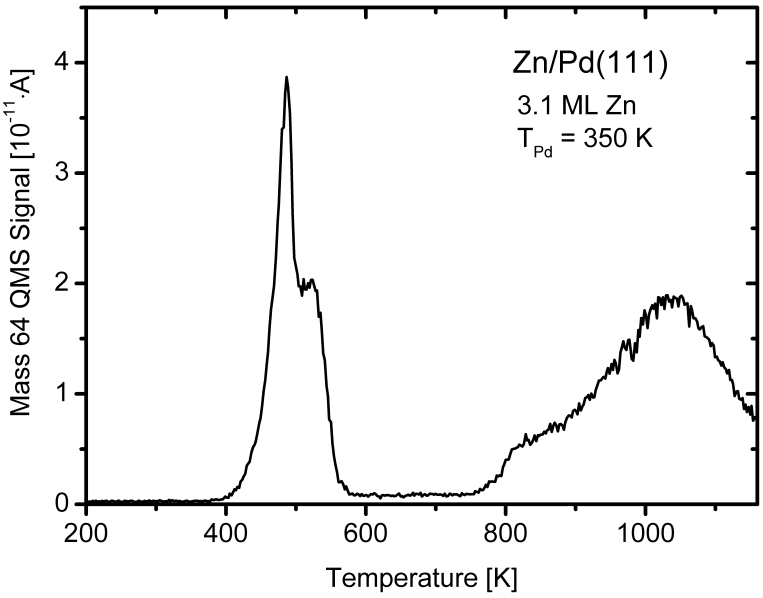

Figure 9.5: Zn TD spectrum obtained after a Zn exposure of 72 Hz at a sample temperature of 350 K. Heating rate 2 K/s.

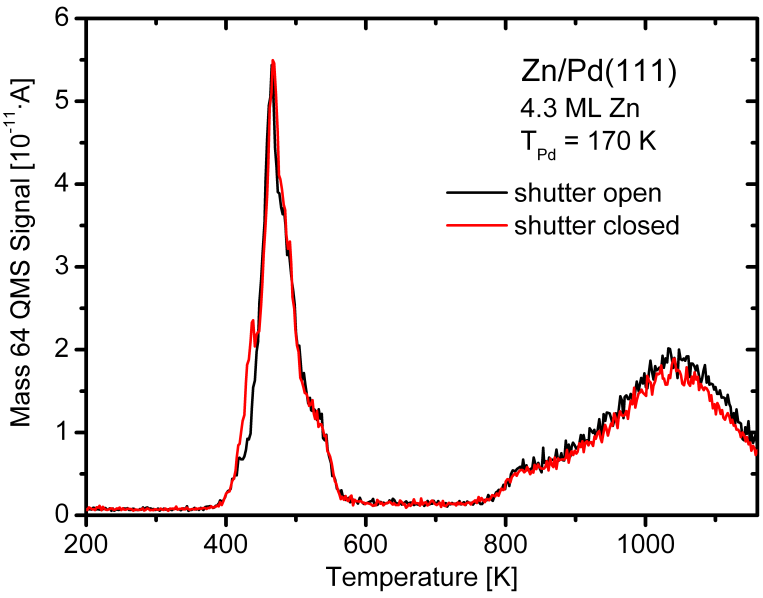

Figure 9.6: Comparison of thermal desorption spectra from identically prepared Zn/Pd(111) samples obtained by direct inline measurement (shutter open) and by measuring the isotropic signa (shutter closed).

9.2 Kinetics of Zn adsorption and desorption on Pd(111)

Even though the system ZnPd has shown interesting catalytic properties concerning methanol processing only a little experimental work is done on the examination of structural and physical properties [30–32; 165]. One way to get insight in the growth and alloying processes is to study the adsorption and desorption kinetics of Zn on palladium. Therefore a number of thermal desorption experiments as well as LEED and AES studies were performed. The results are presented and discussed in the following sections.

9.2.1 Results and Discussion

Increasing amounts of Zn were deposited on the clean Pd(111) surface at sample temperatures of 150 K and 300 K. The obtained TD spectra for Zn deposited onto the palladium sample at 300 K are depicted in figure (9.7(a)) and those at 150 K in figure (9.7(b)).

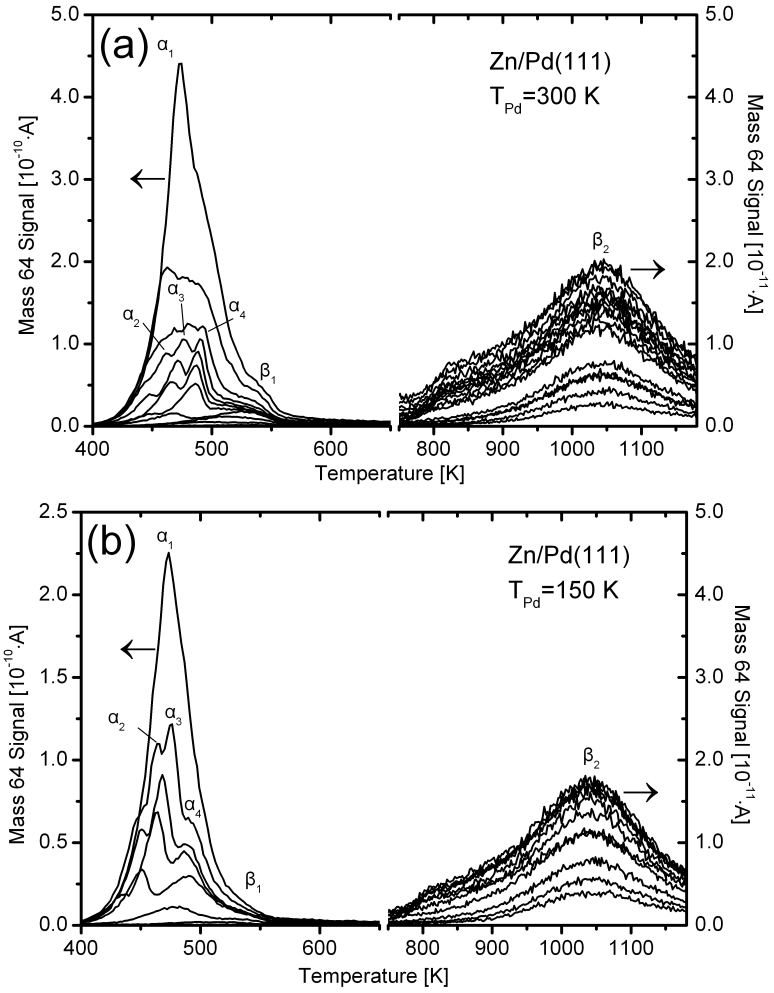

Figure 9.7: Zn TDS series obtained for sample temperatures of 300 K (a) and 150 K (b)

One can easily distinguish a low temperature desorption feature between 400 and 600 K and

a single high temperature desorption peak (labelled β_2) centred at 1040 K (note the different scale for the high temperature peak). The low temperature desorption feature resolves into a complicated multiple peak desorption pattern with increasing coverage, which is also dependent on the substrate temperature during evaporation. It is remarkable that there is not just simple multilayer desorption. As one can easily see in figure 9.7, there are several zero order like desorption states ($\alpha_1 - \alpha_4$) which are individually characterised by common leading edges, and an additional first order like state (β_1), evidenced by a nearly coverage independent desorption peak maximum. For the analysis of these peaks a least squares multiple peak fit procedure was applied, which allowed the determination of the coverage and the desorption energies of the individual adsorption states [166]. For that reason the data were fitted by summing up the desorption rates obtained by simulating the Polanyi-Wigner equation for different initial coverages, pre-exponential factors and desorption energies for the individual desorption states. Within the error both series of TD spectra, Zn deposited at 150 K and 300 K sample temperature, yield the same desorption energies. In particular, for the "true" multilayer peak (α_1) the desorption energy can be determined with high accuracy because its leading edge is not overlapped by other peaks and the "leading edge" or "Arrhenius plot" method (see section 4.2) for zero order desorption is applicable. This evaluation yields a value for the multilayer desorption energy of 119±5 kJ/mol, which is in good agreement with the literature value for the Zn heat of evaporation of 115 kJ/mol. Since the TD spectra have been quantitatively calibrated, the intercept of the straight line in the Arrhenius plot with the Y-axis yields also the pre-exponential factor of $1.15 \cdot 10^{28}$ atoms$\cdot$s$^{-1}\cdot$cm^{-2}. With the surface density of $1.62 \cdot 10^{15}$ atoms cm^{-2} for a zinc (0001) layer this yields a frequency factor of $7 \cdot 10^{12}$ s^{-1}. The best fits for the desorption energies of the $\alpha_2 - \beta_4$ states as obtained from figure 9.7 yield 122±5 kJ/mol (α_2), 124±5 kJ/mol (α_3), 128±5 kJ/mol (α_4) and 137±5 kJ/mol (β_1). The amount of Zn bound in the individual adsorption states was evaluated for the TD series prepared at 300 K (9.7(a)) which provided a rather well defined situation. The saturation coverages of the individual adsorption states $\alpha_2 - \alpha_4$ could be evaluated to be 1 ML within a deviation of 20%. The amount of Zn contained in β_2 was determined to be 0.6 ML with great uncertainty (50%). One has to keep in mind that a fitting procedure involving multiple parameters (coverage, pre-exponential factor, desorption energy, desorption order) is not unambiguous. Nevertheless, the large number of desorption spectra allowed a rather reasonable data evaluation.

A further point to discuss is the desorption order of the individual states. The peak α_1 shows classical zero order kinetics as characteristic for multilayer desorption. More difficult to understand is the shape of the α_2, α_3 and α_4 peaks. All these peaks show a kinetic behaviour similar to zero order desorption. Typically, zero order desorption is just possible if the desorption rate is independent of the coverage. Thus a quasi infinite reservoir of particles is necessary. This requirement is closely fulfilled for a true multilayer, but definitely not for the peaks α_2-α_4, which are constricted to 1 monolayer each. A possible explanation for close to zero order desorption kinetics is the existence of two phases in an adsorbed layer. A dilute phase from which particles desorb directly and a dense phase which compensates the particle loss of the dilute phase by decomposition and transfer of material [62; 64; 65]. Another possibility is fractional order

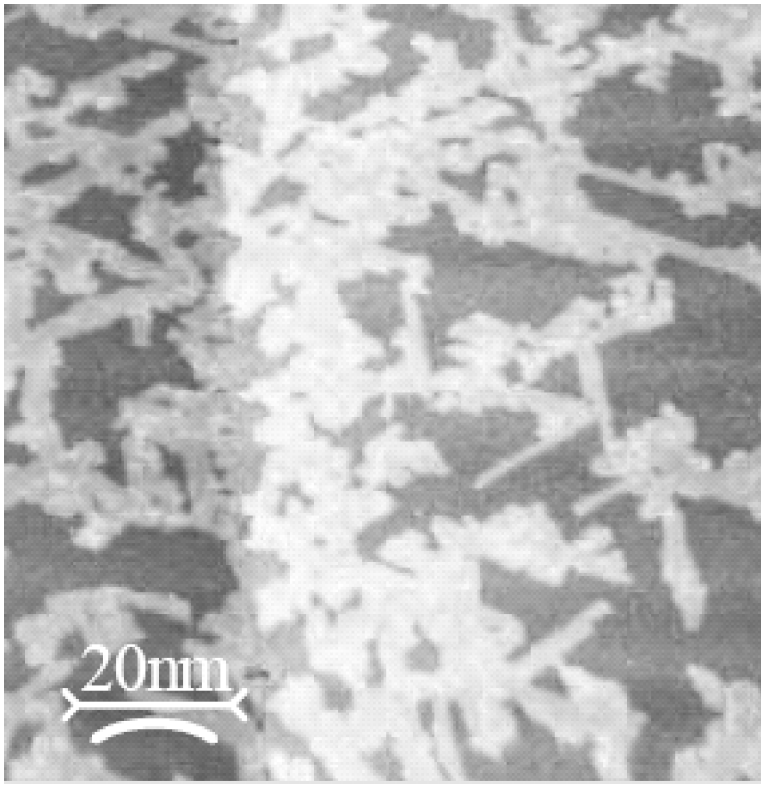

Figure 9.8: STM image of the morphology of the 0.5 ML ZnPd surface. 1000×1000 Å^2, +1V, 1nA (with the friendly permission of DI Gunther Weirum).

desorption. In this case the desorption order can lie between 0 and 1. Fractional desorption kinetics occurs when desorption primarily takes place at the perimeter of islands or clusters [167; 168] . Therefore the coverage dependence is given by the shape, size and number of the islands/clusters. The best multiple Polanyi-Wigner fits to the desorption spectra of figure 9.7 were obtained with a desorption order of 1/2 for $\alpha_2 - \alpha_4$.

Indeed, STM measurements of ZnPd surfaces prepared at 300 K showed that not a strict layer-by-layer growth mode exists (figure (9.8)). The first layer develops by growing 2-dimensional islands which then unify to bigger closed areas, but on these closed areas the second layer starts to grow before the layer beneath is completed. In the STM image one can also see dendritic structures consisting of more or less rectangular shaped sections which seemed to be aligned with specific substrate directions (building up domains which are tilted to each other by 120°). Additionally, one can see in the TDS that successive peaks arise before the foregoing peaks totally saturate, which is in accord with the STM images (figure (9.8)). Comparing the TD spectra obtained from the 300 K and the 150 K sample one finds some interesting differences. First, the β_1 peak which shows a close to first order desorption kinetics is only pronounced at the higher adsorption temperature (300K). This peak stems from desorption of the last Zn layer above the ZnPd interface. For this first order desorption peak which is centred at 520 K a desorption energy of 137±5 kJ/mol was calculate by using the Redhead approximation [89] and assuming a pre-exponential factor of $1{\cdot}10^{13}$ s^{-1}. At 150 K the β_1 peak is hardly detectable.

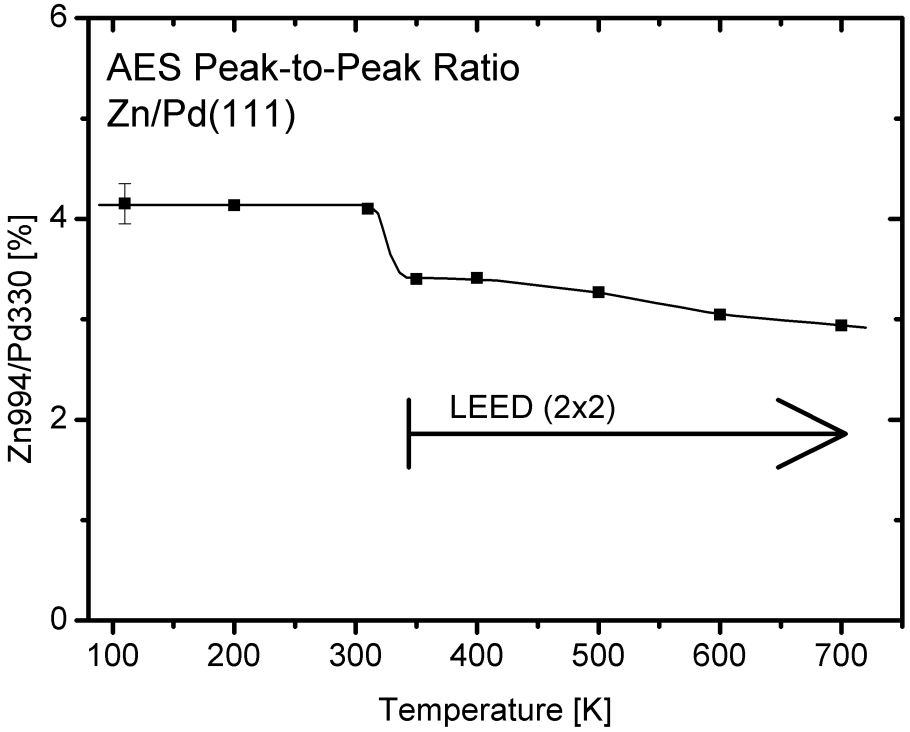

Figure 9.9: Auger intensity ratios of the Zn 994 eV and the Pd 330 eV Auger line plotted versus substrate temperature. The deposited amount of Zn was 30 Hz=1.3 ML for all preparation temperatures.

It just contains 10% of a ML whereas β_1 corresponds to about 0.6 ML at the 300 K sample. The origin of the different development of the TDS at different adsorption temperatures is not quite clear. A further discussion about this issue will be continued later.
The influence of the substrate temperature on the diffusion which finally leads to the formation of a ZnPd alloy can be seen by AES and LEED. In figure (9.9) the Auger intensity ratios of the Zn 994 eV peak and the Pd 330 eV peak for about 1.3 ML Zn deposited on Pd(111) at various substrate temperatures ranging from 105 K to 700 K is shown. Below 300 K no influence of the substrate temperature is detectable, but between 300 K and 350 K the intensity ratio drops from 4.1% to about 3.4% indicating an exchange of Zn and Pd atoms in the topmost layers. Additionally, a (2×2) LEED pattern occurs at around 350 K which can be attributed to the formation of an ordered ZnPd surface alloy. This finding is in good agreement with the results found by XPS measurements [30].

STM measurements at high resolution as shown in figure (9.10) reveal that the (2×2) LEED pattern actually stems from different domains of a (2×1) structure. This (2×1) structure was also predicted by theory [169] but has still been under discussion in the literature due to the lack of a direct evidence [30; 31; 163]. Above 400 K the Zn/Pd intensity ratio shows a further slight decrease indicating further diffusion of Zn into the subsurface region. DFT calculations for different numbers of Zn layers on a Pd/Zn interface yield values for the binding energies of the individual layers which are in rather good agreement with the experimentally obtained desorption energies but reproduce the trend that the desorption energy increases from α_1 to

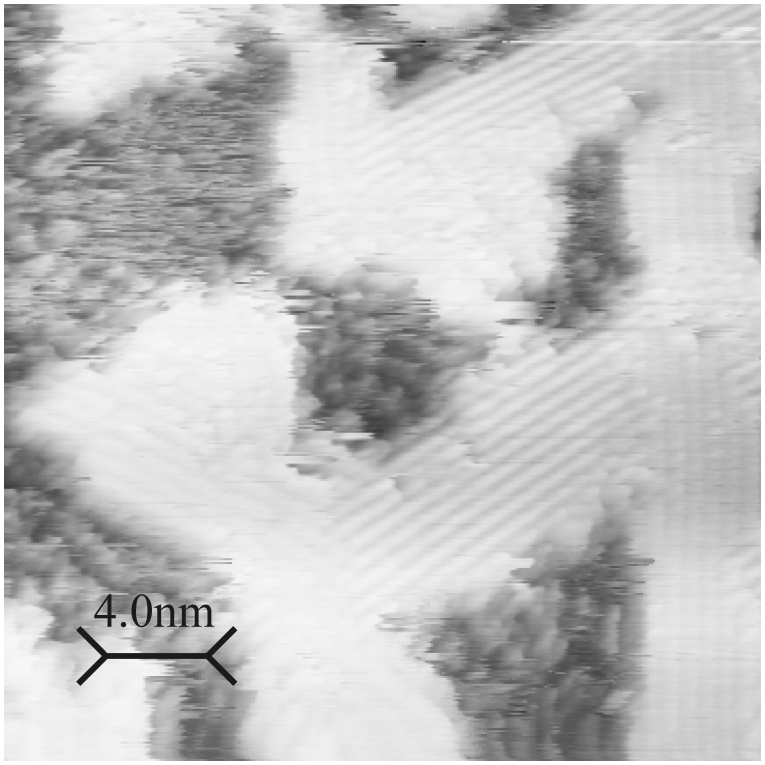

Figure 9.10: STM image of an approx. 0.5 ML Zn covered Pd(111) surface prepared at 300 K. 200×200 Å^2, +0.14 V, 2 nA (with the friendly permission of DI Gunther Weirum).

β_1. The theoretical and experimental results are compiled in table (9.1).

As shown in figure (9.7) after desorption of the multilayer states between 400 K and 600 K desorption starts again above 750 K. This high temperature peak β_2 is centred at 1040 K and shows first order desorption characteristics indicated by a coverage independent desorption peak maximum. According to the Redhead approximation the desorption energy was calculated to be 281±5 kJ/mol, assuming a pre-exponential factor of $1{\cdot}10^{13}$ s^{-1}. With increasing Zn coverage a shoulder arises around 800 K when the first order peak β_1 at 520 K appears. The large temperature gap between the high and low temperature desorption features can be attributed to the high binding energy of Zn to Pd at the interface compared to the smaller energy of Zn-Zn bonds. One would be apt to define the saturation of the β_2 peak as one monolayer. However, in the present case the situation is not that simple. As already pointed out in section 9.1 it turned out that according to the quartz microbalance the coverage of the β_2 peak corresponds to a coverage of about 2 ML right before the β_1 peak arises. A further increase of the β_2 peak takes place with increasing Zn coverage. This increase is partially, but not exclusively, caused by a rise of the Zn background level during desorption of larger amounts of Zn. The Zn uptake curves created by plotting the integrated TD spectra versus the Zn exposure, for T = 150 K and T = 300 K, respectively, are shown in figure (9.11). For both sample temperatures the Zn uptake curve of the total amount just shows a linear increase with Zn exposure. This means a constant sticking coefficient over the whole coverage range. This again shows that the assumption of a Zn sticking coefficient of unity on both substrates Pd and Zn is justified, at

Table 9.1: Zn desorption energies for different adsorption states
Desorption energies, deduced from TDS, are oppossed to the theoretical values for the most stable adsorption sites. Adsorption sites: hcp...hexagonal close packed; fcc...face centred cubic close packed; hcp^{2Pd}...hcp; fcc^{2Pd}...fcc

TDS peak	experimental (kJ/mol)	theoretical (kJ/mol)	adsorption site	Zn coverage (ML)
α_1	119	114	hcp	3.0
α_2	120	115	hcp	2.0
α_3	123			
α_4	127	141	hcp,fcc	1.0
β_1	137	147(135)	hcp^{2Pd},fcc^{2Pd}	0.5(0.25)

least up to room temperature.

The maximum coverage of 2 monolayers for the β_2 state can not be considerd to be the saturation coverage because it rather depends on the preparation conditions. To confirm this statement a set of experiments was carried out by preparing a Zn/Pd surface with constant Zn exposure ($\approx$ 4 ML) at different sample temperatures, ranging from 165 K to 750 K. The obtained TD spectra are compiled in figure (9.12). Obviously, increasing substrate temperatures during Zn deposition lead to an increased Zn amount contained in the β_2 state. Additionally, one can see the clear change in the low temperature desorption feature due to the different substrate temperatures as already discussed. In figure (9.13) the integrated TD peak signals are plotted versus the preparation temperature. From that one can clearly see a variation of the total adsorbed amount of Zn with sample temperature. The Zn uptake kept nearly constant up to 400 K and decreased beyond this temperature due to the simultaneous desorption of the multilayer. Interestingly, the total Zn uptake increased again at sample temperatures above 500 K, which is due to the increase of the high temperature peak. This behaviour is apparently a consequence of different surface Zn concentrations at different sample temperatures. Since at temperatures above 500 K obviously Zn does not stick to Zn (multilayer desorption) the sticking coefficient is mainly determined by Pd adsorption sites. Above 550 K due to increased Zn diffusion into the bulk more Pd sites are available and more Zn can be adsorbed.

In the following the desorption behaviour of the high temperature peak will be discussed in more detail. From the fact that β_2 contains about 2 monolayers, a simple first order desorption kinetics can be excluded. Based on the observed (2x2) LEED pattern and the reported literature it is suggested that the Zn on Pd exists in form of several layers of a 1:1 Zn/Pd alloy [30]. Therefore one has to assume that the desorption kinetics will be strongly influenced by bulk to surface diffusion. The Zn concentration profile, which influences the desorption peak shape, is determined by the preparation conditions. In addition to that, crucial diffusion processes will occur during the TDS experiment. Simultaneous desorption and diffusion of Zn and formation or decomposition of different ZnPd alloy phases can take place during the temperature raise.

There are further observations which indicate that the high temperature desorption is not

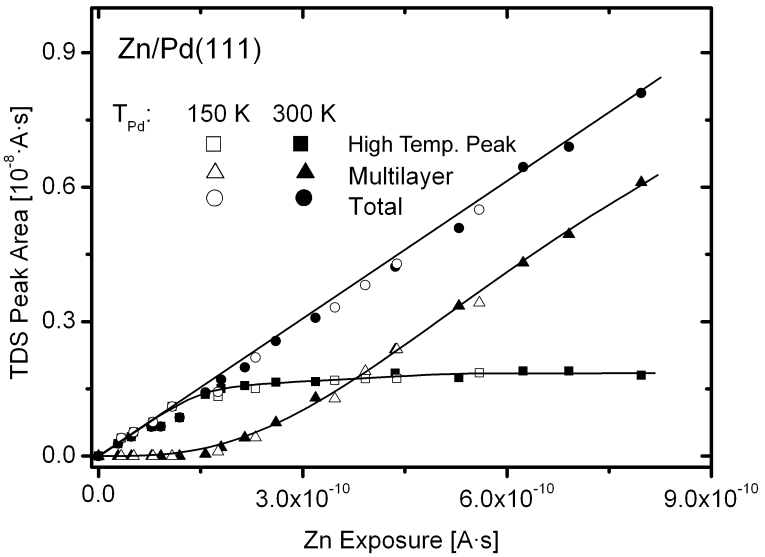

Figure 9.11: Zn uptake on clean Pd(111) at 150 K (open symbols) and 300 K (full symbols).

governed by simple first order desorption kinetics. Ignoring the low temperature shoulder the desorption peak β_2 is rather symmetric relative to its maximum, which should not be the case for a simple first order desorption. Also, the full width at half maximum (FWHM) of more than 200 K is far too big compared to typical first order desorption peak shapes. Lateral repulsive interaction of the adsorbates would lead to a broadening but would additionally result in an asymmetric peak shape and cause a shift of the peak maxima towards lower temperatures with increasing coverage. Nevertheless, a change of the binding energy with the variation of the Zn coverage is likely just due to the fact that ZnPd alloys of different composition exhibit different energetic stability. DFT calculations show that the 1:1 ZnPd alloy is energetically the most favourable one [169; 170].

The whole Zn desorption spectra can be rationalized by consideration of diffusion processes. As initial configuration several MLs of Zn shall be deposited onto the Pd(111) surface at low temperature (150 K). When the sample temperature is raised diffusion processes are getting important and between 300 K and 350 K the (2×1) surface alloy starts to form at the Zn/Pd interface. Due to the large Zn concentration gradient at the interface and the energetically more favourable ZnPd configuration Zn diffuses deeper into near surface regions of the substrate already at this temperature [30; 170]. The Zn concentration gradient decreases throughout the progress of diffusion and therefore the migration decelerates, especially in the deeper layers. Additionally, the regions with a 1:1 Zn to Pd ratio, which is energetically the most stable [169; 170] configuration, might act as a diffusion barrier because any change in concentration costs energy. While this subsurface diffusion is going on above 400 K the Zn multi-layers start to desorb, where the β_1 state corresponds to Zn atoms desorbing from top of the alloyed ZnPd surface. After this the Zn reservoir on the sample surface has depleted and the Zn concentration gradient at the interface is now inverted. With further temperature increase the decomposition of the ZnPd surface alloy starts, leading again to Zn desorption above 800 K. Due to the emerging concentration gradient diffusion of Zn from the subsurface region to the

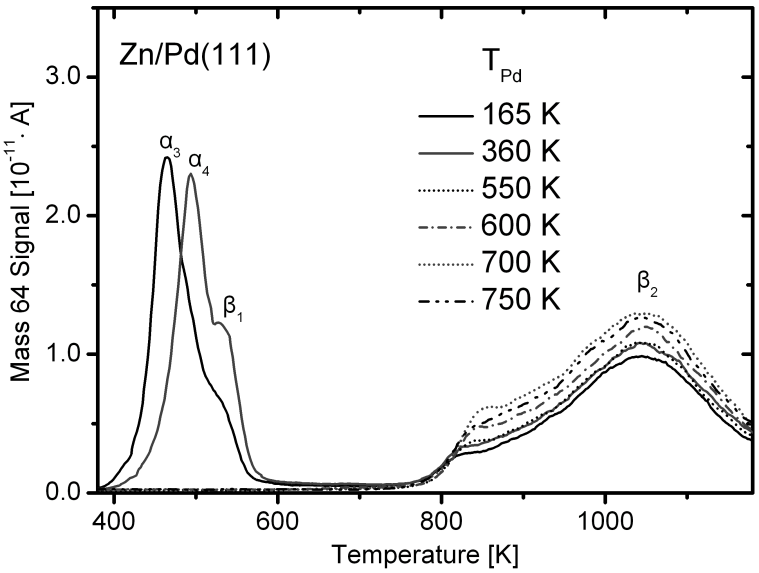

Figure 9.12: Zn TD spectra for 4 ML Zn deposited on Pd(111) at different sample temperatures.

surface becomes more likely than into the bulk and continues as long as Zn exists in the surface near region. Thus, the desorption kinetics of the high temperature peak is mainly limited by the Zn diffusion from the surface near region to the surface, at least for the second half of the spectrum.

A further point to discuss is the quite clearly defined shoulder of the high temperature peak around 750 K, which is only pronounced when the Zn coverage was initially high. This feature might originate from Zn atoms which were driven into the subsurface region in excess of the 1:1 ZnPd composition. These Zn atoms are less stable and diffuse easily to the surface from where they desorb immediately, because the situation is now comparable to that for the β_1 state, namely desorption of Zn atoms from the ZnPd surface alloy. A similar, but even more pronounced peak in the same temperature region has been described by Gabasch et al. [31] when they evaporated large amounts of Zn onto the palladium surface at 750 K. Additionally, they observed a significant increase of the β_2 state with increasing Zn exposures at this temperature.

Finally a comment on the β_1 shall be given here. According to the AES measurements (figure (9.9)) a noticeable interchange of material between the adsorbed Zn layer and the Pd substrate starts at room temperature. Preparing a Zn layer at room temperature might already lead to Zn which has gone sub surface during the deposition. Contrary to this no Zn subsurface diffusion occurs when the sample is prepared at lower temperatures. This means that the initial configuration when the TDS is started is not quite the same. Simultaneously to the multilayer desorption diffusion of Zn from the adlayers into the Pd bulk takes place. The β_1 peak stems from the residual Zn which is adsorbed on the ZnPd surface. Therefore β_1 can be considered as a kind of left over from the competing processes desorption and bulk diffusion. Is the Pd surface region already enriched in Zn, as it is the case for preperation at 300 K, more Zn is left for for β_1. For a Zn poor substrate, as it is present for cold preparation, the diffusion from

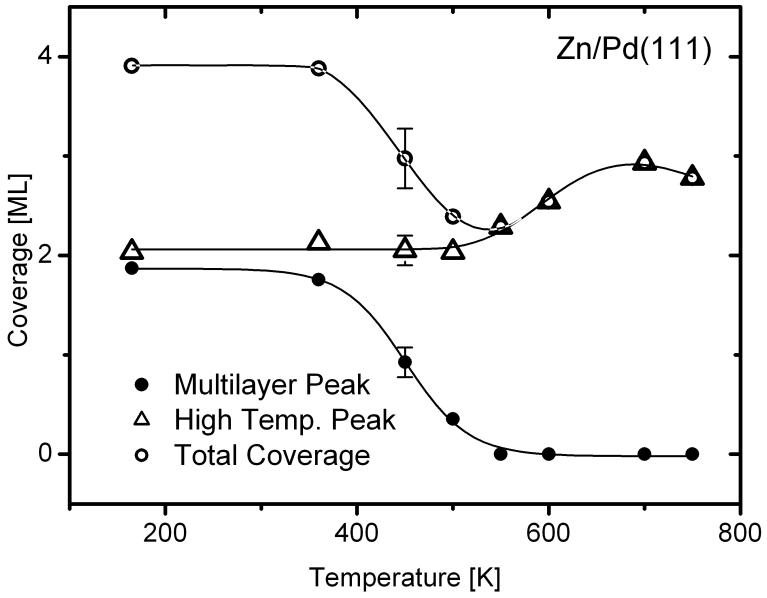

Figure 9.13: Zn uptake of Pd(111) for different sample temperatures. Total Zn coverage (○); Multilayer (●); High Temperature peak β_2 (△)

the interface layer into the bulk is more pronounced and therefore less Zn is left over in the β_1 state.

9.3 Summary of chapter 9

9.3.1 Zn coverage calibration

It was demonstrated that the assumption that metal atoms stick everywhere with a probability of unity at room temperature is not generally valid. Comparing the Zn uptake of a clean Pd(111) sample with those of a sulphur contaminated palladium surface yielded that on the sulphur covered surface the Zn sticking probability is reduced compared to the clean palladium. Sulphur turned out to segregate onto the surface and prevent Zn from sticking. Although sulphur shows this segregation tendency, it can totally be covered by greater amounts of Zn which results in an increase of the total sticking probability up to the value of the clean palladium surface, which is unity. This finding has severe consequences on the sample preparation and especially on the quantification of the deposited Zn amount. The "normal" metal film on a quartz micro balance can be considered as dirty which results in a sticking coefficient for Zn which is neither unity nor constant. Therefore a quartz microbalance is not a reliable instrument for the determination of the Zn deposition rate until the quartz surface is covered by a thick Zn layer (quartz exposed to over 1000 ML) that covers all the impurities. Due to the rather small sticking coefficient of Zn on the contaminated chamber walls one can also find considerable amounts of Zn vapour in the residual gas. Therefore, during evaporation, the Zn signal in a quadrupole mass spectrometer in off-line position can alternatively be used for the deposition rate control. Additionally, classical CO titration experiments and AES measurements were performed on the Zn covered

Pd(111) surface for comparison. The CO titration experiments showed perfect agreement with the properly prepared microbalance. The evaluation of the Auger intensity ratios of the Zn 994 eV signal and the Pd 330 eV signal yield a Zn994/Pd330 ratio of 3.8% for 1 ML Zn, which corresponds to a coverage which is about 20% higher than obtained by the other calibration methods. This difference is probably due to a deviation from a perfect layer-by-layer growth as assumed for Zn on Pd(111). Additionally, a number of parameter values were taken from the literature which might not have reassembled the actual situation well. Application of the microbalance calibration on the Zn TD spectra shows that the single high temperature peak β_2 corresponds to 2±0.2 ML.

9.3.2 Zn Adsorption/Desoption Kinetics on Pd(111)

Using TDS, AES, LEED and DFT the adsorption/desorption behaviour of Zn on Pd(111) has been studied from submonolayer coverages up to the multilayer regime (16 ML). The Zn TD spectra exhibit a low temperature desorption feature between 400 K and 600 K and a high temperature peak starting at 780 K (heating rate 2K/s). The low temperature feature can be devided into a multilayer peak α_1, 3 fractional desorption order peaks ($\alpha_2 - \alpha_4$) and a first order peak β_1. The corresponding desorption energies are listet in table (9.1).
The high temperature peak β_2 is centred at 1040 K (heating rate 2K/s) and already contains about 2ML of Zn when the multilayer peaks start to develop. Additionally, it turned out that the form of the TD spectra, especially the Zn amounts contained in β_1 and β_2 depend on the preparation temperature. This can be rationalized by considering diffusion processes from the Zn layer into the Pd bulk during the TD experiment. The β_2 peak just stems from the decomposition of a ZnPd alloy which has formed in the surface near region of the palladium substrate due to Zn diffusion. In figures (9.14(a)) to (9.14(g)) a visualization of the processes concerning desorption, diffusion/alloying and Zn uptake is shown.

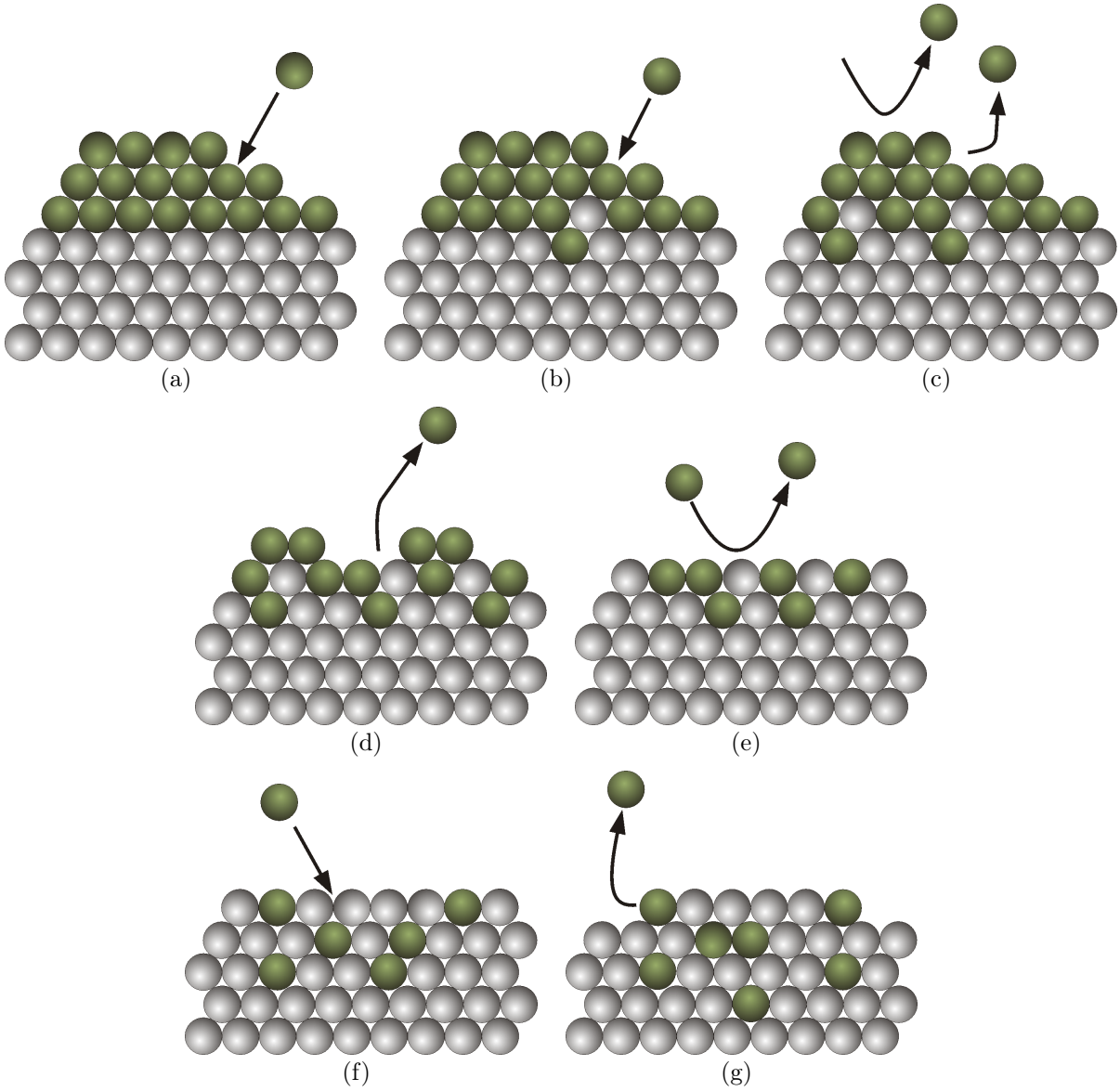

Figure 9.14: Evolution of the Zn/Pd(111) system with temperature. The diffusion as well as the Zn uptake behaviour is indicated. **a)** $\mathbf{T}_{Pd} < \mathbf{300\ K}$ **:** Zn sticks to Pd as well as to Zn, multilayer formation is possible, no Zn diffusion into the Pd substrate. **b)** $\mathbf{300\ K} < \mathbf{T}_{Pd} < \mathbf{400\ K}$ **:** Zn adsorption is still possible, pronounced diffusion processes take place in the interface region (2D-alloy formation). **c)** $\mathbf{400\ K} < \mathbf{T}_{Pd} < \mathbf{500\ K}$ **:** Zn multilayer desorption ($\alpha_1 - \alpha_4$), no sticking of Zn on Zn at this temperatures, ZnPd alloy formation goes on simultaneously. **d)** $\mathbf{500\ K} < \mathbf{T}_{Pd} < \mathbf{550\ K}$ **:** desorption of the residual Zn adsorbed on the ZnPd-alloy surface (β_1), no Zn adsorption possible on ZnPd surface at this temperature. **e)** $\mathbf{550\ K} < \mathbf{T}_{Pd} < \mathbf{750\ K}$ **:** Zn bulk diffusion leads to depletion of Zn at the surface, Zn can stick to bare Pd which is now available. **f)** $\mathbf{750} < \mathbf{T}_{Pd}$ **:** ZnPd alloy decomposes and resurfacing Zn desorbs (β_2), no Zn adsorption possible on Pd.

10 H_2 and CO on Zn modified Pd(111)

As already stated in chapter 9 the reforming of methanol is one of the most promising approaches in the field of hydrogen storage and fuel cell design [21; 28; 29]. In methanol (MeOH) steam reforming the reactants MeOH (CH_3OH) and steam (H_2O) interact with the surface of a metal-based catalyst which yields hydrogen (H_2) and carbon dioxide (CO_2). The most commonly used and studied catalysts are based on Cu/Zn or Cu/ZnO [161; 162; 171–173]. These Cu based catalysts suffer from rapid deactivation due to sintering of the metal grains at temepartures above 573 K [130]. Here catalysts based on Pd/Zn [14–16; 20; 24; 25; 27] and Pd/ZnO [17–19; 21–23; 26] come into play because of their higher thermal stability. The studies have mainly been carried out on real catalyst systems like powders or fine-particle granulate. Detailed studies dealing with the systematic investigation of gases with well defined single crystal surfaces are rare [31; 32]. The kinetics of adsorbed Zn on the Pd(111) has been discussed in chapter 9. Therefore the focus of the following chapter is set on influence of adsorbed Zn on the adsorption and desorption processes of H_2 and CO on Pd(111).

10.1 H_2 on Zn/Pd(111)

H_2 on clean Pd(111)

The adsorption of hydrogen on Pd(111) has already been studied in the past [54; 174–178]. Hydrogen adsorbs dissociatively on Pd(111) and can be absorbed by the bulk easily. For the sake of comparison with the Zn/Pd system a series of H_2 TD spectra is shown in figure (10.1). The spectra were taken after exposing the Pd(111) sample to hydrogen at 150 K. The H_2 was dosed directly onto the sample surface by a stainless steel tube. The applied heating rate was 2 K/s. As can be seen from figure (10.1) (curves a and b) low hydrogen exposures lead only to a saturation of the chemisorbed surface layer without any penetration of the subsurface region. The adsorbed hydrogen atoms form a (1×1) structure corresponding to a saturation coverage of 1 ML [176; 177]. The surface layer desorbs as single, second-order desorption peak which is denoted as β-peak. The β-peak maximum is located at 305 K. With increasing exposure a second desorption peak, denoted as α, arises with a peak maximum at 200 K. Gdowski et al. [175] assigned this desorption feature to hydrogen which is absorbed in a subsurface state. Furthermore they reported that hydrogen bulk penetration can occure readily between 90 K and 200 K substrate temperature. Consistently with this observation one can see from figure (10.1) (curves c-h) that the α-peak grows with increasing hydrogen exposure not showing any saturation. This in fact indicates that adsorbed hydrogen diffuses into the palladium bulk. The

slight enhancement of β with the appearence of α might just be due to an overlap with the increasing α-peak.

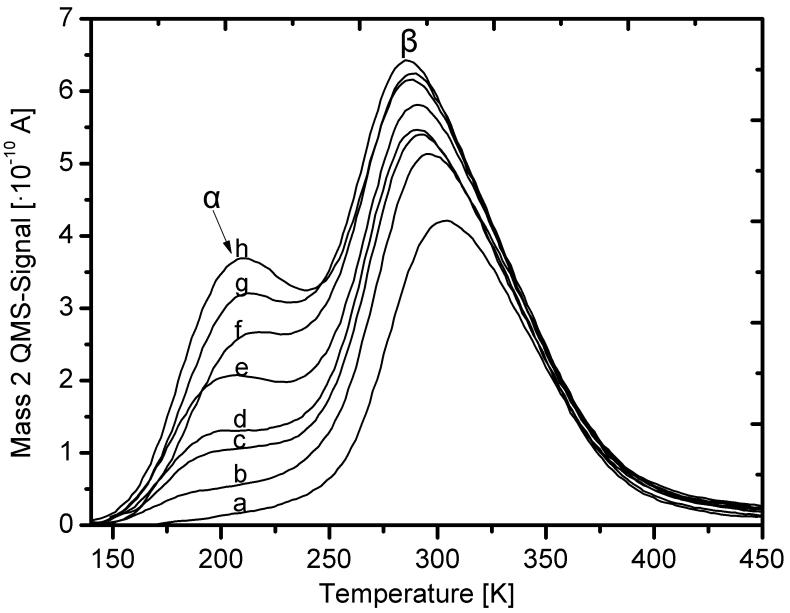

Figure 10.1: TD spectra of H_2/Pd(111) subsequent to dosing hydrogen at 150 K. Exposures are: (a) 2, (b) 22, (c) 76, (d) 108, (e) 216, (f) 346, (g) 690, (h) 1036 L.

H_2 on Zn/Pd(111)

Thick Zn layers ($\approx$ 10 ML) prepared at 150 K are sufficient to inhibit the hydrogen adsorption on Pd(111). Removing the upper Zn layers by heating the sample up to 600 K yields the formation of an ordered ZnPd surface which exhibits a (2×1) structure as already described in chapter 9. In figure (10.2) a series of TD spectra subsequent to hydrogen dosing onto the latter specified surface is shown. Both, the surface peak β and the subsurface peak α still exist and appear at the same desorption temperatures as on the clean Pd(111) surface (see figure (10.1)). It is outstanding that the β-peak is much smaller compared to clean palladium but the α-peak seems almost uninfluenced. This indicates that the Zn atoms at the surface do not provide changes in the energy but only in the number of hydrogen adsorption sites. A comparison between the H_2 desorption peak areas of the clean and Zn modified palladium sample yield that the amount of adsorbed hydrogen on the ZnPd surface alloy is 55% smaller than on clean Pd(111). This seems to be a quite plausible finding, because the ZnPd surface exposes only half the number of palladium atoms than the clean Pd(111) surface. Therefore only one half of the adsorption sites are available on the surface whereas bulk diffusion is still possible and hence the α-peak can still grow with increasing exposure.

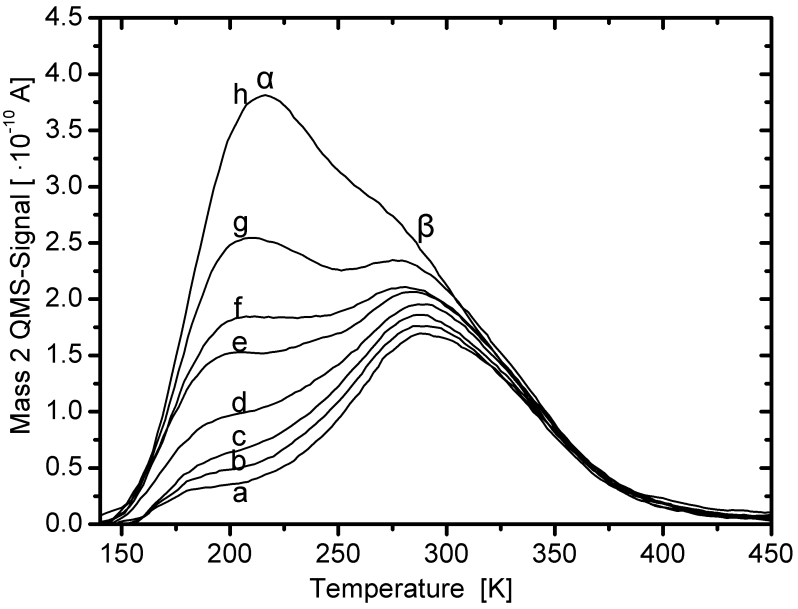

Figure 10.2: TD spectra of H_2/Zn/Pd(111) subsequent to hydrogen dosing at 150 K sample temperature. Exposures are: (a) 4,(b) 14, (c) 22, (d) 70, (e) 170, (f) 216, (g) 432, (h) 1728 L.

From the TD series shown in figures (10.1) and (10.2) one can generate hydrogen uptake curves by relating the peak areas to the corresponding coverage and plotting them versus the exposure. In this case the coverage was calibrated via the saturation of the β-peak for the clean Pd(111) sample. In figure (10.3) the corresponding uptake curves for the clean and the Zn modified surface are depicted.

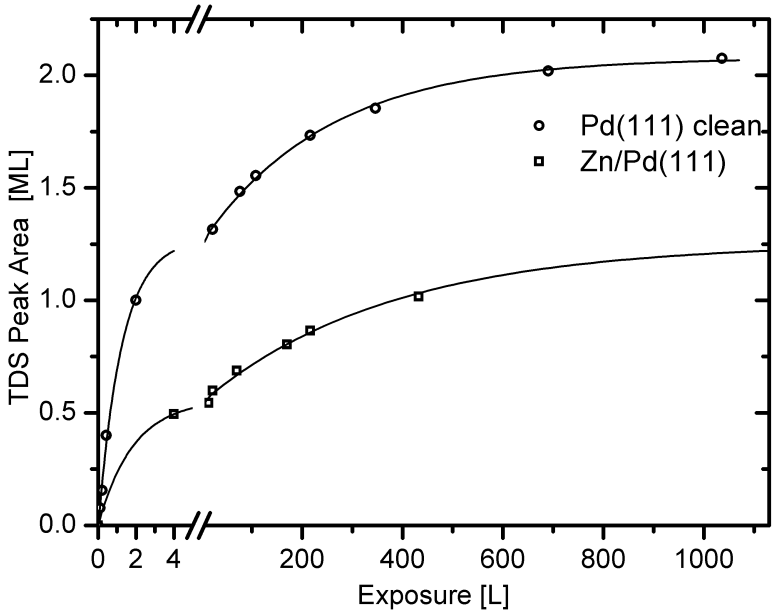

Figure 10.3: Hydrogen TDS peak areas from clean Pd(111) and the ZnPd surface alloy plotted versus the exposure.

The hydrogen sticking coefficient can be deduced from the slope of the uptake curve. Thus the initial sticking coefficient (initial slope of the uptake curve) of the clean Pd(111) sample was determined to be 0.5±0.1 which is in good agreement with the literature data [54; 174]. The corresponding value for the ZnPd surface is about 4 times smaller (0.14±0.05) than on clean Pd(111). Since each impinging H_2 molecule needs two vacant Pd sites for dissociative adsorption (second order process) this is a quite intuitive result, because every second Pd atom on the surface was replaced by Zn. At high exposures both curves in figure (10.3) exhibit the same slope since the adsorbed Zn amount is determined by hydrogen diffusion into the subsurface region.

10.2 CO on Zn/Pd(111)

CO on clean Pd(111)

The system CO/Pd(111) was also intensively studied in the past as a model system for CO adsorption [5; 153; 179–182]. As reported by Guo and Yates [183], CO has a desorption energy of 148.6 kJ mol^{-1} and a preexponential factor of $10^{15.3}{\cdot}s^{-1}$ for small coverages. At low temperatures CO saturates at a coverage of 0.75 ML and forms a p(2×2)-3CO structure. STM measurements revealed that the unit cell of this structure is built of one CO molecule sitting on a Pd top-site and two molecules, which are bound to fcc and hcp threefold hollow sites, respectively. The interaction of CO with the clean Pd(111) was initially characterized by TDS and LEED to provide data for comparison with the ZnPd surface. In figure (10.4) a CO TDS

from Pd(111) subsequent to an CO exposure of 8.5 L at 150 K sample temperature is shown (solid line). It exhibits a peak centred at 440 K and a broad desorption band extending down to about 200 K.

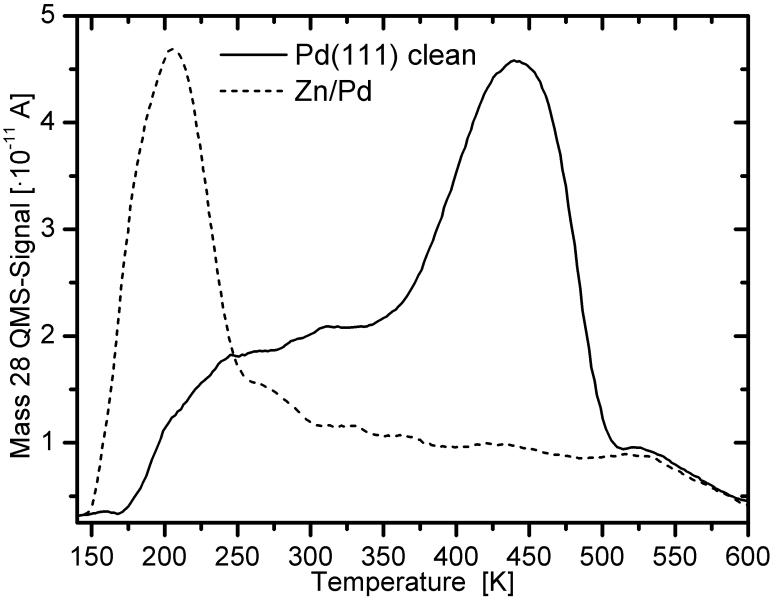

Figure 10.4: TD spectra of CO/Pd(111) and CO/Zn/Pd(111). CO exposure: 8.5 L; adsorption temperature: 150 K.

CO on Zn/Pd(111)

One monolayer of Zn deposited at 373 K is sufficient to block any adsorption of CO at room temperature [31]. However, when decreasing the adsorption temperature to 150 K, a new CO desorption feature starts to evolve around 220 K. In figure (10.4) this new desorption peak is indicated by the dashed line (Zn layer prepared at 350 K). The same observation can be made when the ZnPd surface is prepared by evaporation of Zn at 150 K and subsequent annealing to 600 K, which gives rise to a well ordered surface alloy [30]. A series of CO TD spectra was measured on the ZnPd surface in order to gain additional information about the low temperature CO adsorption state. The corresponding spectra are depicted in figure (10.5).

Obviously there are still Pd atoms available on the surface but the presence of the Zn atoms decreases the CO adsorption energy. The CO uptake curves for clean Pd(111) and the Zn/Pd(111) surface are compiled in figure (10.6).

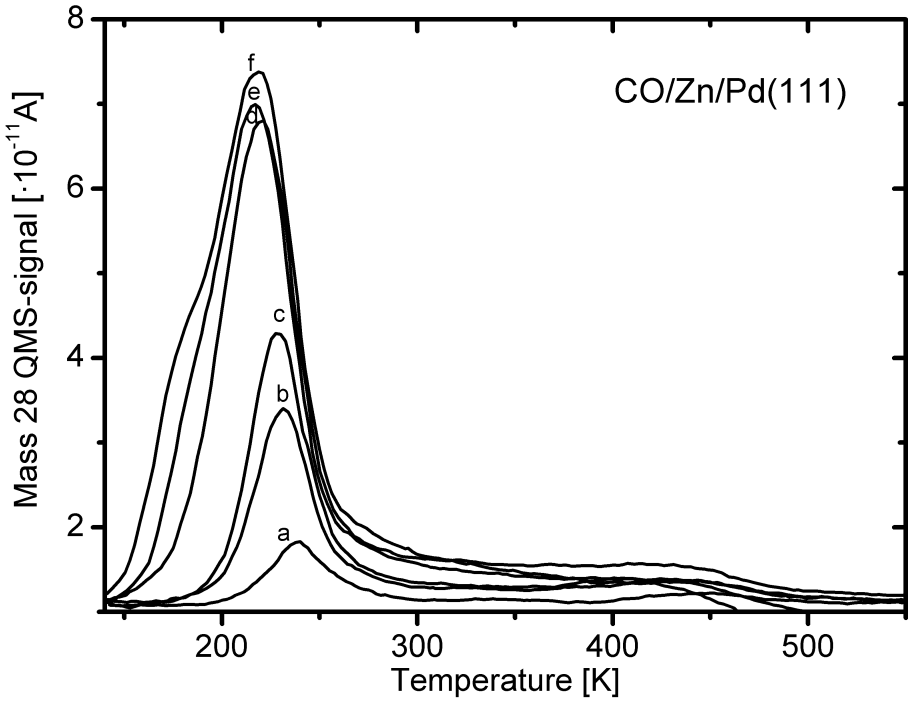

Figure 10.5: TD spectra of the ZnPd-alloy surface subsequent to CO exposure at 150 K. Exposures are: (a) 0.2, (b) 0.4, (c) 0.9, (d) 1.4, (e) 2.9, (f) 14.7 L.

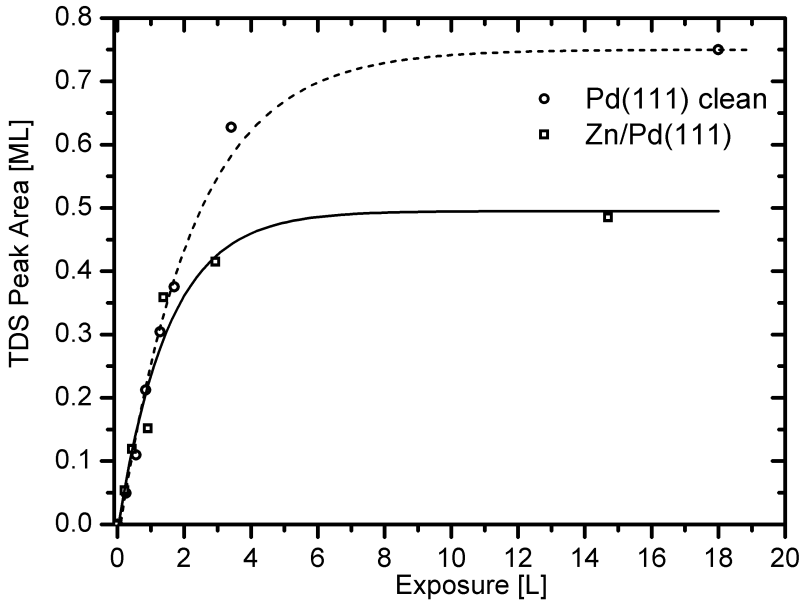

Figure 10.6: CO TDS peak areas plotted versus exposure for clean Pd(111) (dashed curve) and the ZnPd surface alloy (solid curve).

The corresponding peak areas are given in monolayers, where the CO saturation coverage

(0.75ML) on clean Pd(111) was used for calibration. For small exposures the CO coverage increases linarly with exposure for both surfaces. For the ZnPd surface the CO uptake levels off at an exposure of 2 L and saturates then at a coverage of 0.5 ML. CO does not bind to Zn atoms at the applied adsorption temperature [165], which indicates that each available Pd atom on the ZnPd-alloy surface is occupied by a CO molecule. This seems to be quite counter intuitive for two reasons. Firstly, the CO adsorption energy is dramatically lowered by the Zn and secondly the CO molecules have to sit on neighbouring Pd adsorption sites, which is not the case on clean Pd(111). However, due to the alignment in alternating Zn and Pd rows each CO molecules adsobed on a Pd site can only have two neares neighbours and it could be shown that CO may be encircled by three nearest neighbours on similar surfaces [184]. Additionally, high resolution electron energy loss spectroscopy (HREELS) measurements indicate that CO preferably sticks on the Pd atop sites on the ZnPd alloy surface.
The initial sticking coefficient on this surface was deduced form figure (10.6) to be 0.93±0.07. For the clean Pd(111) surface sticking coefficient was determined to be 0.96±0.10, which is in good agreement with the literature [174; 180]. Since just half of the adsorption sites on the ZnPd surface are available compared to clean Pd(111) this suggests a precursor mediated adsorption process. Indeed, according to literature data the CO adsorption on clean Pd(111) is influenced by an extrinsic precursor [174]. Thus, CO adsorption on the ZnPd-alloy surface might be explained by a model where molecules that approach the surface on a Zn site are first adsorbed in a mobile prcursor state before they reach their final adsorption site.
Based on the assumption that CO desorption from the ZnPd surface is a first order process the desorption energy can be estimated by the Redhead formula (4.9) [89]. According to [153] the prexponential factor was taken to be ν=10^{15} s^{-1}. The obtained desorption energies are plotted versus the CO coverage in figure (10.7).

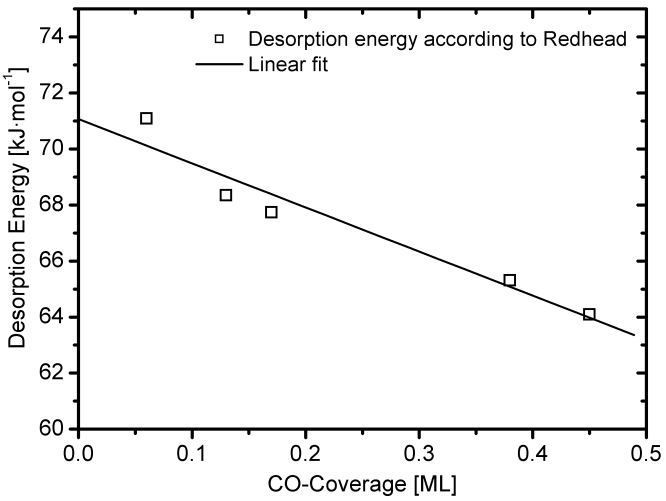

Figure 10.7: Coverage dependence of the CO desorption energy on the ZnPd-alloy surface.

In the zero coverage limit the desorption energy E_{des} equals 71±2 kJ·mol^{-1}. With increasing

coverage E_{des} decreases linearly indicating a repulsive interaction of the CO molecules. The coverage dependence of the desorption energy can be described by $E_{des}(\theta) = E^0_{des} - \omega \cdot \theta$, where θ is the coverage and ω characterizes the repulsive interaction. For the system under consideration the repulsive interaction can be approximated by ω=14±2 kJ·mol^{-1}. Additionally, the obtained desorption energies of CO on ZnPd are close to the values of CO on copper (54 kJ·mol^{-1} for CO on Cu(110)[185] and 47kJ ·mol^{-1} for CO on Cu(111) [186]), which fits well to the calculated similarity of the palladium density of states (DOS) in the ZnPd alloy to those of copper [169]. The effects of different Zn loadings as well as the influence of different preparation temperatures on the CO adsorption on Zn/Pd(111) were investigated in further experiments. Figure (10.8) shows a series of TD spectra subsequent to an CO exposure of 34 L at 150 K. The Zn layers were prepared by Zn deposition at 150 K. The effect of increasing Zn coverages can be seen in figure (10.8).

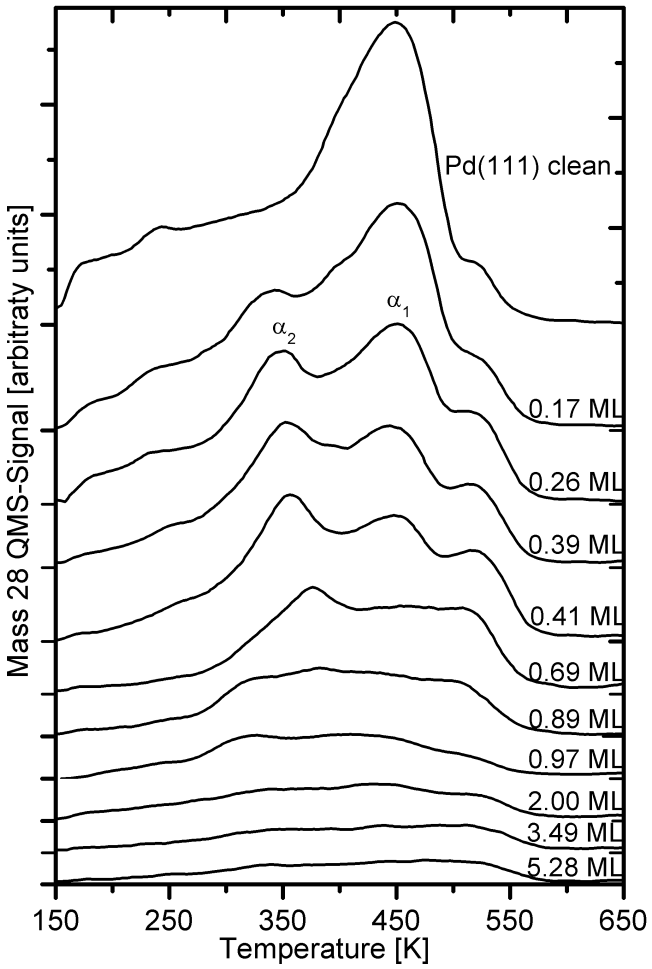

Figure 10.8: CO TD spectra from Zn/Pd surfaces subsequent to a CO exposure of 34 L. The individual Zn layers were prepared at 150 K. The corresponding Zn coverages are given in the figure.

The CO desorption maximum at 440 K (α_1), which is well known from the clean Pd(111) remains at its position but decrases in size with increasing Zn coverage. Already for small Zn coverages a second peak (α_2) arises at around 350 K but decreases again at higher Zn coverages ($\approx$ 0.5 ML). At about 1 ML Zn coverage the amount of adsorbed CO becomes very small. Above 1 ML there is hardly any change in the TD spectra visible. Interestingly, there is a shoulder around 510 K visible in the CO desorption spectrum even on the clean Pd surface. This shoulder keeps unchanged independent of Zn coverage. A CO desorption feature at 510 K was also observed on Pd(112) and was attributed to CO molecules bound to bridge sites at step edges of the Pd(112) surface [187]. Therefore it is reasonable to assume that the shoulder in the CO TD spectra also stems from molecules adsorbed at step edges.
The analogous experiment was carried out with a sample which was prepared at 350 K. At this temperature a ZnPd surface alloy is formed. The obtained TD spectra are depicted in figure (10.9).

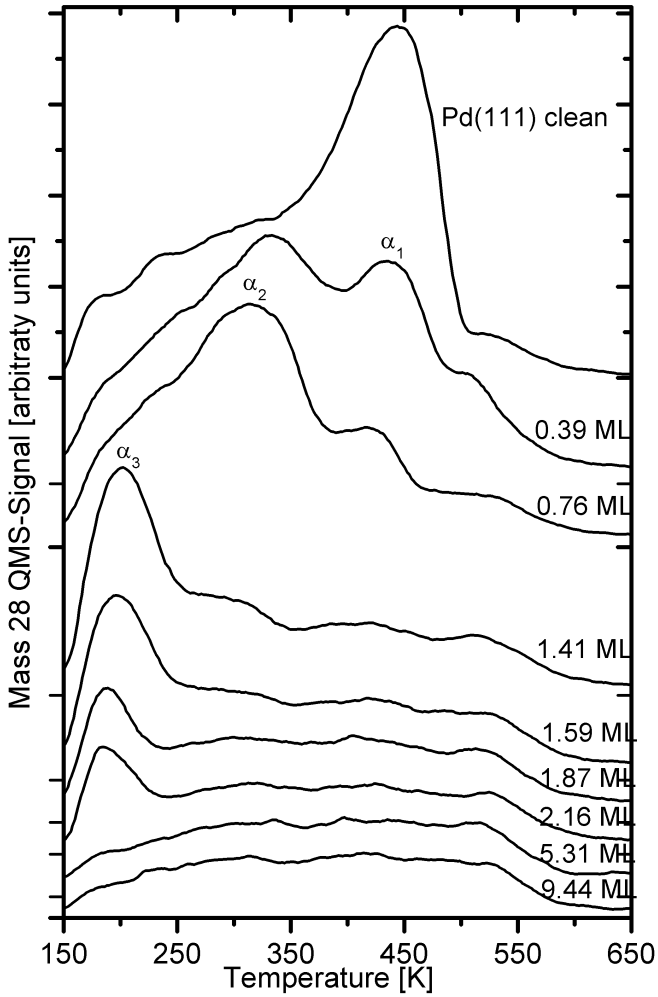

Figure 10.9: CO TD spectra from Zn/Pd surfaces subsequent to a CO exposure of 34 L. The individual Zn layers were prepared at 350 K. The corresponding Zn coverages are given in the figure.

Again a suppression of the α_1 peak is observable as well as the evolution of the α_2 peak. At higher Zn coverages a third peak (α_3) develops at around 220 K. Whereas α_1 and α_2 vanish at Zn coverages above 1 ML the α_3 state remains and shows a slight shift towards lower temperatures with increasing Zn coverages. At a Zn coverages of about 2 ML the α_3-peak also starts to disappear. It is remarkable that even at high Zn coverages there is still significant CO adsorption possible which was not the case for the surface prepared at 150 K.
In figure (10.10) the evolution of the adsorbed amount of CO with Zn coverage is compared for the two different preparation temperatures.

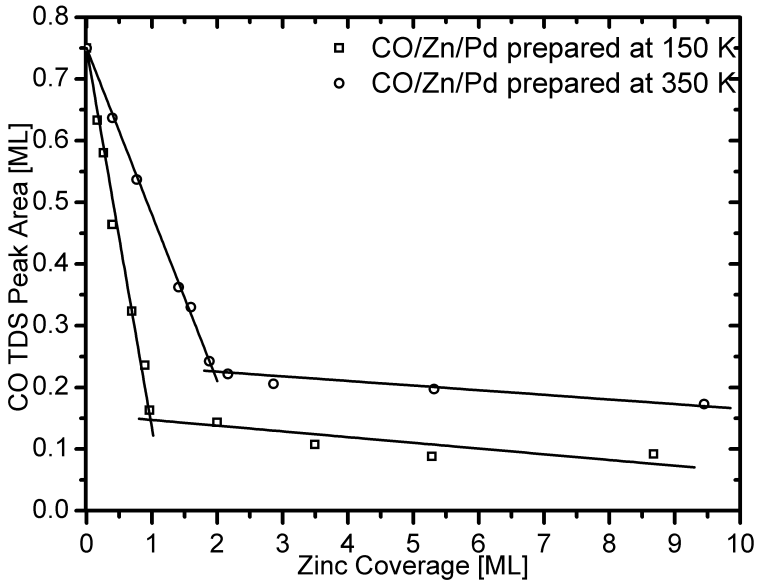

Figure 10.10: TDS peak area of CO adsorbed on Zn/Pd(111). The CO exposure always was 34 L. The Zn layer preparation was done at 150 K and 350 K, respectively.

The amount of adsorbed CO initially shows a strong linear decrease with Zn coverage. At a Zn coverage of about 1 ML the strong descent suddenly drops to a smaller linear decrease. According to Rodriguez CO does not stick to metallic Zn above 100 K and therefore the CO coverage should vanish at 1 ML Zn [165]. The observed residual CO might be caused by a mixing with the offline signal on the one hand and on the other hand by CO desorbing from Pd step edges as pointed out before. Nevertheless, the sharp bending in the evolution of the CO coverage at 1 ML indicates the formation of a closed Zn layer. The evolution of the adsorbed amount of CO on the sample prepared at 350 K shows a similar behaviour. In contrast to the cold prepared sample the slope of the initial linear decrease is somewhat smaller and the kink appears not until a Zn coverage of 2 ML is reached. Additionally, the residual amount of adsorbed CO is somewhat higher than for the sample prepared at 150 K.

Before going into a more detailed discussion of the TDS results it is appropriate to compare the present findings with the data in the corresponding literature. The investigations of Gabasch et al. [31] led to similar CO TD spectra on Zn/Pd sufaces for coverages up to 1 ML. In their work they prepared the Zn/Pd surfaces at a sample temperature of 373 K. Due to the fact that they adsorbed CO at room temperature they observed the α_1 and α_2 peaks but not the low temperature peak α_3. In addition a linear decrease of the CO uptake with increasing Zn coverage was reported which approached zero at a Zn coverage of 1 ML. These findings might be correct in case of CO adsorbed at room temperature, because the α_3 peak occurs far below room temperature. In the work of Jeroro et al. [32] CO TD spectra were measured on Zn/Pd surfaces annealed at 550 K. In order to saturate only the threefold hollow sites of the Pd(111) surface they just dosed 0.5 L CO at a sample temperature of 100 K. Thus, the CO exposure was too small to achieve a total saturation of all accessible adsorption sites. Therefore they measured just an CO uptake from 0.3 ML for clean Pd(111) down to zero on a 1 ML covered

Zn/Pd(111) surface.
The discussion about the CO uptake for the differently prepared samples shall be continued at this point. One might expect that the difference in the resulting CO uptake as a function of the Zn coverage is caused by temperature induced morphological changes of the Zn layers at 150 K and 350 K, respectively. Looking at the TD spectra in figures (10.8) and (10.9) one can find three different desorption peaks (α_1-α_3), which indicate three different adsorption states. The α_1-peak centred at 440K which corresponds to CO adsorbed on clean Pd(111) is already suppressed by the small Zn coverages in both cases. This desorption feature can be assigned to CO adsorbed on uninfluenced Pd sites outside of already formed Zn or ZnPd-alloy islands. In contrast to that the α_3 peak appears only on the sample prepared at 350 K and was already assigned to CO bound to palladium atoms within the ZnPd alloy phase. Since the alloying process might involve deeper layers of the substrate this peak remains even at higher Zn coverages and is responsible for the smoother descent in the number of adsorbed CO molecules. The third peak α_2 which occurs at intermediate desorption temperatures is again observed in both cases. Due to its desorption temperature and the fact that even at elevated temperatures no strict layer-by-layer growth could be observed (see chapter 9) α_2 might stem from CO bound to Pd atoms located next to Zn atoms as can be found at the edge of Zn and ZnPd islands, respectively. Moreover, the higher amount of CO adsorbed on thick Zn layers prepared at 350 K could be caused by additional adsorption sites provided by single Pd atoms that diffuse to the surface at this temperature [170].
These additional Pd sites may be probed as a function of temperature treatment by CO titration. The CO desorption data reveals that the ZnPd alloy which is formed at 350 K does not change up to 600 K. In figure (10.11) the change in the CO TD spectra after annealing the ZnPd surface alloy at different temperatures is shown.

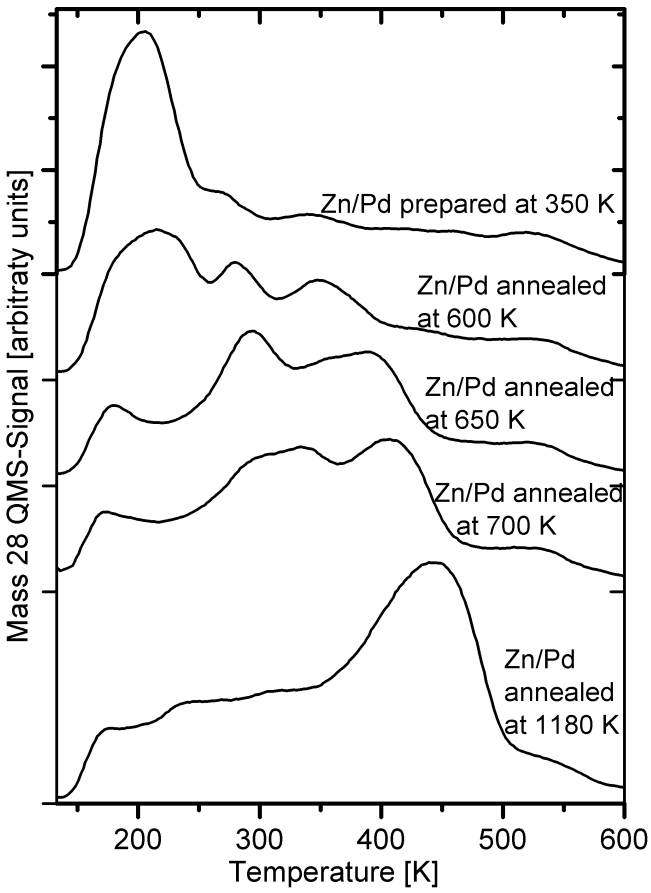

Figure 10.11: Evolution of the CO TD spectra after annealing of the ZnPd surface alloy (prepared at 350 K) at different temperatures (annealing time: 10 min; CO exposure: 34 L).

Only annealing from 600 K on shows an influence on the CO TDS. The spectra exhibit a gradual change in shape and show the peaks shifting to higher desorption temperatures when the annealing temperature was increased. This shift to higher desorption temperatures is equivalent to an increase of the CO binding energy on the surface. Additionally, the shape of the spectra converts more and more to the shape of the CO TD spectrum from clean Pd(111). Moreover, as already presented in chapter 9 the Auger Zn/Pd ratio decreases with increasing annealing temperature indicating an accumulation of Pd on the surface. Due to the fact that Zn desorption can be excluded below 750 K this means that Pd atoms segregate on top of the Zn or Zn diffuses deeper into the bulk. Anyway, the result of the temperature induced segregation is that more Pd atoms are available on the surface which gives rise to a stronger CO-Pd binding. The latter observation coincides with the work of Bayer et al. who found an increase of the Pd $3d_{5/2}$ XPS intensity in their grazing emission spectra after heating the

sample to 600 K [30]. They also interpreted this observation as an enrichment of Pd in the surface region due to the temperature treatment.

10.3 Summary of Chapter 10

The obtained H_2 and CO TDS results show that thick Zn layers prepared at low temperatures inhibit the adsorption of carbon monoxide and hydrogen at least at adsorption temperatures above 100 K. Zn layers prepared at 300 K and above show a different behaviour due to the formation of a PdZn alloy. In case of hydrogen the Zn atoms on the surface just act as site blockers but do not influence the energetics. The number of hydrogen atoms adsorbed on the surface is reduced by 1/2 on the ZnPd surface, whereas the subsurface diffusion is uninfluenced. The initial sticking coefficient of hydrogen decreased from 0.5 on the clean Pd(111) to 0.14 on the ZnPd surface alloy.
TDS of CO on the ZnPd surface alloy reveals that the heat of adsorption is lowered significantly compared to the clean sample. No CO adsorption is possible at 300 K sample temperature but at low adsorption temperatures a CO desorption peak occurs at 220 K. For the low coverage regime a CO desorption energy of 71 ± 2 kJ·mol^{-1} was determined. The CO adsorption energy is reduced due to a change in the electronic structure of the Pd caused by the Zn-Pd interactions in the surface, which leads to a decrease in the CO-Pd binding strenght. The CO uptake curve initially shows a linear increase and saturates then at a CO coverage of about 0.5 ML. This means that each Pd atom, present on the surface, is occupied by on CO molecule. Due to an initial sticking coefficient which remains close to unity even on the ZnPd surface alloy, the involvement of a prcursor state in the adsorption kinetics is indicated. Additionally, the CO adsorption as a function of the Zn coverage prepared at 150 K and 350 K sample temperature was studied. Plotting the total amount of adsorbed CO versus the Zn coverage yields a linear decrease of the CO coverage with increasing Zn coverage for both the samples prepared at 150 K and 350 K. The CO uptake levels off at 1 ML Zn coverage for the sample prepared at 150 K and at 2 ML for the sample prepared at 350 K. In the latter case there a ZnPd surface alloy has formed, already, which gives rise to a smoother descent in the adsorbed CO amount. Although the heat of adsorption on the ZnPd surface alloy is lowered there still is CO adsorption possible for Zn coverages up to 2 ML.
The formation of additional surface Pd sites due to heat treatment has been probed by CO titration experiments. The CO TD data indicate that the ZnPd surface alloy prepared at 350 K does not change up to 600 K. Heat treatment at 600 K or above leads to a gradual change in the shape of the CO desorption spectra. This change in the desorption spectra is accompanied by a decrease of the Zn/Pd Auger intensity ratio. This indicates a migration of Zn atoms into the subsurface region or a segregation of Pd atoms on top of the Zn, because Zn desorption below 750 K can be excluded.

11 Summary

Within this thesis kinetic and dynamic aspects of the interaction of gases with clean and modified Pd(111) single crystal surfaces have been treated. The Pd(111) surface was modified either by metallic layers like zinc and pottasium or by oxidic layers like vanadium oxide. The used gases were H_2, D_2, O_2 and CO where hydrogen and deuterium were supplied via permeation from the sample bulk for some experiments. As the results obtained from various experimental methods for the different systems have already been discussed in the corresponding chapters, here only a short, general summary shall be given.

D_2 on Pd(111):
The angular distribution of desorbing D_2 from Pd(111) has been studied at 523 K and 700 K. The deuterium supply was performed via permeation through the bulk. The angular distribution at 523 K was close to a cosine ditsribution, whereas those at 700 K was somewhat forward focused ($cos^{1.9}\theta$). This behaviour could be explained by comparison with adsorption and time-of-flight data via application of the detailed balancing principle and normal energy scaling (NES). Most important is that these basic features were also applicable to the desorption process when deuterium is fed to the surface via permeation.

D_2 on K/Pd(111):
Measurments on the angular distribution of desorbing D_2 from potassium modified Pd(111) yielded a strongly forward focused distribution ($cos^3\theta$) compared to the clean Pd(111). The deuterium supply was again provided by permeation through the single crystal bulk. Comparison of the angular distribution data with kinetic energy data of the deuterium desorption flux and application of detailed balancing leads to the conclusion that normal energy scaling (NES) is fulfilled. This can be rationalized by considering the built up of a nearly one dimensional activation barrier.

D_2O formation on Pd(111):
The D_2O formation from impinging O_2 and permeating D on the Pd(111) single crystal surface was studied at 523 K and 700 K. The water formation turned out to be more effective at the lower sample temperatures which coincides with a higher sticking probability of oxygen at this temperature. All the effusing deuterium was either converted into D_2O or desorbed associatively as D_2. The activation energy for OD formation was calculated to be 0.56 eV and the pre-exponential factor was determined to be $8.6{\cdot}10^{-8}$ $cm^2{\cdot}atoms^{-1}{\cdot}s^{-1}$.

D_2O formation on VO_x modified Pd(111):
The influence of various vanadium oxides on the D_2O formation reaction as well as on the deuterium desorption was investigated at sample temperatures of 523 K and 700 K. The reaction was fed with O_2 from the gas phase and permeating deuterium from the Pd bulk. Attention was directed on the structural stability of the oxide layers under reaction conditions as well as on the angular and time-of-flight (translational kinetic energy) distribution of the desorbing reaction products. Additionally, the kinetic aspects of the water formation reaction were examined.
Below 700 K the (2×2) s-V_2O_3 oxide phase turned out to be the most stable. Even during pure deuterium exposure no structural change could be observed. At 700 K the VO "waggon wheel" structure is favored, but changes to a structure with rectangular unit cell under water formation conditions.
The desorbing deuterium at 523 K and 700 K shows slightly different time-of-flight spectra which is due to changes in the deuterium adsorption behaviour on the differnt oxide phases. Thick vanadium oxide layers, which exhibit the V_2O_3-bulk structure lead to theramlized TOF spectra, which might be caused by the rather rough morphology of these layers.
The TOF distributions of the desorbing D_2O are slightly hyperthermal on thin VO_x layers which might indicate that on these layers the hydroxyl intermediate preferentially reacts with deuterium atoms of high energy. On the thick oxide layers the water molecules exhibit a translational energy distribution which is thermalized with the surface. This might again be the case due to the rough surface morphology of these layers.
The presence of a thin VO_x layer like the s-V_2O_3 induces no change in the angular distribution of the desorbing deuterium compared to the clean Pd(111). The s-V_2O_3 forms a porous network which leaves small Pd areas open. Obviously the electronic influence of the VO_x is of short range character and therefore the deuterium recombination on the Pd can take place unaltered.
Measurements on the water formation kinetics on VO_x modified surfaces reveal that the oxide film hinders the water formation reaction. For both sample temperatures, 523 K and 700 K, the water formation is less efficient than on the clean Pd. The initial reaction probability as well as the total amount of converted D_2 are reduced.

Zn on Pd(111):
Different methods for the Zn coverage calibration were discussed including the measurement of the isotropic Zn QMS-signals during deposition, Auger electron spectroscopy, CO titration experiments and quartz microbalance measurements. It turned out that Zn does not stick well to contaminated surfaces at room temperature. Therefore the sticking coefficient of Zn on the clean Pd surface and the ill defined quartz crystal surface of a microbalance are initially not the same which violates the basic requirement for an appropriate coverage calibration. Nevertheless, the quartz crystal can be prepared by extensive Zn exposure ($>$ 1000 ML), which finally covers all the impurities and yields a pure Zn surface. On such a surface the sticking coefficient for Zn is unity at room temperature and the microbalance can be used riskless. Alternatively, the exposure can be determined, at least relatively, by measuring the isotropic mass 64 signal

with the mass spectrometer. The CO titration just works properly if the Zn grows in a more or less perfect layer-by-layer mode (excludes preparation at temperatures above 300 K) and just for coverages up to 1 ML. The determination of the Zn coverage by AES also demands a good layer-by-layer growth mode and works for not too thick layers. Moreover the AES calibration method involves a number of parameters which have to be taken from the literature.
The kinetics of Zn adsorption/desorption was studies by TDS, LEED, AES, STM and DFT from the sub monolaery regime up to the multilayer regime. Zn deposited at sample temperatures above 300 K forms a (2×1) surface alloy. At temperatures higher than 600 K Zn starts to migrate deeper into the palladium bulk. This ZnPd alloy decomposes at temperatures above 780 K which gives rise to a broad desorption feature centred at 1040 K (β_2) (at a heating rate of 2 K/s). The multilayer desorption takes place between 400 and 600 K and exhibits a multiple peak structure. A zero order peak α_1 followed by 3 fractional order peaks (α_2-α_4) and a first order peak β_1. The β peaks turned out to depend on the preparation temperature which can be attributed to enhanced Zn diffusion at elevated temperatures. Generally, the Zn desorption from Pd(111) turned out to be crucially influenced by diffusion and alloying processes.

H_2 and CO on Zn/Pd(111):
H_2 and CO adsorption is blocked by thick Zn layers on Pd(111), at least for adsorption temperatures above 100 K. On the ZnPd surface alloy, which is formed above 300 K, the hydrogen adsorption is reduced by simple cite blocking due to the Zn atoms, which is indicated by non shifting desorption maxima. Therefore the number of available hydrogen adsorption states on the surface is reduced, whereas the hydrogen subsurface states keep uninfluenced.
Different to that the CO desorption spectrum is significantly altered due to the presence of Zn. Additional peaks appear and shift downwards with increasing Zn coverage. On the ZnPd surface alloy, which can be formed either by deposition at elevated temperatures or annealing of the Zn layer, CO can adsorb on the surface even at initial Zn coverages exceeding 1 ML. However, in this case the CO binding energy is reduced drastically compared to the clean Pd(111) surface. The binding energy of CO on the ZnPd surface alloy is close to those of specific copper surfaces. This outlines the similarity of the Pd density of states in ZnPd and the DOS of copper.

12 Bibliography

[1] H. Schulz. Short history and present trends of Fischer-Tropsch synthesis. *Applied Catalysis A: General*, 186(1-2):3, October 1999.

[2] G. Ertl. Elementarschritte bei der heterogenen Katalyse. *Angewandte Chemie*, 102:1258, 1990.

[3] J. Schoiswohl, S. Surnev, and F.P. Netzer. Reactions on Inverse Model Catalyst Surfaces: Atomic Views by STM. *Topics in Catalysis*, 36:91, 2005.

[4] F. P. Leisenberger, S. Surnev, L. Vitali, M. G. Ramsey, and F. P. Netzer. Nature, growth and stability of vanadium oxides on Pd(111). *Vacuum Science and Technology A*, 17:1743, 1999.

[5] S. Surnev, L. Vitali, M. G. Ramsey, F. P. Netzer, G. Kresse, and J. Hafner. Growth and structure of ultrathin vanadium oxide layers on Pd(111). *Phys. Rev. B*, 61(20):13945, May 2000.

[6] C. Klein, G. Kresse, S. Surnev, F. P. Netzer, M. Schmid, and P. Varga. Vanadium surface oxides on Pd(111): A structural analysis. *Phys. Rev. B*, 68(23):235416–, December 2003.

[7] J. Schoiswohl, M. Sock, S. Eck, S. Surnev, M. G. Ramsey, F. P. Netzer, and G. Kresse. Atomic-level growth study of vanadium oxide nanostructures on Rh(111). *Phys. Rev. B*, 69(15):155403, April 2004.

[8] S. Surnev, G. Kresse, M. Sock, M. G. Ramsey, and F. P. Netzer. Surface structures of ultrathin vanadium oxide films on Pd(1 1 1). *Surface Science*, 495(1-2):91, December 2001.

[9] S. Surnev, M. Sock, G. Kresse, J.N. Andersen, M.G. Ramsey, and F.P. Netzer. Unusual CO Adsorption Sites on Vanadium Oxide-Pd(111) "Inverse Model Catalyst" Surfaces. *J. Phys. Chem. B*, 107(20):4777, 2003.

[10] G. Pauer. *Desorption and Reaction Dynamics of Hydrogen on Clean and Modified Rhodium and Palladium Crystal Surfaces.* PhD thesis, Graz University of Technology, 2005.

[11] G. Pauer, M. Kratzer, and A. Winkler. Reaction and desorption kinetics of H_2 and H_2O on activated and non-activated palladium surfaces. *Vacuum*, 80(1-3):81–86, October 2005.

[12] G. Pauer, M. Kratzer, and A. Winkler. Manipulating the activation barrier for $H_2(D_2)$ desorption from potassium-modified palladium surfaces. *J. Chem. Phys.*, 123(20):204702, November 2005.

[13] M. Kratzer. Flugzeituntersuchungen von Desorptions-und Reaktionsprodukten an modifizierten Pd-Oberflächen. Master's thesis, Graz University of Technology, 2004.

[14] N. Iwasa, T. Akazawa, S. Ohyama, K. Fujikawa, and N. Takezawa. Dehydrogenation of methanol to methyl formate over supported Ni, Pd and Pt catalysts. Anomalous catalytic functions of PdZn and PtZn alloys. *Reaction Kinetics and Catalysis Letters*, 55:245, 1995.

[15] N. Iwasa, S. Kudo, H. Takahashi, S. Masuda, and N. Takezawa. Highly selective supported Pd catalysts for steam reforming of methanol. *Catalysis Letters*, 19(2):211, June 1993.

[16] N. Iwasa, T. Mayanagi, N. Ogawa, K. Sakata, and N. Takezawa. New catalytic functions of PdZn, PdGa, PdIn, PtZn, PtGa and PtIn alloys in the conversions of methanol. *Catalysis Letters*, 54(3):119, September 1998.

[17] N. Iwasa, N. Ogawa, S. Masuda, and N. Takezawa. Selective PdZn Alloy Formation in the Reduction of Pd/ZnO Catalysts. *Bulletin of the Chemical Society of Japan*, 71(6):1451, 1998.

[18] N. Iwasa, S. Masuda, N. Ogawa, and N. Takezawa. Steam reforming of methanol over Pd/ZnO: Effect of the formation of PdZn alloys upon the reaction. *Applied Catalysis A: General*, 125(1):145, April 1995.

[19] N. Iwasa, O. Yamamoto, T. Akazawa, S. Ohyama, and N. Takezawa. Dehydrogenation of methanol to methyl formate over palladium/zinc oxide catalysts. *Journal of the Chemical Society, Chemical Communications*, page 1322, 1991.

[20] N. Iwasa, T. Mayanagi, W. Nomura, M. Arai, and N. Takezawa. Effect of Zn addition to supported Pd catalysts in the steam reforming of methanol. *Applied Catalysis A: General*, 248(1-2):153, August 2003.

[21] S. Liu, K. Takahashi, and M. Ayabe. Hydrogen production by oxidative methanol reforming on Pd/ZnO catalyst: effects of Pd loading. *Catalysis Today*, 87(1-4):247, November 2003.

[22] S. Liu, K. Takahashi, K. Uematsu, and M. Ayabe. Hydrogen production by oxidative methanol reforming on Pd/ZnO. *Applied Catalysis A: General*, 283(1-2):125, April 2005.

[23] S. Liu, K. Takahashi, H. Eguchi, and K. Uematsu. Hydrogen production by oxidative methanol reforming on Pd/ZnO: Catalyst preparation and supporting materials. *Catalysis Today*, 129(3-4):287, December 2007.

[24] C. Fukuhara, Y. Kamata, and A. Igarashi. Catalytic performance of plate-type Pd/Zn-based catalysts for steam reforming of methanol, prepared by electroless plating. *Applied Catalysis A: General*, 330:108, October 2007.

[25] Y. Suwa, S.-i. Ito, S. Kameoka, K. Tomishige, and K. Kunimori. Comparative study between Zn-Pd/C and Pd/ZnO catalysts for steam reforming of methanol. *Applied Catalysis A: General*, 267(1-2):9, July 2004.

[26] E. S. Ranganathan, S. K. Bej, and L. T. Thompson. Methanol steam reforming over Pd/ZnO and Pd/CeO_2 catalysts. *Applied Catalysis A: General*, 289(2):153, August 2005.

[27] J. Araña, N. Homs, J. Sales, J. L. G. Fierro, and P. Ramirez de la Piscina. CO/CO_2 hydrogenation and ethylene hydroformylation over silica-supported PdZn catalysts. *Catalysis Letters*, 72:183, 2001.

[28] S. Ahmed and M. Krumpelt. Hydrogen from hydrocarbon fuels for fuel cells. *International Journal of Hydrogen Energy*, 26(4):291, April 2001.

[29] P. J. de Wild and M. J. F. M. Verhaak. Catalytic production of hydrogen from methanol. *Catalysis Today*, 60(1-2):3, July 2000.

[30] A. Bayer, K. Flechtner, R. Denecke, H.-P. Steinrück, K. M. Neyman, and N. Rösch. Electronic properties of thin Zn layers on Pd(111) during growth and alloying. *Surface Science*, 600(1):78, January 2006.

[31] H. Gabasch, A. Knop-Gericke, R. Schlögl, S. Penner, B. Jenewein, K. Hayek, and B. Klötzer. Zn Adsorption on Pd(111): ZnO and PdZn Alloy Formation. *J. Phys. Chem. B*, 110(23):11391, 2006.

[32] E. Jeroro, V. Lebarbier, A. Datye, Y. Wang, and J. M. Vohs. Interaction of CO with surface PdZn alloys. *Surface Science*, 601(23):5546, December 2007.

[33] S. Holloway and J. Norskov. Bonding at surfaces. *Surface Science lecture notes*, 1, 1991.

[34] Harald Ibach. *Physics of Surfaces and Interfaces*. Springer Verlag, 2006.

[35] Richard I. Masel. *Principles of Adsorption and Reaction on Solid Surfaces*. John Wiley & Sons, Inc., 1996.

[36] Andrew Zangwill. *Physics at Surfaces*. Cambridge University Press, 1988.

[37] Klaus Christmann. *Introduction to Surface Physical Chemistry*. Springer Verlag, 1991.

[38] J.E. Lennard-Jones. Process of Adsorption and Diffusion on Solid Surfaces. *Trans. Faraday Soc.*, 28:333, 1932.

[39] J. C. Polanyi. Some Concepts in Reaction Dynamics. *Science*, 236(4802):680, May 1987.

[40] C. Crespos, M. A. Collins, E. Pijper, and G. J. Kroes. Multi-dimensional potential energy surface determination by modified Shepard interpolation for a molecule-surface reaction: H_2 + Pt(111). *Chemical Physics Letters*, 376(5-6):566, July 2003.

[41] G. R. Darling and S. Holloway. The dissociation of diatomic molecules at surfaces. *Reports on Progress in Physics*, 58(12):1595, 1995.

[42] A. Gross and M. Scheffler. Influence of molecular vibrations on dissociative adsorption. *Chemical Physics Letters*, 256(4-5):417, July 1996.

[43] D. A King and M.G. Wells. Molecular-Beam Investigation of Adsorption Kinetics on Bulk Metal Targets-Nitrogen on Tungsten. *Surface Science*, 29:454, 1972.

[44] A. Winkler. Absolute Calibration of Small Gas Amounts. *Journal of Vacuum Science and Technology A*, 5:2430, 1987.

[45] A. Winkler and K. D. Rendulic. Sticking of Molecular Hydrogen on Simple, Noble and Transition Metal Surfaces. *International Reviews in Physical Chemistry*, 11:101, 1992.

[46] K. Oura, V.G. Lifshits, A.A. Saranin, A.V. Zotov, and M. Katayama. *Surface Science. An Introduction.* Springer Verlag, 2003.

[47] R. I. Masel. *Theoretical Surface Science.* Springer Verlag, 2003.

[48] M. J. Cardillo, M. Balooch, and R. E. Stickney. Detailed Balancing and Quasi-Equilibrium in the Adsorption of Hydrogen on Copper. *Surface Science*, 50:263, 1975.

[49] G. Comsa. Angular and Velocity Distributions in Molecular Beam Scattering at Solid Surfaces. In *7th International Vacuum Congress and 3rd International Conference on Solid Surfaces*, 1977.

[50] H. P. Steinrück, K. D. Rendulic, and A. Winkler. The sticking coefficient of H_2 on Ni(111) as a function of particle energy and angle of incidence: A test of detailed balancing. *Surface Science*, 154(1):99, May 1985.

[51] J. S. Thomsen. Logical Relations among the Principles of Statistical Mechanics and Thermodynamics. *Physical Review*, 91:1263, 1953.

[52] M. Dürr and U. Höfer. Dissociative adsorption of molecular hydrogen on silicon surfaces. *Surface Science Reports*, 61:465, 2006.

[53] W. Brenig. *Springer Series in Surface Science 8: Kinetics of Interface Reactions*. Springer Verlag, 1987.

[54] M. Beutl, M. Riedler, and K. D. Rendulic. Strong rotational effects in the adsorption dynamics of H_2/Pd(111): evidence for dynamical steering. *Chemical Physics Letters*, 247(3):249, December 1995.

[55] A. Gross, S. Wilke, and M. Scheffler. Six-Dimensional Quantum Dynamics of Adsorption and Desorption of H_2 at Pd(100): Steering and Steric Effects. *Phys. Rev. Lett.*, 75(14):2718, October 1995.

[56] G. Comsa and R. David. Dynamical parameters of desorbing molecules. *Surface Science Reports*, 5(4):145, December 1985.

[57] C. Eibl. *Kinetik und Dynamik der Adsorption und Desorption von Wasserstoff (Deuterium) auf Vanadiumoberflächen.* PhD thesis, Graz University of Technology, 2001.

[58] M. Karikorpi, S. Holloway, N. Henriksen, and J. K. Nørskov. Dynamics of molecule-surface interactions. *Surface Science*, 179(1):L41, January 1987.

[59] S. Holloway. Dynamical Processes at Surfaces. *Journal of Vacuum Science and Technology*, A5:476, 1987.

[60] K. D. Rendulic, G. Anger, and A. Winkler. Wide range nozzle beam adsorption data for the systems H_2/nickel and H_2/Pd(100). *Surface Science*, 208(3):404, February 1989.

[61] G. Anger, A. Winkler, and K. D. Rendulic. Adsorption and desorption kinetics in the systems H_2/Cu(111), H_2/Cu(110) and H_2/Cu(100). *Surface Science*, 220(1):1, October 1989.

[62] R. Opila and R. Gomer. Thermal desorption of Xe from the W(110) plane. *Surface Science*, 112(1-2):1, December 1981.

[63] R. G. Jones and D. L. Perry. The chemisorption of mercury on tungsten (100): Adsorption and desorption kinetics, equilibrium properties and surface structure. *Surface Science*, 71(1):59, January 1978.

[64] H. Asada. A model for the zero order desorption kinetics. *Journal of the Research Institute for Catalysis, Hokkaido University*, 30:55, 1982.

[65] H. Asada and M. Masuda. Bilayer model for zero order desorption. *Surface Science*, 207(2-3):517, January 1989.

[66] J. A. Venables and M. Bienfait. On the reaction order in thermal desorption spectroscopy. *Surface Science*, 61(2):667, December 1976.

[67] K. Nagai, T. Shibanuma, and M. Hashimoto. Zero-order desorption kinetics based on phase equilibrium. *Surface Science*, 145(1):L459, September 1984.

[68] R. G. Jones and D. L. Perry. Fractional and zero order desorption kinetics of adsorbed monolayers: The role of attractive lateral interactions in the Hg/W(100) system. *Surface Science*, 82(2):540, April 1979.

[69] W. T. Thomson. On the equilibrium of vapour at a curved surface of liquid. *Philosophical Magazine*, 42:448, 1871.

[70] J. R. Sambles, L. M. Skinner, and N. D. Lisgarten. An Electron Microscope Study of Evaporating Small Particles: The Kelvin Equation for Liquid Lead and the Mean Surface Energy of Solid Silver. *Proceedings of the Royal Society of London. Series A, Mathematical and Physical Sciences (1934-1990)*, 318(1535):507, September 1970.

[71] W. Ostwald. *Lehrbuch der Allgemeinen Chemie, vol. 2, part 1.* Leipzig, Germany, 1896.

[72] L Ratke and P. W. Voorheers. *Growth and Coarsening: Ostwald Ripening in Material Processing.* Springer, 2002.

[73] M. A. Morris, M. Bowker, and D. A. King. *Comprehensive Chemical Kinetics.* Elsevier, Amsterdam, 1984.

[74] T. Y. Zhang and Y. P. Zheng. Effects of absorption and desorption on hydrogen permeation-I. Theoretical modeling and room temperature verification. *Acta Materialia*, 46(14):5023–5033, September 1998.

[75] E. Fromm and E. Gebhardt. *Gase und Kohlenstoff in Metallen.* Springer-Verlag Berlin Heidelberg New York, 1976.

[76] S. N. Sankaran, R. K. Herrmann, R. A. Outlaw, and R. K. Clark. Barrier-layer formation and its control during hydrogen permeation through Ti-24AI-11Nb alloy. *Metallurgical and Materials Transactions A*, 5:89–97, 1994.

[77] S. A. Kofler, J. B. Hudson, and G. S. Ansell. Hydrogen Permeation Through Alpha-Palladium. *Transactions of the Metallurgical Society of AIME*, 245:1735, 1969.

[78] V. A. Gol'tsov and P. V. Gel'd. *Phys. Met. Metallogr.*, 29:1305, 1970.

[79] *Staib Instruments, Instruction Manual: Electron Spectrometer Model ESA 100.*

[80] C. C. Chang. Auger Electron Spectroscopy. *Surface Science*, 25(1):53, March 1971.

[81] D. Briggs and M. P. Seah. *Practical Surface Analysis by Auger and X-Ray Photoelectron Spectroscopy.* John Wiley & Sons, Chichester/ New York/ Brisbane/ Toronto/ Singapore, 1983.

[82] G. Ertl and J. Küppers. *Low Energy Electrons and Surface Chemistry, Volume 4 of Monographs in Modern Chemistry.* Verlag Chemie, Weinheim, 1974.

[83] H. Bubert and H. Jenett. *Surface and Thin Film Analysis: Principles, Instrumentation, Applications.* Wiley-VCH, Weinheim, 2002.

[84] D. P. Woodruff and T. A. Delchar. *Modern Techniques of Surface Science.* Cambridge University Press, Cambridge, 1986.

[85] J. B. Pendry. *Low Energy Electron Diffraction.* Academic Press, London, New York, 1974.

[86] A. Winkler and J.T. Yates Jr. Capillary array dosing and angular desorption distribution measurements: A general formalism. *Journal of Vacuum Science and Technology*, 6:2929, 1988.

[87] A. Winkler, X. Guo, H. R. Siddiqui, P. L. Hagans, and J. T. Yates. Kinetics and energetics of oxygen adsorption on Pt(111) and Pt(112)- A comparison of flat and stepped surfaces. *Surface Science*, 201(3):419, July 1988.

[88] J. Stettner. Angular distributions of deuterium desorption form modified Pd(111) surfaces. Master's thesis, University of Technology Graz, 2007.

[89] P. A. Redhead. Thermal Desorption of Gases. *Vacuum*, 12:203, 1962.

[90] H. Conrad, G. Ertl, J. Küppers, and E. E. Latta. Interaction of NO and O_2 with Pd(111) surfaces. II. *Surface Science*, 65(1):245, June 1977.

[91] F. P. Leisenberger, G. Koller, M. Sock, S. Surnev, M. G. Ramsey, F. P. Netzer, B. Klötzer, and K. Hayek. Surface and subsurface oxygen on Pd(111). *Surface Science*, 445(2-3):380, January 2000.

[92] B. Klötzer, K. Hayek, C. Konvicka, E. Lundgren, and P. Varga. Oxygen-induced surface phase transformation of Pd(1 1 1): sticking, adsorption and desorption kinetics. *Surface Science*, 482-485(Part 1):237, June 2001.

[93] E. Demirci and A. Winkler. Quantitative determination of reaction products by in-line thermal desorption spectroscopy: The system methanol/Pd(111). *Journal of Vacuum Science and Technology A*, 26:78, 2008.

[94] H. Pauly. *Atom, molecule and cluster beams I: basic theory, production and detection of thermal energy beams.* Springer , Berlin HeidelbergVerlag, 2000.

[95] J. L. Falconer and R. J. Madix. Flash Desorption Activation Energies: DCOOH Decomposition and CO Desorption From Ni(110). *Surface Science*, 48:393, 1975.

[96] A. M. de Jong and J. W. Niemantsverdriet. Thermal Desorption Analysis: Comparative Test of Ten Commonly Applied Procedures. *Surface Science*, 233:355, 1990.

[97] C.-M. Chan, R. Aris, and W. H. Weinberg. An Analysis of Thermal Desorption Mass Spectra I. *Applications of Surface Science*, 1:360, 1978.

[98] C.-M. Chan and W. H. Weinberg. An Analysis of Thermal Desorption Mass Spectra II. *Applications of Surface Science*, 1:377, 1978.

[99] K. H. Allers. *Winkel- und Energieverteilung und deren Korrelation bei thermisch desorbierten Molekülen.* PhD thesis, Technische Universität München, 1992.

[100] K. H. Allers, H. Pfnür, P. Feulner, and D. Menzel. Angular and velocity distributions of CO desorbed from adsorption layers on Ni(100) and Pt(111): examples of non-activated desorption. *Surface Science*, 291(1-2):167, July 1993.

[101] I. N. Bronstein and K. A. Semendjajew. *Taschenbuch der Mathematik.* Harri Deutsch Thun und Frankfurt/Main, 1989.

[102] W. D. Eadie, D. Drijad, F. E. James, M. Roos, and B. Sadoulet. *Statistical Methods in Experimental Physics.* Amsterdam, North-Holland, 1971.

[103] J. A. Alcalay and E. L. Knuth. Molecular-Beam Time-of-Flight Spectroscopy. *Review of Scientific Instruments*, 40:438, 1969.

[104] S. Ichimura and R. Shimizu. Backscattering correction for quantitative Auger analysis: I. Monte Carlo calculations of backscattering factors for standard materials. *Surface Science*, 112(3):386, December 1981.

[105] S. Ichimura, R. Shimizu, and T. Ikuta. Backscattering correction for quantitative Auger analysis: II. Verifications of the backscattering factors through quantification by AES. *Surface Science*, 115(2):259, March 1982.

[106] S. Tanuma, C. J. Powell, and D. R. Penn. Calculations of electron inelastic mean free paths for 31 materials. *Surface and Interface Analysis*, 11(11):577, 1988.

[107] S. Tanuma, T. Shiratori, T. Kimura, K. Goto, S. Ichimura, and C. J. Powell. Experimental determination of electron inelastic mean free paths in 13 elemental solids in the 50 to 5000 eV energy range by elastic-peak electron spectroscopy. *Surface and Interface Analysis*, 37(11):833, 2005.

[108] N. W. Ashcroft and N. A. Mermin. *Festkörperphysik.* Oldenbourg Verlag München Wien, 2005.

[109] P. Hohenberg and W. Kohn. Inhomogeneous Electron Gas. *Phys. Rev.*, 136(3B):B864, November 1964.

[110] W. Kohn and L. J. Sham. Self-Consistent Equations Including Exchange and Correlation Effects. *Phys. Rev.*, 140(4A):A1133, November 1965.

[111] J. P. Perdew, J. A. Chevary, S. H. Vosko, Koblar A. Jackson, M. R. Pederson, D. J. Singh, and C. Fiolhais. Atoms, molecules, solids, and surfaces: Applications of the generalized gradient approximation for exchange and correlation. *Phys. Rev. B*, 46(11):6671, September 1992.

[112] G. Kresse and J. Hafner. Ab initio molecular dynamics for open-shell transition metals. *Phys. Rev. B*, 48(17):13115, November 1993.

[113] G. Kresse and J. Hafner. Ab initio molecular dynamics for liquid metals. *Phys. Rev. B*, 47(1):558, January 1993.

[114] G. Kresse and J. Hafner. Ab initio molecular-dynamics simulation of the liquid-metal-amorphous-semiconductor transition in germanium. *Phys. Rev. B*, 49(20):14251, May 1994.

[115] G. Kresse and J. Furthmüller. Efficient iterative schemes for ab initio total-energy calculations using a plane-wave basis set. *Phys. Rev. B*, 54(16):11169, October 1996.

[116] G. Kresse and J. Furthmüller. Efficiency of ab-initio total energy calculations for metals and semiconductors using a plane-wave basis set. *Computational Materials Science*, 6(1):15, July 1996.

[117] H. J. Monkhorst and J. D. Pack. Special points for Brillouin-zone integrations. *Phys. Rev. B*, 13(12):5188, June 1976.

[118] M. Methfessel and A. T. Paxton. High-precision sampling for Brillouin-zone integration in metals. *Phys. Rev. B*, 40(6):3616, August 1989.

[119] G. Alefeld and J. Völkl, editors. *Hydrogen in Metals II, Topics in Applied Physics, vol 29.* Springer Verlag, Berlin-Heidelberg-New York, 1978.

[120] P. L. Cabot, E. Guezala, and J. Casado. Fuel cells based on the use of Pd foils. *Journal of New Materials for Electrochemical Systems*, 2:253, 1999.

[121] T. Engel and H. Kuipers. A molecular-beam investigation of the scattering, adsorption and absorption of H_2 and D_2 from/on/in Pd(111). *Surface Science*, 90(1):162, December 1979.

[122] L. Schröter, C. Trame, R. David, and H. Zacharias. State specific velocity distribution of hydrogen isotopes desorbing from Pd(100). *Surface Science*, 272(1-3):229, 1992.

[123] F. Solymosi and I. Kovács. Adsorption of hydrogen and deuterium on potassium-promoted Pd(100) surfaces. *Surface Science*, 260(1-3):139, January 1992.

[124] W. Dong, V. Ledentu, P. Sautet, G. Kresse, and J. Hafner. A theoretical study of H-induced reconstructions of the Pd(110) surface. *Surface Science*, 377-379:56, 1997.

[125] M. Skotte, R. J. Behm, and G. Ertl. LEED structure analysis of the clean and (2x1)H covered Pd(110) surface. *Journal of Chemical Physics*, 87:6191, 1987.

[126] J.-W. He, D. A. Harrington, K. Griffith, and P. R. Norton. The Interaction of Hydrogen with a Pd(100) surface. *Surface Science*, 198:413, 1988.

[127] J. Yoshinobu, H. Tanaka, and M. Kawai. Elucidation of hydrogen-induced (1x2) reconstructed structure on Pd(110) from 100 to 300 K. *Physical Review B*, 51:4529, 1995.

[128] M. G. Cattania, V. Penka, R. J. Behm, K. Christmann, and G. Ertl. Interaction of Hydrogen with a Pd(110) surface. *Surface Science*, 120:382, 1983.

[129] V. Ledentu, W. Dong, and B. Sadoulet. Ab initio study of dissociative adsorption of H_2 on the Pd(110) surface. *Surface Science*, 412/413:518, 1998.

[130] N. Takezawa and N. Iwasa. Steam reforming and dehydrogenation of methanol: Difference in the catalytic functions of copper and group VIII metals. *Catalysis Today*, 36(1):45, April 1997.

[131] C. Resch, H. F. Berger, K. D. Rendulic, and E. Bertel. Adsorption dynamics for the system hydrogen/palladium and its relation to the surface electronic structure. *Surface Science*, 316(3):L1105, September 1994.

[132] A. E. Dabiri, T. J. Lee, and R. E. Stickney. Spatial and speed distributions of H_2 and D_2 desorbed from a polycrystalline nickel surface. *Surface Science*, 26(2):522, July 1971.

[133] G. Comsa, R. David, and K. D. Rendulic. Velocity Distribution of H_2, HD, and D_2 Molecules Desorbing from Polycrystalline Nickel Surfaces. *Phys. Rev. Lett.*, 38(14):775, April 1977.

[134] G. Comsa, R. David, and B.-J. Schumacher. Fast deuterium molecules desorbing from metals. *Surface Science*, 95(1):L210, May 1980.

[135] H. A. Michelsen, C. T. Rettner, and D. J. Auerbach. State-specific dynamics of D_2 desorption from Cu(111): The role of molecular rotational motion in activated adsorption-desorption dynamics. *Phys. Rev. Lett.*, 69(18):2678, November 1992.

[136] G. Pozgainer, K. D. Rendulic, and A. Winkler. Laser spectroscopy on hydrogen desorbing from nickel. *Surface Science*, 307-309(Part 1):344, April 1994.

[137] M. Kratzer, J. Stettner, and A. Winkler. Angular distribution of desorbing/permeating deuterium from modified Pd(111) surfaces. *Surface Science*, 601:3456, 2007.

[138] M. Riedler. Untersuchung von Vorläuferzustaenden zur Chemisorption. Master's thesis, Graz University of Technology, 1996.

[139] A. C. Luntz, J. K. Brown, and M. D. Williams. Molecular beam studies of H_2 and D_2 dissociative chemisorption on Pt(111). *J. Chem. Phys.*, 93(7):5240, October 1990.

[140] D. A. Papaconstantopoulos, editor. *Handbook of the Band Structure of Elemental Solids*. Plenum Press, New York, 1986.

[141] K. D. Rendulic. Sticking and desorption: a review. *Surface Science*, 272(1-3):34, 1992.

[142] K. D. Rendulic and A. Winkler. Adsorption and desorption dynamics as seen through molecular beam techniques. *Surface Science*, 299-300:261, January 1994.

[143] K. D. Rendulic and A. Winkler. The Influence of Surface Defects and Foreign Atoms on the Adsorption Kinetics. *International Journal of Modern Physics B*, 3:941, 1989.

[144] E. Bertel, P. Sandl, K. D. Rendulic, and M. Beutl. Tailoring Surface Electronic Properties to Promote Chemical Reactivity. *Berichte der Bunsengesellschaft fuer Physikalische Chemie.*, 100(2):114, 1996.

[145] C. Resch, V. Zhukov, A. Lugstein, H. F. Berger, A. Winkler, and K. D. Rendulic. Dynamics of hydrogen adsorption on promoter-and inhibitor-modified nickel surfaces. *Chemical Physics*, 177(2):421, November 1993.

[146] J. K. Brown, A. C. Luntz, and P. A. Schultz. Long-range poisoning of D_2 dissociative chemisorption on Pt(111) by coadsorbed K. *J. Chem. Phys.*, 95(5):3767, September 1991.

[147] H. P. Bonzel. Alkali-metal-affected adsorption of molecules on metal surfaces. *Surface Science Reports*, 8(2):43, 1988.

[148] J. Libuda. Reaction kinetics on model catalysts: Molecular beam methods and time-resolved vibrational spectroscopy. *Surface Science*, 587(1-2):55, August 2005.

[149] T. Engel and H. Kuipers. A molecular-beam investigation of the reaction $H_2 + O_2 \rightarrow H_2O$ on Pd(111). *Surface Science*, 90(1):181, December 1979.

[150] T. Mitsui, M. K. Rose, E. Fomin, D. F. Ogletree, and M. Salmeron. Coadsorption and interactions of O and H on Pd(1 1 1). *Surface Science*, 511(1-3):259, June 2002.

[151] T. Mitsui, M. K. Rose, E. Fomin, D. F. Ogletree, and M. Salmeron. A scanning tunneling microscopy study of the reaction between hydrogen and oxygen to form water on Pd(111). *J. Chem. Phys.*, 117(12):5855, September 2002.

[152] C. Clay, L. Cummings, and A. Hodgson. Mixed water/OH structure on Pd(111). *Surface Science*, 601:562, 2006.

[153] X. Guo, A. Hoffman, and J. T. Yates, Jr. Adsorption kinetics and isotopic equilibration of oxygen adsorbed on the Pd(111) surface. *J. Chem. Phys.*, 90(10):5787, May 1989.

[154] J. Goschnick, M. Wolf, M. Grunze, W. N. Unertl, J. H. Block, and J. Loboda-Cackovic. Adsorption of O_2 on Pd(110). *Surface Science*, 178(1-3):831, December 1986.

[155] J. N. Smith, Jr. and R. L. Palmer. Molecular Beam Study of the Oxidation of Deuterium on a (111) Platinum Surface. *J. Chem. Phys.*, 56(1):13, January 1972.

[156] S. Surnev, G. Kresse, M. G. Ramsey, and F. P. Netzer. Novel Interface-Mediated Metastable Oxide Phases: Vanadium Oxides on Pd(111). *Phys. Rev. Lett.*, 87(8):086102, August 2001.

[157] J. Schoiswohl, M. Sock, Q. Chen, G. Thornton, G. Kresse, M. G. Ramsey, S. Surnev, and F. P. Netzer. Metal supported oxide nanostructures: model systems for advanced catalysis. *Topics in Catalysis*, 46:137, 2007.

[158] J. Völkl and G. Alefeld, editors. *Hydrogen in Metals I.* Springer, Berlin, 1978.

[159] H. Kobayashi, N. Takezawa, and C. Minochi. Methanol-reforming reaction over copper-containing catalysts -The effects of anions and copper loading in the preparation of the catalysts by kneading method. *Journal of Catalysis*, 69(2):487, June 1981.

[160] T.-J. Huang and S.-W. Wang. Hydrogen production via partial oxidation of methanol over copper-zinc catalysts. *Applied Catalysis*, 24(1-2):287, July 1986.

[161] S. Velu, K. Suzuki, M. Okazaki, M. P. Kapoor, T. Osaki, and F. Ohashi. Oxidative steam reforming of methanol over CuZnAl(Zr)-oxide catalysts for the selective production of hydrogen for fuel cells: Catalyst characterization and performance evaluation. *Journal of Catalysis*, 194(2):373, September 2000.

[162] S. Murcia-Mascarós, R. M. Navarro, L. Gómez-Sainero, U. Costantino, M. Nocchetti, and J. L. G. Fierro. Oxidative Methanol Reforming Reactions on CuZnAl Catalysts Derived from Hydrotalcite-like Precursors. *Journal of Catalysis*, 198(2):338, March 2001.

[163] K. M. Neyman, K. H. Lim, Z.-X. Chen, L. V. Moskaleva, A. Bayer, A. Reindl, D. Borgmann, R. Denecke, H.-P. Steinrück, and N. Rösch. Microscopic models of PdZn alloy catalysts: structure and reactivity in methanol decomposition. *Physical Chemistry Chemical Physics*, 9(27):3470, 2007.

[164] J. G. Chen, C. A. Menning, and M. B. Zellner. Monolayer bimetallic surfaces: Experimental and theoretical studies of trends in electronic and chemical properties. *Surface Science Reports*, 63:201, 2008.

[165] J. A. Rodriguez. Interactions in Bimetallic Bonding: Electronic and Chemical Properties of PdZn Surfaces. *J. Phys. Chem.*, 98(22):5758, 1994.

[166] A. Tamtögl. Adsorptions-und Desorptionsprozesse auf reinem und Zn-modifizierten Pd(111). Master's thesis, University of Technology Graz, 2008.

[167] M. Vollmer and F. Träger. Analysis of fractional order thermal desorption. *Surface Science*, 187(2-3):445, September 1987.

[168] L. Chan and G. L. Griffin. Temperature programmed desorption studies of hydrogen on Zn(0001) surfaces. *Surface Science*, 145(1):185, September 1984.

[169] Z.-X. Chen, K. M. Neyman, A. B. Gordienko, and N. Rösch. Surface structure and stability of PdZn and PtZn alloys: Density-functional slab model studies. *Phys. Rev. B*, 68(7):075417, August 2003.

[170] Z.-X. Chen, K. M. Neyman, and N. Rösch. Theoretical study of segregation of Zn and Pd in Pd-Zn alloys. *Surface Science*, 548(1-3):291, January 2004.

[171] L.-C. Wang, Y.-M. Liu, M. Chen, Y. Cao, H.-Y. He, G.-S. Wu, W.-L. Dai, and K.-N. Fan. Production of hydrogen by steam reforming of methanol over Cu/ZnO catalysts prepared via a practical soft reactive grinding route based on dry oxalate-precursor synthesis. *Journal of Catalysis*, 246(1):193, February 2007.

[172] S. Fukahori, T. Kitaoka, A. Tomoda, R. Suzuki, and H. Wariishi. Methanol steam reforming over paper-like composites of Cu/ZnO catalyst and ceramic fiber. *Applied Catalysis A: General*, 300(2):155, January 2006.

[173] T. Shishido, Y. Yamamoto, H. Morioka, K. Takaki, and K. Takehira. Active Cu/ZnO and Cu/ZnO/Al2O3 catalysts prepared by homogeneous precipitation method in steam reforming of methanol. *Applied Catalysis A: General*, 263(2):249, June 2004.

[174] M. Beutl and J. Lesnik. The influence of subsurface vanadium on the adsorption of hydrogen and carbon monoxide on Pd(111). *Vacuum*, 61(2-4):113, May 2001.

[175] G. E. Gdowski, T. E. Felter, and R. H. Stulen. Effect of surface temperature on the sorption of hydrogen by Pd(111). *Surface Science*, 181(3):L147, March 1987.

[176] H. Conrad, G. Ertl, and E. E. Latta. Adsorption of hydrogen on palladium single crystal surfaces. *Surface Science*, 41(2):435, February 1974.

[177] W. Eberhardt, S. G. Louie, and E. W. Plummer. Interaction of hydrogen with a Pd(111) surface. *Phys. Rev. B*, 28(2):465, July 1983.

[178] L. L. Jewell and B. H. Davis. Review of absorption and adsorption in the hydrogen-palladium system. *Applied Catalysis A: General*, 310:1, August 2006.

[179] H. Conrad, G. Ertl, and J. Küppers. Interactions between oxygen and carbon monoxide on a Pd(111) surface. *Surface Science*, 76(2):323, September 1978.

[180] T. Engel. A molecular beam investigation of He, CO, and O_2 scattering from Pd(111). *J. Chem. Phys.*, 69(1):373, July 1978.

[181] W. K. Kuhn, J. Szanyi, and D. W. Goodman. CO adsorption on Pd(111): the effects of temperature and pressure. *Surface Science*, 274(3):L611, August 1992.

[182] M. K. Rose, T. Mitsui, J. Dunphy, A. Borg, D. F. Ogletree, M. Salmeron, and P. Sautet. Ordered structures of CO on Pd(111) studied by STM. *Surface Science*, 512(1-2):48–60, June 2002.

[183] X. Guo and J. T. Yates, Jr. Dependence of effective desorption kinetic parameters on surface coverage and adsorption temperature: CO on Pd(111). *J. Chem. Phys.*, 90(11):6761, June 1989.

[184] G. Krenn, I. Bako, and R. Schennach. CO adsorption and CO and O coadsorption on Rh(111) studied by reflection absorption infrared spectroscopy and density functional theory. *J. Chem. Phys.*, 124(14):144703, April 2006.

[185] C. Harendt, J. Goschnick, and W. Hirschwald. The interaction of CO with copper (110) studied by TDS and LEED. *Surface Science*, 152-153(Part 1):453, April 1985.

[186] M. Vollmer, G. Witte, and C. Wöll. Determination of Site Specific Adsorption Energies of CO on Copper. *Catalysis Letters*, 152:453, 2001.

[187] A. Wille, P. Nickut, and K. Al-Shamery. Low temperature dissociation of CO at reactive step sites of Pd(112). *Journal of Molecular Structure*, 695-696:345, June 2004.

List of Figures

2.1 Lennard-Jones potentials for activated (a) and non-activated (b) dissociative adsorption. 6

2.2 Contour plot of the PES along a two-dimensional cut through the six-dimensional coordinate space of H_2/Pd(100). The inset shows the location of atoms above the surface as well as the orientation of the molecule axis.(Taken from [42]) . . . 8

2.3 Calculated coverage dependent sticking coefficient $S(\Theta)$ normalized to the initial sticking coefficient $S(0)$ as a function of coverage Θ. Dissociative adsorption with n=2 (a), non-dissociative adsorption with n=1 (b) and precursor mediated dissociative adsorption with n=2 and K=8 (c). 11

2.4 Relationship between a hypothetical sticking coefficient $S(v)$ (a) and the velocity distribution of the desorbing (solid line) and scattered (dashed line) flux (b). The solid line in (a) corresponds to the velocity distribution of the incident flux. . . . 15

2.5 Simulated TPD spectra for kinetic orders $n = 0, 1, 2$. For all spectra a desorption energy of $E_{des} = 2eV$ and a heating rate $\beta = 1K \cdot s^{-1}$ was chosen. The corresponding preexponential factors were chosen to be $10^{28} molecules \cdot cm^{-2} \cdot s^{-1}$ for $n = 0$; $10^{13} s^{-1}$ for $n = 1$ and $10^{-2} cm^2 \cdot s^{-1} \cdot molecule^{-1}$ for $n = 2$. 21

3.1 Illustration of the UHV setup for time-of-flight measurements. 25

3.2 Illustration of the UHV setup for line-of-sight mass spectroscopy. 26

3.3 Topview of the principle arrangement of devices in the main chamber. EU...evaporation unit; IG...ion gun; TOF...time-of-flight spectrometer; KS...potassium source; LEED...low energy electron diffraction optics; QMS...quadrupole mass spectrometer; AES..Auger electron spectrometer 27

3.4 UHV-main chamber setup from the point of view of the evaporation unit as used during the TOF measurements: 1 Permeation source; 2 LEED screen; 3 ion gun; 4 potassium source; 5 AES; 6 tungsten filament; 7 QMS; 8 Knudsen cell. 28

3.5 Picture of the main chamber setup during the LOS mass spectrometry measurements as seen from the Auger electron spectrometer. 1 sample holder with Pd disc; 2 LEED screen; 3 ion gun ; 4 potassium source; 5 atomic hydrogen source; 6 LOS detector + gas dosers; 7 pivoting quartz micro balance from evaporation unit 28

3.6 Cross section of the used permeation source as designed by G. Pauer [10]. 1 palladium crystal; 2 nickel cylinder; 3 molybdenum heating coil nestling between concentric ceramic tubes ; 4 several layers of tantalum foil for heat radiation shielding ; 5 stainless steel cap; 6 stainless steel tube $\frac{1}{16}$"(gas supply). 31
3.7 Calculated equilibrium permeation flux through a 1.5 mm thick palladium membrane according to Sievert's Law (3.1). The right hand side scale indicates the theoretical equilibrium pressure in the UHV chamber assuming an effective permeatiing area of 0.38 cm^2 (circular sample ∅ 7 mm) and an effective pumping speed of 1000 l/s. 32
3.8 Basic assembly for the measurement of a TOF-distribution from a particle flux effusing from the permation source. The walls separating the different chambers are just indicated by thin lines. 33
3.9 Cross section of the line-of-sight detector chamber: 1 palladium sample; 2 entrance aperture; 3 connector ring for gas inlet; 4 flange cover; 5 quadrupole mass spectrometer; 6 cooling finger; 7 flange for turbo molecular pump (detector chamber); 8 shutter; 9 flange for turbo molecular pump (main chamber) 35
3.10 LOS detector chamber. The entrance aperture as well as the $\frac{1}{8}''$ gas dosers are clearly visible. 36
3.11 Cut through the evaporator unit with installed Zn evaporator. The microbalance is positioned for monitoring the deposition rate. The sample disc is indicated at its neutral position and at the optimum distance for Zn deposition (5 mm off neutral position). 37
3.12 Photograph of the evaporation unit with installed Zn source (a) on the vacuum side, (b) on the outside. 38
3.13 Cross section of the Zn Knudsen cell. 39
3.14 Different views on the Zn evaporator. 39
3.15 Generation of a fluorescence photon or an Auger electron due to deexcitation following a primary ionization process. a) and b) are illustrations of two competing deexitation processes as response to a core level ionisation. c) Auger emission process involving valance band states.(after [46; 80]) 41
3.16 Principle arrangement for a LEED experiment. 42
3.17 Scheme of the sample fixing by two intricate tantalum wire loops. 43
3.18 Principle geometric arrangement for measuring the angular distribution of the desorbing flux. 45
3.19 Arrangement for the in-line detection of reaction products formed by effusing/permeating D_2 and dosed oxygen. 46

4.1 Determination of the O_2 dosing enhancement factor by monitoring the D_2O formation at constant permeation flux for direct oxgen dosing and 2π exposure. 49
4.2 Top figure: multilayer Zn desorption spectrum of Zn/Pd(111). Bottom figure: plot of the logarithm of the desorption rate versus 1/T. The slope of the straight part gives the desorption energy. 52

4.3 a): Raw data of the detected flux at different lateral displacements. Approximate acquisition time per position ≈ 60 seconds per position. b): Edited data obtained from (a) normalized to the maxium flux. 54
4.4 Monte Carlo simulation of the flux dependence as a function of the lateral displacement. The parameter n of the angular distribution in form of $cos^n\theta$, ranging from n=1 to 10 with increment 1. The geometric parameters are detector aperture:∅ 8 mm; aperture sample distance: 17 mm; effective sample diameter:∅ 7 mm. 55

5.1 Experimentally obtained change of the deuterium desorption flux signal from clean Pd(111) as a function of the lateral sample displacement, for two different temperatures, 523 K and 700 K, respectively. Best fits of simulated curves to the experimental data are shown as solid lines. 63
5.2 Initial sticking coefficient for deuterium on Pd(111) as a function of the kinetic beam energy (taken from Ref. [138]). The solid line through the data points stems from a polynomial best fit function. The kinetic energy distribution of Maxwellian beams with 523 K and 700 K are included. 65
5.3 Angular distribution of deuterium desorbing from Pd(111) as obtained from molecular beam data (figure (5.2)) by applying NES and DB for two different sample temperatures, 523 K and 700 K. The full line corresponds to a $cos\theta$ distribution which is shown for comparison. 66

6.1 Experimentally obtained change in the desorption flux signal for deuterium from the Pd(111) surface, pre-covered with 0.2 ML potassium, at 523 K. The full line through the data points is the MC simulated signal change according to an angular distribution of $cos^3\theta$. For comparison the signal change of a cosine distribution is shown as dashed line. 68

7.1 Evolution of the deuterium signal (∘) and the D_2O signal (•) versus oxygen pressure during water formation on clean Pd(111) at 523 K. At oxygen pressures above $1.5{\cdot}10^{-7}$ mbar the pressure change was faster. 71
7.2 Comparison between the deuterium decrease at 523 K (∘) and at 700 K (•) as a function of the oxygen impingement rate. Data are normalized to the same flux. 72
7.3 Comparison of the calculated deuterium decrease (solid black lines) during water formation on clean Pd(111) with the measured results (∘). (a) Sample temperature 523 K. The thin black line corresponds to the simulation results obtained by using a rate coefficient of $k_{OD} = 5.4{\cdot}10^{-11}$ cm^2·atom^{-1}·s^{-1} for OD formation (literature value [149]). The thick line was calculated using $k_{OD} = 3.2{\cdot}10^{-13}$ cm^2·atom^{-1}·s^{-1}. (b) Sample temperature 700 K. The thin line was obtained by using a rate factor of $k_{OD} = 7.3{\cdot}\ 10^{-10}$ cm^2·atom$^{-1}{\cdot}$ s^{-1}(literature value [121]), and the thick line was calculated by applying k_{OD}=$8 \cdot 10^{-12}$ cm^2·atom^{-1}·s^{-1}. . . 76

7.4 Evolution of the deuterium (solid black line) and oxygen (dashed line) coverage during water formation as calculated for clean Pd(111) at a sample temperature of 523 K (a) and 700 K (b). 77

8.1 Scheme of the measurement principle using the permeation source. 79
8.2 STM image of various VO_x structures on Pd(111): (a) 4×4 V_5O_{14} (160×160 Å^2, U=2.0 V, I=0.1 nA); (b) 2×2 s-V_2O_3 (78×78 Å^2, U=0.04 V, I=1 nA); (c) "wagon-wheel" VO (70×70 Å^2, U=0.1 V, I=1 nA); (d) rectangular VO_2 (200×200 Å^2, U=0.25 V, I=0.5 nA); (e) bulk V_2O_3 (0001) (200×200 Å^2, U=-0.33 V, I=0.1 nA) 80
8.3 LEED patterns for different 0.3 MLE VOx structures on Pd(111): (a) after preparation at 523 K, 4×4 structure, E=67 eV; (b) during reaction of deuterium with oxygen at 523 K, 2×2 structure, E=60 eV; (c) during deuterium desorption at 700 K, VO structure, E=56 eV; (d) during reaction of deuterium with oxygen at 700 K, 2×2 structure, E=64 eV. 82
8.4 LEED patterns for 1 MLE VO_x structures on Pd(111): (a) after preparation at 523 K, "flower pattern", E=39 eV; (b) during deuterium desorption at 523 K, 2×2 structure, E=40 eV; (c) during reaction of deuterium with oxygen at 523 K, 2×2 structure, E=60 eV; (d) during oxygen exposure at 700 K, 2×2 structure+VO structure, E=58 eV; (e) during reaction of deuterium with oxygen at 700 K, 2×2 structure+rectangular structure, E=57 eV; (f) after reaction at 700 K, VO structure, E=62 eV. 83
8.5 LEED patterns of 5 MLE VO_x structures on Pd(111): (a) after preparation at 523 K, bulk V_2O_3 structure $(\sqrt{3} \times \sqrt{3})$R30°, E=57 eV; (b) during reaction of deuterium with oxygen at 523 K, $(\sqrt{3}\times\sqrt{3})$R30°, E=56 eV; (c) during deuterium desorption at 700 K, $(\sqrt{3}\times\sqrt{3})$R30°, E=63 eV; (d) during reaction of deuterium with oxygen at 700 K, $(\sqrt{3} \times \sqrt{3})$R30°, E=42 eV. 84
8.6 Comparison of the AE spectra for the 5MLE VO_x covered Pd(111) surface before and after reaction at 523 K and 700 K. 85
8.7 (a) LEED pattern of figure (8.4e) with calculated LEED spots and rectangular reciprocal unit cell and (b) corresponding geometrical model in real space. . . . 86
8.8 Time-of-flight spectra for deuterium desorbing from clean Pd(111) at 523 and 700 K, respectively. The best fit temperatures T_{Fit} for a Maxwellian distribution are also given, indicating a thermalized desorption. 87
8.9 (a) Time-of-flight spectra for pure deuterium desorption (curve 1) and deuterium desorption during concomitant oxygen exposure (curve 2) from 0.3 MLE VO_x on Pd(111) at 523 K. (b) Time-of-flight spectrum of D_2O resulting from the reaction of permeating D and impinging O_2 on 0.3 MLE VO_x on Pd(111) at 523 K. . . . 88
8.10 (a) Time-of-flight spectra for pure deuterium desorption (curve 1) and deuterium desorption during concomitant oxygen exposure (curve 2) from 0.3 MLE VO_x on Pd(111) at 700 K. (b) Time-of-flight spectrum of D_2O resulting from the reaction of permeating D and impinging O_2 on 0.3 MLE VO_x on Pd(111) at 700 K. . . . 89

8.11 Maxwellian fit temperatures for desorbing deuterium as a function of the VO_x coverage on Pd(111) at 523 K: (□) pure deuterium desorption and (▲) deuterium desorption during oxygen exposure. 90
8.12 Maxwellian fit temperatures for desorbing deuterium as function of the VO_x coverage on Pd(111) at 700 K: (□) pure deuterium desorption and (▲) deuterium desorption during oxygen exposure. 91
8.13 Maxwellian fit temperature for desorbing D_2O as function of the VO_x coverage on Pd(111) at (▲) 523 K and (○) 700 K. 92
8.14 Structure model of the s-V_2O_3 surface oxide on Pd(111) (after Ref.[3]) 95
8.15 Experimentally obtained change of the desorption flux signal for deuterium from the Pd(111) surface, pre-covered with vanadium oxide.(□) 0.3 MLE V_2O_3 at 523 K, (▲) 0.3 MLE VO at 700 K, (○) 0.5 MLE VO at 700 K. The full lines stem from MC calculations for $cos^n\theta$ functions with n = 1 and n = 2. 96
8.16 Change of the deuterium flux versus oxgen pressure during water formation reaction at different vanadium oxide coverages at 523 K (a) and 700 K (b) sample temperature. Data are normalized to the same initial flux. 97
8.17 Change of the deuterium flux versus oxgen pressure during water formation reaction at different vanadium oxide coverages at 523 K (a) and 700 K (b) sample temperature. Data are normalized to the same initial flux. 99
8.18 Initial reaction probability versus vanadium oxide coverage at 523 K (■) and 700 K (○). 100
8.19 Fraction of the deuterium flux which was consumed by the water formation versus vanadium oxide coverage at 523 K (■) and 700 K (○). 100
8.20 Initial reaction probability versus vanadium oxide coverage at 523 K (■) and 700 K (○). 102
8.21 Fraction of the deuterium flux which was consumed by the water formation versus vanadium oxide coverage at 523 K (■) and 700 K (○). 102

9.1 Integrated Zn TDS signals versus Zn exposure. The open triangles (△) represent the Zn uptake for the clean sample. The open circles (○) and squares (□) show the Zn uptake at different sulphur surface concentrations. The surface temperature was 300 K. 107
9.2 Comparison of the Auger electron spectra of a partially sulphur contaminated Pd surface (spectrum a), the S contaminated surface after Zn exposure (spectrum b) and a clean Pd surface after Zn exposure (spectrum c). The surface temperature was 300 K and the Zn coverage was approximately 4 ML 108
9.3 Evolution of the Zn994/Pd330 AES intensity ratio during Zn deposition on Pd(111) at 105 K. The intensity ratio for a Zn coverage of 1 ML was calculated to be 3.8% 109

9.4 Amount of adsorbed CO obtained from TDS integration versus Zn exposure. The values are normalized to the maximum CO coverage on the clean Pd(111) surface. Zn was deposited at 300 K and CO exposure was done at 150 K sample temperature. 110
9.5 Zn TD spectrum obtained after a Zn exposure of 72 Hz at a sample temperature of 350 K. Heating rate 2 K/s. 111
9.6 Comparison of thermal desorption spectra from identically prepared Zn/Pd(111) samples obtained by direct inline measurement (shutter open) and by measuring the isotropic signa (shutter closed). 111
9.7 Zn TDS series obtained for sample temperatures of 300 K (a) and 150 K (b) . . 112
9.8 STM image of the morphology of the 0.5 ML ZnPd surface. 1000×1000 Å^2, +1V, 1nA (with the friendly permission of DI Gunther Weirum). 114
9.9 Auger intensity ratios of the Zn 994 eV and the Pd 330 eV Auger line plotted versus substrate temperature. The deposited amount of Zn was 30 Hz=1.3 ML for all preparation temperatures. 115
9.10 STM image of an approx. 0.5 ML Zn covered Pd(111) surface prepared at 300 K. 200×200 Å^2, +0.14 V, 2 nA (with the friendly permission of DI Gunther Weirum).116
9.11 Zn uptake on clean Pd(111) at 150 K (open symbols) and 300 K (full symbols). 118
9.12 Zn TD spectra for 4 ML Zn deposited on Pd(111) at different sample temperatures.119
9.13 Zn uptake of Pd(111) for different sample temperatures. Total Zn coverage (∘); Multilayer (•); High Temperature peak β_2 (△) 120
9.14 Evolution of the Zn/Pd(111) system with temperature. The diffusion as well as the Zn uptake behaviour is indicated. **a)** $\mathbf{T}_{Pd} < \mathbf{300\ K}$ **:** Zn sticks to Pd as well as to Zn, multilayer formation is possible, no Zn diffusion into the Pd substrate. **b)** $\mathbf{300\ K} < \mathbf{T}_{Pd} < \mathbf{400\ K}$ **:** Zn adsorption is still possible, pronounced diffusion processes take place in the interface region (2D-alloy formation). **c)** $\mathbf{400\ K} < \mathbf{T}_{Pd} < \mathbf{500\ K}$ **:** Zn multilayer desorption ($\alpha_1 - \alpha_4$), no sticking of Zn on Zn at this temperatures, ZnPd alloy formation goes on simultaneously. **d)** $\mathbf{500\ K} < \mathbf{T}_{Pd} < \mathbf{550\ K}$ **:** desorption of the residual Zn adsorbed on the ZnPd-alloy surface (β_1), no Zn adsorption possible on ZnPd surface at this temperature. **e)** $\mathbf{550\ K} < \mathbf{T}_{Pd} < \mathbf{750\ K}$ **:** Zn bulk diffusion leads to depletion of Zn at the surface, Zn can stick to bare Pd which is now available. **f)** $\mathbf{750} < \mathbf{T}_{Pd}$ **:** ZnPd alloy decomposes and resurfacing Zn desorbs (β_2), no Zn adsorption possible on Pd. 122

10.1 TD spectra of H_2/Pd(111) subsequent to dosing hydrogen at 150 K. Exposures are: (a) 2, (b) 22, (c) 76, (d) 108, (e) 216, (f) 346, (g) 690, (h) 1036 L. 124
10.2 TD spectra of H_2/Zn/Pd(111) subsequent to hydrogen dosing at 150 K sample temperature. Exposures are: (a) 4,(b) 14, (c) 22, (d) 70, (e) 170, (f) 216, (g) 432, (h) 1728 L. 125
10.3 Hydrogen TDS peak areas from clean Pd(111) and the ZnPd surface alloy plotted versus the exposure. 126

10.4 TD spectra of CO/Pd(111) and CO/Zn/Pd(111). CO exposure: 8.5 L; adsorption temperature: 150 K. 127
10.5 TD spectra of the ZnPd-alloy surface subsequent to CO exposure at 150 K. Exposures are: (a) 0.2, (b) 0.4, (c) 0.9, (d) 1.4, (e) 2.9, (f) 14.7 L. 128
10.6 CO TDS peak areas plotted versus exposure for clean Pd(111) (dashed curve) and the ZnPd surface alloy (solid curve). 128
10.7 Coverage dependence of the CO desorption energy on the ZnPd-alloy surface. . . 129
10.8 CO TD spectra from Zn/Pd surfaces subsequent to a CO exposure of 34 L. The individual Zn layers were prepared at 150 K. The corresponding Zn coverages are given in the figure. 130
10.9 CO TD spectra from Zn/Pd surfaces subsequent to a CO exposure of 34 L. The individual Zn layers were prepared at 350 K. The corresponding Zn coverages are given in the figure. 132
10.10TDS peak area of CO adsorbed on Zn/Pd(111). The CO exposure always was 34 L. The Zn layer preparation was done at 150 K and 350 K, respectively. . . . 133
10.11Evolution of the CO TD spectra after annealing of the ZnPd surface alloy (prepared at 350 K) at different temperatures (annealing time: 10 min; CO exposure: 34 L). 135

Publications and Conference Contributions

Publications in reviewed journals

Model reaction studies on vanadium oxide nanostructures on Pd(111)
Kratzer M., Surnev S., Netzer F. P., Winkler, A.
JOURNAL OF CHEMICAL PHYSICS Volume: 125 Issue: 7 Article Number: 074703 Published: August 21 2006

Angular distribution of desorbing/permeating deuterium from modified Pd(111) surfaces
Kratzer M., Stettner J., Winkler A.
SURFACE SCIENCE Volume: 601 Issue: 16 Pages: 3456-3463 Published: August 15 2007

Preparation and Calibration of Ultrathin Zn Layers on Pd(111)
Kratzer M., Tamtögl A., Killmann J., Schennach R., Winkler A.
APPLIED SURFACE SCIENCE in press

Reaction and desorption kinetics of H_2 and H_2O on activated and non-activated palladium surfaces
Pauer G., Kratzer M., Winkler A.
VACUUM Volume: 80 Issue: 1-3 Special Issue: Sp. Iss. SI Pages: 81-86 Published: October 14 2005

Manipulating the activation barrier for $H_2(D_2)$ desorption from potassium-modified palladium surfaces
Pauer G., Kratzer M., Winkler A.
JOURNAL OF CHEMICAL PHYSICS Volume: 123 Issue: 20 Article Number: 204702 Published: November 22 2005

Time-of-flight studies on catalytic model reactions
Author(s): Winkler A., Kratzer M., Pauer G., Eibl C., Gleisbach D.
TOPICS IN CATALYSIS Volume: 46 Issue: 1-2 Pages: 189-199 Published: September 2007

Adsorption/desorption of H_2 and CO on Zn-modified Pd(111)
Tamtögl A. ,Kratzer M., Killman J., Winkler A.
JOURNAL OF CHEMICAL PHYSICS Volume: 129 Issue: 22 Article Number: 224706 Published: December 14 2008

Conference Contributions

Oral contributions

Model reaction studies on vanadium oxide nanostructured Pd(111) using time-of-flight spectroscopy
Kratzer M., Winkler A.
3rd International Workshop "Nanoscience on Surfaces"
Reinischkogel (Austria), November 2005 (talk Kratzer M.)

Time-of-flight spectroscopy on desorbing D_2 and D_2O from VO_x nanostructures on Pd(111)
Kratzer M., Winkler A.
JRP workshop "Nanoscience on Surfaces" 2006
Schlaining (Austria), Mai 2006 (talk Kratzer M.)

Water formation on vanadium oxide covered Pd(111)
Kratzer M., Stettner J., Winkler A.
56. ÖPG Jahrestagung 2006
Graz (Austria), September 2006 (talk Kratzer M.)

Water formation studies on vanadium oxide thin films covered Pd(111)
Kratzer M., Stettner J., Winkler A.
DPG Frühjahrstagung 2007
Regensburg (Germany), March 2007 (talk Kratzer M.)

Influence of ultra thin vanadium oxide layers on the water formation reaction on Pd(111)
Kratzer M., Stettner J., Winkler A.
57. ÖPG Jahrestagung 2007
Krems (Austria), September 2007 (talk Kratzer M.)

Interaction of CO and H_2 with Zn/ZnO modified Pd(111) surfaces
Kratzer M., Tamtögl A., Killmann J., Schennach R., Weirum G., Surnev S.
DPG Frühjahrstagung 2008
Berlin (Germany), February 2008 (talk Kratzer M.)

Kinetics of Zn adsorption/desorption on Pd(111) Kratzer M., Tamtögl A., Killmann J., Schennach R., Koch H. P., Bako I., Winkler A., Weirum G., Surnev S. *56th IUVSTA NFN workshop* Schlaining (Austria), November 2008 (talk Kratzer M.)

Molecular beam and time-of-flight studies on catalytic model reactions on two-component surfaces
Schennach R., Krenn G., Rendulic K. D., Pauer G., Kratzer M., Winkler A.
15th CRC Symposium
Sapporo (Japan), October 2004, (inv. talk Winkler A.)

Control of the desorption barrier of hydrogen desorption on the Pd+K surface
Pauer G., Kratzer M., Winkler A.
1st International Workshop on Nanoscience on Surfaces (NSOS)
Seggau (Austria), October 2004, (talk Pauer G.)

Poster contributions

Time-of-flight studies of hydrogen-oxygen reactions on clean and modified palladium surfaces
Kratzer M., Pauer G., Winkler A.
55. ÖPG Jahrestagung 2005
Vienna (Austria), September 2005

Model reaction studies on ultrathin vanadium oxide films on Pd(111)
Kratzer M., Winkler A.
DPG Jahrestagung 2006
Dresden (Germany), March 2006

Deuterium desorption and water formation reaction on vanadium oxide nanostructures on Pd(111)
Kratzer M., Surnev S., Netzer F. P., Winkler A.
ECOSS 24
Paris (France), September 2006

Water formation studies on vanadium oxide thin film covered Pd(111)
Kratzer M., Stettner J., Winkler A.
Bunsentagung 2007
Graz (Austria), Mai 2007

Kinetics and dynamics of the water formation reaction on palladium surfaces by using atomic and molecular hydrogen
Pauer G., Kratzer M., Winkler A.
12th International Conference on Solid Surfaces
Venice (Italy), June 2004

Reaction and desorption kinetics of H_2 and O_2 on activated and non-activated palladium surfaces
Pauer G., Kratzer M., Winkler A.
10th Joint Vacuum Conference 2004
Portoroz (Slovenia), September 2004

Reaction and desorption kinetics of H_2 and O_2 on activated and non-activated palladium surfaces
Pauer G., Kratzer M., Winkler A.
54. ÖPG Jahrestagung 2004
Linz (Austria), September 2004

Time-of-flight and molecular beam studies on the system H_2-Pd(111) and Pd(111)+K. Application of detailed balancing
Winkler A., Pauer G., Kratzer M., Schennach R.
Symposium on Surface Science 3S06
St. Christof (Austria), March 2006

Methanol adsorption on Cu(110) and the angular distribution of the reaction products
Demirci E., Stettner J., Kratzer M., Schennach R., Winkler A.
Bunsentagung 2007
Graz (Austria), Mai 2007

Adsorption and desorption processes of clean and Zn-modified Pd(111)
Tamtögl A., Kratzer M., Winkler A.
57. ÖPG Jahrestagung 2007
Krems (Austria), September 2007